OPTICAL STUDIES IN HIGH-ENERGY ASTROPHYSICS

by

P. K. M^{c}Gee, B.Sc.(Hons)

Department of Physics and Mathematical Physics

A Thesis submitted to

THE UNIVERSITY OF ADELAIDE

For the Degree of

DOCTOR OF PHILOSOPHY

August, 2001

TABLE OF CONTENTS

ABSTRACT

This thesis describes the use of optical telescopes in the investigation of astronomical objects which have been discovered by Earth-orbiting high-energy astronomical satellites.

In most cases, the time available for satellite observations of a particular source is very limited, and it is not possible fully to characterise the behaviour of such sources from such data alone. A much fuller understanding of their nature comes about from observations extended in time and, very importantly, at other energies or wavelengths.

Optical telescopes can also be used to assist in the operation of, and interpretation of data from, ground-based detectors used in high-energy astrophysics.

Chapter 2 endeavours to give an historical background to astronomical photometry, and an overview of the types of observations employed in the study of cataclysmic binary stars, and the application of the resulting data to the study of their physical natures.

Chapter 3 describes the equipment used for the majority of the data presented in this thesis. Chapters 4 and 5 discuss the methods used in obtaining useful photometric data from the equipment.

Chapters 6, 7, 8 and 9 include the results and discussions for the work carried out on atmospheric monitoring at Woomera, and on the high-energy sources EUVE J1429-38.0, AX J2315-592 and EUVE J2115-58.6, respectively. The data allow for estimation of certain physical parameters of these objects, and also may throw light on competing models for AX J2315-592. For the three sources listed, the results presented here represent, to date, the most extensive photometric data-set for these particular cataclysmic variable stars.

Chapter 10 covers observations of other sources, some of which contributed to multi-site and/or multi-wavelength observing campaigns.

STATEMENT OF ORIGINALITY

This thesis contains no material which has been accepted for the award of any other degree or diploma in any university or other tertiary institution and, to the best of my knowledge and belief, contains no material previously published or written by another person, except where due reference has been made in the text.

I give consent to this copy of my thesis, when deposited in the University Library, being available for loan or photocopy.

Paddy McGee
B. Sc. (Hons)

ACKNOWLEDGEMENTS

Whilst a work of this nature is written by one person, it has, in fact, much contribution from others. Perhaps this contribution was indirect; perhaps it was of considerable and immediate import. Whatever the case, the author is greatly indebted to a number of people for their help along the way.

I offer sincere apologies to any I may have left out, and hope that those mentioned do not take offence by where in the list someone appears- there has been no attempt to order things at all…

: to my supervisors, Dr. Roger Clay and Dr. Bruce Dawson, for valiant years of undinted support and encouragement, and for maintaining casual confidence in the face of much temporal uncertainty;

: to my fellow Goobers over the years;

: to others who have experienced the joys of Woomera and its clear, dark skies- Drs. Gavin Rowell, Mike Roberts, Steven Dazely, Phil Edwards, Greg Thornton, Alan Gregory and others, and to the CANGAROO group;

: to the people and staff of Woomera, for their unreserved assistance;

: to Hayley Bignall (Adelaide), Jonathan Kemp (*ex* Columbia University, now in Hawaii), Drs. Ian Glass and Patricia Whitelock (South African Astronomical Observatory) for obtaining data for me when all I did was ask:

: to Rob McNaught and Dr. Duncan Steele for accommodation and assistance during trips to Siding Spring Observatory;

: to Dr. Andrew Smith for much witty corridor banter, and programming *nous* (for ST6PHOT);

: to Dr. Nahide Craig (then at NASA's Centre for Extreme Ultra-Violet Astrophysics) for getting me started on photometry of some new and fresh cataclysmic variables;

: to Neville Wild for advice on all things electronic and electrical;

: to all Physics Department staff, but especially those in the store- Janet Hobbs, Carmel Palumbo and the late Margaret Whiteford, for ever-cheerful assistance in the face of unrelenting purchases and orders- and Graeme Eames *et al.* in the workshop;

: to Don Creighton and the Science Faculty, for keeping me employed all the while;

: to my family, Lou, all my friends and fellow Grunties- years of companionship, gut-busting laughs and gentle but definite pressure to Get the Thing Done.

NOTES ON COLOUR FIGURES

Some of the figures (specifically Figures 6.4, 7.9, 7.10, 8.0, 9.0, 9.1, 9.2, 9.9, 10.1, 10.6, 10.12 and 10.23) have been reproduced in colour. However, it was discovered at the last minute that, due to limitations of the laser printers available at the time of printing, it was not possible to include these colour figures in the duplex printing of the pages of this thesis.

Therefore, these Figures have been printed separately, as single-sided sheets, and placed as near as possible to the monochrome versions of the same Figures in the text. The reader will, on occasion, be faced with a blank page in the text, or with a page number which is slightly out-of-sequence. These are the unfortunate side effects of having to insert the colour Figures as individual sheets in the thesis.

The author is sorry for any confusion this scheme may cause, and hopes that you, Gentle Reader, will rise above this obstacle…

CHAPTER 1. INTRODUCTION

Optical photometry and its role with regard to high-energy astrophysics

The energy of a photon is, in a way, a signature of the nature of the physical processes that created that photon. A cool, pre-main sequence protostar may emit predominantly in the infra-red; the source is not very energetic, and neither are the emitted photons. The detection of X-ray or γ-ray photons requires the source object to be the site of energetic processes, such as accretion of matter onto a massive, compact object. Having observations of a particular astrophysical source over a wide range of frequencies (that is, energies) allows more complete characterisation of the physics of that source than do data obtained only at one or a few close frequencies.

This is the fundamental importance of multi-frequency observations of objects. From radio to γ-rays, the more data we have, the better we can hypothesise as to What is Going On. A detection is very useful- we can "see" the object, and examine its behaviour. A non-detection also is useful, though we must be aware of the very distinct possibility that it is limitations of our equipment which may be responsible for such a state of affairs.

Thus, optical data are of import in filling one gap of the electromagnetic spectrum, in terms of being a companion to data obtained at other energies. Historically, there is another and no less important role.

The angular resolution of early high-energy detectors was comparatively poor- perhaps degrees-scale, or worse. It would be known that a high-energy source was in a particular region of the sky, but it was not possible to locate it precisely. In such an area, hundreds or thousands of optical sources (stars, galaxies or even supernova remnants) might be present.

The trick was to look for peculiar objects, those that may not have the optical appearance of "ordinary" stars or galaxies, those that exhibit unusual colours, or variability. Very blue stars, disrupted galaxies, supernova remnants, and so on. Such odd objects may be the seat of the highly energetic processes needed for the production of high-energy photons. Not only spatial correlation would be useful, but also temporal correlation- variability at one energy related to variability at another. With the identification of an optical counterpart, location to the arc-second level was possible.

A definite, precise position allows observations by essentially any detector, no matter what its field-of-view. With the reduction, over time, of the field size of high-energy detectors, better characterisation of the behaviour of individual sources is possible, since confusion caused by any background or other sources in the same field would be reduced.

Thus, positive optical identification of a counterpart, allied with the expected increase in angular resolution of high-energy (or HE) detectors, leads to better data on the objects of interest.

Recent or current HE satellite-borne detectors have error regions of the order of one arc-minute in size, and this allows of the ready identification of optical counterparts by photometry or spectroscopy of optical sources within that error region. Many ROSAT, EUVE and ALEXIS satellite sources have optical counterparts found by such methods.

Another application is the optical monitoring of HE sources as a guide to their activity state. For many objects, increase in optical activity (e.g. brightening) is accompanied by an increase in activity at other wavelengths. By the present time, many HE detectors (most likely on satellites) are pointed; that is, they have small fields of view, and the satellite must be oriented correctly in order to bring a given object into view. (This is not the case with wide-field monitors on some satellites, such as the ROSAT All-Sky Monitor). It is clearly not possible to look at all sources all of the time, so a programme of optical monitoring- even by small telescopes under 0.5-metre diameter or so- of known active sources can alert observers as to when an object exhibits a change in optical behaviour. It would then be possible to schedule that object as a Target of Opportunity for a satellite.

A recent example of the importance of optical/HE co-operation is the discovery of optical counterparts to γ-ray bursters (GRB's). Since their discovery in the 1970's by nuclear weapons treaty-monitoring satellites, GRB's have been somewhat mysterious and somewhat controversial. The data suggested either moderately energetic processes occurring nearby (quite possibly galactic), or very energetic, and sometimes untenably so, processes occurring at extra-galactic or cosmological distances. Since these GRB's were very brief, and initial satellite positions were actually large areas of sky, it was not technically possible to observe any possible optical counterpart.

Examination of the archives of wide-field photographic monitoring programmes covering several decades proved inconclusive, as did limited monitoring of well-localised GRB error boxes. Improvements in the localisation of GRB error boxes have allowed the optical imaging of GRB error boxes very soon after the detection of a burst. To date, several optical counterparts to GRB's have been imaged, and it is now known that the sources are extra-galactic, and indeed at cosmological distances. This places limits on the energies liberated in such events, and they are amongst the most energetic (albeit of short duration) phenomena known. This knowledge has come about because of the imaging and spectroscopy of optically-identified counterparts and suspected host galaxies to these bursts.

The above discussion concerns the case where an object is to be detected both by HE and optical detectors, with the HE detector usually in a satellite (although it could be rocket- or balloon-borne). There are situations, though, where a HE detector is in fact ground-based, and uses the Earth's atmosphere as a vital part of the detection process. Whilst the idea of simultaneous monitoring of the source by such a detector and an optical telescope is applicable, and is often undertaken (consider simultaneous γ-ray and optical monitoring of active galaxies; see, for example, Section 10.3), optical observations can be used as an aide to characterise the efficacy of a particular site for such an ground-based detector.

For ground-based experiments such as atmospheric Cerenkov telescopes or nitrogen-fluorescence detectors, the quality of the atmosphere around the installation is of considerable importance. These detectors look for flashes or tracks of light through the air, caused by the passage of sub-atomic particles through the atmosphere. Of import, especially for fluorescence detectors, is the *volume* of atmosphere in which the particle tracks may be seen. This volume is greater for clean air than for dirty, since attenuation over a given distance is smaller. The greater the observable volume, the greater the overall efficiency of the entire detector. Since the aerosol (e.g. suspended dust particles, etc) content above a site varies daily- and sometimes hourly- the air clarity, and hence observable volume- will change on similar time-scales.

Both Cerenkov and fluorescence experiments operate in the ultra-violet to blue (say 300 to 450 nm or so) region of the optical spectrum, and the instrument design may even include optical filters to isolate this wavelength region. It is possible to gain an at least relative quantification of air quality via simple observation of the change in brightness of stars as they rise or set. This is one of the most fundamental procedures in astronomical photometry (see Chapter 4), and is a readily automated process which can be undertaken by a small (5cm to 12cm) telescope.

For more detailed examination of the atmosphere, techniques using pulsed lasers firing directly into the fluorescence detectors observational volume may be used (as is the case for the Fly's Eye experiment in Utah).

It is clear, then, that there exists a fruitful co-existence and collaboration between optical and high-energy astronomy. The two may be complimentary, sometimes seeing what the other cannot; or they may be supportive, enhancing the understanding of phenomena which are observable in both regimes.

The technology of small-scale optical telescopes and instrumentation is ever evolving and improving, and such facilities may now undertake observations which once were the

exclusive province of instruments such as the Hale 5-metre telescope. They can- and do- provide high-quality data which can greatly aid the investigation of many classes of astrophysical objects. This is especially so when one chooses to observe recently discovered objects, ones for which little or no optical data already exists. In such cases, even quite basic optical photometry can yield important fundamental physical parameters, leading to improved interpretation of data obtained at other wavelengths.

With this in mind, a program of observing new cataclysmic variables was initiated. International Astronomical Union Circulars were perused for notification of the discovery of new HE sources which were suspected of being such objects. Far-southern sources were felt to be especially suited, since there would be few facilities capable of extended data runs on these objects (simply due to the relative lack of observatories at southern latitudes). In these circumstances, even a single small telescope, used intensively on a few choice, new sources, could provide significant information on their behaviour.

This was to be the main direction of the work for this thesis. Other areas also were examined, and so the following three general types of observation were undertaken:

(i) long-term photometry of a few, select variable stars, in order to ascertain some basic physical parameters of these binary systems, and also their general behaviour, with these stars being recently discovered by high-energy detectors on satellites;

(ii) site-testing photometry at Woomera, using non-variable stars, in order to gain a relative idea of the air quality at the observatory site. At one time, Woomera was under consideration as a site for a nitrogen-fluorescence detector;

(iii) short-term (over days) photometry of selected active galaxies in association with HE detectors, either local (the Woomera CANGAROO I γ-ray telescope), or as part of international ground-based and satellite-based multi-frequency observing campaigns.

Whilst the basic approach is the same- measuring the variations in brightness of astronomical objects with an optical telescope- there are subtle differences in technique according to the application. Further, the underlying theme is the same- the application of optical astronomy in collaboration with high-energy astronomy for a better understanding of the myriad active objects abounding in the Up-and-Out (apologies to Cordwainer Smith...).

CHAPTER 2. BACKGROUND

The first chapter was intended to give a general "why" of the use of optical photometry in high-energy astrophysics. This chapter aims to give a brief historical context to the methods and instruments of photometry in the first instance, and then to give a background of the observations and astrophysics of cataclysmic variables.

The historical section is not intended- or claimed- to be exhaustive, but aims to give something of a flavour of the development of this most important field.

2.1 A brief history of astronomical photometry

Perhaps the first attempt at photometry (at least in Western science), was the catalogue of some 1,000 stars produced by Hipparchos (160-127 BC). In this catalogue, the stars were divided, according to their apparent brightness, into six classes; those of the "first magnitude" were the brightest, and those of the "sixth magnitude" were the dimmest. This was, of course, a purely visual estimate, and as the eye is rather non-linear in response to light- and is approximately logarithmic in this regard- this ancient magnitude scale set the basis for our logarithmic magnitude-flux relation.

The original scale was formalised by N. R. Pogson in 1856 (Henden and Kaitchuck 1990, Section 1.2). He specified that a magnitude difference of 5 magnitudes corresponded exactly to a flux ratio of 100:1, and this may be expressed as

$$m_1 - m_2 = -2.5 * \log(F_1/F_2)$$

where m_i is the magnitude of a given star and F_i is the observed flux from a given star.

This formalised scale does not, however, have a defined zero point, since it involves only magnitude differences and flux ratios. The Pogson scale was completed by his assumption that the stars Altair and Aldebaran should have magnitudes of 1.0; these were chosen in order to give reasonable agreement between the new scale and the ancient one of Hipparchus.

However, magnitude estimates were still produced by entirely visual means, and this was a source of some difficulty. Errors in visual photometry can come about due to different colour sensitivities in different individual's eyes, for example, and- as ever- measurements of faint stars will have correspondingly larger errors. What was required was an objective and repeatable technique which would remove these visual errors.

The photographic process promised much in this regard. Plates could be exposed for extended periods, thereby increasing the magnitude limit to which measurements could be

made, certainly to fainter than could be achieved by visual means with a given telescope. Also, a permanent record of the data is provided, and this can be examined by many observers, and analysis and reduction of the photographic data undertaken as strictly as possible. Another advantage is that many star images may be recorded on a given plate, so that many calibration points are provided by each plate. Furthermore, *areas* of sky could be surveyed and monitored for suspected or unknown variables with much greater efficacy than with visual means alone.

The basis of photographic photometry is the relation between a star's brightness and the density and diameter of its image on the photographic emulsion. With appropriate exposures on standard stars of known brightness, the images of stars of unknown brightness can be measured and calibrated to yield their magnitudes in the photographic photometric system. With standardisation of observational techniques and equipment, processing and reduction and analysis methods, much of the subjectivity inherent in the purely visual methods can be removed.

However, there are some caveats to be acknowledged. The photographic emulsion is linear in its response to incident light over much of the D-log(E) plot (a plot of emulsion density as a function of exposure given to the emulsion)- but not all. If measurements are to be made outside this linear portion, the non-linearity must be known and accounted for correctly. (It would be better, of course, if the non-linear region were to be avoided altogether, if possible).

A problem in the early days was that the wavelength response of the emulsions in use at the time was somewhat different from the response of the human eye. Namely, emulsions were generally blue-sensitive only, whilst the dark-adapted eye is most sensitive in the yellow-green part of the spectrum. Thus, photographic magnitude differences did not necessarily correspond to visual magnitude differences; the two systems are measuring the starlight over rather different wavelength ranges, and this will have some effect. So, the zero points of the visual system could not be used, and a new set of standards had to be measured.

The era of *photoelectric* photometry began in the 1890's with the work of Monck and Fitzgerald in Dublin during 1892 (Hall and Genet 1988, Section 2.2).. They used a selenium photoconductive cell, which gives a change in voltage or conductivity when the sensitive surface is exposed to light. The cell was used with a 9" refractor and yielded successful measurements of the light from Jupiter and Venus. These results were reported in an 1895 paper by Minchin, who also manufactured the selenium cell.

Further improvements to the cell allowed observations of bright stars using a 24" reflector, this work being accomplished by Wilson, Minchin and Fitzgerald. An 1896 paper by Minchin reported on the observations of ten bright stars. However, the output of the cell was very small, leading to difficulties of measuring the output, and, as the sensitive area itself was minuscule, star acquisition and guiding must have been difficult.

By 1907, Joel Stebbins in the U.S.A. was using selenium cells for photometry, employing a galvanometer to measure the change in the cell's resistance upon exposure to light (Hall and Genet 1988, Section 2.3). It was at this time that the idea of refrigerating the detector first came about. Evidently, it was noted that the cell performed better (a higher signal-to-noise ratio) during cold winter nights; and so artificial cooling of the cell was subsequently employed to improve performance. In 1910, Stebbins published a light curve of Algol, based on his observations, which showed the hitherto unseen secondary eclipse- a testament to the greater precision obtainable by photoelectric means (Henden and Kaitchuck 1990, Section 1.2).

During 1913, Stebbins began using potassium hydride photo-emissive cells (Hall and Genet 1988, Section 2.3). The output is an electrostatic charge which may be accumulated, and then measured when it has reached sufficient size to allow accurate measurements. This was undertaken by an electrometer, a device which both accumulates the charge and furnishes voltage measurement. By the early 1930's, Whitford had applied vacuum tube amplification to the output of the photo-cell, and also isolation of the electrical components of the photometer head in a vacuum- both of which considerably increased signal-to-noise ratio and ease of operation (Hall and Genet 1988, Section 2.3).

In 1932, Hall put the caesium oxide/silver photo-cell into operation (Hall and Genet 1988, Section 2.3). This device demonstrated a broad wavelength response, allowing filtered measurements over a greater range, but also an initially fatally high thermal current. This latter fault was cured by the cooling of the detector to dry-ice temperatures.

A great advancement in the technology of photometry came about when the photo-multiplier tube (PMT) was invented in the mid-1930's. The PMT is a photo-emissive device which converts photons into a burst of electrons in the first instance, and then multiplies this burst by further emission of electrons along a chain of secondary stages. This results in a considerable burst of electrons at the output, and these bursts (or pulses) may either be accumulated by a capacitor to give a continuously varying output, or counted individually. Initially, strip-chart recorders were used to record the data, but pulse-counting methods were developed later as electronics technology improved.

PMT's first came into astronomical use in about 1946 (Hall and Genet 1988, Section 2.4). Major PMT types early on include the RCA 931 and 1P21, with the latter becoming the "standard" tube. Indeed, the first widespread PMT-based photo-electric system was the Johnson-Morgan UBV system of the early 1950's, and this used the 1P21 not only as a detector, but as a defining part of the filter pass-bands. For example, the long-wavelength cut-off of the V band is due to the spectral response of the 1P21 tube. Therefore, any photometer design which employs a detector (PMT or otherwise) having a longer red tail than the 1P21 shows, must include extra filter glasses in order to bring the V pass-band to a suitable form.

The performance of PMT's generally improves greatly when they are cooled, and provision of cooling is a major part of PMT-based photometer design.

PMT design and manufacture has advanced considerably over the decades, such that many spectral responses are now available, with respectable quantum efficiencies, ease of availability and, indeed, ease of use. With suitable mixes of photo-emissive materials, they now provide spectral coverage from the ultra-violet to the infra-red. Also, with improvements to post-PMT electronics (such as for fast pulse-counting techniques), mass data storage and use of computers for data reduction and analysis, PMT-based photometers are still extremely useful for the investigation of high-speed (seconds scale and faster) phenomena in photometry.

With the exception of the photographic plate or film, all the detector types mentioned so far are one-dimensional. That is, rather than recording an image, they record the total intensity of light from a given patch of sky, with the size and shape of that area being determined by the size and shape of the sensitive area of the detector, and the focal length of the preceding optics. If it is desired to build an intensity map of a region of sky, the detector must be moved in some pattern across that region, and the intensity recorded at each point- a tedious and time-consuming approach. Similarly, only one object can be measured at a time, necessitating interpolation between measurements in, for example, the study of short-period variable stars where comparison star, check star, variable star and sky all must be measured. What is wanted is a two-dimensional device, capable of producing an image, with good quantum efficiency and the generally linear response associated with photo-electric devices.

In 1936, Lallemand published a paper in which he proposed and named an "electronic camera" (Young 1974, Section 6.2.4). This type of device (generally referred to as electrographic cameras) has a photo-emissive cathode onto which the telescopic image is focused. This results in release of electrons from the cathode, and these are focused by electrostatic or, more commonly, magnetic, means onto a photographic emulsion or plate.

This is possible since silver grains in such emulsions can be rendered developable by the incidence of electrons, as well as of photons. Note, however, that the use of special nuclear track emulsions improves the overall performance of such a system.

1951 saw Lallemand and Duschesne publish initial results obtained with their camera, and suggested its application to astronomical imaging (Young 1974, Section 6.2.4). Particular benefits of the use of such a camera for astronomy include the linearity of the output (i.e., the density of silver grains in the resultant 'image' being highly linear with respect to the intensity of light incident on the cathode), the high resolution obtainable with correct choice of emulsion, and the complete absence of reciprocity failure which greatly increases the required length of exposures with ordinary photography.

However, Lallemand's design requires that a new cathode be used every time the camera's vacuum seal is broken when it is fitted with a new batch of emulsions. Furthermore, if the data are to be used for photometry, each new cathode must be calibrated, and one of the plates must be sacrificed to this task. Also, the preparation of such a camera for use is an involved process taking several hours.

The U.S. Navy Electronic Camera, developed in the 1960's, is in some senses a refinement of the Lallemand design, in that a cathode is used repeatedly, since plates are introduced into the camera by means of an air-lock, and the high-vacuum region enclosing the cathode is kept quite separate from the plate chamber (Young 1974, Section 6.2.5). Quantum efficiencies of 10-20% at 420 nm are typical with this design.

Another 1960's device was the McGee spectracon in which, similar to the design of the Navy Camera, the emulsion is kept separate from the high-vacuum region (Young 1974, Section 6.2.6). These devices were the most common electrographic cameras in use by the mid-1970's.

As with PMT-based photometers, these devices had their own intrinsic and operational peculiarities, but they had the advantage of being two-dimensional detectors. Therefore, they could provide good photometric data on groups of objects, such as stars in open or globular clusters, or galaxy clusters, or on diffuse sources, or could be used as efficient detectors in spectrographs, where multiple spectra could be recorded on a single electrographic plate. An efficient, linear and easy-to-use area detector would provide perhaps the ultimate in photometric detectors. Electrographic cameras were perhaps close, but not quite there.

A closer approximation to this ideal was born in the early 1970's. The first charge-coupled devices (CCD's) were described by Boyle and Smith in a 1970 paper (Janesick and Elliott 1992, Section 1). Essentially, a CCD is a silicon chip which has been divided up into a

number of discrete, electrically isolated elements, with each of these elements able to hold an electrical charge. With suitable on-chip and off-chip electronics, the amount of charge in each element may be measured. Originally intended as a memory device, the imaging applications of these chips soon became apparent, since the material of which the elements are made is photo-sensitive; the electric charge held by each element can be produced by light falling on the chip.

The CCD's response to light is essentially linear; the charge in each picture element (or *pixel*) is directly proportional to the amount of light falling on that pixel. The charge measurements, after conversion to digital format by an analogue-to-digital converter (ADC), are in a form easily managed by computers, so that data acquisition, reduction and analysis can all be carried out by computer and, indeed, may largely be automated if necessary. Further, since the CCD can be manufactured as an *array* of pixels (with 2,048 x 2,048 being not too uncommon today), we have an imaging, linear photometric detector which is convenient to use and control, and with data in an easily useable format.

Perhaps the first astronomical CCD-based imager was the "Travelling CCD Camera System" developed around 1973 by NASA's Jet Propulsion Laboratory (Janesick and Elliott 1992, Section 1). Its development was initiated by a desire to promote interest in and awareness of the CCD (by then a very little-known device) in the scientific community. To this end, the system was taken around to major observatories, where its remarkable abilities were demonstrated.

The major manufacturers of CCD's in the early 1970's- namely RCA, Texas Instruments and Fairchild- offered devices quite small by today's standards. Early arrays available from Fairchild, for example, were 100 x 1 and 100 x 100 pixels in size (Janesick and Elliott 1992, Section 3). Currently, 1,024 x 1,024-pixel arrays are not uncommon at small or amateur observatories, and 4-megapixel cameras are common at larger facilities.

Whilst extremely useful, CCD's are, however, not *the* absolute photometric detector. They are generally unsuitable for high-speed work, since there is a non-negligible time required to read-out the pixel array. This read-out time can be reduced drastically by using only a portion of the array, but even so, the PMT is still much better when high temporal resolution is required. Also, the physical size of most (and also the more moderately priced CCD cameras) is small compared with the size of readily available and much cheaper photographic emulsions. Therefore, when large sky-coverage is desired, one must balance the high sensitivity (but small area) of the CCD with the low efficiency (but large area) of the photographic plate or film.

For most photometric programmes, this problem of detector area is not a great issue. However, where a large CCD area is essential, this can be achieved by, for example, the placing of four or more large-format CCD's on a single mounting, such that they form as nearly as possible a single, large sensitive area.

Such is the CCD's great virtue in the field of photometry today, it is perhaps now the prime source of data in such studies. It is applicable to stellar, galactic and nebular photometry; to polarimetry; to single- and multiple-object spectroscopy. It can be used from X-rays to the far infra-red, and admits of measurements to magnitude limits far below that which could be achieved using PMT's or photography. It is available in a large range of sizes, and can be obtained either as a discrete device, or in an already-assembled camera which is ready for immediate use.

The influence of associated technologies has been of considerable importance upon progress in photometry in general. This is largely due to advances in electronics, from those employed to measure the output of the detector itself, to data reduction and analysis, and to control of the telescope and photometric instrument.

For example, recording of the output of the detector has changed from hand-written records of galvanometer or electrometer readings, to strip-chart recordings of a PMT output, to computer-based storage of data from pulse-counting equipment and storage of CCD image data. Early on, much reduction would have been necessary before significant use could be made of the readings obtained; today, light curves may be generated in real-time from CCD image data as they come in from the telescope. Of course there is still a lot of data reduction going on before the light curve appears on-screen, but it is all done by the computer, and may be completely automated.

The use of computers is obvious today in data reduction and analysis. All reduction may be done by computer, with the astronomer's role perhaps being just that of guiding the process and checking for errors. This can represent an enormous reduction in the time taken between data acquisition and data analysis, and also free the astronomer from much laborious, repetitive and dull work. It is also the case that much of the observational work done these days would simply not be feasible- or, in some cases, even possible- without the number-crunching activity of computers, due to the extremely large amount of data involved.

With regards to telescope and instrument control, much is now possible that would not have been feasible before. Automated, remotely-controlled telescopes can operate on every clear night, allowing dense coverage of variable stars, of both short and long periods, or else image and search for supernovae in hundreds of galaxies in each night. They can monitor any

sort of variable object, and their automation means that the astronomer need not spend hundreds of hours at the telescope just to image these objects. Groups of telescopes, spread in longitude, can be used to monitor periodic sources, admitting the study of hitherto unobservable frequencies in the light curves of those sources.

The integration of digital electronics and robotic control into telescope mounting design has meant that a small, CCD-equipped telescope can undertake research photometry on a variety of sources previously accessible only to larger instruments, and with great ease of control and use. Such equipment is currently available completely off-the-shelf. This means that the amateur observer- always an important source of data in many photometric programs- can provide very high-quality data and indeed allow certain types of program to be undertaken which would not have been possible before.

Photometry is concerned not only with the measurement of the intensity of light, but also with the variation of this with the wavelength of the light. That is, we are concerned also with colour, and not brightness alone. This is so since, for example, different physical processes or regions of different temperatures, can be examined by studying particular wavelengths or wavelength ranges only, and ignoring- or measuring separately- other wavelengths. As an example, the radial temperature dependence of an accretion disc in a cataclysmic variable can be determined by examining the wavelength dependence of the eclipse in its light curve (if the system is an eclipsing one, of course).

This being so, the use of filters to isolate desired wavelengths is of great importance. The filter is placed before the detector, in the light path of the telescope, so that the detector (whether it be imaging or not) receives and measures only those parts of the spectrum which are wanted.

The earliest work would have been done unfiltered, since the efficiency of the detectors was very low, and the use of any filter means that some light is being removed before the detector. So, for *any* device- and this applies as well to today's highly efficient CCD's- the maximum signal is obtained when no filter is used. Of course, there are exceptions to this; say, when the sole purpose of an instrument is to examine a particular wavelength, such as in the case of a solar telescope used for Hα studies of the solar disk and prominences. Here, the filter or filters used are a defining part of the instrument.

With improvements in detector efficiency, it became possible to use a variety of filters to divide the spectrum into a number of bands. These bands can be quite broad (wide-band filters), where there is often some overlap between pass-bands; medium-band, where band-

widths are narrower and the pass-bands quite separate; or narrow-band, where small or very small band-widths are desired.

The most important wide-band system originated with the Johnson-Morgan UBV system, as first used with- and in part, defined by- the RCA 1P21 PMT. The B (blue) and V (visual) filter glasses were chosen to give good agreement with the pass-bands of the photographic blue (blue) and photovisual (yellow-green) filters, as used for some time in photographic photometry. The U (ultra-violet) is near-UV only, and was intended to be used to measure the Balmer discontinuity (an absorption feature present in the spectra of several classes of star).

This system has been extended into RIJHKLMN pass-bands, which go though red to the near infra-red and the far infra-red. A single CCD can cover the UBVRI bands, and infra-red imaging arrays are now available for use in the far-IR. Table 2.1 gives the centre wavelengths and band-widths of the afore-mentioned filters.

Medium-band systems, most notably the Strömgren *uvby* system, are used to avoid certain spectral features that can cause problems for wide-band systems. Narrow-band systems are used to study, for example, the strength of specific spectral absorption or emission lines.

The wide-band UBVRIJHKLMN filters are the most common, with UBVRI being the most-used subset, since the longer-wavelength filters require careful instrument and telescope design and high-altitude sites for good results. Also, the narrower band-widths of medium- and narrow-band system mean that more light is removed by such filters, and so the limiting magnitude achievable by a given telescope drops, and the number of objects amenable to study decreases also.

A very important consequence of the adoption of any standard filter set for use by all observers, is that data can be directly inter-compared. If all observations are reduced to the standard system via the observation of standard stars as part of the observing program, then all observations are effectively on the same system, and all the reduced data can be assimilated and compared directly. Even if some observers do not undertake this transformation to the standard system, it is very likely that their data can be so used if they observe stars in the field of the program object for which calibrated magnitudes have been obtained by other observers. This is so since, unless the highest accuracy is desired, one observer's uncalibrated but filtered data will likely very nearly be on the standard system anyway, and a few comparison stars in the field with known magnitudes should permit a reasonable calibration to magnitudes in the standard system.

Table 2.1
Characteristics of UBVRIJHKLMN filters

	U	B	V	R	I	J	H	K	L	M	N
λ (nm)	365	440	548	700	900	1200	1300	2200	3600	4900	10000
$\Delta\lambda$ (nm)	136	196	178	440	200	200	300	400	1200	700	5800

Note: (1) λ is the wavelength of peak transmission of the filter
(2) $\Delta\lambda$ is the width of the filter's transmission curve between those points where the transmission is 50% of the maximum
(3) λ and $\Delta\lambda$ may change slightly for different filter glass combinations and detectors

With the current prevalence of CCD's and the UBVRI system in optical photometry, most observers will have instruments with at-least similar spectral responses and, with a filter set designed to get an overall spectral response close to that of the standard system, data can easily be compared and shared without too many tears. There may be something to be said for the added frisson and exotica of local dialectic variations, but at least in photometry, it is best if everyone speaks the same language.

2.2 The nature and observation of cataclysmic variables (CV's)

This section is intended as a general coverage of the sorts of observations undertaken on CV's, and their astrophysical interpretation. However, since only a few specific examples of CV's were observed as part of the author's study, only those classes of CV actually observed will be under consideration here. Thus, the polar and intermediate polar classes only will be discussed, whilst other types such as recurrent and dwarf novae, and, indeed, non-magnetic systems in general, will not be examined. However, much of the following discussion is relevant to such objects as well.

2.2.1 A general description

CV's are binary stars, consisting of a main-sequence secondary star, and a compact, high-mass (relatively) primary star, the latter being a white dwarf. The cause of their considerable activity and interest therein is that the secondary fills its Roche lobe, and there is then transfer of matter from the secondary star to the primary. The Roche lobe is that gravitational surface about a star which represents the limit of that star's gravitational influence over its own atmosphere. In a CV, the Roche lobe of the secondary will shrink as the orbital period decreases over time, and eventually the Roche lobe will "meet" the surface of the secondary. At this stage, some of the secondary's material will come under the gravitational influence of the companion star. If the companion is the more massive of the two, transfer of mass to that star will occur via an accretion stream.

An important location in the binary system is the *inner Lagrangian point.* It is that point, on a line joining the two stars, where the gravitational attraction of each is balanced by that of the other; it is the point of intersection of the Roche lobes of the two stars. The accretion stream *must* pass through this point. It is not necessarily at the barycentre of the system, however.

Magnetic braking and the gravitational tidal interaction between the pimary and secondary will cause the secondary to rotate synchronously with the system as a whole (Warner, Brian *Cataclysmic Variable Stars*, Cambridge University Press, 1995 (hereafter WCVS) Section 2.3). That is, the secondary star's rotation period will be the same as the orbital period of the system. Furthermore, the orbits will be circular.

Generally speaking, it is the interaction of the matter in the accretion stream or disk with the primary which generates much of the observable phenomena, and the range of time-scales involved in this interaction is tremendous- from seconds-scale variations due to inhomogeneities in the accretions stream itself; to hours-scale changes due to orbital motions

of the two stars; to day- or monthly-scale variations in the accretion rate itself; to millions of years as the binary system evolves, and the nature of the physical interaction between the component stars changes.

In polar and intermediate polar (IP) classes- both classed amongst the *magnetic* CV's- the magnetic field of the white dwarf primary does play an important role in the overall behaviour of the system, and thereby in the phenomena which may be observed. At some distance from the surface of the primary, the accreting material will come under the influence of the primary's magnetic field. In polars, the primary has a magnetic field strength of the order of megaGauss, with a range of 11-75 MG (WCVS Section 6.1) being typical. In these systems, for a part of the trajectory of the accretion stream, the stream is under the complete control of the primary's magnetic field. The field strength is such that the stream eventually is constrained to flow along the field lines, and thence to impact upon the primary's surface near one or more of its magnetic poles.

In IP's, the primary's field strength is lower, and the accretion is magnetically controlled only very near the surface of the white dwarf. Outside this radius, an accretion disc forms around the white dwarf, and it is this feature, as well as the region of impact of the stream on the disc, which may dominate the light from IP's.

Another result of the high field strength in the primaries of polars is that the rotation period of the primary is locked to the orbital period of the system; that is, the system is *synchronous*. This implies that only *one* period- namely the orbital period- will be observed at all wavelengths, since the relative geometry of the component stars is fixed. (However, if the system happens to have two active poles, $P_{orb}/2$ may be evident). Any temporal modulation (aside from accretion rate-dependant phenomena such as flickering) will be due to the changing aspect of the binary as it rotates in our line-of-sight, and this will occur at the orbital period.

In IP's, the system is *not* synchronous, and so the primary's rotation period will differ from the orbital period. This will lead to a periodic change, over the beat period between P_{orb} and P_{WD}, of the relative geometry within the system, and several frequencies will be apparent in the observed data. Not only will the orbital and white dwarf rotation periods be evident, but also the beat period between the two.

It is to be noted that, having said that polars are, by definition, synchronous, there are a number of *asynchronous* polars. In these, the amount of asynchronism is very small (of the order of 1%), but has significant observational effects.

Figures 2.1 and 2.2 are diagrammatic representations of a polar and an IP, respectively, and are not to scale. Figure 2.3 shows the definitions of various angles used to define the geometry of polars.

Having given a general impression of the two types, it is now time to go into more detailed discussions, in terms of the sorts of observations employed, and their astrophysical implications.

2.2.2 Polars

2.2.2(a) Optical photometry

Perhaps the simplest observation that can be undertaken is to obtain a light curve of the CV. This may be done using differential methods only (see Section 5.3), or via calibrated photometry which will yield magnitudes on a standard system. Either will do in the first instance, although, of course, much more information can be derived from calibrated magnitudes.

A light curve is just a series of measurements of the brightness of the CV over time, with sufficient temporal resolution to allow examination of short-term features, and of sufficient duration to cover (preferably) at least a full orbital cycle. The data may be obtained using a PMT (which admits of the highest time resolution) or, more commonly, a CCD.

The light curve will, by the definition of a polar, be modulated at the orbital period. Therefore, a period search undertaken on the photometric data should yield the orbital period as the dominant period, although there may be apparently significant alias periods present if the overall time span of the data is small (obtaining a number of light curves over days/weeks/months, or from a number of longitudes, should help to eliminate many of the doubtful periods).

Typically, the time span of coverage of a CV at its discovery by a high-energy satellite is small, and the estimate(s) of orbital period from the satellite data may well have large error limits. The initial detection may even be quite serendipitous, as when the object is detected by a secondary instrument when the primary instrument is pointed at another, known source. In this case, there is no guarantee of good coverage of the orbital cycle of the CV. Furthermore, there may be considerable interference between the satellite's orbital period about the Earth, and the CV's orbital period, making initial estimates of the orbital period doubtful (Craig *et al.* 1996).

A precise, optically-obtained orbital period will allow data from well-separated epochs to be phased correctly, and possibly allow re-examination of archival data with more consistent phasing (e.g. Schwope and Mengel 1997).

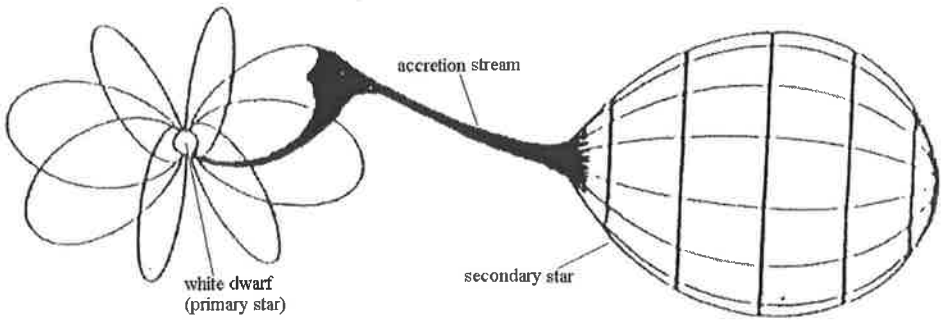

Figure 2.1

Representation (not to scale) of a polar (prepared from WCVS Figure 6.1) Note the tidally-distorted secondary star. Only those magnetic field lines of the primary where the accretion flow couples to it are shown. The region where this occurs is known as the threading region.

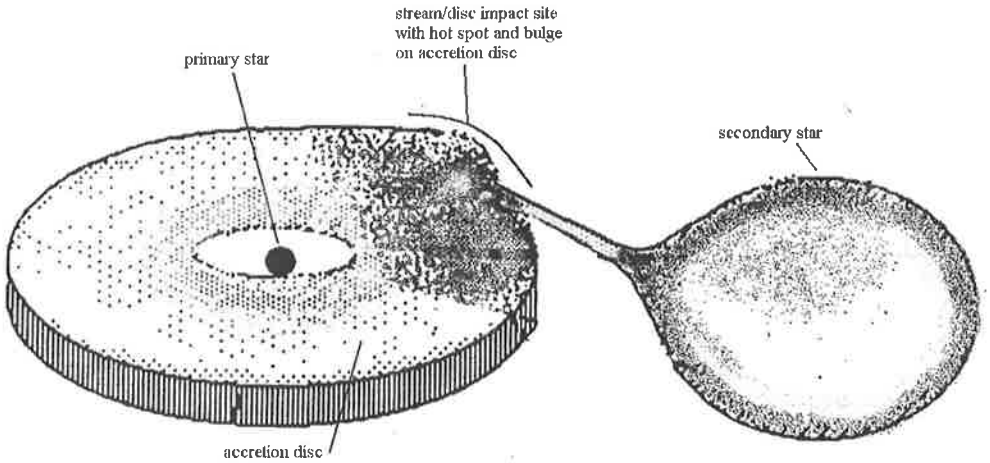

Figure 2.2

Representation (not to scale) of an intermediate polar (prepared from WCVS Figure 7.4) Again, the secondary star is tidally distorted. The accretion disc has a finite thickness, and is hotter towards the centre. At some point near the white dwarf's surface, its magnetic field takes control of the accretion flow, so there will be both disc accretion and accretion onto the primary's surface.
At the point of impact of the stream with the disc, the disc will thicken and also will be hotter.

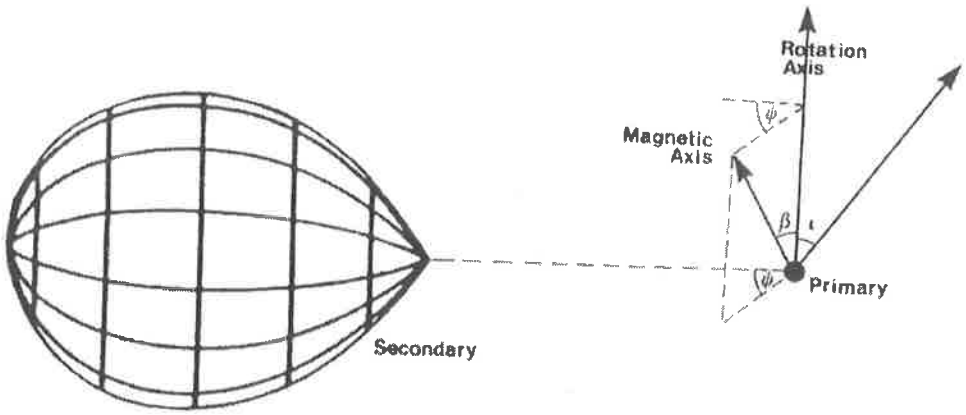

Figure 2.3

Definition of the angles used in describing the geometry of polars (from WCVS Figure 6.3).
i *is the angle between the line-of-sight and the rotation axis of the primary (and of the system as a whole). Similarly, it is also the angle between the plane of the sky and the orbital plane of the system.*
β *is the angle between the rotation axis and the magnetic axis of the primary.*
ψ *is the angle between the line joining the centres of the stars and the projection of the primary's magnetic axis onto the orbital plane. Thus, the magnetic axis may lead or trail the line of centres between the stars. Since some observable phenomena are related to the time of the magnetic axis crossing the line-of-sight, these may occur away from spectroscopic phase zero, which is often defined by the time of crossing of particular spectral lines from blue-shift to red-shift (or* vice versa*). This marks the time at which the line of centres of the stars is in the line-of-sight.*
This definition of i *applies equally to intermediate polars.*
(Adapted from WCVS Figure 6.3).

Having obtained the orbital period from the light curve, some relations may be used to deduce physical parameters of the CV. Such relations have been derived from both theoretical and observational evidence: from Kepler's laws relating orbital period to the masses of the primary and secondary and their separation; considerations of Roche lobe geometry relating the mass ratio to the Roche lobe radius of the secondary and the stars' separation; theoretical estimates of the mass-radius relation for low-mass stars; photometric estimates of the radius of the primary; the relationship between stellar radius, temperature and lunimosity, and so forth. Of course some assumptions must be made, such as the assumed similarity in structure between CV secondaries and main sequence dwarf stars.

The following give the secondary's mass and radius (in units of solar masses) and its absolute V magnitude, as follows (WCVS Equations 2.100-2.102):

$$M_2 = 0.065 P_{orb}^{5/4}(h) \qquad 1.3 \le P_{orb}(h) \le 9 \qquad (2.1)$$

$$R_2 = 0.094 P_{orb}^{13/12}(h) \qquad 1.3 \le P_{orb}(h) \le 9 \qquad (2.2)$$

$$M_V(2) = 16.7 - 11.1 * \log P_{orb}(h) \qquad 2 \le P_{orb}(h) \le 10 \qquad (2.3)$$

where $P_{orb}(h)$ is the orbital period of the system in hours.

Figure 2.4 shows Equation 2.3 graphically (from WCVS Figure 2.46). It can be seen that there is a non-linear departure for $P_{orb} < 2$ hours, and that there is a non-negligible spread about the fit which allows a small range of M_V for a given P_{orb}. This may have significant effect if the CV's apparent and absolute V magnitudes are used to derive its distance. If the CV is not eclipsing, it is necessary that the contribution to the apparent V magnitude from system components besides the secondary star must be estimated. Figure 2.5 shows the relation between the secondary's spectral type and orbital period (WCVS Figure 2.45).

Patterson (1984) gives relations between the secondary's M_V, temperature T_2, mean density ρ, the secondary's mass-loss rate $\dot{M}$, and orbital period, as follows:

$$\begin{aligned} M_V(2) &= 17.7 - 11.00 \log P_{orb}(h) \quad 0.05 < \log P_{orb}(h) < 0.7 \\ &= 22.0 - 17.46 \log P_{orb}(h) \quad 0.7 < \log P_{orb}(h) < 1.1; \end{aligned} \qquad (2.4)$$

$$\begin{aligned} T_2 &= 2630 + 1380 \log P_{orb}(h) \quad 0.05 < \log P_{orb}(h) < 0.7 \\ &= -1800 + 7800 \log P_{orb}(h) \quad 0.7 < \log P_{orb}(h) < 1.1; \end{aligned} \qquad (2.5)$$

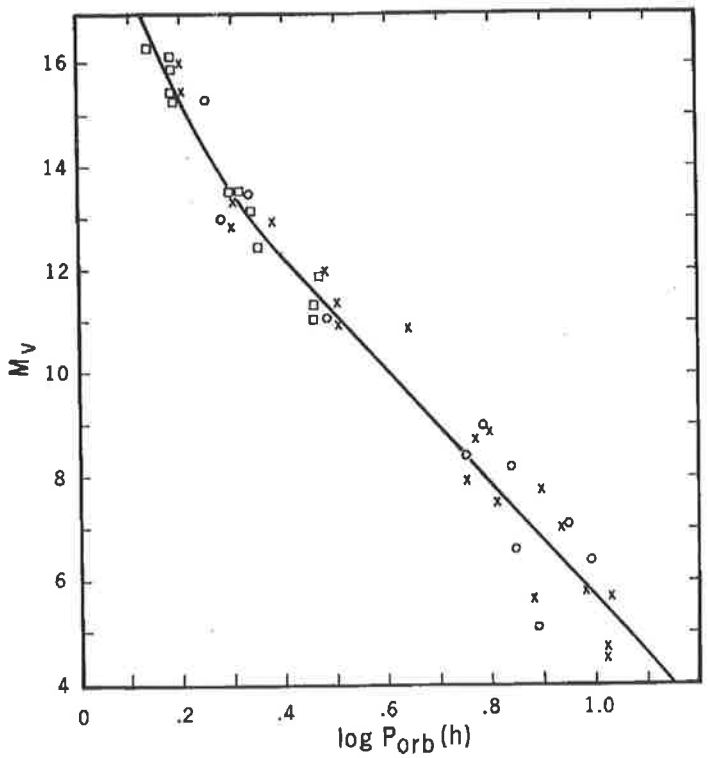

Figure 2.4

The relationship between orbital period and absolute V magnitude of the secondary star (reproduced from WCVS Figure 2.46). Circles represent CV secondaries; squares and crosses are main sequence dwarfs.

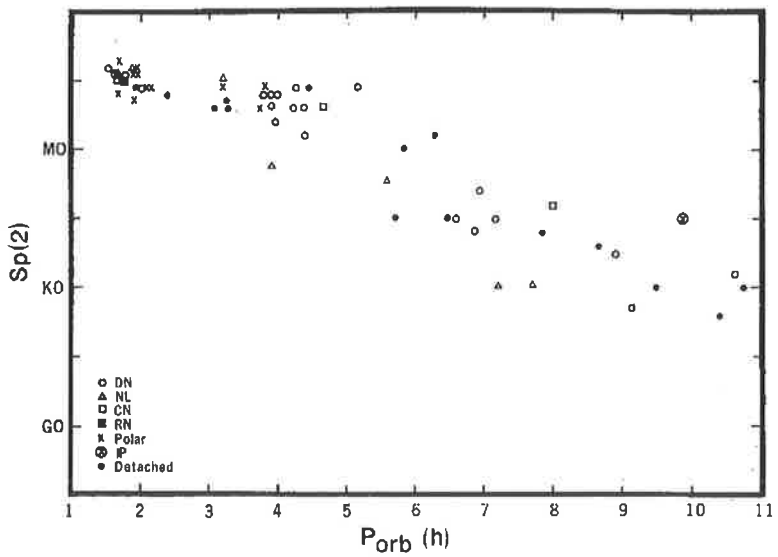

Figure 2.5

The relationship between orbital period and spectral type of the secondary for various classes of CV (reproduced from WCVS Figure 2.45).

$$\rho = \frac{6.905}{(P(h)/4)^2} F(q) \quad \text{g cm}^{-3} \qquad (2.6a)$$

where

$$F(q) = \begin{cases} 1 & q < 0.5 \\ \dfrac{q}{(1+q)(0.38+0.2\log q)^3} & q > 0.5 \end{cases}$$

where

q is the *mass ratio* of the CV, i.e. $q = M_2/M_1$;

{Note: another relation for the mean density of the secondary is the following (WCVS Equation 2.3b):

$$\rho = 107 P_{orb}^{-2}(h) \quad \text{g cm}^{-3} \qquad (2.6b)\}$$

and finally

$$\dot{M} = 5.1^{+3}_{-2} * 10^{-10} * P(h)_4^{3.2\pm0.2} \ \text{yr}^{-1} \qquad (2.7)$$

where

$\dot{M}$ is in units of solar mass per year, and $P(h)_4$ is the period in units of 4 hours.

It is to be noted that these relations apply to all classes of CV, not just to polars.

So, from a simple measurement of the orbital period, the secondary's mass, radius, density, temperature, spectral type and absolute V magnitude may be derived.

As mentioned, if the secondary's absolute V magnitude, M_V, and its apparent V magnitude, m_V, can be found, an estimate of the distance to the CV may be made using the relation:

$$\log d = (m_V - M_V + 5)/5 \qquad (2.8)$$

where d is the distance in parsecs. These magnitudes may be found if the CV is seen to have a full eclipse of the primary, at which time the accretion region(s), and possibly the stream itself, will not be visible. Equation 2.8 does not allow for interstellar absorption along the line of sight; this must either be estimated, or explicitly not accounted for.

Other methods of distance determination which may be applied, with some care and consideration, to CV's in general are those based on infra-red photometry (e.g. Bailey 1982,

Sproats *et al.* 1996) and measurement of linear polarisation (Barrett 1996). For the former, the basic relation is the following:

$$\log d = \frac{K}{5} + 1 - \frac{S_K}{5} + \log \frac{R_2}{R_{sun}} \qquad (2.9a)$$

where

d is the distance in parsecs;

K is the apparent K-band magnitude;

S_K is the K-band surface brightness (which may be estimated if P_{orb} is known);

R_2 is the radius of the secondary star;

R_{sun} is the radius of the sun.

Alternatively, a lower limit to the distance is found from (Harrop-Allin *et al.* 1997)

$$\log d = \frac{K}{5} + \log(R_2) + 1.56 P_{orb} \qquad (2.9b)$$

where P_{orb} is in hours. For this method, the contribution of system components other than the secondary to the total K-band light must be taken into account.

In low-activity states, which occur when the mass transfer rate is reduced, and there will be reduced flux from the accretion region(s) over many wavelengths (but note that, for *polarized* optical flux, the total flux may stay the same, although the wavelength of the peak shifts longward (WCVS Section 6.3.4)). However, the accretion zone(s) will still be active and their locations on the primary may well differ during the low state, due to the lower $\dot{M}$ and changing penetration of the WD magnetic field by the accretion stream (WCVS Section 6.3.4). Since the zones will still be active, and they will still be contributing to the received optical flux, it is expected that there may be changes to the form of the light curve in the low state, quite apart from the gross change in optical flux level.

For eclipsing systems, limits to the inclination, i, of the orbital plane to the plane of the sky, may be obtained. The width of the eclipse is a function of the mass ratio, q, and i. If q is found (see the next section), i may be determined (Stobie et al. 1996).

2.2.2(b) Optical spectroscopy

The richest source of spectroscopic information is the taking of phase-resolved spectra. That is, a sequence of spectra, taken throughout the orbital cycle, with high enough *temporal* resolution to allow differences due to the differing aspect (i.e. phase) of the primary and secondary to be observed and measured. A minimum phase resolution of the order of $\Delta\phi = 0.05$ (Mukai 1988) is recommended. We can derive the orbital period, estimate system inclination and mass ratio, and probe gas velocities within the accretion stream, as well as identifying regions producing different features in the spectra.

The orbital period may be derived from radial velocity measurements of emission lines in the spectra. In the simplest case, the orbital Doppler shifts (which may be presented either as wavelength or velocity shifts) are plotted against time. Their variation will be approximately sinusoidal, and the orbital period is found by fitting a sinusoid to the data.

Assuming a sinusoidal form (that is to say, circular orbits), the radial velocity (RV) curves may be fitted by curves of the form:

$$v(t) = K \sin(2\pi(t-t')) + \gamma \qquad (2.10)$$

where

K is the RV amplitude (usually in km/sec);

t is the time of observation;

t' is some (possibly arbitrary) time zero;

γ is the systemic radial velocity.

If the orbital period is known, Equation (2.10) can be expressed as:

$$v(\phi) = K \sin(2\pi(\phi-\phi')) + \gamma \qquad (2.11)$$

where

ϕ is the phase of the observation

ϕ' is the zero point of phase (defined from polarimetry or zero-crossing of some spectral feature which defines superior/inferior conjunction of the primary).

If the wavelength resolution of the observations is sufficiently high (say, < 2Å or so), it should be possible to differentiate the different components of at least some of the spectral emission lines. Emission lines such as some of the hydrogen Balmer series (notably Hβ and Hγ) or of He (especially He II λ4686), may be composed, for example, of a narrow peak

superimposed on a broader base. A Gaussian may be fitted to the base component in order to estimate its central wavelength, and that of the narrow peak may be taken from the peak of the emission line. It may be found that these components will show different radial velocity curves, with variations in amplitude and phase between the RV curves. There may also be a third component, sometimes referred to as the high-velocity component. These components can be shown to originate in different parts of the CV- from the illuminated face of the secondary star (typically the narrow peak) or from the accretion stream itself in the orbital plane (high-velocity component) and out of the orbital plane (broad base component) (Schwope *et al.* 1997).

The width of the broad base component is due to the large distribution of velocities of the gas in the accretion stream above the accreting pole of the primary (the most simple assumption being that there is just one accreting pole- there may well be two or more, in general). In the case of two accreting poles, the wings of the broad base component may be widened (Mason *et al.* 1989). That is, this component is, at least, velocity-broadened. The width of the narrow component is due partly to the range of orbital velocities found over the illuminated face of the secondary. The phase-resolved observation of these various components can be used to study the relative positions of the various physical components of the CV.

As with period determination from a photometric light curve, a more accurate result will be achieved from measuring RV's over a span of time significantly greater than the orbital period. Also, it is to be hoped that spectra will be taken over as much of the orbit as possible, in order to fill out the RV-time plot and improve the period-finding process.

If the amplitudes, K(1) and K(2), of the RV curves of lines from the primary and secondary can be measured, the mass ratio, q, of the CV can be found:

$$q = \mathrm{K}(1)/\mathrm{K}(2) \qquad (2.12)$$

The determination of q allows a number of physical parameters of the CV to be estimated, via its relation to the Roche lobe geometry of the system. We have (WCVS Table 2.1):

$$R_{L1}/a = 0.500 - 0.227 \log q \quad 0.1 < q < 10 \qquad (2.13)$$

$$R_{L(2)}/a = 0.38 + 0.20 \log q \quad 0.3 < q < 20 \qquad (2.14)$$

$$R_{L(eq)}/a = 0.378\, q^{-0.2084} \quad 0.1 < q < 1 \qquad (2.15)$$

where

R_{L1} is the distance from the centre of the primary to the inner Lagrangian point;

$R_{L(2)}$ is the volume radius of the Roche lobe of the secondary;

$R_{L(eq)}$ is the equatorial Roche lobe radius of the secondary:

a is the separation of the centres of the primary and secondary.

The separation, a, may be found from the relation

$$a = 3.53 * 10^{10} (M_1)^{1/3} (1+q)^{1/3} P_{orb}^{2/3}(h) \quad cm \qquad (2.16)$$

where M_1 may be derived from $q = M_1/M_2$ and M_2 is found from the empirical mass-period relation Equation (2.1).

Some other typical features of the spectra of polars are (Biermann *et al.* 1985) an optical continuum which increases towards longer wavelengths (cf that of disk CV's, where it increases to the blue), and a flat or inverted Balmer decrement.

Evidence of the strong magnetic field of the primary may be found in spectra. However, it is to be noted that the *first* evidence of high magnetic fields in polars came from polarimetry (see the following sub-section). Subsequently, signatures of these fields could be looked for in optical spectra.

An important spectral signature is the presence of cyclotron humps in the red region, observed during the bright portion of the orbital cycle. Depending on the strength of the WD magnetic field, some of the optical emission from the accretion region(s) is in the form of beamed cyclotron radiation, with the wavelength of this radiation being shifted down to the optical region by the high magnetic field of the primary. Information as to the strength and geometry of the field can be gleaned from the variations in the frequencies of the cyclotron humps with orbital phase (WCVS Section 6.5.4).

The Zeeman effect can produce absorption dips near spectral lines (Schwope and Mengel 1997, WCVS Section 6.5.3, Thomas *et al.* 1996), and these can be modelled in order to estimate the strength of the WD field.

2.2.2(c) Optical polarimetry

The magnetic nature of at least one of the binary components of polars became evident with the first polarimetric observations of AM Herculis (Tapia 1977). Both linear and circular polarisations were found, and as significant circular polarisation was an observational trait of magnetic white dwarfs, this suggested the presence of a white dwarf in this system.

Polarimetry of other CV's led to the discovery of other magnetic systems. In a number of these, it was found that the period of the polarimetric variations matched the period of brightness modulation in optical and other wavelengths.

The polarised radiation is produced by cyclotron emission, and Tapia's initial estimate of the strength of the magnetic field in AM Her was of the order of $2*10^8$G. It was later realised that this emission actually comes from cyclotron harmonics, and the requisite field strength could then be considerably reduced (WCVS Section 6.1). Even so, the WD is still the only suitable location in the system for the presence of such strong fields. Thus, the existence of a single period for polarimetric and other data implies that the WD rotation is locked to the orbital period.

Certain features in the polarimetric data can be used to determine the times of appearance of particular physical locations in the binary (such as the accretion zone(s)), or of the relative position of magnetic field lines to the line-of-sight, for example. Since the system is phase-locked, all relative geometry with the binary is fixed, and the timing of features, such as a linear polarisation pulse, can be used to locate the appearance of accretion regions within the orbital cycle, and indeed used as a phase zero (cf timing of red-blue crossing in an RV curve from spectroscopy- which may occur at a different phase).

If linear polarisation is present, a magnetic phase may be determined. Most commonly, magnetic phase zero is defined as that phase at which there is a pulse (i.e. a sharp increase then decrease) in the linear polarisation percentage. This may (but not necessarily so) coincide with a change in sign of circular polarisation (Biermann *et al.* 1985), possibly indicating the appearance of a second accreting pole. This pulse occurs when our line-of-sight is transverse to the magnetic field lines at the accreting pole (Warner 6.3.2.1). Modelling of circular and linear polarisation data can be used to predict the location and extent of accretion regions on the WD surface (Ramsay, G. *et al.* astro-ph/9902324).

In the case of the rare non-synchronous polars (e.g. BY Cam, V1500 Cyg, EUVE J2115-58.6 and a few others), the WD and orbital periods differ at approximately the 1% level. This will lead to a cyclic variation in the relative geometry between the WD and secondary which recurs at the beat period, i.e.

$$1/P_{beat} = 1/P_{WD} - 1/P_{orb} \qquad (2.17)$$

During the beat cycle, it is quite likely that the dominant accreting pole on the WD will change, and this will be seen in the polarimetric data. For example, circular polarisation may

show predominantly positive values at some beat phases; at other beat phases, it will be negative. At the times of pole-switching, where accretion may be occurring at *both* poles, the nett circular polarisation will be close to zero (Ramsay, G. *et al.* 1999).

(A quick word on the non-synchronous polars: these exhibit the strong WD fields typical of polars in general, such that the accretion onto the WD is magnetically controlled. Thus, they will not have accretion discs. The non-synchronism is slight (order of 1%), but may have observational effects which recur at the beat period. The observed phenomena may be explained by the physics of accretion as used for polars, but with the added complication and interest afforded by the slow change in relative geometry within the binary. The asynchronism may be introduced by, for example, a nova explosion in the system).

2.2.3 Intermediate polars

Much of what has been described observationally for polars may be applied to intermediate polars. The complication is that the primary and secondary are not phase-locked, so that a number (indeed, perhaps even a plethora) of periods become apparent.

Part of the definition of an IP is that it be a hard X-ray source and, since X-ray emission may be reprocessed into optical, a detected X-ray periodicity may be expected somewhere in the optical data.

2.2.3(a) Optical photometry

Again, the simplest observation is the obtaining of a time series of the CV. However, since the system is not synchronous, one must expect a number of frequencies to be present in the data, and the interpretation of the output from period-searching routines used on the data is complicated by this. Not only will aliases of true signals be present, but some of the apparent "rubbish" may actually be true signals.

Indeed, there are three basic periods present, and one or more of these may be present in the optical photometry. These will be the rotation period of the primary; the orbital period itself; and the beat period between these two. Note that the degree of asynchronism is much greater than that in the asynchronous polars, so that the IP beat periods are generally shorter. Not only may these basic periods be evident, but various harmonics and *combinations* of harmonics may also be found.

A way through this maze is to obtain long-term photometry (over months or years), and look for stable periods in the data. In the short term, many non-significant alias signals will be present in the data- daily, monthly, some due to the sampling rate of the data. Those

signals due to stable periods in the system- presumably at least the orbital and primary rotation periods- will be present at all epochs, and should be found in period searches undertaken on all sub-sets of the entire photometric archive.

For eclipsing systems, there will be a broad (relative to just the eclipse of the primary) eclipse feature due to the presence of an accretion disc (but note that there may be cases of discless IP's (WCVS Section 7.2.2)). The eclipse may be grazing, where the disc is only partially hidden by the secondary, or total. In the latter case, the eclipse depth may be considerable, as much of the optical emission may come from the disc. Studies of the eclipse profile via high-speed photometry allows the size of the disc to be determined; this may well be variable as the system undergoes changes in the mass-transfer rate over time. High-temporal-resolution filtered data also allow the temperature structure of the disc to be examined.

2.2.3 (b) Optical spectroscopy

As with polars, RV curves, line widths, phase shifts between line components, etc, may be obtained, but the paramount question now is the physical location in the CV of the various emitting regions. There being no unique period for all such regions, the location- face of the secondary, in the stream, in the disc, etc.- must be determined and considered. In general, though, it is considered that RV curves will give a measure of P_{orb}.

2.2.3 (c) Optical polarimetry

The presence of polarisation is part of the definition of a polar; it is necessary, and possibly sufficient. For IP's with a weaker WD magnetic field, polarisation may be observed for those examples with high-strength fields- but it is not expected. The border between the two classes is not absolutely hard and fast, and there will be something of a continuum between high-field IP's and low-field polars.

When circular polarisation is detected, its period of variability tells us about the rotation period of the primary, since such emission is still coming from accretion regions on the WD. The sign of the polarisation tells us which of the accreting regions is currently visible, and the wavelength-dependence may be used to infer the strength of the WD field (WCVS Section 7.4).

2.3 Addendum to 2.2.2(a)

The author's attention has been brought to more recent work on the nature of the secondary star in CV's than was available from WCVS. In particular, two papers were examined which cover this area, namely Smith and Dhillon 1998 and Howell *et al.* 2001.

The former presents observational results in order to establish "new" Sp(2)-period, mass-period, radius-period and mass-radius relations. The latter is based on theoretical evolution of a large sample of binary systems through to the CV phase, of development. It presents, amongst others, radius-period, mass-period and T_{eff}-period relations in the forms of plots showing the expected numbers of systems (at the current epoch in our galaxy) for each co-ordinate in the various phase-spaces. It also examines the question of whether or not CV secondaries can, in fact, be considered as identical to isolated or detached main-sequence dwarfs.

Indeed, CV secondaries may not be considered thus. The modelling suggests that for P_{orb} in the range 3-5 hours, there will be significant differences between main-sequence dwarfs and CV secondaries. For other periods, the discrepancy is somewhat reduced.

Hence, the secondary radii, masses and effective temperatures derived for the systems observed for the author's work, and estimated using the relations in Section 2.2.2(a), will need revising. Those estimates, and those based on the results of the two papers mentioned above, are given below:

Object	P_{orb} (hrs)	source	R_2 (R_{sun})	M_2 (M_{sun})	T_{eff} K
EUVE J1429-38.0	4.765436	2.2.2(a)	0.51	0.46	3565
		Howell *et al.*	0.52-0.53	0.52-0.58	4100
		S&D	0.52±0.04	0.49±0.09	
AX J2315-59.2	1.483975	2.2.2(a)	0.14	0.11	2870
		Howell *et al.*	0.16	0.14	3300
		S&D	0.13±0.03	0.08±0.06	
EUVE J2115-58.6	1.84815	2.2.2(a)	0.18	0.14	2997
		Howell *et al.*	0.20	0.18	3480
		S&D	0.18±0.03	0.12±0.06	

Note that since the plots in Howell *et al.* 2001 show a significant spread in the range of R_2 and M_2 for $3<P_{orb}$ (hr)<6, there is a range of possible values for these parameters for the secondary in EUVE J1429-38.0. For the other systems, there is only a very small spread in the

plots at the relevant periods. The values from Smith and Dhillon 1998 incorporate the limits from the fits to their data.

Compared with the modelling of Howell *et al.* 2001, the relations in Section 2.2.2(a) underestimate all the given parameters. Similarly, the values from Smith and Dhillon 1998 are also lower, but the modelled parameters are just at the top end of the error limits of the former.

Adopting the modelled parameter values will slightly alter some of the numerical results derived in the observation chapters on the three CV's mentioned. However, the changes are not great, and do not alter any of the fundamental points of those sections. They will not be incorporated in this work. However, it will be noted that it cannot be assumed that CV secondaries are equivalent to isolated main-sequence dwarfs, and that the relations give in Section 2.2.2(a) are no longer the most reliable.

CHAPTER 3. EQUIPMENT

3.1 Woomera observatory

The observatory is located at the Department of Physics and Mathematical Physics' field station (for the CANGAROO gamma-ray telescopes) at Range G in the Woomera Prohibited Area. It was established for the author's project, so the work required to prepare such a facility- from digging foundations to first light- was a necessary preamble to any observational work. Longitude and latitude are 136° 47' East, and 31° 6' South. The altitude of the site is about 165 metres above sea level.

The locality is characterised by flat or gently rolling terrain, covered in a red clay soil, and gibber stones. The horizon is clear in all directions, except where obscured by the CANGAROO sheds and various single-storey buildings at the site (to the south and east of the observatory). There are three aerial masts to the west and south-west which preclude tracking an object when the line-of-sight passes through a mast. This is not often a problem.

The weather at the site generally is favourable, and typically only a few days in a row will be clouded out. This is not a strict rule, of course- sometimes up to five nights consecutively have been useless. Conversely, two-week stretches of clear nights are not unknown. Typically, a night which starts clear will stay clear.

There often is some wind at the site, which sometimes can gust to 20 knots or more quite suddenly, or maintain a good 5-10 knots or so throughout a night. Provided that precautions such as appropriate rotation of the observatory building, and use of a windshield in the observatory aperture, are taken, telescope performance does not suffer excessively in such conditions.

There are occasional moderate-to-heavy rains which have the effect of increasing dewing during subsequent cold nights, especially if the air is calm. Due to the rather low humidity typical of the site, dewing is very infrequent, and tends to be restricted to periods following within about a week of significant rainfall.

The observatory site is about 15 km north-north-west from the Woomera village, and a few kilometres by direct line to the airfield. Roxby Downs is about 80 km to the north. There is thus some interference from lighting to the SE, with noticeable skyglow, but it is by no means excessive, and the general sky brightness is sufficiently low for the zodiacal light to be visible, and most distinct, essentially every night. On some occasions the gegenschein is also visible.

A "typical" value for the sky brightness at the site, estimated from data taken using the photometer described in Section 3.4 during U-band extinction photometry, and an absolute calibration obtained during some moonlit sky brightness measurements, is

66 photons/square metre/microsecond/square degree (in the U band).

These units were used in order to aid discussion of the merits of Woomera as a potential site for a ground-based high-energy particle detector array employing the nitrogen fluorescence technique. The sky brightness, of course, can vary on a number of time scales, as well as with zenith angle, galactic latitude and longitude, ecliptic latitude and longitude, or solar activity, so any such given value is rather approximate.

3.1.1 Telescope

The Woomera observatory houses a Celestron C14 0.35-metre Schmidt-Cassegrain telescope (SCT), used with an Santa Barbara Instrument Group (SBIG) ST-6 CCD camera for imaging (see Section 3.3 for details of the CCD cameras employed). The nominal focal ratio is f/11. In practice, however, a Celestron telecompressor lens, is used. This is a positive lens, of short focal length, placed before the telescope focus in order to reduce the telescope's effective focal length. This lens provides a wider field of view for the imaging CCD, and hence reduces the difficulty in finding objects given the comparatively small size of the imaging CCD. This yields a focal ratio of approximately f/7.

With the mechanical design of the Celestron C14 optical tube assembly, focus is achieved by varying the primary-secondary mirror separation. This varies both the position of focus and the effective focal length of the system, and thus incidentally entails a slight image-scale change in the process. As the tube is not made from a material of low co-efficient of thermal expansion, focus change will also occur with a change in ambient temperature, due to expansion/contraction of the optical tube material parallel to the optic axis. Such a change in ambient temperature occurs during any night, to a variable degree, and will generally be enough so that the C14 must be refocused a number of times during a night. This restricts the maximum length of a single data-taking run somewhat, to perhaps two or three hours.

Due to inaccuracies in the construction of the mounting (for example, non-orthogonality of the RA and Dec axes), error in polar alignment of the mount, error in the tracking rate of the RA drive, varying atmospheric refraction at different zenith angles (thus causing a shift in the apparent position of a star), etc, provision must be made for slight adjustments in the telescope's position whilst tracking an object. This can be done via a suitable detector in the focal plane of the main telescope, or via a similar device at the focus of

a smaller telescope on the same mounting. Such an "auto-guiding" device senses changes in the position of a star (the guide star), and issues commands to the mounting's drives in order to keep the guide star at the same location in the focal plane. At Woomera, a Celestron C5 SCT is mounted alongside the C14. The C5 is placed in a cradle which permits adjustment of the direction of its optical axis with respect to that of the C14. The fork arms of the C5's original equatorial mounting, and a tangent arm, are used to provide the orthogonal motions. This arrangement allows one to select a suitable guide-star without affecting the pointing of the C14.

The telescope mounting employed, manufactured by Optic-Craft Machining of Michigan, U.S.A., (Figure 3.1) is a two-tine fork mounting, of sufficient depth to allow full clearance of the focal plane instrument package when viewing the celestial pole. Stepper motors are used on the drives for both axes; the RA drive has a 12"-diameter worm wheel, whilst the Dec drive has a 6.6"-diameter worm wheel. The RA drive is used to effect the rotation of the mounting's polar axis to allow the telescope to track celestial objects, and therefore is in continual operation during observations. The Dec drive is used mainly to effect guiding corrections in declination. The drive motors are run (via controller circuits in a separate box) at stepping rates necessary to produce appropriate angular motion rates for control of the mounting during tracking/guiding and setting. The original stepper motor controller cards were modified slightly to allow control of motor rates and direction by a hand paddle, with the usual four momentary push-buttons for guiding motions, as well as switches for the selection of rates, and direction (e.g. normal/reversed) for the RA drive, as well as an interface to the relays of the ST-4 auto-guiding CCD's control box.

The rates provided are tracking/guiding rates in RA, a guiding rate in Dec, and setting rates in both RA and Dec. The setting rates are sufficient for centring an object in the finder telescope cross-hairs, but are insufficient for slewing the mounting. Thus, slewing is accomplished manually. At the present, there is no facility for computer control of the mounting, so that object acquisition is entirely by manual means.

The RA and Dec axes of the mounting were eventually fitted with Lumicon Sky Vector encoders, which give a numerical read-out of telescope position to 1' of RA and 6' of Dec. Whilst that is the resolution of the encoder display, it is not necessarily the accuracy of the setting of the telescope position. Due to inaccuracies in the mounting construction, in its polar-alignment, initial star alignment of the encoders on the night of observation, etc, the encoder position may be

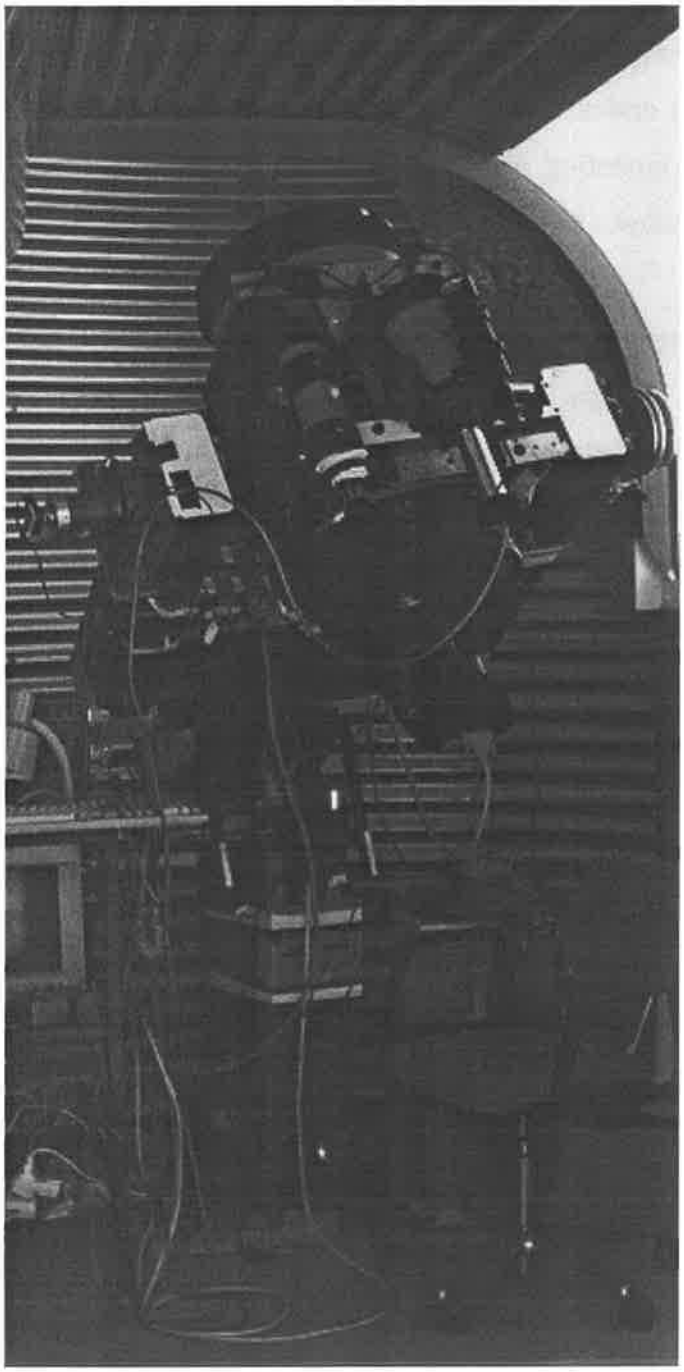

Figure 3.1
C14 and C5, with CCD's, in the Woomera observatory.
Computers are on the trolley to the left.
Stepper motor controllers are in box strapped to pier.
Declination encoder is visible on axle stub
on the left fork tine of the mounting.

up to a few tens of arc minutes in error, and this effect is not repeatable- sometimes the read-out is essentially "spot-on"; at other times, the error may be about 0.5 degrees. However, the accuracy is sufficient to place the telescope near enough to the intended position that a few minutes' work will have the correct field on the CCD.

The C14 and C5 have been fitted with heating collars for their corrector plates, for those comparatively rare nights when condensation on these optical surfaces is a problem.

3.1.2 Building

As with any optical telescope, the C14 is housed in a building in order to protect it from the elements when not in use, to shield it from wind when in use, and to protect ancillary equipment and the observer. In the case of the site at Woomera, these functions are most essential. The location experiences high day-time temperatures in the summer, harsh sunlight, occasional heavy rains, considerable wind, and significant wind-borne dust at ground level.

The observatory building ("shed") is, in essence, a cylinder of some three metres in both diameter and height (Figure 3.2). It is constructed of corrugated and sheet metal over a steel frame, with a standard door for access. An opening of about 1.5 metres width, and continuing over to above the centre of the floor plan, is the equivalent of the traditional dome slit in this case, and gives the C14 complete access from the zenith to the horizon over about 60 degrees in azimuth at the horizon for any given rotational position of the shed. A roller door is used to close the opening. The circular base of the shed runs on six rollers set into a steel ring which defines the extent of the floor, so that the entire shed revolves. The shed was lowered into position over the floor, by crane, on a calm day.

The unusually large slit, whilst causing some problems on windy nights at Woomera (which are not rare) does mean that the shed position (azimuth) need be changed infrequently, if at all, during a night's run on a particular object, especially if the object is of far southern declination. This is of benefit when the telescope has been set on an object, the auto-guider and main CCD are running and the set-up is left unattended for some time. With a customarily thin slit- of width similar to the telescope aperture- one must either manually adjust the dome azimuth frequently, or have an automatic dome rotation facility.

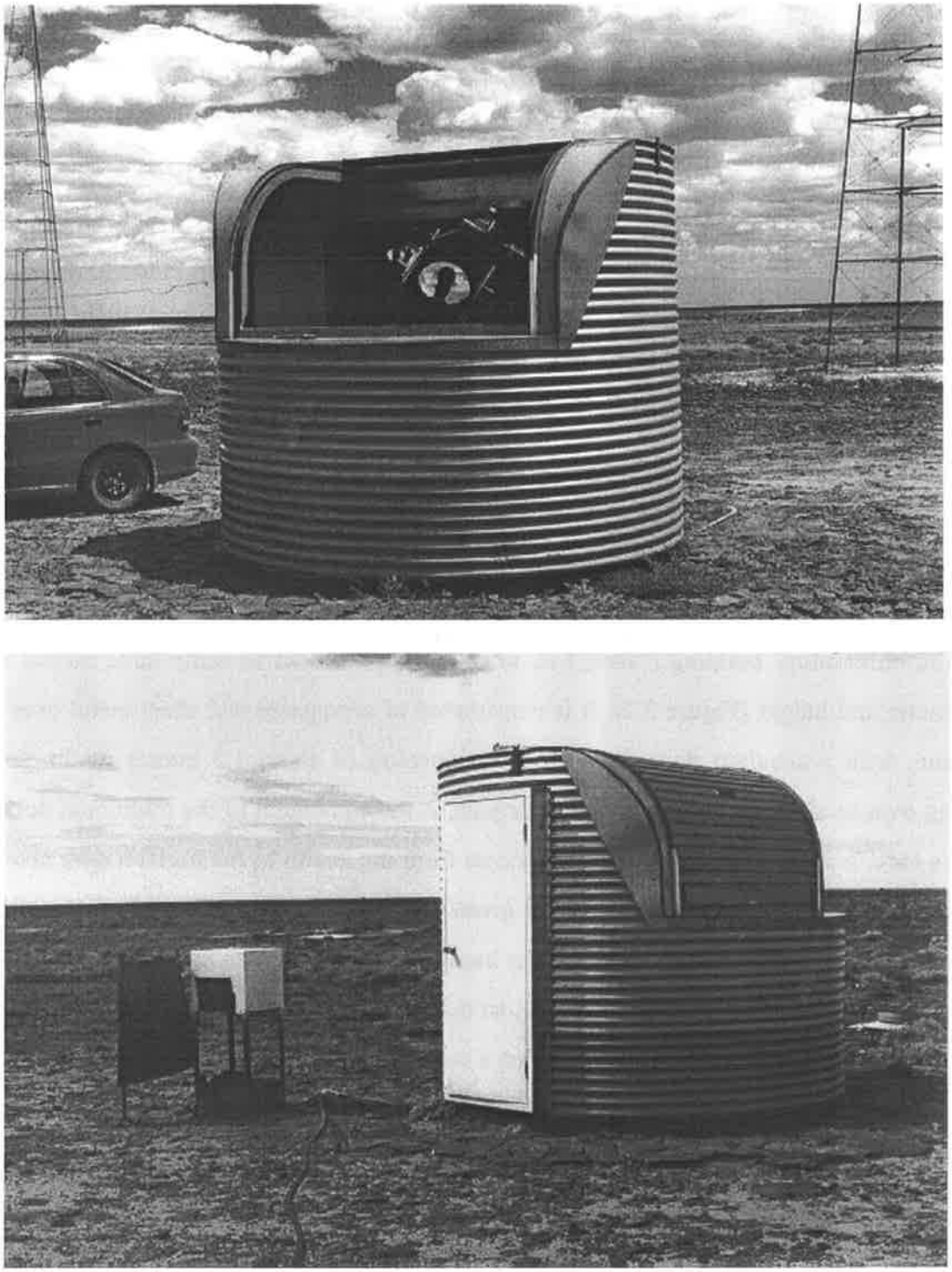

Figure 3.2
External views of the observatory.
Top: shutter open, with view to the NW.
Bottom: shutter closed, view to NE.
In the lower view, also shown is an extinction monitoring camera established by Dr. Masahiro Teshima of the Institute for Cosmic Ray Research, Tokyo.

3.2 Siding Spring Observatory 0.6-metre telescope

In July 1996, observations were carried out over a three-week period using the SSO 0.6m reflector. This is an f/18 Cassegrain by Boller and Chivens, on a torque-tube mounting. The back plate carries an off-axis guider assembly with an xy-stage. An xy-stage is a mechanical device which allows the main instrument to be fixed at the focal plane, and has provision for a secondary detector (e.g. an eyepiece, CCD, etc) to be moved about the focal plane in orthogonal directions, and to be independently focused. The main instrument focus- and approximate xy-stage focus- is obtained by moving the telescope's secondary mirror along the optic axis. The secondary detector is then free to choose a suitable guide star, etc, once the telescope (and hence the main detector) have been positioned on the object of interest. Figure 3.3 shows the imaging and auto-guiding CCD's on this assembly.

The mounting has recently been upgraded with a PC-based control system, used, at the time of observation, essentially as an accurate pointing system. It was found that pointing errors were of the order of 1'. Also, an interface has been made between the drive control system and an SBIG ST-4 CCD (for more detail on the ST-4, see section 3.3.2 below) to enable auto-guiding. However, the field-of-view of an ST-4 at a focal length of 10.8 metres is only about 50", and some searching for a suitable guide star is required.

The 0.6m was used with the same SBIG ST-6 CCD and filters (and SBIG ST-4 CCD) and telecompressor lens as are used at Woomera; the effective focal ratio was found to be approximately f/8. With the telecompressor, the approximate field-of-view of the ST-6 is 6'x 4.5'. Without it, we have 2.7' x 2', and it was felt that with the limited size of the ST-6 chip, use of the telecompressor to enlarge the field was called for.

In order to obtain focus with the instrument package used, it was necessary to remove all the spacing plates from the back of the xy-stage. The use of the telecompressor requires that this package be placed much closer to the secondary mirror than is customary for the instruments usually used on this telescope, and considerable surprise was expressed by the SSO technician as to the amount of shift needed.

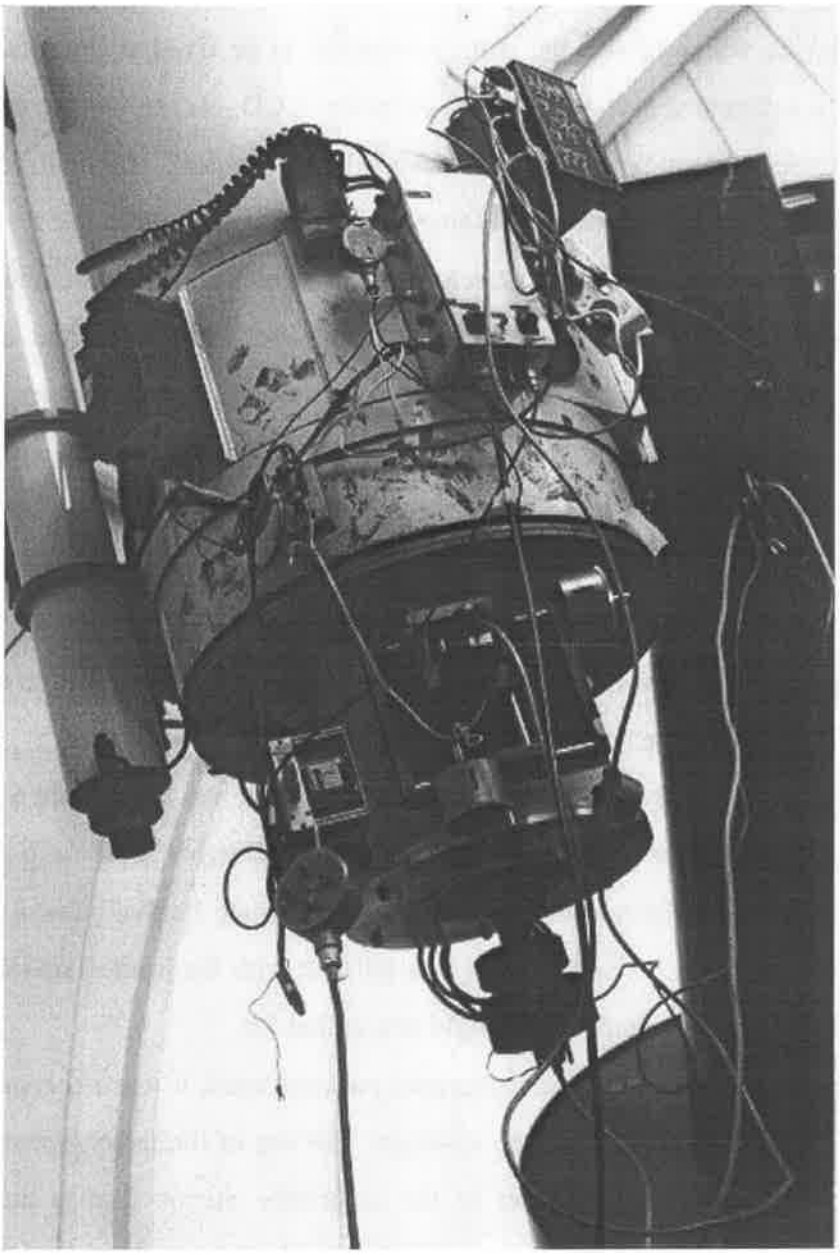

Figure 3.3
The business end of the SSO 0.6-metre in July 1996. The ST-6 and filter wheel are at the main focus position; the ST-4 is mounted on the XY-stage at the secondary instrument focus. The control box for the ST-4, interfaced to the mounting's drives, is near the top of the image. The mount is of the torque-tube design.

3.3 CCD's- imaging and auto-guiding

This section covers the CCD cameras used, and endeavours to give some account of details of their practical use in the observatory. Firstly, though, a brief summary of the CCD detector itself.

The heart of the CCD camera is the CCD chip, which is a silicon-based, solid-state device, initially intended for memory applications. The surface of the chip is divided into a large number of separate regions, each of which, by virtue of the nature of the materials used, and the presence of controlling micro-electronic devices built into the chip structure itself, is capable of holding an amount of charge independent of that of its neighbours.

Other electronics on the chip, as well as some external to it, are used to transfer the charges in each cell, sequentially, to an output stage, where the amount of charge in the corresponding cell is measured. The resultant stream of individual charge measurements then corresponds to the amount of charge in each cell, measured in some particular order. The CCD may be consist of a single line of cells or, as is usually the case, a two-dimensional array of cells.

The material used for the construction of the active areas of the chip is photosensitive. That is, photons falling onto the cells will cause the release of electrons from the material and, over time, an electric charge will build up in the cell. The amount of charge will be, to a first approximation, directly proportional the amount of light falling on that cell. When the chip is read-out, the data stream will be a representation of the distribution of light intensity over the entire chip. Clearly, if an image is focused onto the chip, then we have a two-dimensional imaging detector.

The charge measurements made during read-out are converted to a digital format, using an analogue-digital converter (ADC) in the camera electronics. The resulting numbers are often known as "analogue-digital units" (ADU's). Thus, the image is represented by a digital data stream, which can readily be converted back to a two-dimensional map of the light intensity distribution over the CCD chip-which is to say, the image at the telescope's focus. In this imaging context, where each cell corresponds to a small, discrete element of the image, the cells on the chip are known as *pixels* (from "picture elements").

These data are easily stored and manipulated by computers, and so the entire process from camera control, data acquisition, to data reduction and analysis can be undertaken from a single host computer running the appropriate software.

The CCD is a very efficient detector, having peak quantum efficiencies up to about 90% for the best such devices. This compares very well against more "traditional" detectors

such as photographic emulsions and photo-multiplier tubes, where values of a few to perhaps 20% are found.

The spectral sensitivity of typical CCD's is such that a single device can make useful measurements from B to I and, with much reduced sensitivity, in U as well. UV fluorescent coatings can be applied in order to improve the short-wavelength response.

Cooling of the chip is required for extended exposures of sources of low intensity, as there is thermal production of electrons in the pixels as well as that due to exposure to light, and the eventual amount of thermal charge accumulated over time may swamp the desired signal, or at least significantly reduce accuracy. The rate of production of these thermal charges (known as the "dark current" in general terms) is very temperature dependent; exact values vary, but, typically, an increase of chip temperature of about 6° will double the dark current. Cooling may be achieved by use of liquid nitrogen or by thermo-electric devices such as Peltier modules, for example.

3.3.1 SBIG ST-6 CCD

The Santa Barbara Instrument Group ST-6 CCD uses a Texas Instruments TC-245 CCD array (see Figure 3.4 for the quantum efficiency (QE) curve). The CCD is cooled by a two-stage Peltier device, to a nominal maximum differential of 40° C below ambient (the operating temperature is user-specified in the camera control software). The waste heat from the cooler is removed by heat sink fins on the body of the CCD head, and thus the attainable cooling is very dependent on the ambient conditions. These vary greatly in practice. During summer, when night-time air temperatures can be up to 30° Celsius, the CCD may reach no cooler than -10° to -20° C. In winter, the camera may readily be cooled to around -35° C. As the thermal "current" in the CCD approximately halves for a decrease in chip temperature of about 6°-7° C, this change in cooling level varies the accuracy of the dark frame subtraction during a run. Whilst, in general, the cooler the CCD the better, it is found that condensation on the CCD chamber window can be a problem if the CCD is cooled to temperatures below about -35° C.

The CCD is used with an SBIG CFW-6A filter wheel, which can accommodate up to six circular filters mounted in threaded holders. At Woomera, standard Bessell UBVRI filters, and a clear filter (i.e. even transmission over the entire wavelength range of the CCD), manufactured by Omega Optical of Vermont, U.S.A., are fitted. All filters are of the same optical thickness so that

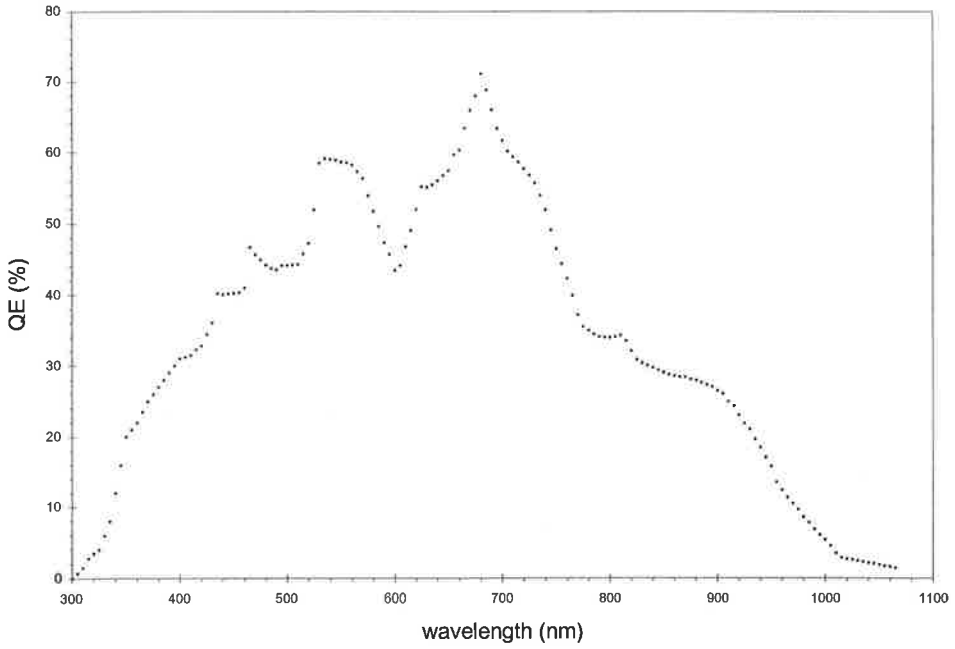

Figure 3.4

Typical SBIG ST-6 CCD quantum efficiency curve. Taken from a Texas Instruments data sheet for the TC-245 chip, and from the SBIG web-site (www.sbig.com).

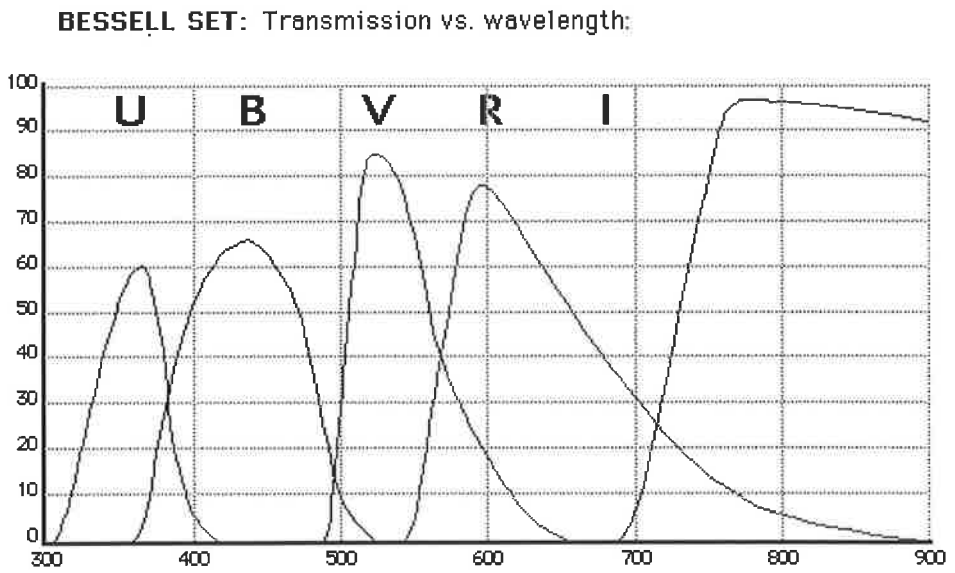

Figure 3.5

Omega Optical UBVRI filter transmission curves.
Ordinate is percent transmission, abscissa is wavelength (nm).
The combination of filters glasses used for each filter is based on a recipe by Dr. Mike Bessell.

no refocusing is required after filter changes. Figure 3.5 shows the manufacturer-supplied transmission curves for this particular filter set. The filter wheel is motor-driven, and filter changes are made from within the SBIG CCDOPS camera operating software.

The camera uses a 16-bit analogue-digital converter, and with 90,375 pixels, a full, uncompressed frame is 180.75 kilobytes in size. With the 115 kilobaud transmission rate between CCD and host computer, a full frame at full resolution takes approximately forty seconds for digitisation and down-load. This places a limit on the temporal resolution obtainable with this CCD when observations are undertaken in standard tracking mode. There are other observing methods, e.g. trailing the images along the CCD during exposure by use of the declination slow-motion, or a non-tracking RA rate (Howell and Jacoby 1986), which allow higher time resolution, but are more involved observationally and in data reduction. For short exposures, this 40-second loss can represent a significant amount of dead-time between exposures.

It is possible to reduce this dead-time by (1) binning the pixels on the CCD, where pixels are grouped together at readout to form larger "super-pixels", thus effectively reducing the number of pixels to be digitised and downloaded; or (2) by using only the central half or quarter (by linear dimension) of the CCD, or (3) by both. The limitation of (1) is the decrease in angular resolution thus entailed; of (2), that there be sufficient stars in the area for appropriate data reduction, and that guiding is sufficient to keep all programme stars within the smaller area; of (3), all problems of (1) and (2) together.

It was found that there is a drift between optical axes of the auto-guider C5 and the C14, such that although guiding appears to be perfect in terms of staying on the guide star in the C5 focal plane (and hence, presumably, maintaining the location of the C14 also), there is a long-term drift in the position of objects on the C14 focal plane. The extent of this drift varies; sometimes it is only a few pixels over, say, two hours, and sometimes it can be a pixel between successive exposures. The cause (and remedy) of this drift is not clear, although suspect areas are the C5 support cradle and possible primary mirror movement in one or both telescopes. The drift can be of sufficient magnitude, however, for one or more programme stars to drift off a half-frame image during a long series of exposures.

The camera, therefore, has been used, with only a few nights' exception, in full-frame mode, and at full resolution (i.e. unbinned).

The ST-6 is run by a 33MHz 486 PC with 1.2Gb hard disc, using SBIG's CCDOPS camera control software for the DOS operating system on the PC. CCDOPS is the software which controls all aspects of CCD camera and filter wheel operation, and is available either as

a DOS or Windows application. As the DOS version is keyboard-based, its use at the telescope is favoured. Images are stored in native SBIG image format using the compression algorithm implemented in

CCDOPS, and a full, high-resolution frame takes about 100kb of memory when compressed. At the end of a night's work, all data are backed-up on an Iomega Zip drive. Data are eventually archived on to CD-ROM.

3.3.2 SBIG ST-4 CCD

The ST-4 uses a Texas Instruments TC-241 array and is cooled by a single-stage Peltier device. This CCD is used on the C5 for guiding. For auto-guiding, the camera takes a reference frame, and the user selects a star image on that frame for the guide star. The camera will then take a continual series of images, digitising and down-loading a 30-pixel box around the initial guide star pixel location. The pixel location of the centroid of the guide star's image in the current frame is compared with that in the reference frame; a change in location causes a relay(s) in the ST-4 control box to trip, which is equivalent to operating the appropriate slow-motion in the hand paddle, in order to bring the guide star back to its original location. In this technique, we have closed-loop tracking.

For this to work, the software (SBIG CCDTRACK) must be calibrated; that is, it must have the value of pixels/second (of time) that operating the drive slow-motions will produce as a movement of a star image on the ST-4 CCD. Also, it must know the "sense" of the slow motions- which one corresponds to an increase/decrease in pixel location for the two axes of the CCD chip. All these are best derived empirically at the telescope. Also, it requires that the hand-paddle be interfaced with the ST-4 relays.

In practice, a guide star near the programme star is chosen using the off-set cradle which holds the C5 alongside the C14 (see section 3.1.1), the reference frame taken, the guide star image selected and the auto-guiding started. Exposures of around five seconds are typical. It is usually not feasible to guide on the programme star, as these are faint (magnitude > 15) and below the detection limit of the ST-4 on the C5.

Clouds can cause problems with the auto-guiding. If the guide star's brightness falls to about one-third of that in the reference frame, for three successive exposures, the software assumes that the guide star is lost, and will not issue further guiding corrections (even though the star may still be detected). If the guide star then drifts out of the guiding box before the cloud thins and its original brightness is resumed, auto-guiding is lost completely.

With the differential reduction of CCD data (see Section 4.3), clouds cause loss of light, and thereby a decrease in accuracy, but useful data are still obtainable if the programme stars are still detectable. This is not the case with photography or single-channel photometry, for example. So, the above-mentioned "loss of guide star" condition can be quite an annoyance when undertaking differential CCD photometry. It can be side-stepped, to some degree, if the observer masks a significant portion of the C5 aperture during the taking of the reference frame- this artificially reduces the brightness of the guide star in the reference frame, enough to mimic the passing of a significant amount of cloud. Hence, the ST-4 will continue to track through considerable cloud which would otherwise have caused tracking to be lost. This technique thus reduces the likelihood that cloud would cause the loss of guiding.

3.4 Photo-multiplier tube

A photo-multiplier tube (PMT) is an opto-electric device which, in essence, converts a photon into a burst of electrons. This is achieved by the use of a photo-emissive plate (the photo-cathode), which first converts a photon into an emitted electron, and then by a series of multiplicative stages which amplify the electron burst at each stage. Eventually, a single photon can give rise to a burst of, say, a million electrons.

At each multiplicative stage, the electrons' paths are guided by magnetic fields defined by the shape and separation of the electron-emitting plates (dynodes) which physically constitute each stage, and the provision of a voltage difference between each dynode. At the photo-emissive stage, the electron path guided as a result of a voltage difference between the cathose and the first dynode.

The photo-cathode is placed either at the end of the tube (i.e. "end-on"), or facing out the side of the tube's glass envelope (i.e. "side-on") as in the archetypal astronomical PMT, the RCA 1P21.

After the final stage, the electrons can be collected in one of two ways, namely (1) the stream of electron bursts can be integrated by a capacitor, and thus yield a continuously varying current with a particular time-constant, which is proportional to the time-averaged arrival rate of photons at the photo-cathode; (2) photon-counting (also known as pulse-counting), where the following electronics are such as to convert, within particular limits, an electron burst at the final stage into a single, easily detected pulse, with the pulse rate proportional to the photon arrival rate.

In either case, a high-voltage power supply is needed, in order to provide the differential voltage cascade across the dynode chain. The electronics used to measure the output of the PMT depend on which of the aforementioned techniques is employed.

With photon-counting techniques, there is a characteristic of the PMT and electronics known as *dead time*. This is the inability of the electronics to detect separate pulses which are caused by photons arriving within a certain time interval of each other. Such closely-timed photons will be counted only as a single pulse. It is necessary to correct the observed count rate for this dead time; the dead time can be found experimentally, or is given by the manufacturer. See section 4.2.3 for details.

The spectral response of the PMT is defined by the materials used in the photo-cathode, and, to some extent, by the composition of the glass used for the tube's envelope, which has its own wavelength-dependent transmission curve. With different materials, coverage extends from the U band through to the near-IR. Also, as there is always some thermal emission of electrons from the photo-cathode, it is customary to cool the PMT to reduce this dark current below acceptable levels. However, this is not always necessary.

A Hamamatsu HC124-03 bi-alkali photon-counting PMT was obtained for use in the extinction photometry programme. This is an end-on PMT, with the tube, high-voltage supply and photon-counting electronics integrated into a single package. An external low-voltage supply is the only other component necessary for a useable system. Figure 3.6 shows the spectral response curve. In this case, the high-voltage supply was programmed via a trimpot in the low-voltage supply as per the manufacturer's data-sheet. No cooling of the PMT was employed; the dark (i.e. no illumination of the photo-cathode) count rate is typically below 100Hz for a tube voltage of 1000V, quite acceptable for the observation programme in question.

For data-logging, a PC counter card was obtained, and a simple, task-specific Pascal program written to control the card and log data. This gave a choice of gate times and overall length of acquisition. The PMT could be (and was) used with a stand-alone frequency counter on some occasions.

The tube was housed in a very simple photometer, containing just a focal plane aperture, a Fabry lens and the PMT. A Fabry lens is a small positive lens placed before the PMT photo-cathode, but after the telescope focus. The telescope focus is, in fact, co-incident with the aperture

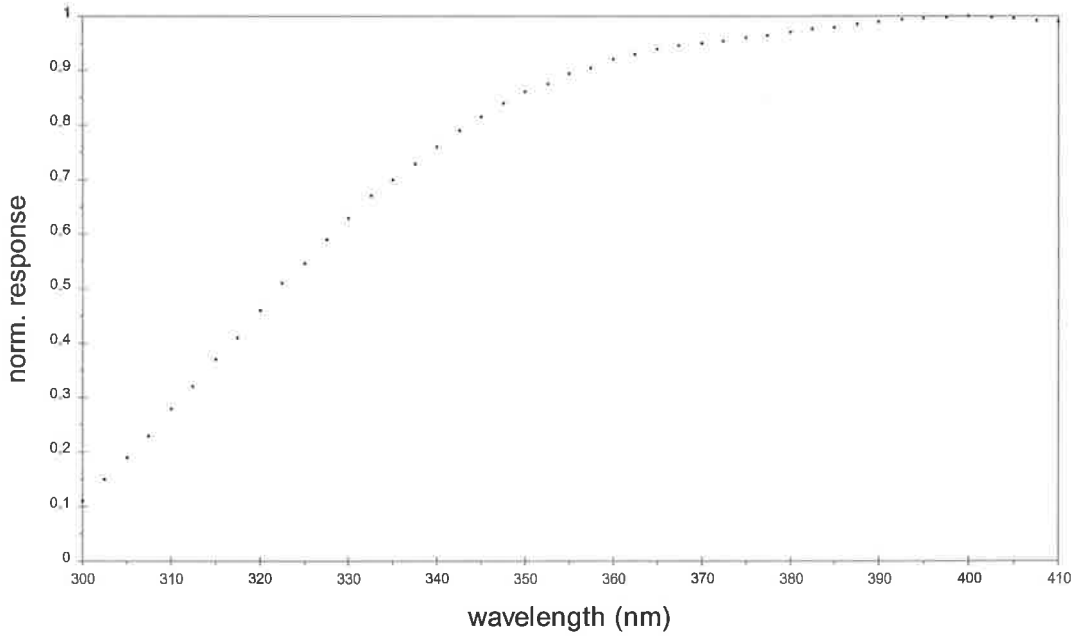

Figure 3.6
Normalised response of the Hamamatsu PMT over the short-wavelength range of the UG-1 filter.

diaphragm used to define the field-of-view of the PMT. Instead of the aperture wheel or slider typically incorporated into a photometer, this design uses individual aperture discs which require partial disassembly of the photometer for changing. It was felt that there would be little need for providing different apertures during data-taking, so this simple alternative was adopted. Also, no filter carrier was incorporated.

The Fabry lens acts to image the telescope objective onto the PMT cathode. As the sensitivity of the cathode can vary across its surface, focusing the telescope directly onto the cathode would result in a variable output signal. Due to tracking errors, movement of the star image due to seeing, etc, the position of the star image on the cathode would change, and hence produce a varying signal. Such variation is quite separate from any intrinsic source variability, and would be practically non-repeatable. Imaging the telescope objective onto the cathode ensures that the light illuminating the cathode stays fixed in position on the cathode, since the physical elements of the photometer/telescope are fixed relative to each other.

The Fabry lens is chosen to suit the cathode size, according to the following relation (Henden and Kaitchuk Section 6.1):

$$F = b * f / D \qquad (3.1)$$

where

F is the focal length of the Fabry lens,

b is the diameter of the image of the telescope objective on the PMT cathode,

f is the telescope focal length,

D is the telescope aperture.

This basic photometer was used with the C5 (having its optical axis co-aligned with that of the C14 for this work), with the C14 used as a finder for the C5. For the extinction photometry, we had a five-inch-diameter Hoya UG-1 filter (as used for the Fly's Eye I experiment) and this suggested using the C5, with the filter being placed in front of the C5's corrector plate, rather than with a small filter piece being placed near the PMT.

There was no attempt to include a filter to block any red-leak associated with the long-wavelength transmission of the UG-1 filter (see Figure 3.7 for the UG-1 transmission curve), as the PMT response in that spectral region is minimal, and such a blocking filter is not included in the Fly's Eye or Auger fluorescence detector designs.

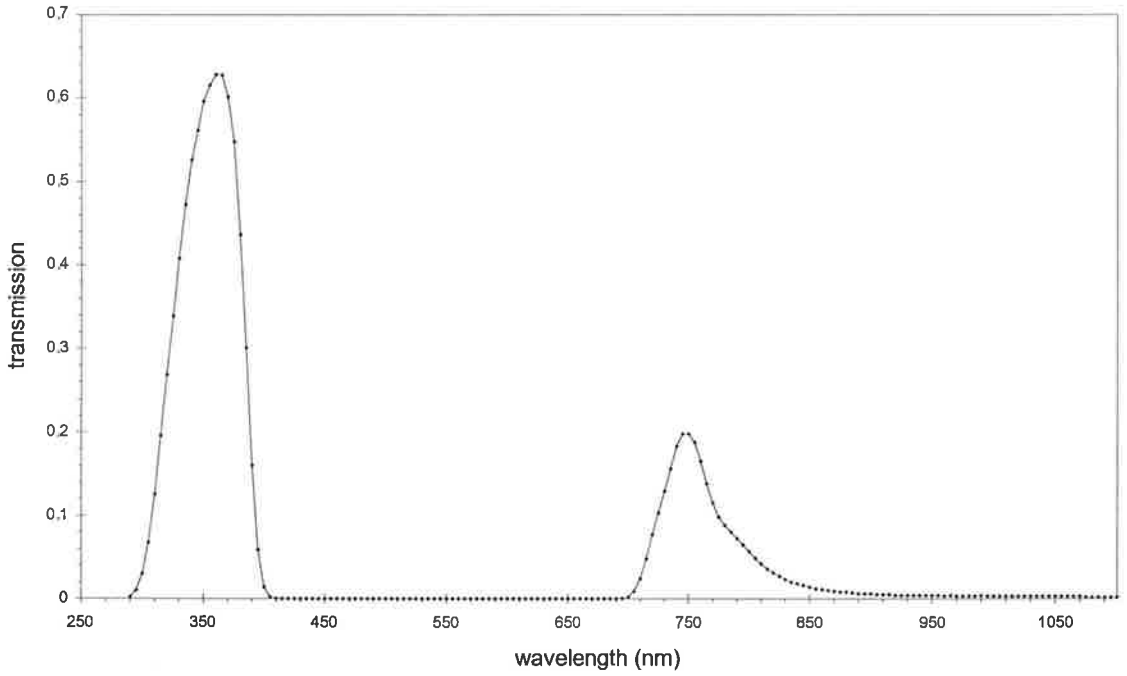

Figure 3.7

Transmission curve of a 2-mm-thick Schott UG-1 filter. Note the considerable red leak around 750 nm. For the PMT used, this did not cause problems, since the PMT response in that region is negligible. It would, however, cause difficulties for red-sensitive PMT's, or for CCD's.

CHAPTER 4. OBSERVATIONAL TECHNIQUES AND DATA REDUCTION: EXTINCTION PHOTOMETRY

The Earth's atmosphere will absorb or scatter, to a greater or lesser degree according to wavelength, the radiation coming from any astronomical source. Thus, at the Earth's surface, the observed flux from any source will be lower than that which would be observed above the atmosphere. At some wavelengths, this is quite fortunate for us; at others, it may be considered as something of a hindrance, or at least a complication.

With regard to observations in the optical region of the electromagnetic spectrum, the presence of the atmosphere has a number of important ramifications. Rather obviously, there is the presence of clouds which, when thick enough, effectively preclude the undertaking of optical observations. There are also the phenomena known as scintillation and seeing. Scintillation is a rapid modulation of the observed intensity of a non-extended, or point, source (e.g. a star). "Seeing" is caused by image motion, which is the apparent, and comparatively slight, movement of an image about its expected position (note: this is quite separate from the quite predictable and slower change in apparent position due to refraction near the horizon). At any given time, there is not necessarily any correlation between the severity of these two effects. The more pronounced the effects of scintillation and seeing, the worse the night is for observation.

Of interest here is that phenomenon known as "atmospheric extinction", which shall be considered only in the optical region of the electromagnetic spectrum. It is the reduction in intensity of a light beam, along its length, as it passes through greater amounts of the atmosphere away from its source. Of primary concern is its effect on astronomical sources; that is, for sources above the atmosphere. In terms of practical observation, it means that a star will appear dimmer when closer to the horizon, when its light is passing through greater amounts of air, than when it is higher up in the sky. Of course, it is present also for any light source within the atmosphere as well, be it one some distance away on the Earth's surface, or aloft in the air.

4.1 Definitions and theory

4.1.1 The physical mechanisms behind attenuation

There are two processes behind the attenuation of light as it passes through the atmosphere- absorption, and scattering. Absorption involves the transferral of a photon's energy to an atom or molecule, after which that energy may be re-radiated. Scattering involves

the change in direction of the photon's travel after a non-destructive interaction with a suspended body, be it atomic, molecular, or even solids such as dust.

The absorption component of extinction is due to ozone and water molecules. This will occur in particular lines and bands, and so is not a smooth function of wavelength. The amount of extinction depends on the total amount of ozone and water above the observatory. Whilst both are rather variable, the former, at least, may be predicted to some degree.

Scattering consists of two parts: Rayleigh scattering (involving air molecules), and aerosol scattering (involving dust, water droplets, pollutants, etc). Rayleigh scattering is proportional to local atmospheric pressure, since it depends on the total amount of air molecules above the observer. The scattering probability varies as λ^{-4}, leading to a strong wavelength-dependence in total observed extinction.

Aerosol scattering is caused by suspended particulate matter which has a varied range of sizes, and the wavelength dependence is given by a power law, $\lambda^{-\alpha}$. The value of α is found to be positive, so the effect decreases for longer wavelengths- as one may expect. Since the nature and amount of aerosols above a particular site is highly variable, the value of this exponent will be different for each location and for different times.

For these scattering components, each is proportional to the amount of air above the observatory, given as h kilometres; that is, proportional to exponential($-h/H$), where H is the scale height (in km). Hayes and Latham (1975) find H = 7.996 km for Rayleigh scattering, and H = 1.5 km for aerosol scattering, but note that the scale height may vary by a factor of 2 or so from night to night.

Whatever the cause, photons are lost along the path of a light beam through air. This will occur for all wavelengths, but with different severity for each. Considering the case of monochromatic (i.e. at a single wavelength only), we have

$$dI(l,h) = -I(\lambda,h)\, A(\lambda,h)\, ds \qquad (4.1)$$

where $dI(\lambda,h)$ is the change in intensity at wavelength λ, at height h above the ground,

$A(\lambda,h)$ is the opacity of a unit thickness of air,

$I(\lambda,h)$ is the intensity of the monochromatic light beam,

ds is the thickness of the layer of air which is traversed.

Substituting ds = sec(z) dh and X = sec(z) (see Section 4.1.1 for definitions of z and X), with dh the *vertical* thickness of air traversed, we find

$$dI(l,h) = -I(\lambda,h)\, A(\lambda,h)\, \sec(z)\, dh \qquad (4.2)$$

or

$$dI(l,h) = -I(\lambda,h)\, A(\lambda,h)\, X\, dh \qquad (4.3)$$

The intensity of light from a star, observed at the ground, $I(\lambda)$, is the integral of this, over all heights, h. That is,

$$I(\lambda) = I_o(\lambda)\, e^{-X} \int_0^\infty A(\lambda,h)dh \qquad (4.4)$$

where $I_o(\lambda)$ is the intensity above the atmosphere. Converting this expression to the usual magnitude scale, we obtain

$$m(\lambda) = m_o(\lambda) + 1.086\, X \int_0^\infty A(\lambda,h)dh \qquad (4.5)$$

which may be represented as

$$m(\lambda) = m_o(\lambda) + X\, a(\lambda) \qquad (4.6)$$

with $a(\lambda)$ being the monochromatic extinction function. This is one form of the Bouger relation (see Section 4.1.3).

For practical applications, we deal not with monochromatic light, but with a range of wavelengths admitted by whatever filter is employed. This same relation applies, but instead of regarding single wavelengths, we have the magnitudes as observed over the filter's entire passband, and consider the corresponding extinction coefficient, k_λ (again, see Section 4.1.3).

4.1.2 Air mass

The air mass through which a star is observed is, by definition, the amount of the Earth's atmosphere through which its light has passed in order to reach the observer. Generally in astronomical photometry, it is used as a relative measure rather than as some absolute quantity, such as a column density.

When observing at the zenith, one is looking through the smallest possible amount of atmosphere; this is, by definition, one air mass. If one models the atmosphere by a single layer

of constant density with height and horizontal distance, with the ground and atmosphere parallel and flat (as in Figure 4.1), one has what is termed the *slab model* of the atmosphere.

Here, the amount of air through which a star is observed will vary as sec z, where z is the angle of the light path from the zenith, i.e. the zenith angle of the star. We have, then:

$$X = \sec z \qquad (4.7)$$

where X denotes the air mass.

This model does not, however, accurately represent the actual nature of the atmosphere. There are several differences, including:

(a) the Earth's surface and its atmosphere are not plane-parallel

(b) the atmosphere is not a single layer of uniform density

(c) aerosols, water vapour, etc, are not distributed uniformly in height.

In spite of this, the slab model is generally taken to be a valid approximation for zenith angles less than about 60°. For larger zenith angles, one must use more complex models. Even these will, when independently compared, give different air masses at very large zenith angles (e.g. near 90°).

Relations which can be used above X=2 (i.e. z = 60°) are the following (Hall and Genet 1988, Equation 9.1.3):

$$X = \sec z - 0.0018167(\sec z - 1) - 0.002875(\sec z - 1)^2 - 0.0008083(\sec z - 1)^3 \qquad (4.8)$$

which is based on work by Bemporad early in the 20th century. Here, z is the apparent (i.e., refracted) zenith angle, and not the true zenith angle. Though much used, this relation is itself approximate, and refers to the specific altitude for which it was derived.

Another relation, useful to larger zenith angles, is (Hall and Genet 1988, Equation 9.1.4):

$$X = \sec z\,(1 - 0.0012(\sec^2 z - 1)) \qquad (4.9)$$

which is useful up to X = 4, or approximately z = 75°.

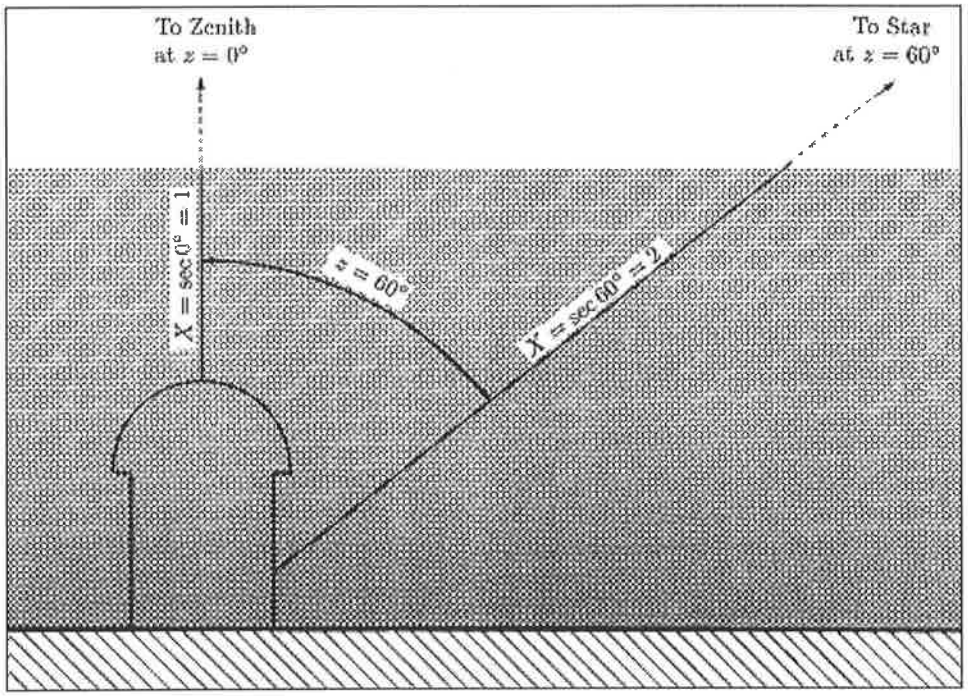

Figure 4.1
Slab model of the atmosphere (from Hall and Gennet 1988, Figure 9-1). The atmosphere is assumed to be of constant density with height, and the ground and atmosphere are both flat and parallel. This is, of course, a simplification, but works well up to zenith angles (z) of 60° to 70°.

4.1.3 Instrumental magnitude

If the telescope and its detector make some measurement, F, of the apparent brightness of a star, its *instrumental magnitude*, m, is defined here to be

$$m = -2.5*\log(F) + C \qquad (4.10)$$

where C is a constant. However, since in all the work that follows (be it PMT- or CCD-based, extinction or time-series photometry), we will consider only *changes* in brightness as measured with the same instrumentation for a particluar data-set, it is possible to set C = 0. This is the star's magnitude as found with that particular telescope and detector, at the time of observation. It applies only to that particular observation; even if the star is constant, statistics and measurement errors will mean that another measurement which follows immediately would be slightly different, and yield a slightly different instrumental magnitude. Clearly, the total amount of radiation received also depends on the total duration of the observation, so some allowance must be made for different PMT or CCD integration times. Furthermore, any given measurement F is made at some particular air mass, and this alone would alter m as time passes, by an amount which varies strongly with the wavelength at which the measurements are undertaken.

4.1.4 Bouger plot and the extinction coefficient

The relationship, known as Bouger's law, between a star's magnitude outside the atmosphere (i.e. at X = 0), in the instrumental system, and its measured instrumental magnitude at a particular air mass, X, is

$$m_o = m - k_\lambda X \qquad (4.11)$$

where

m is the instumental magnitude,

m_o is the extra-atmospheric magnitude, and

k_λ is the extinction coefficient, in units of magnitude/air mass.

If the star is observed at a range of air masses, and the corresponding instrumental magnitudes obtained, one may plot the m values against the corresponding X values, and obtain a series of points distributed along a straight line, the slope of which line is the extinction coefficient., k. Figure 4.2 shows an example of such a Bouger plot.

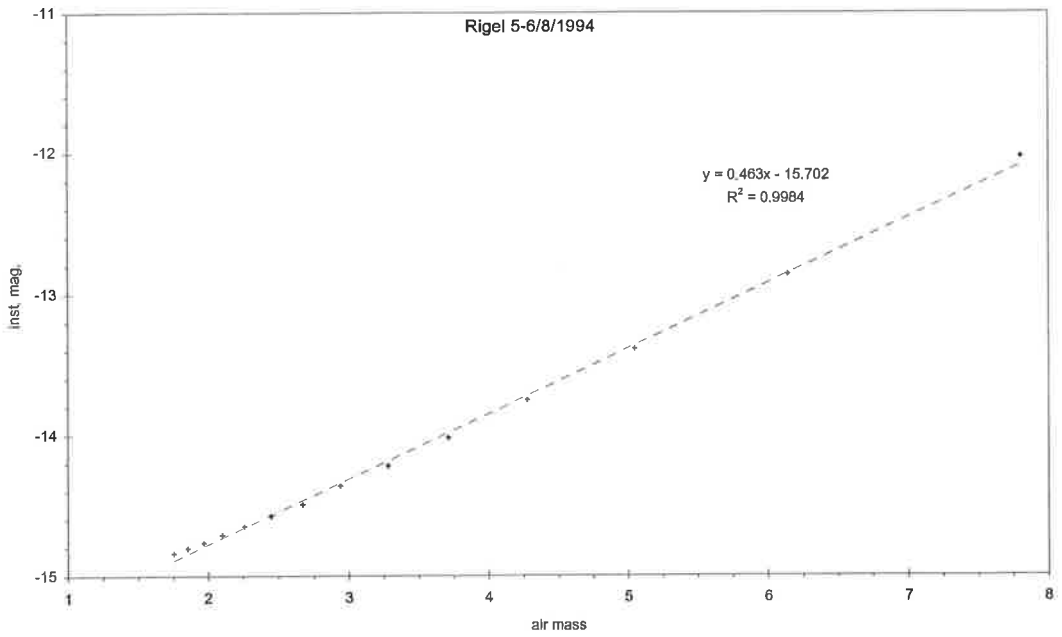

Figure 4.2

An example of a Bouger plot. As the star was rising during the observations, it passed through less and less air mass as time progressed. As a consequence, it brightened and its instrumental magnitude (as defined here) became more negative. The slope of the plot of instrumental magnitudes vs. air mass, as given by the linear regression result included, is the value of the extinction coefficient for that star for that night.

Whilst this plot is based on data taken with a PMT and U filter, the same approach is used for other filters, or with a CCD.

Note also the slight non-linear trend to the low-air-mass values on this night. This may indicate varying photometric conditions, possibly thin, high cloud not visible to the eye, or increasing humidity or aerosols. The inclusion of these later (in time) points would result in a different co-efficient than that which would have been obtained if observations had ceased earlier.

Note that the extinction coefficient is a function of wavelength, as the Rayleigh component of the attenuation is highly wavelength-dependent. Figure 4.3 shows the variation of k with wavelength obtained using narrow-bandwidth filters (Hayes and Latham 1975). Thus, k must be determined for each filter used.

The value of the extinction coefficient also is dependent somewhat on the colour of the star used for the measurements. Strictly speaking, the Bouger relation is

$$m_o = m - k'_\lambda X - k''_\lambda X(B-V) \qquad (4.12)$$

where

k'_λ is the first-order extinction coefficient,

k''_λ is the second-order extinction coefficient, and

(B-V) is the colour index of the star.

k''_λ typically has a small absolute value, between about 0 and 0.04 depending on the filter used (Hall and Genet 1988, Section 9.1), and (B-V) is often small, and is in fact defined to be zero for A0 stars. Therefore, it frequently is possible to ignore the second-order term completely, for a slight, and perhaps negligible, increase in error.

For the program of site-monitoring at Woomera, only the first-order term was considered, so I will generally use k, not k'.

It is to be noted that the Bouger plot will yield a straight line only when the atmospheric conditions which govern the amount of extinction present are constant during the period of observation, and indeed also over the range of azimuths involved. Variable extinction during the observations will impart a concave or convex trend to the data points, if the extinction variation is of a longer time-scale than the observations. Shorter variations may cause one or more points to differ from the general trend.

If there are local topographic features which may significantly affect the presence of aerosols in their vicinity, an azimuthal trend may also be present. This may produce a change in the Bouger plot if the observations are carried out across and beyond the affected azimuths, or perhaps different extinction values for different parts of the sky if the azimuth ranges of the observations are limited (Young 1974, Section 3.1.4.2.2).

It is to be noted that the general discussion above (and especially line-fitting of the data points) refers to measurements which are made when the star under observation does not cross the meridian. If it does so, the data points will "wrap-around" at the maximum X value. Furthermore, if there is indeed some azimuthal change in atmospheric content in the two sky

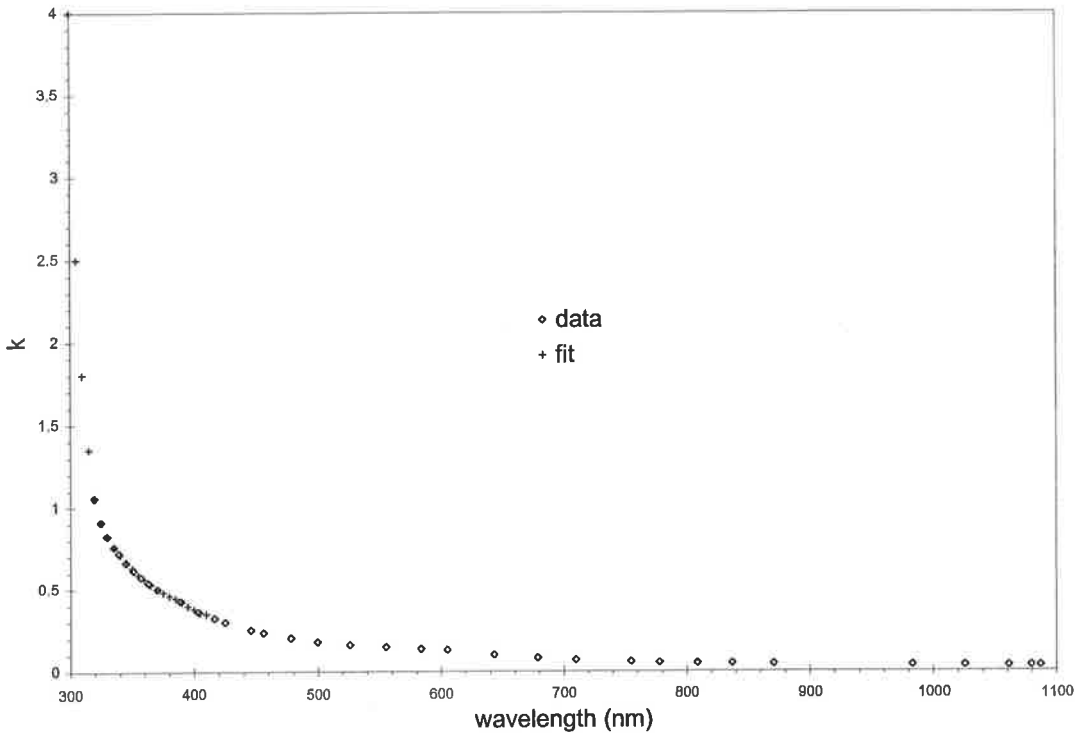

Figure 4.3

Monochromatic extinction values. Data are from Hayes and Latham 1975; crosses are a short-wavelength fit and extrapolation (by this author) down to 300nm used for calculations towards Figure 6.4.

quadrants thus observed, the two segments of the Bouger plots will have different slopes, and an attempt to fit a single line (and thereby k) to the entire such data set will give a most confusing result. Conversely, if the sky is quite isotropic, then the two segments should overlay each other (given also uniformity over the *time* of observations) (Young 1974, Section 3.1.4.2.2).

As is most likely to be the case anyway, extinction measurements should not be carried out across the meridian if all the data are to be examined together- unless such effects are those which are under study.

4.2 PMT methods and reduction

4.2.1 Equipment

The photometer described in Section 3.4 was mounted on the C5. The output pulses were counted using either the counter card and programme in the auto-guiding PC, or a stand-alone frequency counter.

Some early data, obtained before the observatory was established, were taken using the same equipment on the C5, but with the C5 on its own mounting and stand. The frequency counter was used for these data. Times for all data were taken from a separate clock, with the setting of this clock being checked each night before observations.

Typically, a 5mm diameter aperture was used in the photometer, corresponding to an angular aperture diameter of 13.75'. This is much larger than the range of diameters customarily employed in photometry, say from 10" to 60"or so; but with the choice of a sufficiently bright and isolated star, errors caused by sky levels or background stars were small. Also, the lack of a preview eyepiece to view the aperture diaphragm would make star centring in a small diaphragm difficult. All PMT extinction data were taken using the Hoya UG-1 filter on the C5, so the PMT data all refer to the U band.

4.2.2 Observations

Generally, a star in the eastern half of the sky would be observed, preferably actually near to East itself, to enable measurements to be made over a large range of air masses quite quickly. The actual star chosen would depend on which bright star was conveniently placed on a given night.

The observing routine involved taking a series of (typically) four 10-second integrations with the telescope pointed at the star; this would yield the count rate for (star + sky), as the area of the sky defined by the photometer aperture would include both the star and

surrounding sky. Immediately would follow a similar series measuring just the sky, by moving the telescope a suitable distance in RA or Dec and counting again. The effective time of observation of the star was taken to be the time of mid-point of the star measurements. Count rates and times were recorded in a log book.

Some time later, after the star had risen somewhat and therefore at a different air mass, another set of measurements was made. This cycle would be repeated for as long as desired. The interval between each set of observations would be smallest when the star was nearer the horizon, since the air mass would be changing most rapidly there. The gap would be perhaps two or three minutes at first. Once the star was higher, say about 70° zenith angle, and changing air mass much more slowly, the interval would be increased somewhat.

4.2.3 Data reduction

The times and count rates have then to be converted to air masses and instrumental magnitudes. The raw data, including site and star co-ordinates, are entered into a Microsoft Excel spreadsheet. The spreadsheet is used to convert times and co-ordinates into zenith angles and thence to air masses, and also to convert raw counts into instrumental magnitudes. The (star + sky) and sky counts are averaged, and converted to counts/second if need be. The counts are then corrected for the dead-time of the tube, according to the manufacturer's instructions, using the following relation:

$$N = M*e^{(MT)} \qquad (4.13)$$

where

N is the corrected count rate,

M is the observed count rate,

T is the dead time (given as 100 ns in the data sheet).

As the dark count is included in both the (star + sky) and sky measurements, it will be automatically removed when the difference ((star + sky)-sky) is taken, which then yields the counts/second for the star alone. (Strictly speaking, the dead-time correction should be applied to (star+sky) and (sky) separately, with the difference calculated after that. However, the sky rate is generally so small compared with the star rate, and the tube infrequently operated at very high count rates, that the error introduced by not doing so is minimal).

The counts/second for the star are converted into instrumental magnitudes by taking

-2.5*log(counts/second). These magnitudes are then plotted against air mass to give the Bouger plot. A linear least-squares fit of these data will then give the first-order extinction coefficient, k', and the instrumental magnitude at zero air mass. The Excel least-squares routine also gives error estimates for the various parameters in the regression. For this work, only the first-order extinction was determined; no attempt was made to allow for the colour terms in the measurements.

There will always be some variation in the observed value of k', as the extinction is variable on many time scales, due to changes in atmospheric pressure, aerosol and moisture content, and so on. These variations were found to be above the level of the variations due to measurement error. However, for a given star (which is itself assumed not to be variable), the derived instrumental magnitude at X = 0, obtained from setting X = 0 in the regression equation on the data, *should* be constant over time, since it is the above-atmosphere magnitude of the star in the instrumental system.

Therefore, the behaviour of the X = 0 instrumental magnitudes over time, for the same star, will give an indication of the stability of the photometric equipment in use at the site of observation. Variations in these values will be due to both measurement errors and any instrumental drifts in the system. It is to be hoped that there is none, or very little indeed, of the latter.

4.3 CCD Methods and reduction

Whilst this section deals specifically with the use of the ST-6 CCD in extinction measurements, there are certain fundamentals of the observation and reduction methods which are applicable also to the use of the CCD in stellar photometry (which also includes AGN in my discussion). Thus, the areas in the stellar photometry sections (Chapter 5) already covered here will not be covered again in that chapter.

4.3.1 Equipment

The ST-6 CCD was used on the C14, in conjunction with the telecompressor and UBVRI filter set, as described in Section 3.2. The times of exposures were taken from a separate clock (not the PC clock time, as recorded in the CCD image header), and recorded in a log book.

4.3.2 Observations

A star was chosen according to the criteria of Section 4.2.2, except that much fainter stars were necessary, due to the larger aperture of the C14 and the higher quantum efficiency of the CCD. The *SAO Bright Star Catalogue* and the *Uranometria 2000.0* star atlas were consulted to find suitable program stars.

The CCD admitted of observations over the entire filter range, from 360nm (i.e. U) to 800nm (i.e. I), so the CCD data were taken using all the filters. This allows one to examine the variation of the extinction coefficient with wavelength. As the CCD efficiency changes somewhat with wavelength, the exposure used for each filter was varied, in order to avoid saturating the pixels in the images, especially with the R filter (where CCD QE is highest). Typical exposures were of the order of a few seconds, to perhaps 60-seconds for the U filter, where the CCD efficiency is very low. Exposure times also were recorded in the log book.

For the BVRI filters, usually two exposures were made in each filter, with half-frame mode on the CCD being used to decrease the dead-time between exposures due to digitisation and down-loading. Usually only one U frame was taken.

There would thus be a sequence of UBVRI (or sometimes only BVRI) images obtained for each data point; as for the PMT data, the sequence would be repeated as long as desired. However, due to the more time-consuming nature of the CCD sequence, as compared with the PMT measurements, there often was no gap between the filter sequences.

4.3.3 Image processing required for photometry

The conversion from raw CCD images to useful numbers is rather more involved than the corresponding process for PMT data. The CCD is a two-dimensional detector, so we now have to deal with images. That said, there also are advantages in using CCD's. One such advantage appropriate here is that we have both the star and sky in the image, so there is no need to obtain separate sky measurements.

This section will discuss those observational and reduction steps necessary to obtain good data from CCD images. Thus, there is considerable overlap with the intent of Section 5.3, as mentioned previously.

The image-processing steps to be applied to the CCD image, before meaningful data can be extracted from it, are as follows:

(a) dark current subtraction, and

(b) flat fielding.

These shall now be discussed in detail.

4.3.3(a) Dark subtraction

As mentioned in Section 3.3, there is a build-up of charge in a pixel due to the thermal release of electrons in the CCD material. This amounts to an extra component of the image which is not due to incident light, and must be removed. The amount of thermal charge generated in a given time will be different for different pixels on the CCD. Thus, it is not possible to remove the dark current by simple subtraction of a constant value from the ADU value for each pixel. What is required is the distribution of dark current over the CCD.

This is obtained by allowing the CCD to integrate as per a usual exposure at the telescope, but with the CCD chip itself shielded from all light. When the CCD is read-out, what we will have is an image, as it were, of the dark current in the CCD for that given exposure time. As the thermal charge build-up is proportional to integration time (and temperature, of course), it is necessary to have the dark frame of the same duration, and same temperature, as the light frame for which it is intended to be used for correction.

If the CCD characteristics are sufficiently well known, it is possible to take a dark frame of different integration time, and temperature, than the light frame, and scale the ADU values appropriately. This technique is not applicable in all cases, however, and for all observations discussed here, same-duration and same-temperature dark frames were employed.

The intensity of a given pixel (i,j) on the CCD can be represented by the following relation:

$$R(i,j) = D(i,j) + I(i,j) \qquad (4.14)$$

where

R(i,j) is the value of that pixel in the raw image

D(i,j) is the value of the dark current of pixel (i,j)

I(i,j) is that part due to the presence of incident light.

Removing the dark frame removes D(i,j) from the above relation, and we are then left with the pixel intensity due to the passage of incident light through the optical system to the CCD chip itself. However, since the dark frame cannot *exactly* mimic the production of dark current in the image frame, the dark subtraction will introduce some error into the dark-subtracted data.

The temperature-dependence of the dark current means that the actual intensities of the dark frame's pixels can be reduced dramatically by lowering the temperature of the CCD. The

dark current will be approximately halved for a particular drop in CCD temperature (different for different CCD's- about 6°-7°C for the ST-6's TC-245 chip). This reduces the actual dark count in each pixel, and, since the noise in the dark count is the square-root of the dark count itself, will reduce the error introduced by the dark subtraction as well. Figure 4.4 shows a raw, unprocessed ST-6 image; Figure 4.5 shows the same image after dark frame subtraction.

4.3.3(b) Flat-fielding

If the telescope images a uniformly-illuminated source (for example, the twilight sky if one is using a small-format CCD) onto the CCD, the resulting image, after dark subtraction, will not be of uniform intensity. There are several reasons for this, namely:

(i) vignetting caused by the telescope optics, including, if used, a telecompressor lens

(ii) vignetting caused by filters, if they are too small to accept the entire light bundle provided by the telescope

(iii) shadows caused by dust particles in the optical system, especially on the filters and the window in the CCD head

(iv) reflections within the optical system

(v) variations in pixel sensitivity across the CCD chip.

Factors (i) to (iv) are specific to the telescope optics and filters, whilst (v) is a result of unavoidable manufacturing tolerances in the production of the CCD chip.

The most noticeable artefact of non-uniform image plane illumination is a radial gradient in the intensity of the sky background in a CCD image, which can readily be visualised by altering the image display parameters when viewing the CCD image on the PC. This will be especially evident, and bothersome, when the sky itself is bright- e.g., near the Moon, in images taken from urban locations- or when very long exposures are undertaken.

For purely pictorial applications, flat-fielding may be a cosmetic aid which may be able to be ignored; but for photometric purposes, it is of great importance. Methods of photometric reduction require that the relative intensity of star images (and of various locations of the sky background itself) in the CCD image correspond directly to their true relative intensities. The flat-fielding correction must be applied if this is to be so.

As mentioned, the flat field image is an image taken with the telescope facing a uniformly-illuminated source. This source can be the twilight sky, or an artificial source in the observatory, such as a suitably illuminated screen. Such an image gives us the variation in focal plane illumination due to factors (i)-(v) above. It must, of course, also be dark-subtracted.

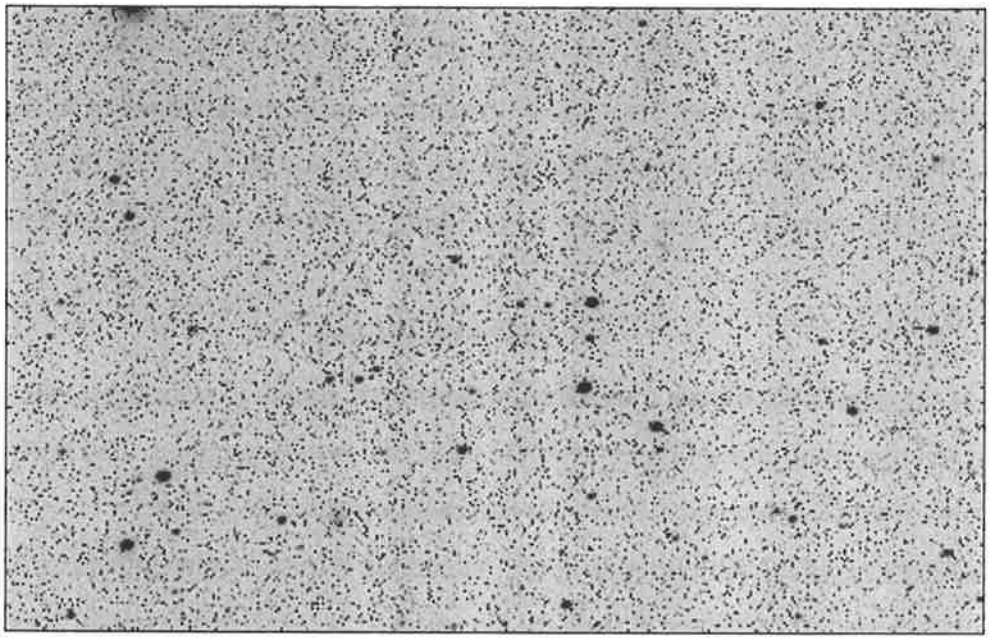

Figure 4.4
A raw ST-6 image. Visible are bright stars, and the false "signal" due to thermally-generated counts in the CCD pixels. Note that the image is presented as a negtive.

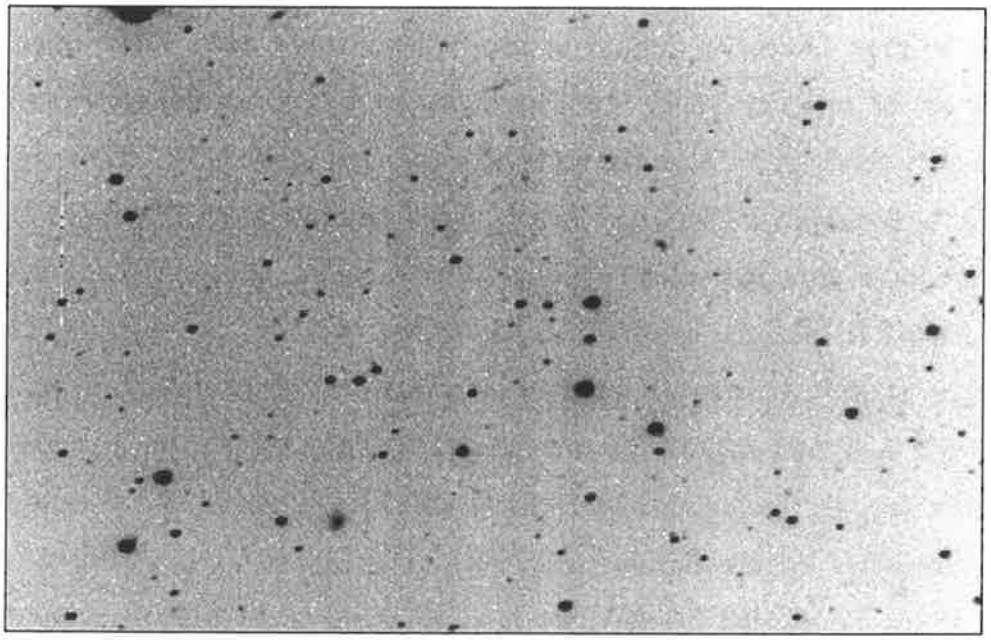

Figure 4.5
Same image, but with the dark frame subtracted. Now visible is the approximately radial gradient in intensity due to vignetting by various components of the optical system.

Mathematically, the correction is applied as follows:

$$E(x,y)=K*I(x,y)/F(x,y) \qquad (4.15)$$

where

E(x,y) is the processed image (dark-subtracted and flat-fielded)

I(x,y) is the image to be flat-fielded (which has already been dark-subtracted)

F(x,y) is the flat-field image (which has already been dark-subtracted)

K is a constant, given by the average pixel value of the flat-field image.

Each image pixel's value is divided by the value of the corresponding pixel in the flat-field frame, and the constant approximately restores processed values to those in the original frame. Figure 4.6 shows a (dark-subtracted) flat-field image. Figure 4.7 shows the same image as for Figure 4.5 after flat-fielding.

There are certain provisos as to the use of flat-fields. Some of the more important are discussed below:

(a) the same mechanical and optical configuration of the telescope must be used for both the flat-field image and the image or images to be corrected. Altering the position, etc, of any component will alter the appearance of vignetting, dust shadows, etc at the focal plane, and therefore invalidate the flat-field correction;

(b) separate flat-field images should be taken for each filter used. Firstly, the non-uniformity of pixel sensitivity across the CCD usually is wavelength-dependent, so that a B flat will not be the same as an I flat, for example. Secondly, the location of dust specks, etc, on each filter will be different, and will cause slight variations in the images through different filters. Of course, accurate and repeatable positioning of the filters is necessary.

(c) Several flats per filter should be obtained, to enable them to be averaged or median-filtered. This will reduce the noise in the final flat-field image, and thus improve the flat-field correction. Usually, four per filter were obtained.

(d) In SBIG's CCDOPS software, there is no facility for removing star images, and there is no median-filter function. Therefore, there should be no star images on any of the flats, as they will still be present in the final averaged flat-field image. Many image-processing packages do have median-filter routines, and so a large number of images of different parts of the night sky may be used to generate a night-sky flat field. Night-sky flats are preferable in that the spectral distribution of the light source for the flat (i.e. the night sky) is the same as that for the background of the image frames (i.e. the night sky, again). However, this

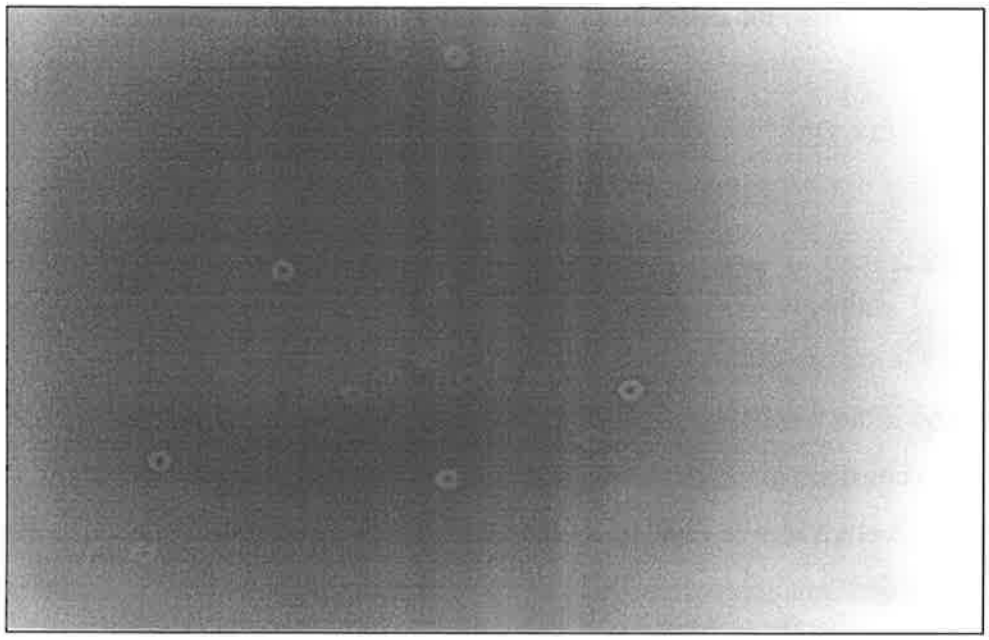

Figure 4.6
A flat field image, produced by taking an exposure of the twilight sky. The vignetting, and shadows caused by dust on the optics, are evident.

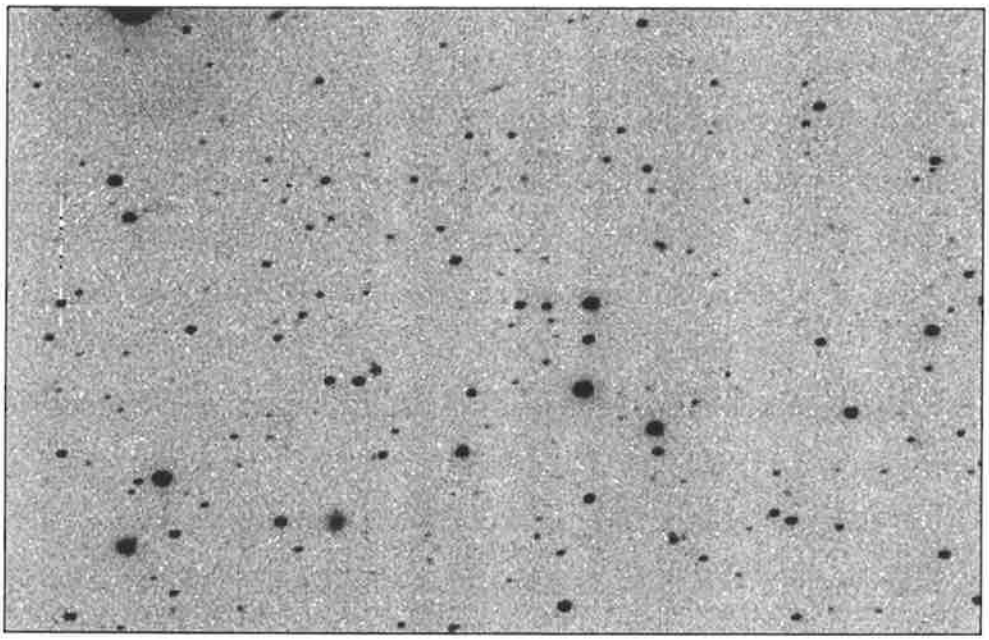

Figure 4.7
A fully-processed image. Dark-subtraction and flat-fielding have both been applied. Note the defective pixels near the left-hand edge (actually on column 21 of the CCD chip). This artefact may be removed via software.

approach is not always possible, due to observational constraints or software limitations. Twilight or artificial "dome" flats were used in this program.

4.3.4 Data reduction

One may now extract useful photometric information from the dark-subtracted and flat-fielded image. This was achieved by the technique known as *aperture photometry*. Here, the intensity of any part of the overall CCD image is measured by summing up all the pixel intensities in selected regions of the image, with these regions corresponding to the locations of star images, sky background, etc, on the image. This is undertaken using suitable image display/analysis software. If the measuring aperture is set to be only one pixel in size, one can measure the intensity only of individual pixels. In stellar photometry, the aperture size is set large enough to incorporate all the light from the image of the star of interest. This is analogous to using a sufficiently large focal plane aperture in the PMT photometry to include all of a star's light; but here we are dealing with a software aperture, not a mechanical aperture. With the CCD image we can place the aperture anywhere within the image; with the PMT, we would have to move the telescope itself to measure the same locations. There is a technique known as "curve of growth" aperture photometry, where the aperture is smaller than a star image (Howell 1989). This is useful for faint star photometry or crowded fields.

The SBIG CCDOPS software was used to examine the images and for manual extraction of the photometric data. This software allows the user to set an aperture size from 3x3 pixels up to 31x31 pixels. Thus, the aperture always is a square. The software will display the average intensity of pixels within the box, e.g. 32 ADU/pixel in a 5x5 box, corresponding to 800 ADU total.

As in the PMT photometry, one needs to derive the signal due to the star alone. The aperture is placed over the star image, to yield the ADU values for (star + sky). The aperture is then moved to a neighbouring sky region, to give (sky) alone. Usually, more than one sky measurement is taken, and the average used.

It is customary to factor out the exposure time by dividing the measured intensity by the exposure time in seconds, to give a final value in ADU/second. This value is calculated as follows:

Star brightness = ((star+sky)-sky)*area/exposure

where

(star+sky) is the average value of the (star+sky) region, in ADU/pixel

sky is the average value of the sky region(s), in ADU/pixel

area is the total area of the measuring aperture, in pixels

exposure is the CCD image exposure time, in seconds.

This value, in ADU/second, is analogous to the counting rate, counts/second, in the PMT method. It is determined for each image in turn, and if there is more than one image for each filter in a measurement sequence, the average brightness is used. These results, for each filter, as well as time of exposure, star RA and Dec, observatory longitude and latitude, are entered in Excel spreadsheets, and reduced as per the PMT data. The instrumental magnitude of a particular star image can be determined by taking -2.5*log(Star brightness). We then have the extinction coefficients for the UBVRI filter set.

It is to be noted that there has been no effort to convert ADU/sec to electrons/sec (these being related by the gain of the camera) or photons/sec, since all the data reduction will involve measuring only changes in brightness (or measuring relative brightness as in differential photometry, Section 5.3.3(a)).

The comments as to system stability applied to the PMT data also apply here.

CHAPTER 5. OBSERVATION TECHNIQUES AND DATA REDUCTION: STELLAR PHOTOMETRY

5.1 Introduction

The previous chapter discussed techniques for determining the influence of the Earth's atmosphere on the photometric measurement of starlight; specifically, the influence of atmospheric extinction on the observed magnitudes of stars. Of interest was the use of such measurements to characterise the quality of the atmosphere above the observatory site, where the observed stars were used essentially as standard light sources, with no further interest therein.

This chapter is concerned with the techniques used when we are interested in the intrinsic variations of the stars themselves (or, indeed, of the brightness of any other astronomical source). Atmospheric extinction must be taken into account, but its measurement is not the primary objective.

Since, in both extinction and stellar photometry, we are undertaking photometry of stars as the source of data, there are many common components to the two fields. Those aspects of stellar photometry already covered in the previous chapter will be taken as understood, and not discussed in detail; those which are new will be treated fully.

5.2 PMT methods and reduction

The PMT was not used to any significant extent for stellar photometry at Woomera. The most that was done were some test runs on a few bright stars, as well as on the highly-active cataclysmic variable (CV) AE Aquarii. The brief career of the PMT photometer was due to the arrival of the ST-6 CCD, which allowed more accurate photometry, over a greater wavelength range and with a full UBVRI filter set, to fainter magnitude limits, and with easier and more robust data reduction, albeit with a reduction in temporal resolution. Nevertheless, I shall discuss the basics.

5.2.1 Equipment

The photometer was attached to the C14, with the C5 being used for the ST-4 auto-guiding CCD. Since the photometer has no preview eyepiece, object acquisition involved removing the main photometer housing- leaving the diaphragm in place- replacing it with a

parfocal eyepiece (that is to say, an eyepiece so mounted as to have its focal plane at the position of the photometer diaphragm), finding the desired star, removing the eyepiece and then replacing the housing. All in all, a very tedious process, which would have lead to a redesign of the photometer had not the ST-6 CCD become available.

At the full focal length of the C14, the field-of-view with a 10mm-diameter aperture was some 8.8' in diameter. No filters were used anywhere in the optical path, so that the spectral response is essentially that of the PMT itself (see Figure 3.6).

5.2.2 Observations

After the target star was acquired, and the photometer reassembled, the auto-guider was started. As the intention was to examine the efficacy of the photometer in detecting short-term variations in a star's brightness (say, down to a few seconds or so) over time spans up to an hour or more, the PC counter card was employed. Various integration times were used, with one second being typical. One would then have, for example, an hour's continuous run at one-second temporal resolution.

Sky readings, when taken, were done before and after a run, by using the Dec slow-motion for a given number of seconds to set the telescope off the target star, and then to return it. Occasionally, a reading would be taken during a run. At such times, the auto-guider would temporarily be stopped. The start time of a run was taken from a clock, and written in the observing log.

5.2.3 Results

No data reduction, as such, was carried out- the data were simply viewed as a plot of counts/integration vs. time. Evident on the plots was the scatter due to scintillation, the change in count rate due to changing air mass during a run, and the change in sky brightness at different zenith angles (with air mass and zenith angle varying with time during a single, continuous data run).

For the AE Aquarii data, there was some evidence of flaring.

The data showed that the PMT could well be used for observations of short-term (seconds scale) variability, for sufficiently bright stars, and if the system was used unfiltered for fainter stars. The crude photometer design employed was a hindrance in this work, and would have had

to be greatly changed and improved if anything useful were to be accomplished. This work was of a very preliminary nature, and no quantitative results were obtained.

5.3 CCD methods and reduction

Most of what is required for extraction of photometric information from CCD frames has already been discussed with regards to extinction photometry. In that section we dealt with the repeated measurement of a single star; here, we deal with the repeated measurement of a number of stars (all visible on a single CCD frame), in order to ascertain the intrinsic variability of one of them

5.3.1 Equipment

The ST-6 CCD and filter wheel were mounted on the C14. The C5 and ST-4 CCD were used for auto-guiding.

5.3.2 Observations

As the concern here is the temporal variability of a source, the basic observational technique is that of repeated exposures of the same target field, with the time interval between exposures being such as to allow the expected variability to be examined (Howell and Szkody 1988). For long-period variables, this may mean no more than one exposure per day. For CV's, minutes-scale is more appropriate, and even seconds, if such resolution is attainable given the limitations of telescope, CCD hardware and software in use.

The observer must determine what integration time is appropriate, given the target's magnitude; what filter, if any, is to be used; approximate limits to observational error, which will be larger for shorter integration times on a particular source; the desire for sufficient temporal resolution of the brightness variations, and so on. These factors are all inter-related, and the actual exposure time chosen is a compromise based on considering all of them.

In practice, the telescope is moved to the co-ordinates of the target star and, with reference to suitable finding charts, the telescope is moved about until the correct star is placed well within the CCD image. For this, the CCD is set to low-resolution (3x3 binning) focus mode, which allows fast download of a continuous sequence of images (without saving each image on the PC). The CCD is then set to full resolution, and a test exposure taken. This duration of this test

exposure is set to that expected to give good results. The downloaded image is then checked for focus and ADU levels of selected star images to guard against saturation. If need be, the exposure time can be changed and another test taken.

If all is well, the CCDOPS software is used in Autograb mode to take a series of exposures of specified integration time, time interval between frames, and number of frames. Each frame is saved after it is downloaded. Dark frame subtraction is usually done at this stage. CCDOPS is set to take a new dark frame every 8 frames, the dark frame being stored in the camera head, and subtracted from each light frame before downloading. The start time of the first frame is taken from a clock and recorded in the log book, along with the PC saving directory, object name, CCD temperature and Autograb parameters.

As dictated by the night's observing schedule, the Autograb sequence for the source is repeated as long as desired, or a new source is chosen.

5.3.3 Data reduction

The fundamental objective is to obtain a magnitude and time of observation for the variable star (or other object) under investigation. The technique of *differential photometry* was employed.

5.3.3(a) Differential photometry

This method relies upon the taking of *differences* between the instrumental magnitudes of star images recorded on a single CCD frame. The instrumental magnitude is obtained in the same manner as that for extinction photometry. However, here we measure at least two stars per frame, and preferably three or more.

There is the variable star (denoted V); a comparison star (denoted C), and a check star (denoted K). There may be more than one check star, though. For each frame, the instrumental magnitudes for these stars are obtained, and then we take the differences

C-V and C-K

where C,V and K denote the instrumental magnitudes for the respective stars (or the stars themselves, depending on the context). If more than one check star is used, they are denoted by K1, K2, etc, and we would determine the values of C-K1, C-K2, and so on.

As the C and K stars are constant (which we assume *a priori*), the values of C-V for different frames will vary according to the intrinsic variations in the V star, and the values of C-K will vary about an average value. In a plot of these values against time, there will therefore be two series- one will vary according to the variations in the V star, and the other will be an essentially straight, flat line. There will, of course, be scatter in both of these series due mainly to instrumental or measurement error, quite apart from any true variability in V.

There are a number advantages inherent in this method:

(i) the statistics of the C-K values yield an estimate of the error in the C-V values (see 5.3.3.b).

(ii) atmospheric extinction is automatically accounted for. The angular extent of a typical CCD image is rather small- typically 10' or so- and for the range of zenith angles usually encountered in observation, the difference in air mass between any two stars in such a CCD field will be negligible. Thus, all stars on the frame are observed at practically the same air mass, and therefore suffer the same amount of extinction. When the magnitude differences are taken, the extinction terms cancel out. This approximation is especially valid for the longer wavelengths, where the CCD is most sensitive, and where the value of the extinction co-efficient is quite small.

(iii) instrumental drifts are accounted for. Any change in system sensitivity will affect the measurement of all stars in the field equally, and so will be cancelled out when magnitude differences are taken.

(iv) changes in sky transparency are accounted for. Again, since all stars are nearby, and are measured at the same time, any change in the gross transmission of the air will be equal for all stars, and the effects negated by the taking of differential magnitudes. This applies also to the presence of cloud, as long as its thickness is constant across the CCD field. Thus, differential photometry may be undertaken under conditions which would prohibit other methods.

(v) an advantage peculiar to CCD differential photometry is that all the components necessary for the reduction process - V, C and K stars, and sky regions, are likely to be available on the same image. This represents a very efficient use of observing time- the variable star is almost always under study, and all data necessary to obtain its brightness at a particular epoch are taken at the same time.

There are, of course, also some provisos:

(i) that the program stars be of similar colour. If there is a significant difference in spectral type between one or more of the stars, there will be a relative drift in the instrumental magnitudes

quite apart from any intrinsic brightness changes. This is so since the stars will suffer differential extinction because of their colours- there is a colour term in the Bouger relation for the extinction co-efficient. The severity of this effect will be proportional to air mass, and later-type stars on a CCD frame will suffer less extinction than earlier types, and will thus brighten relative to them as air mass increases. A colour difference may not always be avoidable, but it should be minimised by suitable choice of C and K. For this reason, BVRI, or at least VRI, frames of the field of a new source are taken prior to initial observations, in order to check the colours of prospective C and K stars.

(ii) that suitable C and K stars are in the same CCD field, and of such brightness that a reasonable exposure time neither saturates any of them, or is so short as to degrade measurement accuracy for any of them.

(iii) that the differential magnitudes are only in the instrumental system, and cannot directly be compared with those obtained by other observers. Observations of standard stars are necessary for the conversion to magnitudes in a standard system. Of course, it is quite possible that *filtered* instrumental differential magnitudes correspond closely to differential magnitudes in the standard system, so all that is needed is the standard magnitude of the C star (and preferably K as well) for conversion to standard absolute photometry.

5.3.3(b) Error estimation in differential photometry

In a differential time-series using multiple check stars, the values of $C\text{-}K_n$ will, for each check star, vary about an average magnitude, whilst C-V varies with the intrinsic variations of V. This is with the assumption that C and K are both steady, and with proviso (i) as given above. The scatter in each check star's time series will give an indication of the relative photometric accuracy achieved in the measurement of that star.

For fainter K, this scatter will increase, since the CCD is receiving fewer photons (and thereby yields fewer ADU at the end of the exposure), thus reducing measurement accuracy. It is found that the scatter (i.e. standard deviation (in magnitudes) of the time series) increases exponentially with increasing (i.e. fainter) differential magnitude of K.

It is possible (Howell *et al.* 1988) for this error to be estimated *a priori*, based on knowledge of the CCD characteristics (e^-/ADU, read noise, etc), exposure time, pixel counts and so on. This path is rather involved, and may not be desirable (or even feasible) for many observers.

The method of using the *observed* scatter in C-K_n values is most common, and is very direct and robust since it does not rely on assumptions about CCD behaviour. The catch is to find a check star of similar magnitude to the variable, since then the C-K statistics will be similar to those for C-V, allowing the C-K scatter to be used directly as an error estimate for C-V. However, this may not be possible in practice and, if V is highly variable, C-V and C-K may match for only short sections of the light curve. This will mean that σ(C-K) is over- or under-estimating σ(C-V) for much of the data.

The method to be employed for most of the data presented here, is to measure several check stars, both brighter and fainter than the variable (and approximately the same, if possible). Up to a dozen or so K_n may be defined and measured for a particular field. For each night's data, σ(C-K_n) are found, and these are plotted against $\overline{(C-K_n)}$, as in Figure 5.1. An exponential is fitted to these points, and thus the expected error (i.e. scatter) for any differential magnitude may be found. Of course, this must be done separately for each night's data on a particular object, but this is a natural consequence of the data reduction in any case.

This allows each individual C-V measurement to be assigned its own error, as shown in Figure 5.2. For each data point, the CV's differential magnitude at that point is used with the exponential fit to the σ(C-K_n) to yield an estimated σ(C-V) for each single observation. If only one or two K were measured, this would not be possible. One would estimate a *single* magnitude error to be applied uniformly to *all* data points, since there would not be enough (or any) information on how the error increases with Δm to do anything more.

A caveat of this multiple-K technique is that the photometric quality of the night be more-or-less constant during the observations, if one is treating all the data together. If the night starts clear, but turns cloudy (or *vice versa*), the quality of the "clear" data (as judged by the estimated error derived from the C-K_n scatter) will be reduced by the poorer statistics of the "cloudy" data. Whilst useful data may still be gathered when observing through cloud, it may be profitable to reduce "clear" and "cloudy" data separately when the most accurate results are desired.

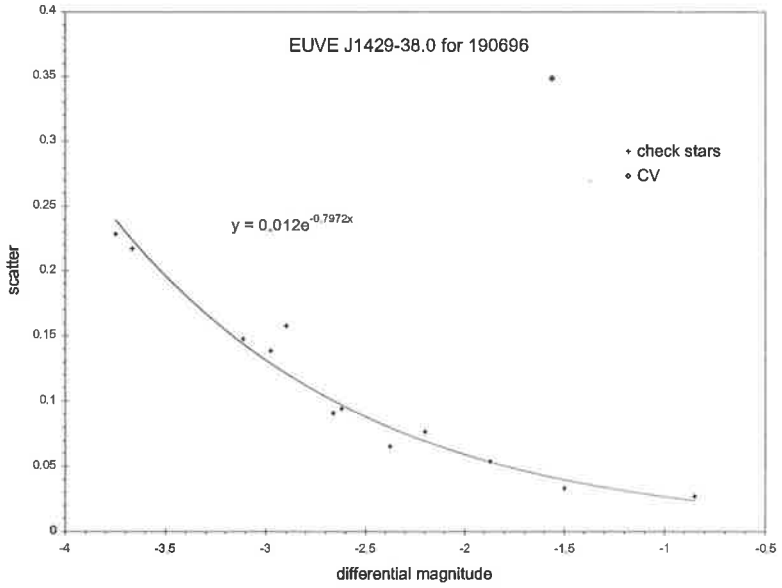

Figure 5.1

An example of a magnitude-scatter plot for one night's observations of the field of EUVE J1429-38.0. A more negative differential magnitude means a fainter star, and so the scatter (i.e. measurement error in the data, or $\sigma(C\text{-}K_n)$) increases. This is observed for the K stars (crosses). An exponential has been fitted to the K data (with the resulting equation shown).

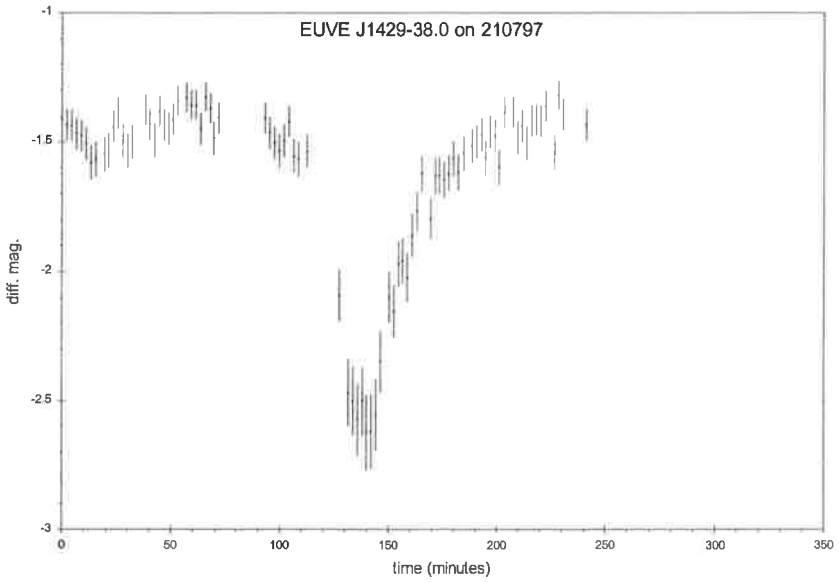

Figure 5.2

An example of a night's data on a source, with error bars included. The errors were estimated based on the CV's differential magnitude for each data point, and an exponential fit to the set of K star scatters in that particular night's magnitude-scatter plot.

5.4 CCD reduction software

The very nature of CCD time-series differential photometric data suggests a certain amount of automation in the reduction of such data. There is a large number of essentially identical image frames which are to be processed in an identical way and, all being well and initial essential parameters given, reduction can then be fully automatic.

However, all rarely is quite so well, and at least some level of human intervention often is required. This is especially so in the telescope system employed here. There are occasional significant excursions in pixel locations of star images between frames, besides the "typical" long-term drift mentioned already, as well as loss of images due to cloud. Widespread high-level reduction applications such as IRAF and DAOPHOT do allow for some movement of images between frames- but not excessive cases, and also require conversion of CCD frames to standard formats (FITS, for example). The implementation of these packages may not be feasible due to hardware/software limitations at a given observatory, so the user may have to look elsewhere.

For the author's work, Dr. Andrew Smith (a colleague in the research group at Adelaide) developed a semi-automatic package for the Windows operating system. It provides for differential photometry of any number of stars in an ST-6 CCD image (the current version of the software assumes that all images are in the native SBIG ST-6 format). The required input files are the CCD image files which are to be reduced, a flat-field image, and a "profile" file (see below); the output is in the form of a text file, containing columns of Julian day of mid-exposure, heliocentric Julian day (HJD) of mid-exposure, C-V and C-K_n. The relative timing of images in a sequence is derived from the PC clock times recorded in each image file's header; the "absolute" time of each is calculated from the relative time since the first image, and the start time of the first image as noted from a clock and written in the log. Thus, the effect of drift in the PC clock is reduced to that experienced over the duration of an image sequence.

For each image file directory to be processed, the user must specify the Universal Date and Time of the first image; the J2000.0 RA and Dec of the V star (for the heliocentric correction, determined for the time of each image); PC clock drift rate (for correction of the image time, taken from the image file header), if considered necessary. Also required are the names and locations of the image, flat-field, profile and output files.

The profile file contains the pixel locations and sizes for the software star and sky apertures which are used in the differential photometric reduction. If no profile file is specified, the user must create and edit one when the first image is displayed; otherwise, the specified one is

used. Whilst the boxes may be moved around during reduction (individually or as an ensemble) to allow for image drift, the size of each one is fixed at creation (at that stage, the size of each box is adjustable, also).

In practice, the user specifies the above-mentioned files and parameters, the software flat-fields all image files (it assumes that dark subtraction has already been applied), and the first image is displayed. If the profile file was specified, the aperture boxes are displayed also, and the user shifts them so that they are over the correct stars. (If the profile was *not* specified, the user needs to create one at this stage). The user then has the option to accept or ignore the current image. If accepted, the software determines all differential instrumental magnitudes and the HJD of mid-exposure for the current frame, and writes them to the output (*.dat) file. If ignored, the output data are not written to the output file. Then the next image is displayed, the profile shifted if need be, and so on...

Whilst this is a fairly basic reduction package (there is no facility for accounting for hot pixels in sky regions by median averaging, for example, and apertures are only square or rectangular), and user intervention is required to accept or reject every image- and move the profile about if necessary- the reduction procedure is quite robust, since every frame is briefly examined by eye for defects, and it is quite quick- a few seconds per image, unless the profile must be adjusted.

CHAPTER 6. EXPERIMENTAL RESULTS: EXTINCTION PHOTOMETRY

6.1 Extinction photometry at Woomera

A program of semi-regular extinction photometry was undertaken at Woomera over the period August 1994-September 1996, primarily as site-testing for the consideration of Woomera as a possible southern hemisphere site for the Auger project. This project involves the construction of two very large cosmic ray particle detector arrays, each containing optical detectors looking for related activity in the near ultra-violet.

Of prime interest was the general value of the U-band extinction coefficient for the observatory site at Woomera, and thereby an estimation of the mean extinction length in the U-band. This region of the spectrum was of prime interest since it is that region where the atmospheric nitrogen fluorescence phenomena to be studied by the proposed Auger detectors occur.

Also of interest were temporal variations in k_U, ranging from anticipated diurnal changes, to possible seasonal trends. Of secondary interest, but perhaps important, was the influence of the spectral type of the observed extinction star(s) on the extinction coefficient, via the presence of the second-order colour term in the Bouger relation (see Section 4.1.3).

The equipment and reduction methods employed have been described in Sections 4.2 and 4.3. Most of the U-band data were obtained with the Hamamatsu PMT and Hoya UG-1 filter. After May 1995, data were obtained using the SBIG ST-6 CCD and Optec UBVRI filters. On one night, simultaneous PMT and CCD U-band data were obtained on a number of stars, in order to compare the instrumental magnitudes derived in the two systems, and thereby explore the validity of direct comparison of PMT and CCD extinction measurements.

6.2 PMT data

6.2.1 The measured k_U

Table 6.1 shows the PMT U-band extinction coefficients obtained. Included are the range of air masses over which the data were obtained, and also the "instrumental magnitude" (see below, Section 6.2.2) of the observed star at X = 0; that is to say, its ex-atmospheric "instrumental magnitude". As described in Section 4.2.3, this value should remain essentially constant for a given star, a given filter, and a stable telescope/detector system. Therefore, the behaviour of this value should give some indication of the stability of the system (as mentioned previously, this applies equally well to the CCD data).

Table 6.1
Woomera PMT U-band extinction observations

Date	star	k(ln)	X=0 "mag"	k(mag)	X=0 mag	X min	X max
5-6/8/94	Rigel	0.43±0.01	-14.46±0.02	0.46±0.01	-15.70±0.02	1.6	7.8
7-8/9/94	Tau Cet	0.56±0.01	-10.55±0.01	0.61±0.01	-11.45±0.01	1.4	3.6
8-9/11/94	Procyon	0.46±0.01	-13.66±0.02	0.50±0.01	-14.83±0.02	1.6	4.8
9-10/11/94	Procyon	0.57±0.01	-13.83±0.04	0.62±0.01	-15.02±0.04	1.5	12.75
1-2/12/94	Procyon	0.48±0.01	-13.72±0.01	0.52±0.01	-14.90±0.01	1.4	6.2
1-2/12/94	Beta CMi	0.52±0.01	-12.31±0.01	0.56±0.01	-13.37±0.01	1.4	5.4
1-2/12/94	Gamma CMi	0.51±0.01	-8.00±0.03	0.56±0.01	-8.69±0.03	1.4	5.3
2-3/12/94	Procyon	0.50±0.01	-13.69±0.02	0.54±0.01	-14.86±0.02	1.3	1.7
3-4/12/94	Procyon	0.50±0.01	-13.72±0.02	0.54±0.01	-14.89±0.02	1.2	8.3
5-6/1/95	Procyon	0.54±0.01	-13.72±0.01	0.58±0.01	-14.90±0.01	1.25	2.5
5-6/1/95	Beta CMi	0.59±0.01	-12.35±0.01	0.64±0.01	-13.41±0.01	1.3	12.5
5-6/1/95	Epsilon Cen	0.57±0.01	-13.32±0.03	0.62±0.01	-14.47±0.04	2.25	5.8
3-4/3/95	Xi Oph	0.52±0.01	-10.33±0.01	0.57±0.01	-11.21±0.01	1.3	2.8
4-5/3/95	Procyon	0.47±0.01	-13.66±0.02	0.50±0.01	-14.83±0.02	1.8	3.5
4-5/3/95	Eta Cor	0.50±0.01	-10.36±0.02	0.55±0.01	-11.25±0.02	1.3	2.8

Note : k(ln), is the extinction coefficient found when taking -ln(counts).
: X=0 "mag", is the extrapolation to zero air mass of the instrumental magnitude of a star when the instrumental magnitude is found by taking -ln(counts).
: k(mag), is the extinction coefficient found when taking -2.5log(counts) for a star; that is, the usual astronomical magnitude scale.
: X=0 mag, is the extrapolation to zero air mass of the instrumental magnitude of a star when these are found by taking -2.5log(counts).
: X min and X max refer to the minimum and maximum air masses for a given run.

Figure 6.1 shows the individual nights' Bouger plots, whilst Figure 6.2 shows the coefficients vs date.

6.2.2 Exponential extinction length

Whilst it is customary to take the logarithm in base 10 to determine astronomical magnitudes from observed fluxes, the natural logarithm (ln) is used in this discussion. Thus, here, the "instrumental magnitude" of a star which yields a detected flux F, is taken to be ln(F). In the data reduction, this is done simply by taking ln(counts/second) for the sky-subtracted flux detected from an observed star.

This definition was chosen since it easily leads to a determination of the distance which is required for a light beam to reduce in intensity by a factor of 1/e. The inverse of the extinction coefficient as defined here (i.e. using ln(F)), gives the number of atmospheres required for this (let this be called the "exponential extinction length"). That is,

exponential extinction length (E.E.L) = $(1/k_U)$ in atmospheres.

If we want a distance, we must derive the equivalent "length" of the atmosphere in kilometres, if we are to consider horizontal extinction. That is to say, what depth would the atmosphere have if it were compressed to a single layer, at ground level, at Standard Temperature and Pressure (STP)- and then consider this also as the equivalent horizontal distance of one atmosphere.

Standard atmospheric pressure is taken to be 1013 hPa. Values from the Woomera Meteorological Station, recorded on several nights during the extinction program, indicated that the pressure for Woomera varied between about 990 hPa and 1010 hPa. Assuming 1000 hPa for an average Woomera pressure, the standard pressure of 1013 hPa is only about 0.013% different, and this is quite negligible. The value of 1013hPa converts to 1035.62 g/cm^2.

The density of air at STP at ground level is taken to be 1.29 kg/m^3, or 1.29 10^{-3} g/cm^3. Therefore, for a single, uniform layer of constant density and pressure, the atmosphere has an equivalent height of

$$1035.62/1.29\ 10^{-3}\ \text{cm},$$

or about 8.03 km. We consider this also as the horizontal length (at ground level) of the equivalent of one atmosphere. Figure 6.3 shows the exponential extinction lengths, expressed in kilometres, as derived from the measured k_U, plotted against date. Since the nitrogen fluorescence detector component of the Auger project observes at low elevations, large e.e.l.'s

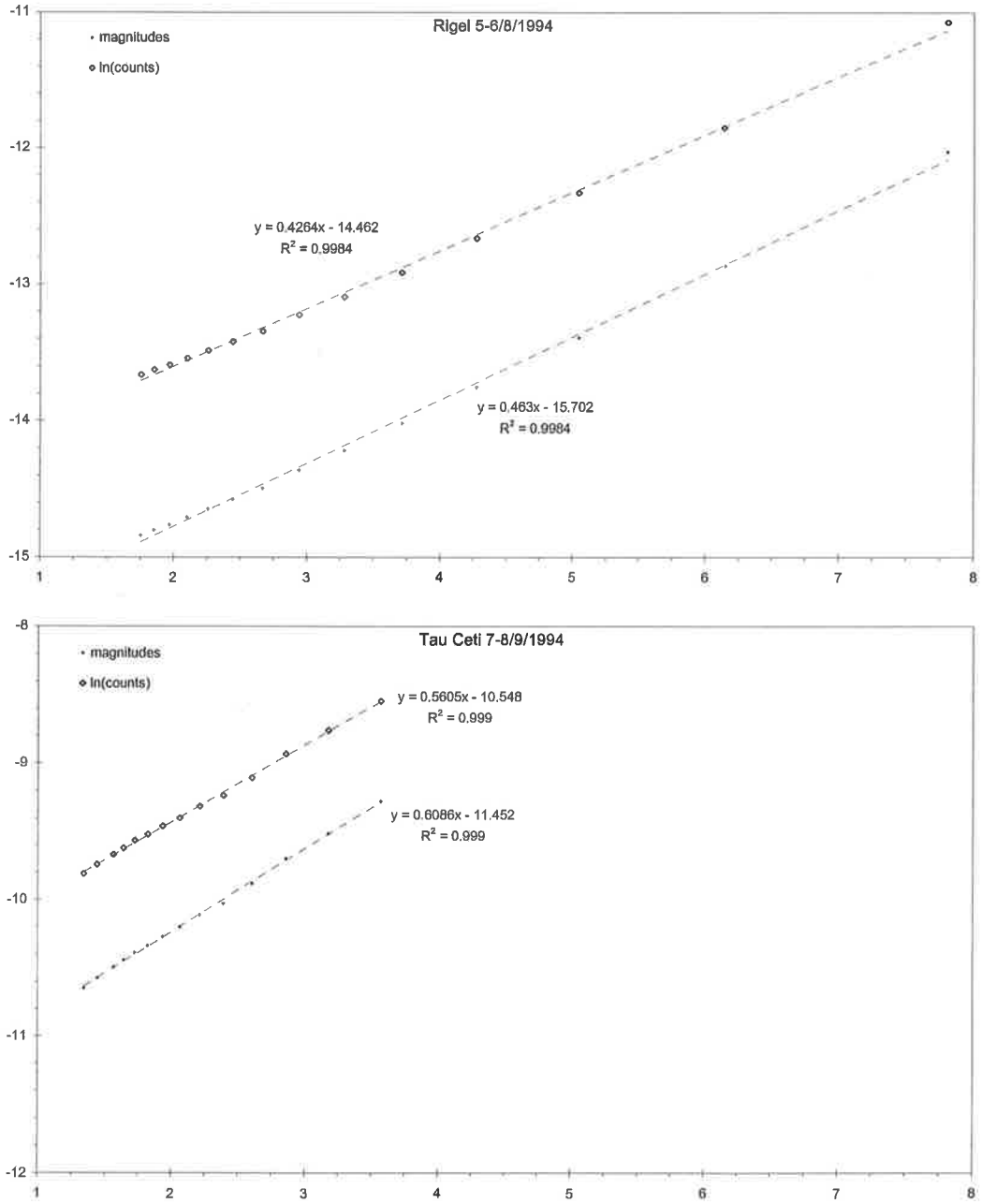

Figure 6.1

Woomera PMT U-band Bouger plots.
Ordinate is in "magnitudes" (see text); abscissa is air mass.

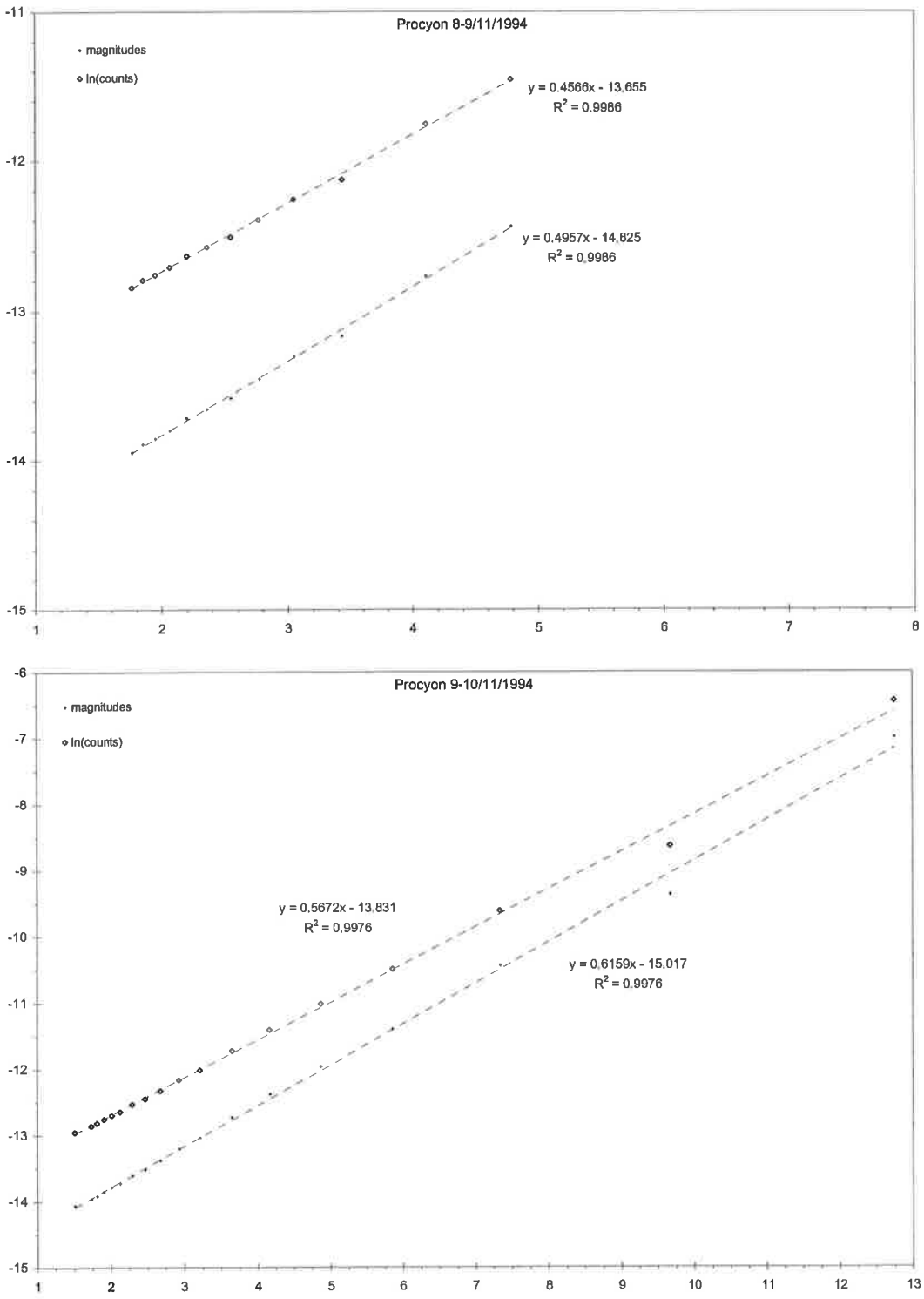

Figure 6.1 continued
Woomera PMT U-band Bouger plots.
Ordinate is in "magnitudes" (see text); abscissa is air mass.

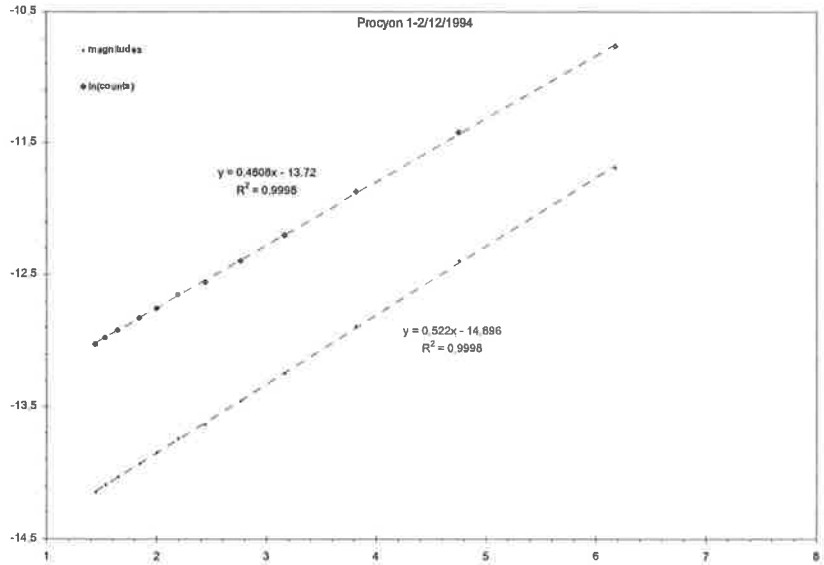

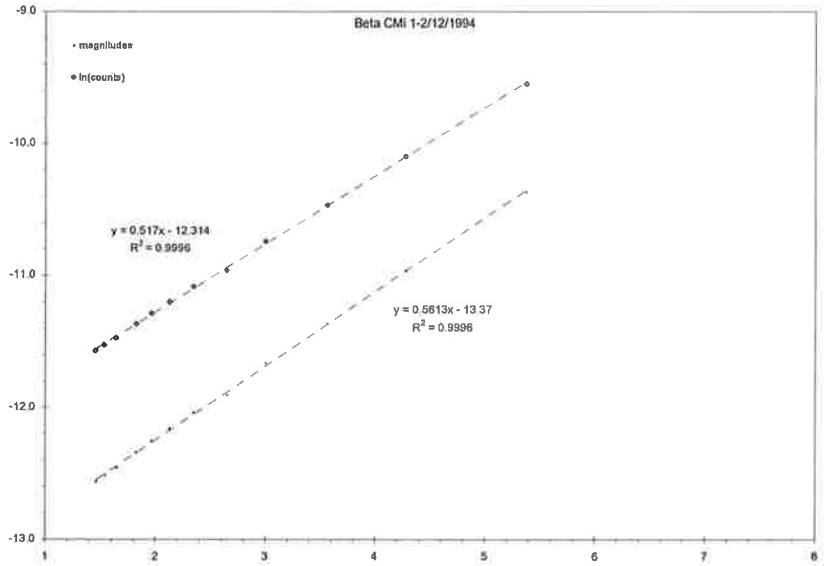

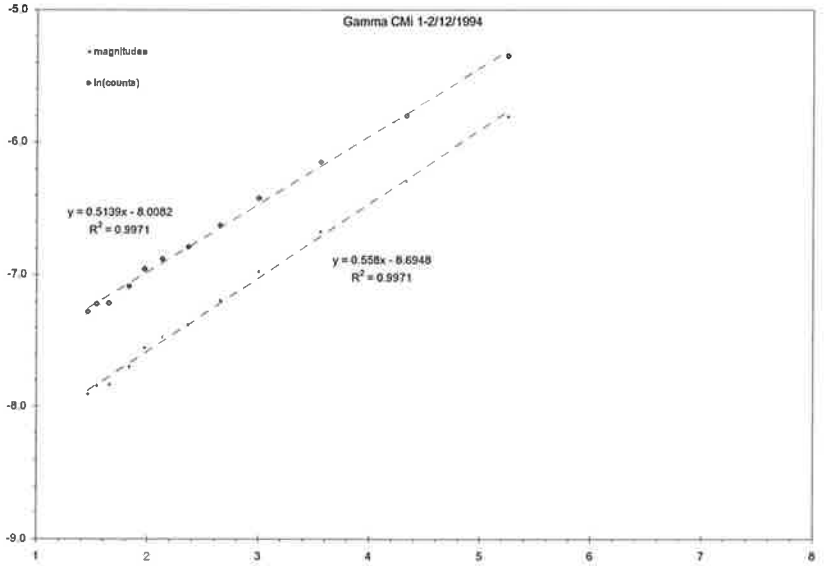

Figure 6.1 continued
Woomera PMT U-band Bouger plots.
Ordinate is in "magnitudes" (see text); abscissa is air mass.

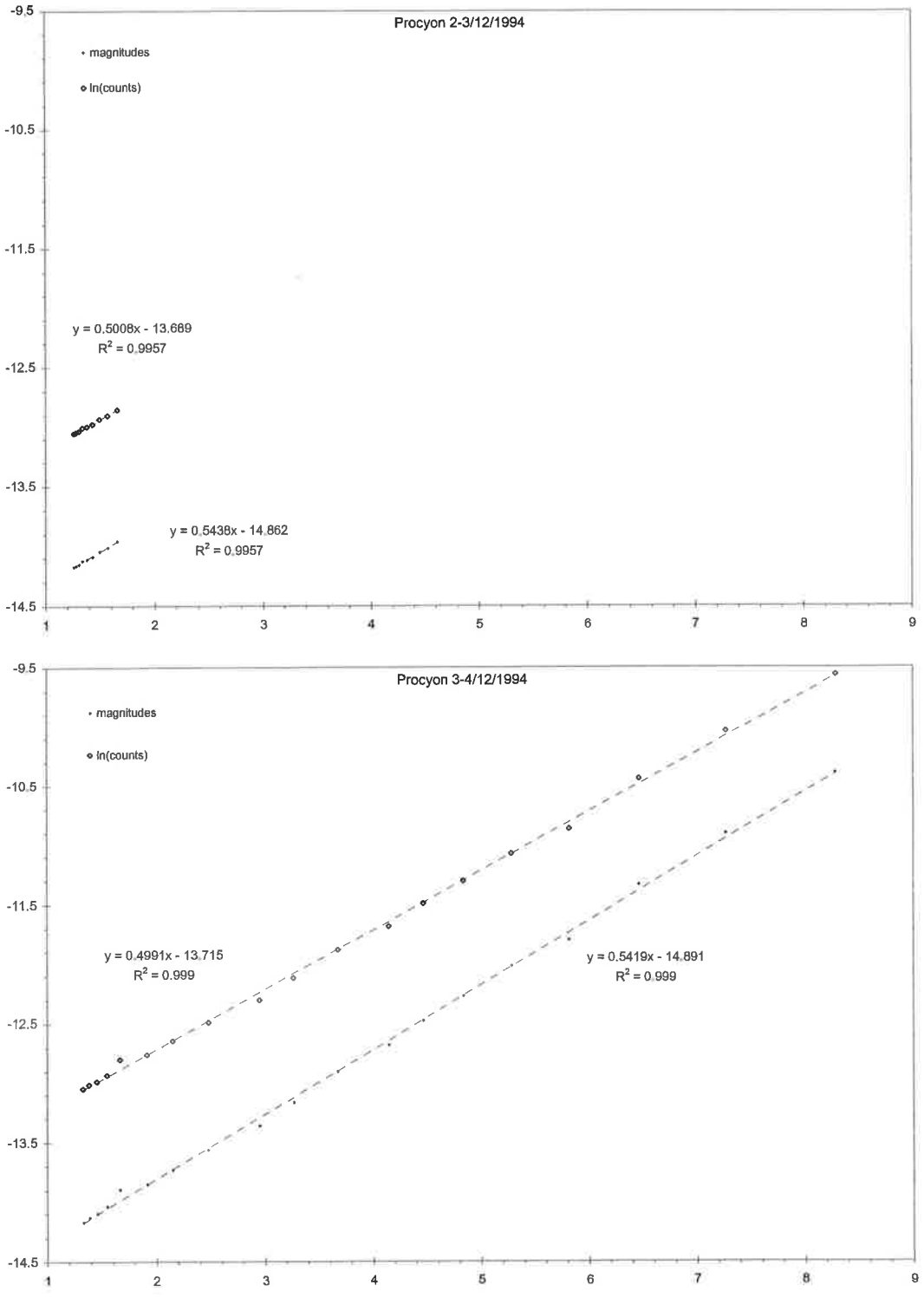

Figure 6.1 continued
Woomera PMT U-band Bouger plots.
Ordinate is in "magnitudes" (see text); abscissa is air mass.

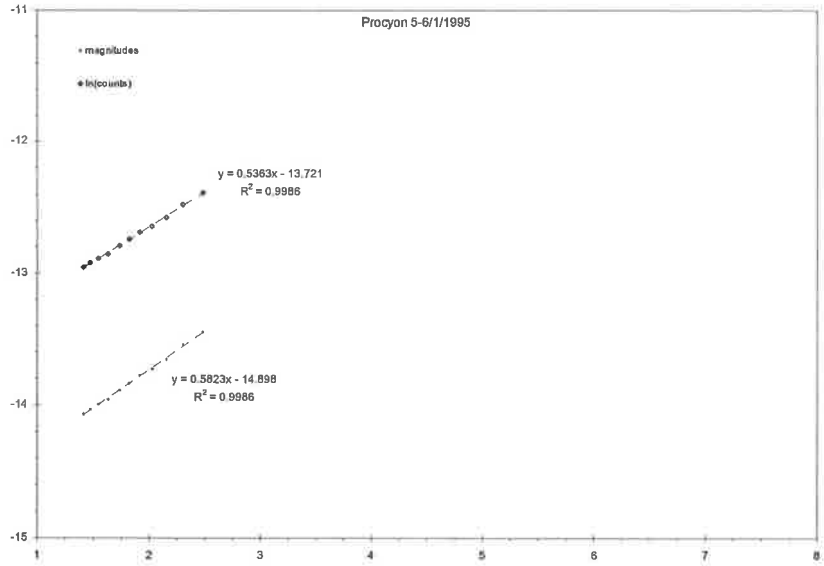

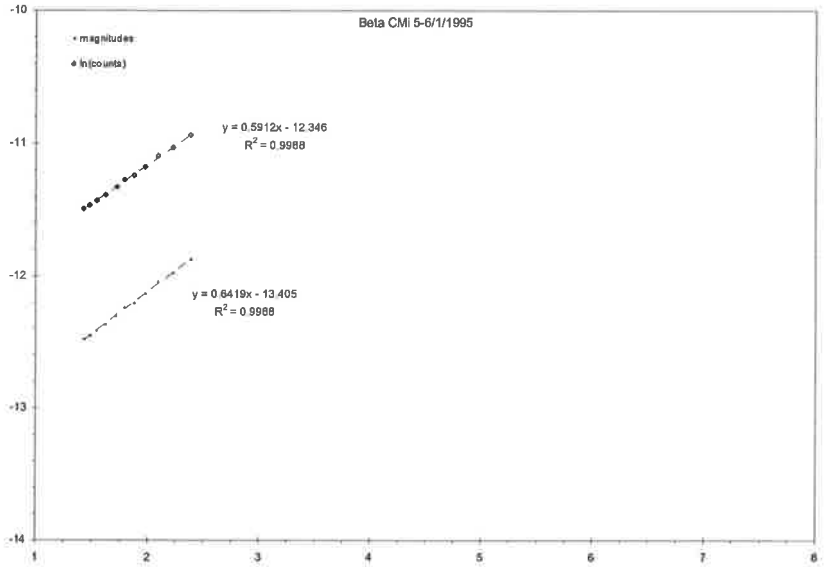

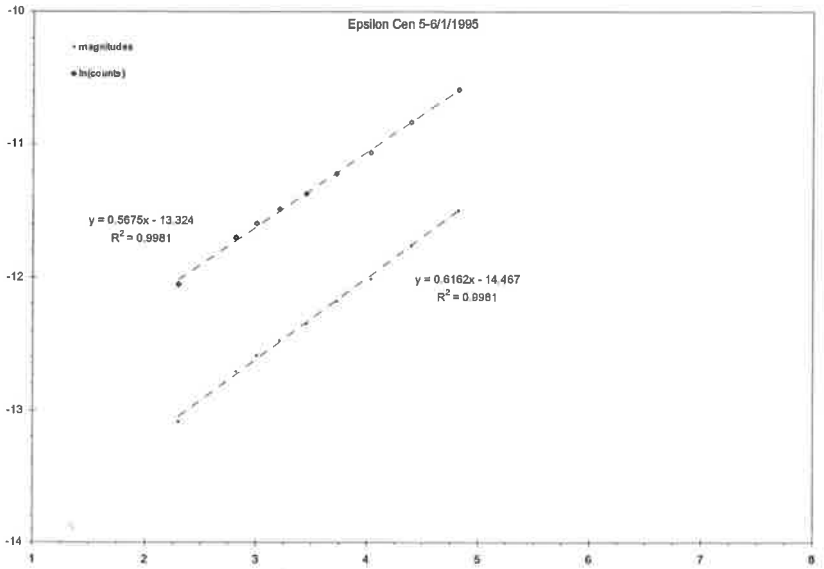

Figure 6.1 continued
Woomera PMT U-band Bouger plots.
Ordinate is in "magnitudes" (see text); abscissa is air mass.

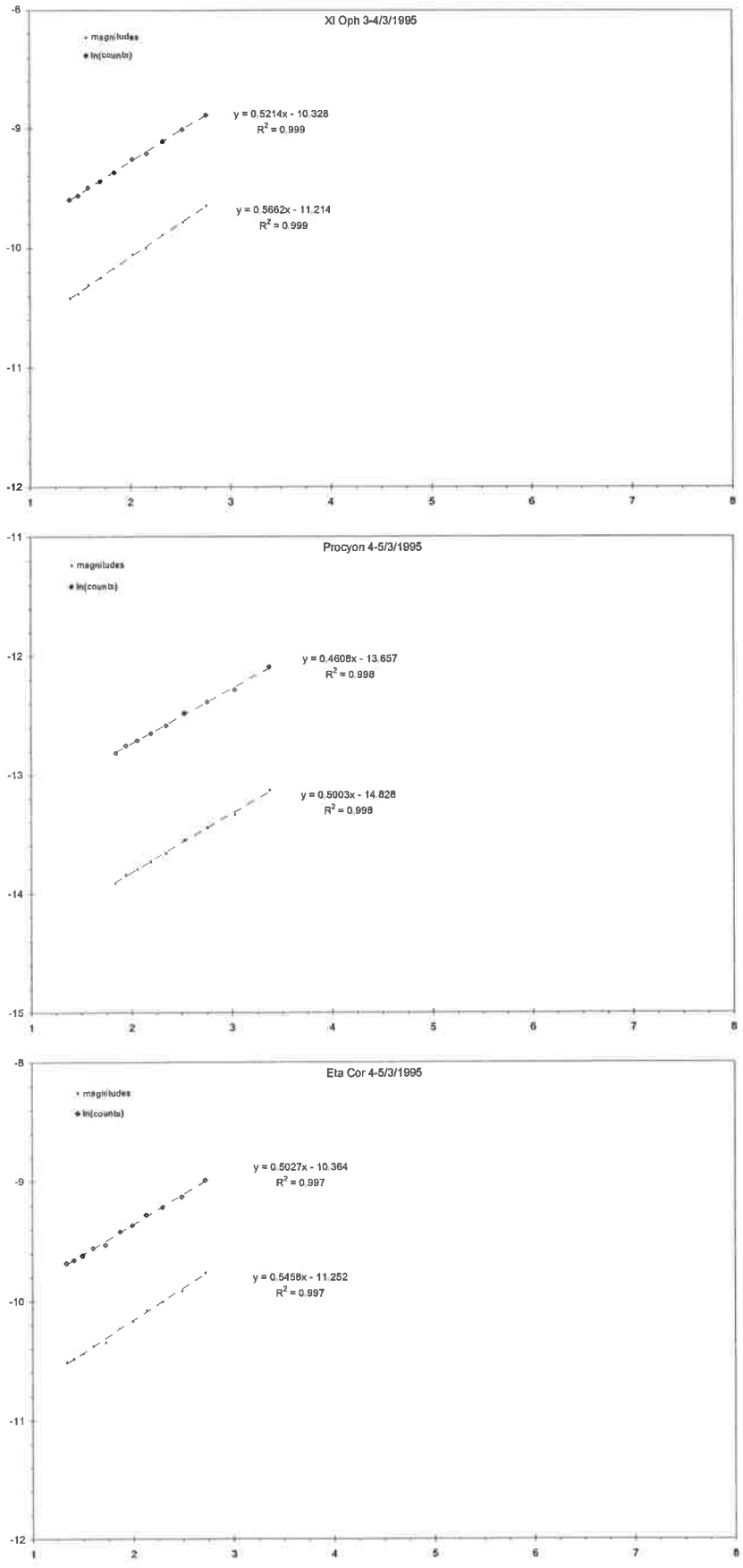

Figure 6.1 continued
Woomera PMT U-band Bouger plots.
Ordinate is in "magnitudes" (see text); abscissa is air mass.

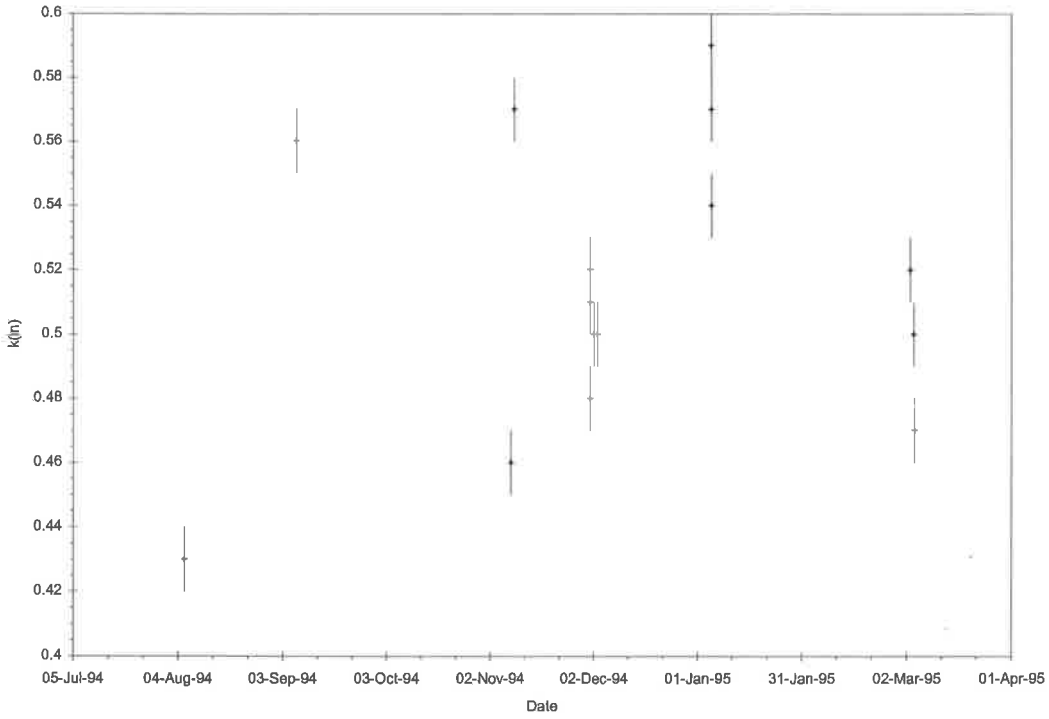

Figure 6.2
Woomera PMT U-band extinction co-efficients vs. date.
Note: use of ln(counts) in reducing the data.

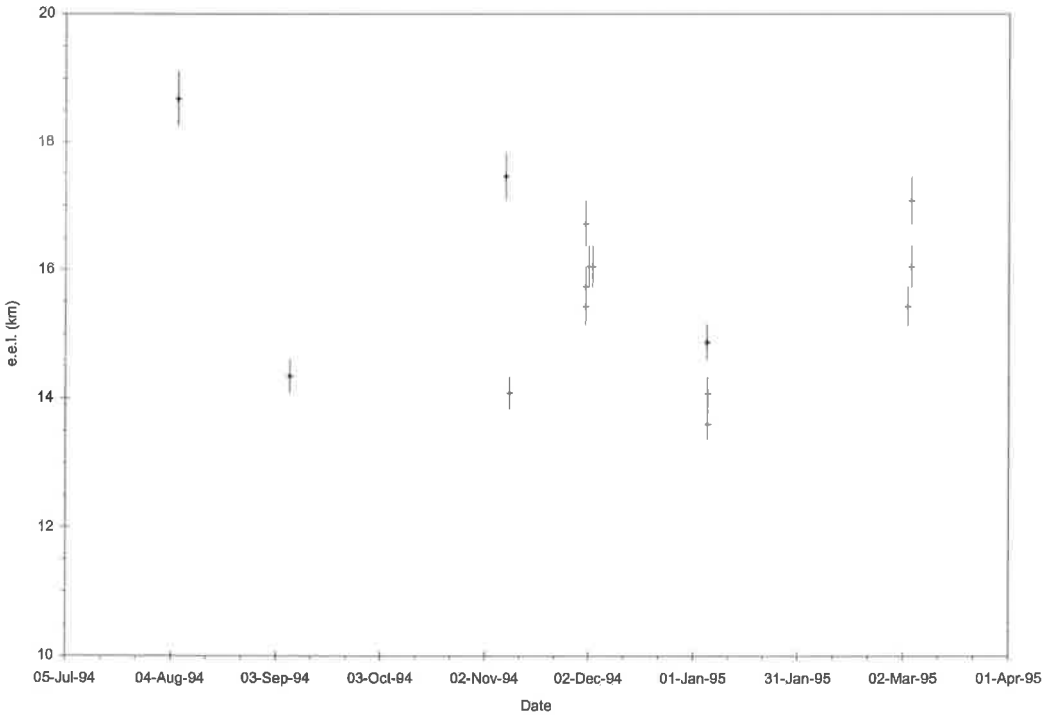

Figure 6.3
Woomera U-band exponential extinction lengths vs. date.
These are the (near-horizontal) distances, in km, required to reduce the intensity of a light beam (in the U-band) by a factor of 1/e.

will enable the detector to look out to considerable (nearly) horizontal distances, and thereby increase its collecting area.

6.2.3 Temporal variations

6.2.3(a) Short-term changes

The individual Bouger plots (Figure 6.1) show, in general, little evidence for variation in extinction during any given night's data run. There is only slight indication of a concave or convex trend to a few individual plots, this suggesting stability on a time-scale at least comparable to that of the data run, usually a couple of hours or so.

However, there is some suggestion of non-random scatter of data points about the fitted line in some plots. The appearance is that of a low-level "wave" in the data, of full amplitude less than about 0.1mag at worst. This "wave" suggests slight changes in extinction on time-scales of 20-30 minutes or so- but without any obvious longer-term (~hours) changes. The strength of this possible effect does not seem to vary clearly with air mass.

This observed effect *may* be due to measurement error and real, random changes in k, but the trend-like appearance (e.g. not equally distributed about the fitted line) does suggest a non-random origin. In any case, the effect is slight, and does not alter the night's "average" extinction.

(Note: if this effect *is* real, it warns against the use of very short data runs (<~0.5 hour or so) in order to characterise the night's extinction. The amplitude of this effect is slight, but if the data run is short, it may significantly affect the derived k. If the time available for extinction observations is limited, it would be wiser to take the same number of data points separated widely in time, perhaps an hour between points. This would give a better indication of the general quality of the night, whilst ignoring the possible shortest-term variations).

6.2.3(b) Diurnal, monthly and seasonal variations

Since extinction is influenced by meteorological conditions (e.g. Reimann *et al.* 1992), one may expect that there will be seasonal variation in k, as local conditions do change somewhat with season. Whilst such an effect may well be negligible at some sites, it is indeed apparent at others (Roosen *et al.* 1973). Apart from seasonal changes, there may also be trends over years-scale intervals, and it is to be noted that repeated seasonal trends may have slightly different phases according to the filter used (Rufener 1986).

Whilst the Woomera data are not extensive or dense enough fully to examine the question of seasonal variability, consideration of Table 6.1 and Figure 6.2 allows us to make some generalisation about the diurnal and monthly behaviour of k.

For those months where multiple measurements are available, it is clear that there can be significant variation in the average k from month-to-month (e.g. 0.50, 0.57, 0.50 for December 1994, January 1995, February 1995 respectively). Also, apparent is that the spread in values within a month (i.e. maximum k_U-minimum k_U) may vary somewhat. It is to be admitted that there are not enough data to look at these inter- and intra-month trends in great detail, either. What can be said is that such behaviour occurs, even if we cannot characterise it fully.

Therefore, if a precise measure of the extinction is required, it is best to obtain the requisite data nightly, at the same time as the other data for which k is to be used as a correcting parameter. This is so since the data show that there can be significant changes in k from night-to-night, and from month-to-month, with no definite pattern yet evident (but note here the relative paucity of the data for considering such patterns).

That said, the average k_U from these data is 0.51 (corresponding to an average e.e.l. of 15.72 km), with a standard deviation of 0.05 (1.40 km), and the greatest excursions from this average being within 0.08 (3 km).

So, whilst no patterns in the k_U (and, hence, e.e.l.) values are discernible, monthly averages are within about 0.05 of each other, and if this level of error is acceptable, the observer may use a long-term average k value without undue fear. That is, unless, significant transient events, such as severe dust storms or volcanic eruptions, occur. In such cases it is obvious that the extinction values will be altered greatly from the average.

6.2.4 The influence of spectral class on k_U

As stated in Section 4.1.3, there is a colour term (i.e. (B-V)) in the Bouger relation, which suggests that the spectral type of the observed extinction star can influence the derived extinction coefficient. Instrumentally, the effective peak wavelength of the photometeric system is a convolution of the PMT response, the filter (and telescope) transmission, and the observed star's spectral emission in the wavelength region of the filter (ignoring any atmospheric influence). Early-type stars will shift the peak wavelength shorter; late-type stars will shift it longwards, generally speaking.

To estimate the severity of this effect, the UG-1 filter response and a typical bi-alkali PMT response were multiplied together, and then normalised, with a resolution of 2.5 nm.

This was taken to be the effective instrumental response. This was then multiplied, in turn, by the model spectra for classes O5, B0, B5, A0, A5, F0, F5, G0, G5, K0, K5, M0, M5 and M9 (using *Visual Spec* software by V. Desnoux, http://valerie.desnoux.free.fr/vspec/), with the spectral resolution degraded to that of the estimated instrumental response curve. This yielded the filter*tube*spectrum curves shown in Figure 6.4. It is clear that these *effective* spectral curves, over the wavelength region of the UG-1 filter, vary considerably. One may regard each curve as the spectral distribution of a light beam (from a star) which is then to suffer wavelength-dependent absorption and scattering as it passes through the Earth's atmosphere. A star having a bluer spectral distribution will suffer more extinction than one having a red distribution, since the monochromatic extinction decreases rapidly with wavelength in the spectral range under examination.

If we multiply the curves in Figure 6.4 by the monochromatic extinction as given in Figure 4.3, we can estimate the relative total extinction suffered by a star of given spectral type. Summing the area under the filter*spectrum*tube*extinction curves for each class (discretely, since we do not have continuous functions for each of these "curves"), we find the relative totals as displayed in Figure 6.5. It is seen, as is expected, that A0 stars suffer a comparatively low level of extinction, due to their severe Balmer discontinuity around 360 nm. This discontinuity reduces the short-wavelength intensity of A-type stars relative to that of neighbouring classes. This gives A-types a comparitively "red" spectral distribution, and thereby comparitively low U-band extinction. Indeed, it is not until perhaps G4 or so that similar values are again found. These estimates suggest quantitatively that an M9 star suffers about one-quarter the U-band extinction of an O or B star. The data are not sufficient, however, to determine whether or not this effect is actually visible to such an extent.

We may thus expect that spectral class does have an influence on observed extinction, and this may well be observable for sufficiently precise and accurate photometry (e.g. change in k of 0.005 to 0.03, depending on spectral type and filter, Dachs *et al.* 1966). However, it may not even be significant in light of the daily or monthly variations actually seen in the Woomera data.

On one night (JD 2,449,688), data were taken on three stars over the same interval of time, namely Alpha, Beta and Gamma CMi. Their spectral types are F5 IV-V, B7 V and K3 III, with (B-V) colours -0.09, +0.42 and +1.43 respectively.

Figure 6.6 is a plot of the observed k_U against the (B-V) colour index of the star used in the measurement of that data point; the spectral classes range from B7 V to K3 III. There are, admittedly, not sufficient points to examine this question fully. For example, there should

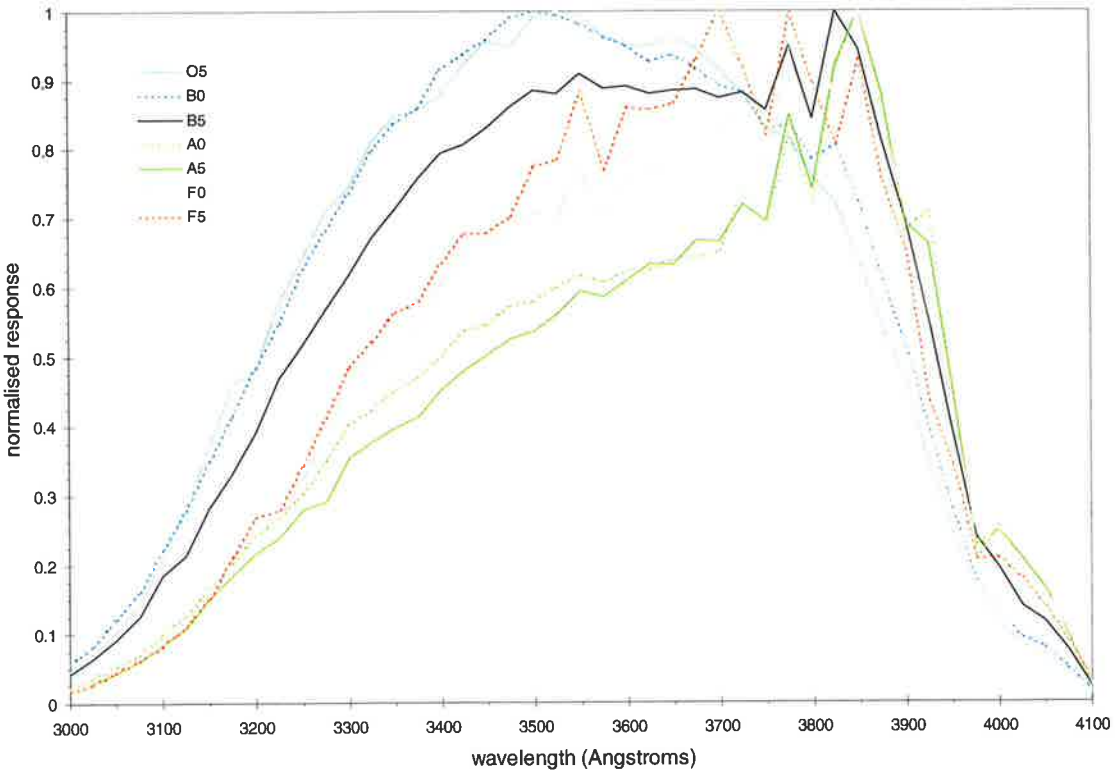

Figure 6.4
Effective spectral response vs. wavelength. The response is the product (tube QE)(filter transmission)*(spectral model).*

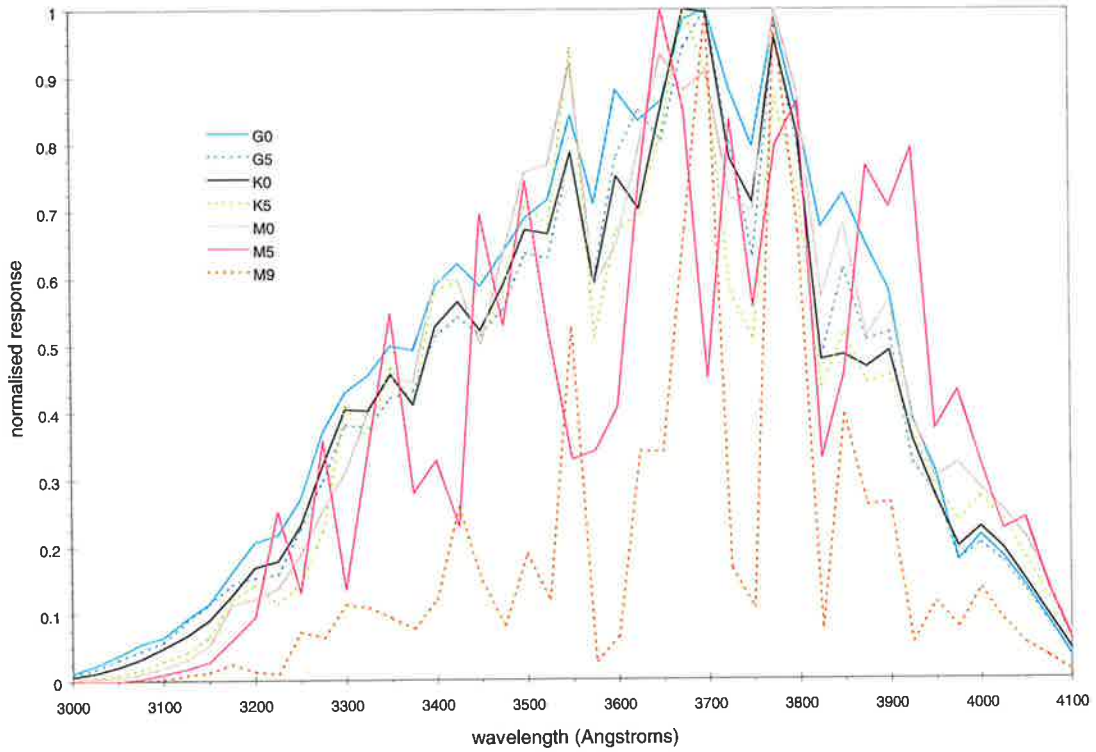

Figure 6.4 continued
Effective spectral response vs. wavelength. The response is the product (tube QE)(filter transmission)*(spectral model).*

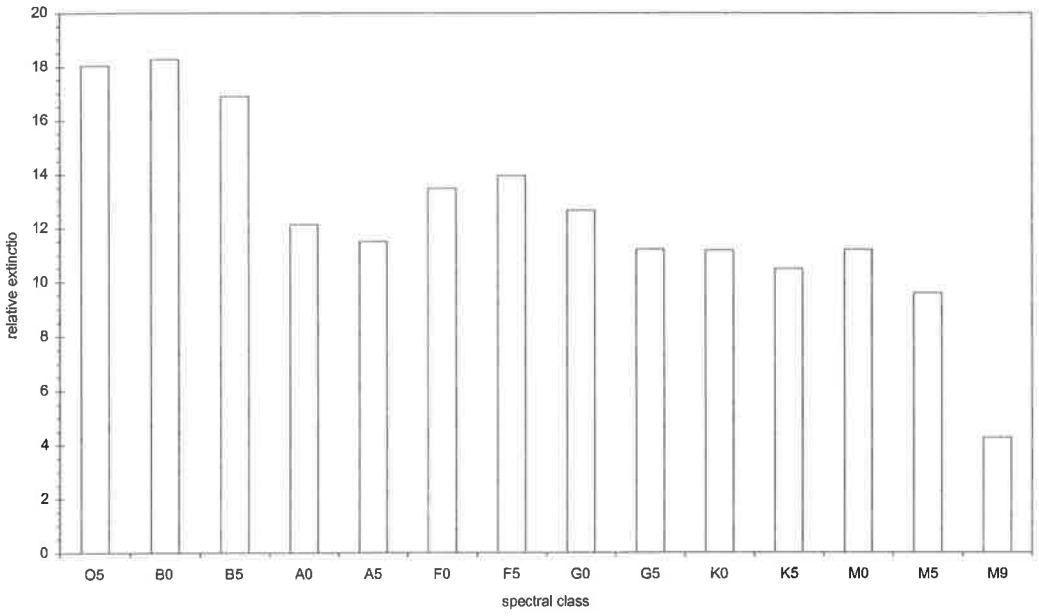

Figure 6.5

Estimated relative total extinction as a function of spectral class.

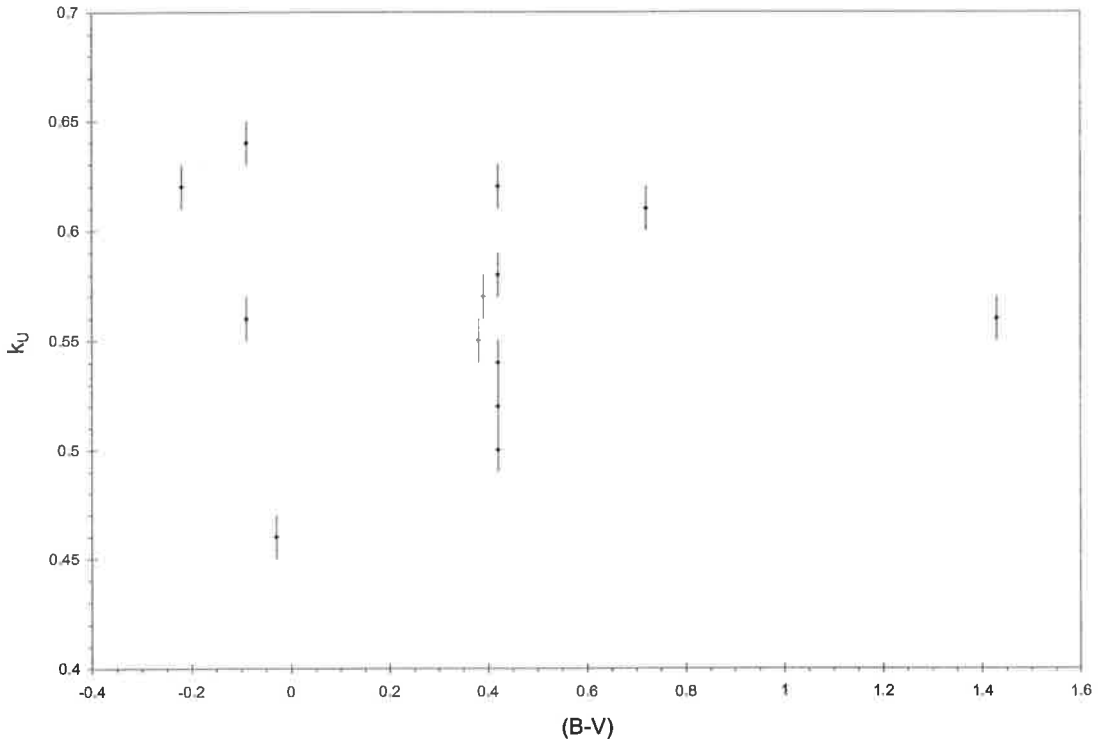

Figure 6.6

Variation of k_U with colour index. These are PMT data only. Note that the data were reduced using the usual astronomical magnitude scale, i.e. -2.5log(counts). There is no evident trend across the range of colours observed, which corresponds to spectral classes B7 to K3. However, the quantity of data is not sufficient to address this issue satisfactorily.

be multiple measurements of each star, as well as more stars of different (B-V). However, what is clear is that there is as much range in the observed k_U for one star (Procyon, (B-V) = +0.42) as there is between all the stars observed. This suggests- though, due to the incompleteness of the data, does not prove- that the influence of spectral class on observed k_U is not significant compared with the variations thereof due to environmental factors.

Tentatively, then, it can be suggested that this sort of extinction photometry may be carried out without too much care as to the type of star observed, except to say that perhaps using as similar spectral classes throughout the observations as is feasible will remove the possible variability due to spectral class.

6.2.5 Comparison of PMT and CCD U-band data

On the night of 30-31/5/1995 (local dates), simultaneous PMT and CCD U-band observations were made on ten stars, in order to examine the question of directly comparing PMT- and CCD-derived extinction coefficients.

(Note: In this sub-section, instrumental magnitudes are taken as -2.5 log(counts)).

The method used was to obtain instrumental magnitudes for each star, using ten-second (star+sky) and (sky) integrations for the PMT, and a ten-second exposure for the CCD. These magnitudes would then be plotted against each other on a scatter plot. If the PMT and CCD photometric systems are directly comparable, the points should lie along a line of slope = 1, since magnitude *differences* should be the same in each system. However, a line fitted to the points need not pass through the origin of the plot, since the systems will have different zero points.

Figure 6.7 is a scatter plot of the obtained instrumental magnitudes, with a least-squares fitted line also shown. The regression yields a slope of 0.960 ± 0.036. Although the range of magnitudes is fairly limited, and this check was done only once, it suggests that it is not unreasonable to assume direct comparability between the PMT- and CCD-based extinction coefficients for the U band.

As a point of interest, Figure 6.8 shows the CCD-based extinction coefficients obtained after May 1996. No analysis, as such, was undertaken with these data.

6.3 Comparison with other observatories

Aside from simply knowing the extinction coefficient and the corresponding e.e.l. for Woomera, it is of interest to know how this site compares with other observatory sites in this

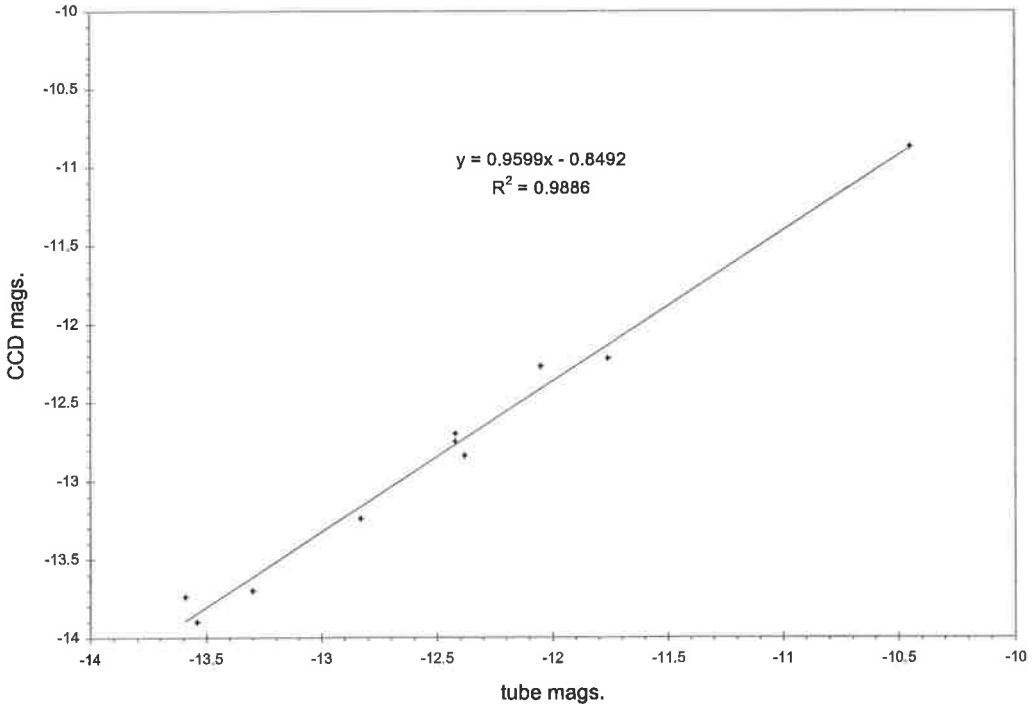

Figure 6.7

Comparison of tube-based and CCD-based U-band instrumental magnitudes. Included is a linear least-squares fit to the data.

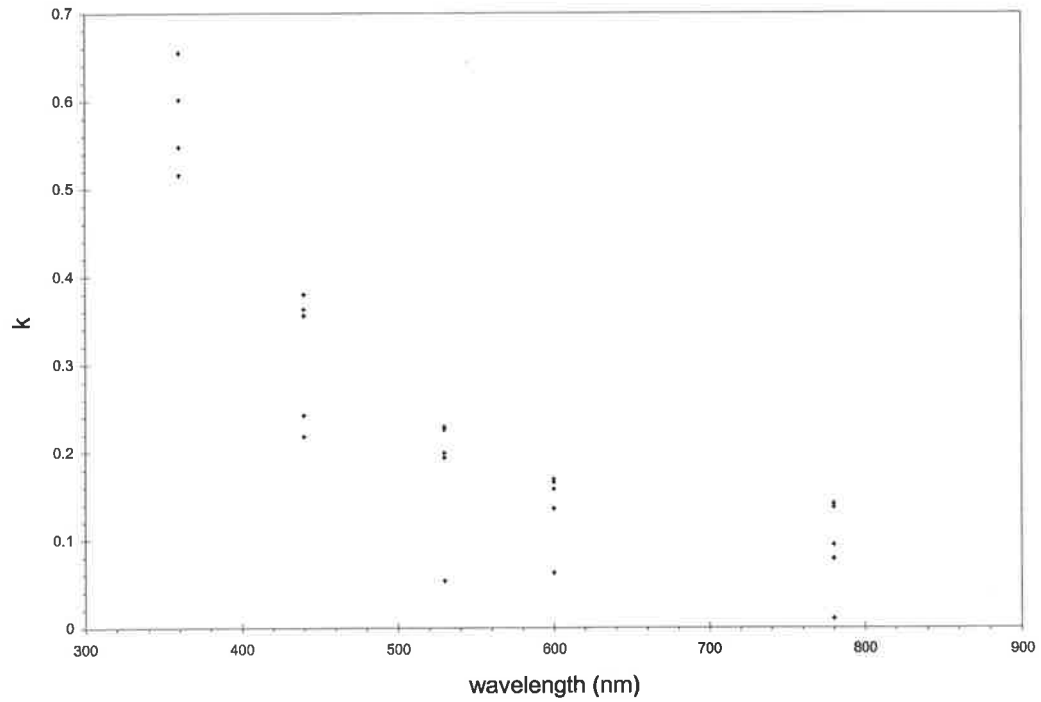

Figure 6.8

Woomera CCD-based extinction co-efficients. The range of k_U values is comparable to that found from PMT-based observations. The variation of k with wavelength is similar to that seen in Figure 4.3.

regard. In the literature can be found papers reporting the extinction values for other sites, often in a discussion of their long-term behaviour.

(Note: In this sub-section, instrumental magnitudes are taken as -2.5log(counts)).

Since the extinction coefficient is most often given as a relative quantity, based on a change in magnitudes for a given change in air mass, it is usually safe to compare directly the values found by different observers using UBVRI filters. This is so since magnitude (or flux) *differences (or ratios)* recorded using standard filters by different telescope systems should correspond quite closely, even if the zero points of the different instruments are quite disparate. That is to say, in the transformation equations from the instrumental to the standard system, the transformation coefficients should be (and we expect, *are*) close to unity for all observers, even if the zero points are quite different. The author has found this to be so for the Woomera system, from comparison of observed filtered differential magnitudes with calibrated absolute photometry of the same stars from the literature or from co-workers.

However, what must be taken into account is the difference in atmospheric depth between the sites. Consider two sites which are at different altitudes (and therefore which have different *absolute* amounts of atmosphere above them), but have the same "clean and clear" air. (Note that we do not consider the question of the whether or not the higher site is above the worst aerosol-laden layers which plague the lower site- which, for simplicity, we say is at sea level).

Furthermore, one undertakes identical extinction photometry at each site, using the same equipment, and observing the same star(s), etc., and that diurnal and seasonal effects are not an issue. System stability is assumed *a priori*.

After data reduction, it will be found that the exatmospheric magnitude of the extinction star is the same for both sites. That is, at X = 0, the instrumental magnitude of this star is the same, since it is the "observed" magnitude in the absence of any atmosphere, and we have assumed complete system stability. This condition *must* be satisfied.

Consider observations at zenith, i.e. at X = 1. At the sea-level site, the starlight has travelled through a greater amount of atmosphere, and will therefore be dimmer, than at the higher site, even though the clarity of the air is the same. Thus, the instrumental magnitudes at X = 1 will differ. Since that at X = 0 is fixed and the same for both sites, the Bouger plots for both sites will have different slopes, and will thereby give different extinction coefficients.

To remove this effect, one can multiply k from the other site by the ratio of the atmospheric depths of the two sites. This will act to increase the k from higher sites, or

conversely to decrease that for lower sites. All locales are now effectively at the same atmospheric depth (or altitude) and the k values are directly comparable.

Table 6.2 shows U-band extinction coefficients for Woomera and for a number of other observatories, as found in the literature (Calar Alto: Leinert *et al.* 1995; McDonald: de Vaucouleurs 1965; Dugway: Cassiday *et al.*; Kilmartin and Gilmore 1994). The correction for different altitudes has been applied. It can be seen that the quality of the atmosphere at Woomera compares very favourably with that at other sites.

(For this, no attempt has been made to account for the stratification of the atmosphere or the distribution of aerosols, etc. It was assumed that the atmosphere is uniform, and that a simple ratio of atmospheric depths would correctly scale the observed extinction coefficients. This is somewhat of a simplification).

6.4 System stability

It has already been mentioned that the long-term stability of the photometric system (i.e. telescope, filters and detector) can be gauged from the behaviour of the exatmospheric magnitudes (m_0) of the observed extinction star(s).

In a stable system, these magnitudes should be constant for each star; there should be no temporal variation at all, as we are considering the flux above the atmosphere, and we also assume that the star itself is non-variable. In Table 6.3 are shown the m_0 for extinction stars for which multiple PMT observations were obtained. There is not a great enough time base in the data for any star used for CCD extinction measurements to enable long-term CCD stability to be examined (the longest time between points for any such star is one week).

The standard deviation of the total α CMi data set, in terms of a percentage of the average flux of those measurements, is just under 7%. This suggests that the system is quite stable.

It is to be noted, however, that Young (Young 1974, Section 3.1.5.1.3) warns against the simple extrapolation of the Bouger plot from moderate or high air masses to $X = 0$, especially for the U band. There will be a slight, wavelength-dependent curve in the Bouger plot at very low X which will not be accounted for by linear least-squares extrapolation from higher X, and so there will be an error in the derived m_0. An example is given in the afore-mentioned reference, showing an error in m_0 of 0.25 mag in the U band, if a straight-line extrapolation to $X = 0$ is made.

Table 6.2
Comparison of other k_u with that observed at Woomera

Obs.	Alt. (m)	depth (g/cm^2)	date	mean k_U	range	mean k_B	range	mean k_V	range	k_U (W)	k_B (W)	k_V (W)
Yonsei			82-89	0.9	0.5-1.8	0.5	0.2-1.8	0.3	0.1-1.5			
Mt. John	1027	914	88-93	0.45	0.36-0.6	0.25	0.2-0.4	0.12	0.1-0.25	0.49	0.27	0.13
McDonald	2075	803	60-64	0.5	0.48-0.58	0.22	0.23-0.31	0.15	0.14-0.21	0.63	0.28	0.19
KPNO	2120	800	60-69	0.56	0.56-0.68	0.27	0.26-0.29	0.16	0.15-0.19	0.70	0.34	0.20
Mt. Rockdale			61-62	0.49	0.45-0.61	0.26	0.23-0.36	0.12	0.1-0.23			
La Silla	2400	770	75-85	0.6	0.54-0.7	0.25	0.22-0.34	0.12	0.1-0.2	0.78	0.33	0.16
Calar Alto	2168	795	90	1.02		0.45		0.3		1.29	0.57	0.38
	2168	795	90	0.96		0.4		0.23		1.21	0.51	0.29
	2168	795	90	0.62		0.32		0.22		0.78	0.40	0.28
Dugway	931	860	88	0.76						0.89		
Woomera	165	1004	94-95	0.56	0.46-0.65	0.34	0.3-0.38	0.21	0.18-0.23	0.56	0.34	0.21

Notes to the table

(i) date specifies the years (19xx-19xx) over which the data were obtained, or the single year (19xx) when the data were obtained

(ii) Calar Alto measurements are for three single nights only, and show the effect of a volcanic eruption

(iii) Altitude information not available for Yonsei or Mt. Rockdale. k are given for interest only

(iv) Dugway measurement is for a single night only

(v) (W) indicates that k has been corrected to the atmospheric depth of Woomera

(vi) Scaling between depth and altitude was found to be

depth = -0.1046*altitude + 1021.4 (g/cm^2)

Table 6.3
Exatmospheric magnitudes (inst. mag. = -ln(counts))
for stars with multiple PMT U-band extinction measurements

Date	**Alpha CMi**	**Beta CMi**
8-9/11/94	-13.65 ± 0.02	
9-10/11/94	-13.83 ± 0.04	
1-2/12/94	-13.72 ± 0.01	-12.31 ± 0.01
2-3/12/94	-13.69 ± 0.02	
3-4/12/94	-13.72 ± 0.02	
5-6/1/95	-13.72 ± 0.01	-12.35 ± 0.01
4-5/3/95	-13.66 ± 0.02	

6.5 How did Woomera fare?

The extinction co-efficients for Woomera are, when corrected for atmospheric depth, similar to those for a number of established and major optical observatories. This suggests that the air at Woomera is very clean, and would therefore be a very favourable site for the Auger fluorescence detector, or indeed any other particle detector which relies on atmospheric effects for operation.

Alas, the decision was later made to locate the southern hemisphere component of the Auger project in South America. This decision was, as may be expected for an international project of such scale, based on a great many factors. One may be confident that it was not the quality of the Woomera atmosphere that led to this choice, however.

CHAPTER 7. EXPERIMENTAL RESULTS- PHOTOMETRY OF EUVE J1429-38.0

7.1 Discovery by satellite and EUV behaviour

EUVE J1429-38.0 (also known Cen 2 or V895 Cen, following Downes *et al.*) was discovered by NASA's Extreme Ultra-violet Explorer (EUVE) satellite. Initial observations were obtained with EUVE's Right-Angle Program (RAP) instruments in 1993. This first detection was quite serendipitous since the principal target at the time was Markarian 421; Cen 2 just happened to lie in the RAP field when the satellite's primary instruments were pointed at the former.

Some 70 hours of observations began on March 4th 1993, and the source was detected at a S/N ratio of 12 in the 0.071-0.214 keV or 58-174 Å range (the EUVE Lexan/B filter) (Craig *et al.* 1996). The nominal source position from the EUVE data was (J2000.0) 14:29:24.0 -38:04:05.2 with an error circle radius of 1'.

The initial EUVE RAP observation yielded a count rate of 0.017±0.004 counts per second. Fourier analysis of the data showed strong signals at the *satellite's* orbital period and its first harmonic (present both in the source aperture and a surrounding sky aperture- therefore not related to the source itself), and lesser ones at 57 and 142 minutes. Subsequently, 142 minutes was taken to be the orbital period of this system.

Further RAP pointings have shown Cen 2 to be variable in the overall count-rate observed; from clear detection through to non-detection.

7.2 Optical identification

Craig et al. 1996 obtained optical spectroscopy of likely candidate stars with the EUVE error circle, using the CTIO 1.5m telescope. One star within the circle showed spectral features typical of a CV, making it suspect of being the optical counterpart to the EUV source. Strong Balmer and He emission lines were seen. Figure 7.1 is the flux-calibrated discovery spectrum. Whilst this candidate is not at the centre of the error circle, it is within 20" thereof.

No photometric colours were given in the discovery paper, but the candidate star was noted to have an apparent V magnitude of 16.5. Given the likelihood of variability on an orbital time-scale, as well as longer-term state changes, this must be taken only as an approximate indicator of the star's likely brightness at any given time. (Indeed, later photometry from CTIO shows that Cen 2 has a mid-eclipse m_v of 17.8). The optical position of the source is (J2000.0) 14:29:27 -38:04:10.

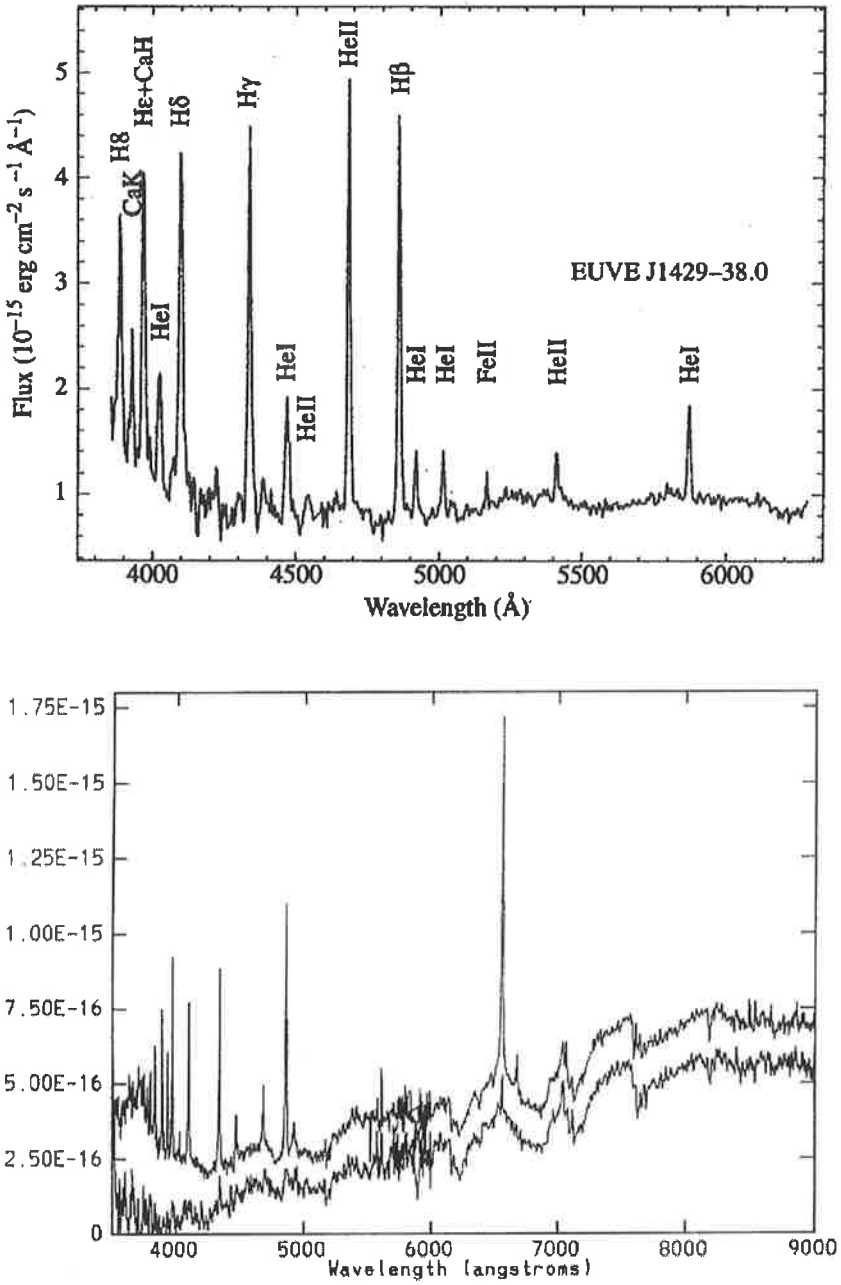

Figure 7.1

Spectra of Cen2.

Top panel: Discovery spectrum from Craig et al. *1996. Note the strong H and HeII lines, suggestive of an accreting system.Cen 2 was in an active state. Bottom panel: spectra from Stobie* et al. *1996. Lower plot is for the CV during eclipse; upper plot is for the CV out of eclipse. Cen 2 was in a low state when these spectra were obtained, as is suggested by the increasing red continuum (disc CV's increase to the blue when active), and also the reduced flux levels of both the emission lines and the continuum, as compared with the high-state spectrum in the upper panel.*

7.3 Woomera, SSO and CTIO photometry

Woomera observations: Cen 2 was first observed at Woomera in February 1996, following publication of IAUC 6201. Integrations were typically 90-120 seconds, taken as time series using the C14 with the ST-6 in Autograb mode. Auto-guiding was supplied by the C5/ST-4, as usual. Durations of the time series vary from maybe 20 minutes (in order simply to confirm what activity state the CV was in) to a few of around 300 minutes (in order to obtain a full orbital cycle of coverage). The data were reduced differentially, with a local field star chosen as comparison, and a number of others as check stars. Errors for each point were derived from a fit to each night's plot of scatter vs. average differential magnitude for the check stars. The stars used are shown in Figure 7.2. The clear filter was used for the majority of the data.

SSO observations: In July 1996, the SSO 0.6-metre was used with the ST-6. Auto-guiding was supplied by an ST-4 placed at the secondary instrument focus. Clear-filtered integrations were typically 75 seconds long, whilst some VRI time series were obtained using 240-second integrations for all filters. Differential reduction was undertaken. The stars used for the white-light data are shown in Figure 7.3. For the VRI data, star 2 was used as the comparison star, with star 1 as the only check star.

CTIO observations: V-band data, of 15-second or 30-second integrations, were obtained in February and August 1998, using the CTIO 0.9-metre telescope (courtesy of Jonathan Kemp, then at the Centre for Backyard Astrophysics, Columbia University). The February data were quasi-simultaneous with some observations at Woomera. Attention was directed primarily at obtaining several time series around the time of eclipse; another gave a full cycle of coverage, and some short series at other phases also were obtained. Data reduction was differential with respect to star 6 of Figure 7.4, but calibration data were obtained which allowed V-band magnitudes for several field stars to be obtained. These are given in Table 7.1, with numbering as per Figure 7.4.

Also, UBV photometry was undertaken by Imants Platais and Vera Kozhurina-Platais using the Yale 0.9-m telescope (Craig, e-mail 3/3/97). Their data are given in Table 7.2, with the same numbering.

It is to be noted that all the optical photometry up to and including those obtained in August 1996 (Woomera and SSO; see Table 3) were included and discussed in Howell *et al.* 1997, for which this writer was a co-investigator. All CTIO data and those from Woomera after that date are presented for the first time in this volume.

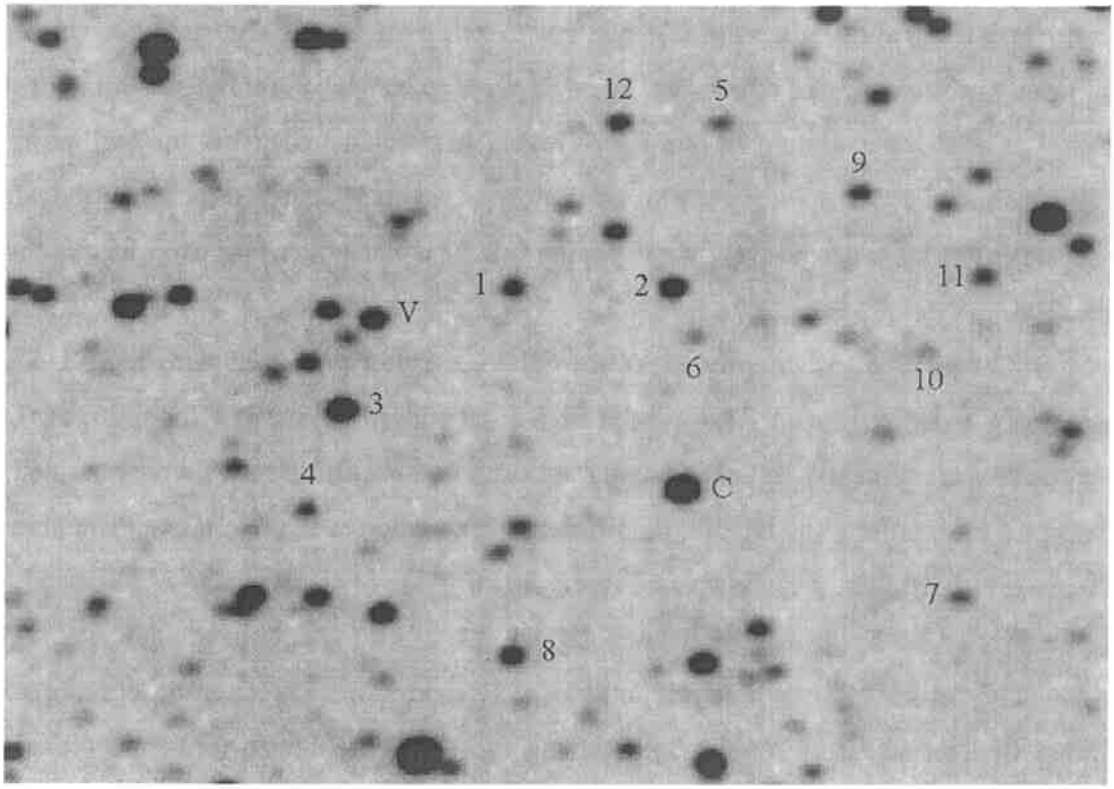

Figure 7.2
Cropped Woomera ST-6 image showing the stars used in the differential reduction.
V = variable; C = comparison star; check stars are numbered.
North is to the top, east to the left.
Approximate field centre and size: (J2000.0) 14:29:22 -38:04:40 6.1' wide 4.8' high.

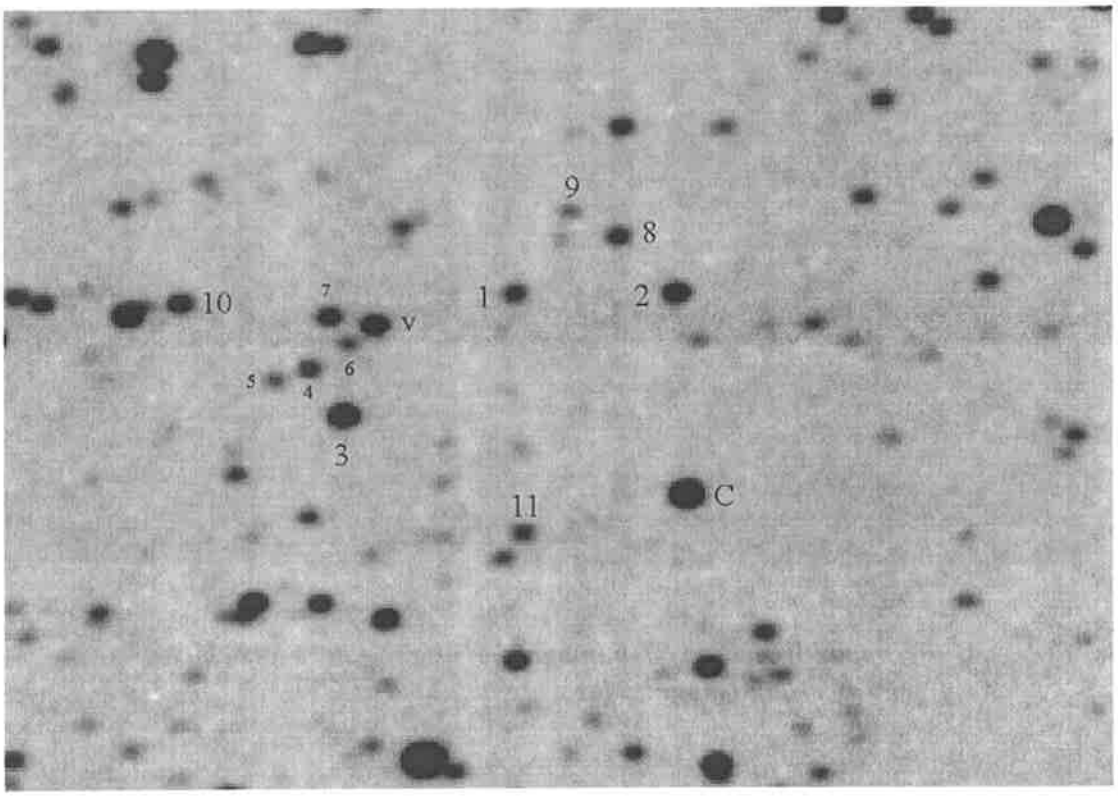

Figure 7.3

Cropped Woomera ST-6 image showing the stars used in the SSO white-light differential reduction.

V = variable; C = comparison star; check stars are numbered.

North is to the top, east to the left.

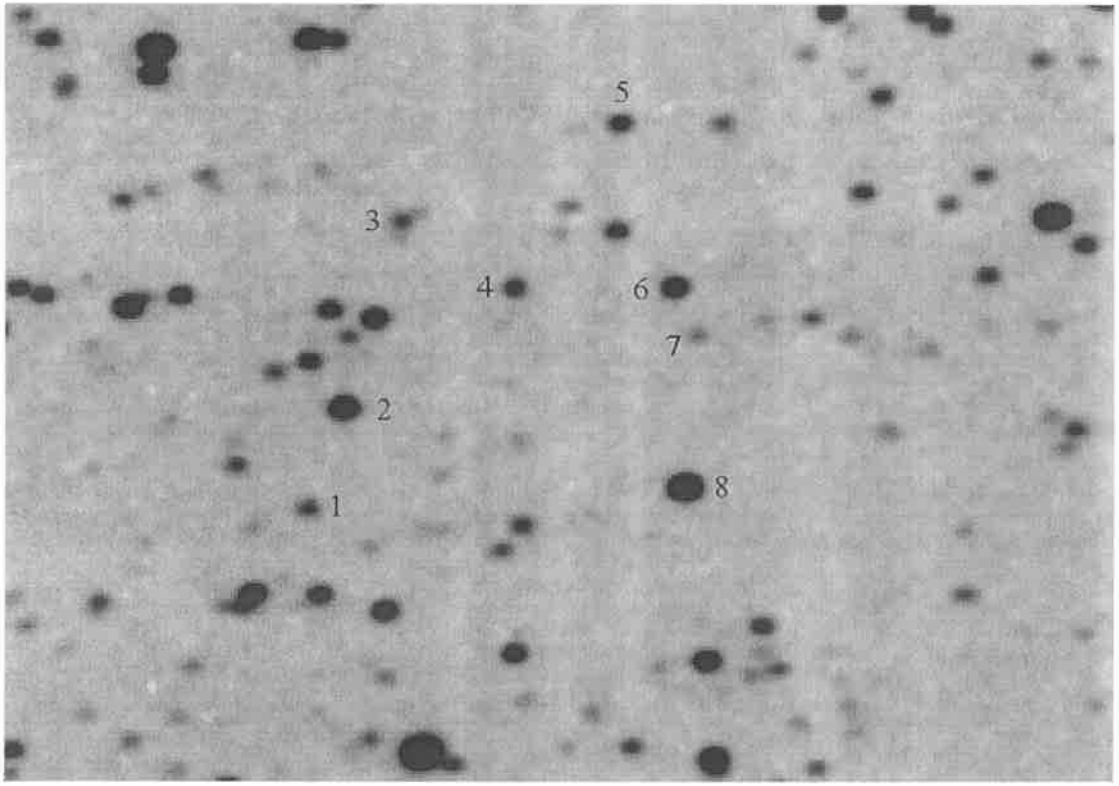

Figure 7.4
Cropped Woomera ST-6 image showing the stars for which V-band magnitudes were obtained at CTIO.

Table 7.1
Magnitudes from CTIO photometry

Star number	V magnitude
1	17.55
2	15.57
3	17.76
4	17.16
5	16.95
6	16.25
7	18.44
8	14.76

Whilst no formal errors were provided for these magnitudes, it is estimated that the error is likely to be of the order of ± 0.05 mags.

Table 7.3

Cen 2 observing log

Date	Duration (mins)	Exposure (s)	HJD start (- 2,450,000)	Filter	Site
210296	190	75	135.1387	clear	Woomera
230296	190	75	137.1350	"	"
140496	310	90	187.9587	"	"
150496	310	90	188.9503	"	"
160496	315	90	189.9526	"	"
170496	270	90	190.9480	"	"
200496	160	90	193.9213	"	"
210496	580	90	194.9341	"	"
170696	180	90	251.9251	"	"
190696	270	90	253.9909	"	"
200696	200	90	254.9220	"	"
180896	220	90	313.9130	"	"
121096	38	90	368.9275	"	"
070197	60	100	456.2066	"	"
150197	130	100	464.1687	"	"
160197	130	90	465.1615	"	"
110297	180	90	491.0764	"	"
120297	280	90	492.0959	"	"
130297	290	120	493.0884	"	"
190797	300	90	648.9052	"	"
210797	240	90	650.9051	"	"
260797	110	90	655.9200	"	"
240298	160	90	869.1654	"	"
250298	90	90	870.1703	"	"
270298	110	90	872.1667	"	"
280298	90	90	873.1515	"	"
020398	140	90	875.1117	"	"
210798	200	120	1015.9344	"	"

Table 7.3 continued

220798	120	120	1016.9237	"	"
250798	76	120	1019.9532	"	"
160998	65	120	1072.9375	"	"
170998	90	120	1073.9134	"	"
090796	180	75	273.9347	"	SSO
110796	310	75	275.8684	"	SSO
160796	310	240	280.8865	V and I	SSO
180796	340	240	282.8654	V and I	SSO
220796	300	240	286.8850	V and R	SSO
240796	320	75	288.8702	clear	SSO
260298	56	15	871.6928	V	CTIO
270298	80	15	872.7604	V	CTIO
280298	70	15	873.7629	V	CTIO
020398	290	30	875.7079	V	CTIO
070898	170	15	1033.4663	V	CTIO
110898	105	15	1036.5550	V	CTIO
120898	64	30	1037.5738	V	CTIO
140898	88	15	1040.4592	V	CTIO

Table 7.2

Yale 0.9-m UBV photometry, 23-24/1/1997

Star	V	B-V	U-B	formal errors		
4	17.26	0.95	0.66	0.016	0.036	0.128
CV	16.88	0.34	-1.22	0.012	0.017	0.019
3 from discovery paper	17.76	0.66	-0.08	0.025	0.045	0.092
2	15.68	0.66	0.01	0.005	0.008	0.016
6	16.33	0.61	-0.05	0.008	0.013	0.026

It may be seen that the V mags agree with the CTIO values to within 0.1 magnitudes. However, it is not known what integration times were used for the data on the CV, and at what CV orbital phases they were taken, so it cannot be claimed that the colours for the CV are simultaneous. Data from the South African Astronomical Observatory (Stobie *et al.* 1996) show B-V = 1.32 in eclipse, and B-V = 0.78 and U-B = -0.86 outside eclipse for Cen 2 in a low state. From the Woomera data, Cen 2 was probably in a mid-intermediate state at the time of the Yale observations. This would account for the bluer colours, due to the presence of more-active accretion regions.

Table 7.3 gives a log of the Woomera, SSO and CTIO optical observations described above. Individual nights' light curves derived from these observations are given in Figure 7.5 (presented at the end of the chapter due to the large number of plots). All data were phased according to the best-fit ephemeris as follows:

phase zero = HJD 2450289.027

period = 17155.57 ± 0.02s.

These values are based on those in Howell *et al.* 1997, but were adjusted slightly as more data became available. The period estimate is consistent with published values, but is more constrained due to the great temporal extent of these data.

The resulting nightly phase plots are shown in Figure 7.6 (also at the end of the chapter).

The ephemeris period was estimated by phasing all the data, and adjusting the period so as to produce the least amount of smearing during the eclipse portion of the orbit. Due to the large temporal extent of the data, the period can be specified quite precisely. The zero of phase is taken as the centre of the low-state ellipsoidal minimum which corresponds closely (though not necessarily exactly) to the centre of the high-state eclipse (Howell *et al.* 1997).

It is to be noted that all differential data are in the sense C-V, so that an increasing differential magnitude means that V is brightening with respect to C. All CTIO magnitude data are calibrated V magnitudes.

7.4 Analysis: orbital period

The first estimate, based on the satellite data alone, was for an orbital period of about 142 minutes. This was not inconsistent with the initial Woomera photometry, which was obtained with the CV in a low state (and therefore showing only a sinusoidal light curve), and with errors sufficient to mask the features noted in the Stobie *et al.* 1996 low-state data. Those features (namely a short but definite eclipse, and unequal maxima and minima) are sufficient to reject the 142-minute period; but they were not seen in the comparatively noisy Woomera data.

A refinement to this "half-period" estimate came when the second month's data were reduced, and a substantial phase shift from the first month's data was noted. Rather than demanding a physical cause within the CV itself, this phase shift was explained in terms of a small error in the assumed period, which was unnoticable for short-duration runs (e.g. a few days), but had considerable effect over the span of a few weeks. Adjusting the period slightly resulted in a tidy phase plot.

With the first observation of the CV in a high state, and with its characteristic deep and wide eclipse, it was found that the eclipse was occurring every *second* orbit- an obviously unsatisfactory situation. It became clear that the hitherto assumed period was, in fact, only half the correct period, and that the modulation seen in the low state data was due to ellipsoidal modulation of the light from the distorted secondary star in the binary. (It is to be noted that, at this time, the Stobie *et al.* 1996 data were unpublished, and there was no reason to expect such a period. In hindsight, it can be said that many magnetic CV's do exhibit ellipsoidal modulation in their optical light curves, and so this should have been considered as a possibility).

As more months of data were obtained, the period could be refined via examination of the phase plot. The process used is to phase all the data using some assumed period, and note that which appears (by visual inspection only) to give the neatest phase plot, especially around mid-eclipse. Nominal limits to the period are estimated by noting the offsets from the best period which give obvious phase shifts around mid-eclipse. This has led to the estimate given in the ephemeris above.

7.5 Interpretation of the orbital period

Having obtained a good orbital period, it is possible to estimate some of the physical parameters of the CV. Generally, it is assumed that the secondary is a Roche lobe-filling main sequence star. We will employ the relations between P_{orb} and various system parameters given in Equations 2.1 to 2.7.

The data on which the M_V-period relation (Equation 2.3) is based were shown in Figure 2.3; it is seen that there is a non-linear trend for $P_{orb}(h) < 2$. Furthermore- and perhaps more importantly- there is a scatter of perhaps up to ± 1 magnitude from the best-fit line represented by Equation 2.3. This must be taken into account when considering the estimation of distance to a CV from the apparent V magnitude (m_V) of the secondary- if this can be isolated (for example, during the total eclipse in a high-inclination system, such as Cen 2).

There is also an observed trend between spectral type of the secondary and P_{orb}, as was shown in Figure 2.4.

So, by simple determination of P_{orb}, one can obtain a certain amount of information on the nature of the secondary star in the CV. In the case of Cen 2, with a P_{orb} of 4.765436(3)h, we obtain:

M_2	R_2	T_2	ρ_2	$M_V(2)$	$M_V(2)$	$\dot{M}$
0.46	0.51	3565	4.71	9.2	10.24	$>5.24\ 10^{-10}$ $<1.47\ 10^{-9}$
M_{sun}	M_{sun}	K	g cm^{-3}			$M_{sun}\ yr^{-1}$

for the relations given in Equations 2.1-2.7, and with a spectral type of about M1-M3 from Figure 2.4 (Howell *et al.* 1997 find M2 $\pm$ 2 from low-state spectra).

The CTIO V-band data (see Figure 7.10) show that there is a flat bottom to the mid-eclipse region, which suggests that the eclipse there is total. That is, we expect that there is no contribution to the system's light at those phases from the white dwarf, accretion stream or accretion disc, and we are seeing light only from the secondary. Therefore, the apparent V magnitude at these phases is that only of the secondary. Combining this with the absolute V magnitude of the secondary derived from the empirical M_V-period relation (Equation 2.3), we can estimate the distance to Cen 2.

In the first instance, we assume no interstellar absorption; that is, $A_V = 0.0$ mags. We will take $m_V = 17.85$ and $M_V = 9.2$; this yields a distance of 537 pc. As mentioned, there is some scatter about the M_V-period relation; we will assume ± 0.5 mags in the region of log $P_{orb} = 0.68$. Also, we will consider up to $A_V = 1.0$ mag in the direction of Cen 2 (Howell *et al.*

1997), as well as the second $M_V(2)$-P relation above. Table 7.4 gives the distances to Cen 2 under these assumptions.

Table 7.4

Distance (in pc) to Cen 2

		M_V				
		8.7	9.2	9.7	10.2	10.7
A_V	0	676	537	427	339	269
	0.5	537	427	339	269	214
	1.0	427	339	269	214	170

Thus, depending on the amount of interstellar absorption assumed, and M_V, 676<d (pc)<170. From spectrophotometry, Stobie *et al.* 1996 find $m_V = 18.1$ in eclipse (during a low state), and Howell *et al.* 1997 find $m_V = 17.4$; the latter assume $M_V = 10$ for an M2V secondary, and $A_V = 1.0$, to yield $250 < d(pc) < 295$. This latter range is based on estimates of the density of the interstellar medium in the vicinity of the direction of Cen 2, and is claimed to be quite tight. Therefore, the larger estimates in Table 7.4 may well be viewed with caution.

As an alternative method of distance determination, one could use the apparent K-band magnitude (see Equation 2.9). Since, in applying this method, one must include (or at least estimate and allow for) the contribution from the accretion disc to the K-band flux, it would be best to obtain the appropriate data for Cen 2 during mid-eclipse, when it is expected that the disc and stream are essentially fully eclipsed- as is the WD. Conversely, during a low state, data could be obtained at any phase, with minimal contribution from the disc and stream. In this case, estimates of flux contamination would have to be made.

In the absence of IR observations of Cen 2, we may estimate the in-eclipse m_K using Equation 2.9a, $S_K = 4.5 \pm 0.5$ (Sproats *et al.* 1996), $R_2/R_{sun} = 0.51$, and $250 < d(pc) < 295$. We obtain $12.5 < m_K < 13.3$.

Some IR data have been obtained (Dr. Patricia Whitelock, SAAO, private e-mail) for this source. JHK magnitudes were obtained, as follows:

HJD-2,425,000	phase	filter	mag.	error
32.354	0.862	K	13.48	0.06
33.395	0.105	K	13.48	0.06
33.401	0.135	H	13.56	0.04
33.407	0.165	J	14.38	0.10

Unfortunately, it is not known what activity state the CV was in at the time of these observations, and none of the data were obtained during the total eclipse phase.

Let us first assume that the CV was active and its behaviour directly comparable with that at the time of the filtered SSO observations (and of the CTIO V-band data). From Figure 7.6 (SSO VRI data), we see that the magnitude changes from phase 0.862 to total eclipse to be approximately $\Delta V = 1.1$mag, $\Delta R = 0.9$mag, $\Delta I = 0.9$mag. From totality to phase 0.105, we have $\Delta V = 1$mag, $\Delta R = 0.8$mag, $\Delta I = 0.8$mag. That is, the magnitude change at disc ingress or egress is decreasing with increasing wavelength (implying a hot disc). We may tentatively estimate a change of $\Delta K = 0.4$mag for the same phase interval. From the Whitelock data, then, we estimate $K = 13.88 \pm 0.06$ during totality. This yields d = 380 pc, with limits of 501 pc and 295 pc, using Equation 2.9 again.

Assuming the low state, and allowing $\Delta K = 0.1$mag due to ellipsoidal modulation and stream contribution, we have $K = 13.58 \pm 0.06$ at totality. This yields d = 331 pc, with limits of 436 pc and 257 pc.

We appear to be no better off in refining a distance estimate than we were before. However, the *a priori* estimation of m_K during totality derived above, and assuming $250 < d(pc) < 295$, is *brighter* than the observed m_K at phases -0.14 or 0.1, when there may be some contribution from the disc or stream. This in itself may be enough to suggest that the distance to the CV is greater than 295 pc.

7.6 The light curve- activity (or state) changes

Most (if not all) CV's undergo some gross changes in activity apart from that observed on the orbital (or finer) time scale. Some of these are sudden, as in the novae; or somewhat slower, as in the change from low-to-high or high-to-low activity shown by polars. Whatever the case, one must be aware that behaviour can change over long (days to months) times. It is found that variation can occur in both the overall brightness of the system and in the shape of the light-curve.

Figure 7.7 shows all Woomera data phased; Figure 7.8 shows the same data plotted against HJD. As may be seen from these plots and Figure 7.5, there is considerable variety in

the shape of the light curve shown by Cen 2. There is, perhaps, something of a continuum of states in which this CV may be found, and this is evinced by the progression in form of the light curve. We can specify three main forms:

(i) low state: light curve is (within errors of the Woomera photometry) sinusoidal, of amplitude 0.4 magnitude and dominated by ellipsoidal modulation from the secondary star;

(ii) high state: light curve dominated by an eclipse of approximately 1.2 magnitude in depth and phase width of 0.2, with ellipsoidal modulation still visible outside eclipse. System is about 1 magnitude brighter at phase 0.5;

(iii) intermediate state: shows both strong ellipsoidal modulation and eclipses of varying depth. There may be a continuum of these intermediate states between the limiting low and high states, but the monitoring of this CV is not sufficiently complete to support or deny this- the apparent prevalence of lower activity states may be due to denser data runs in some months, rather than true behavioural biases.

The changing form of the light curve is, of course, a result of changing physical conditions with the CV. From the presence of typical CV emission lines in the discovery spectrum, it is known that there is accretion- and therefore mass transfer- taking place. The variable light curve can be explained in terms of changing mass transfer and accretion behaviour, as follows.

In the low (i.e. inactive) state, there is minimal mass transfer. Some is present, since there is evidence for an accretion *stream* eclipse in the Stobie *et al.* 1996 data. However, its effect is minor, and the dominant influence on the light curve is the tidally-distorted shape of the secondary star. This leads to ellipsoidal modulation of the brightness, where the secondary presents maximal surface area (and therefore brightness) at phases 0.25 and 0.75, and minimal area and brightness at phases 0 and 0.5. This will be especially evident in the unfiltered Woomera data, since the overall system response is somewhat red, and thus the secondary star should be fairly prominent in those data. The light curve is the typical sinusoid exhibited by this phenomenon. There is very little, if any, accretion disc present.

In the high (active) state, the mass transfer rate is increased, and an accretion disc has built up around the primary. The dip in the light curve is due to the eclipse of this accretion disc by the secondary (with this placing limits on the inclination of the system; $i > 72°$). The eclipse is

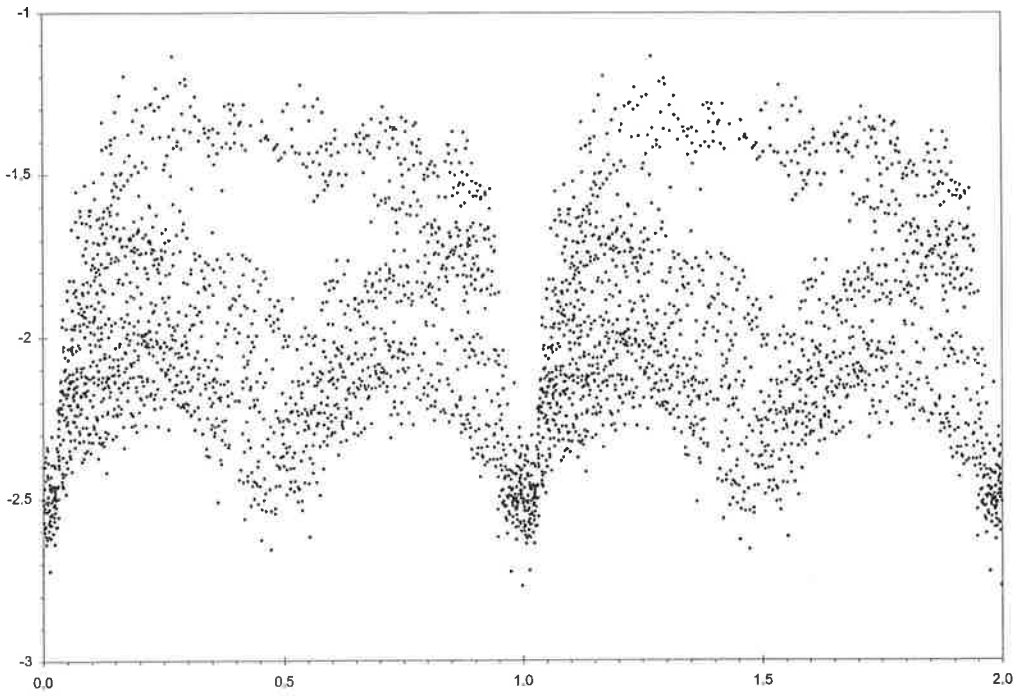

Figure 7.7

Woomera white-light photometry.
Ordinate is differential magnitude, abscissa is orbital phase.

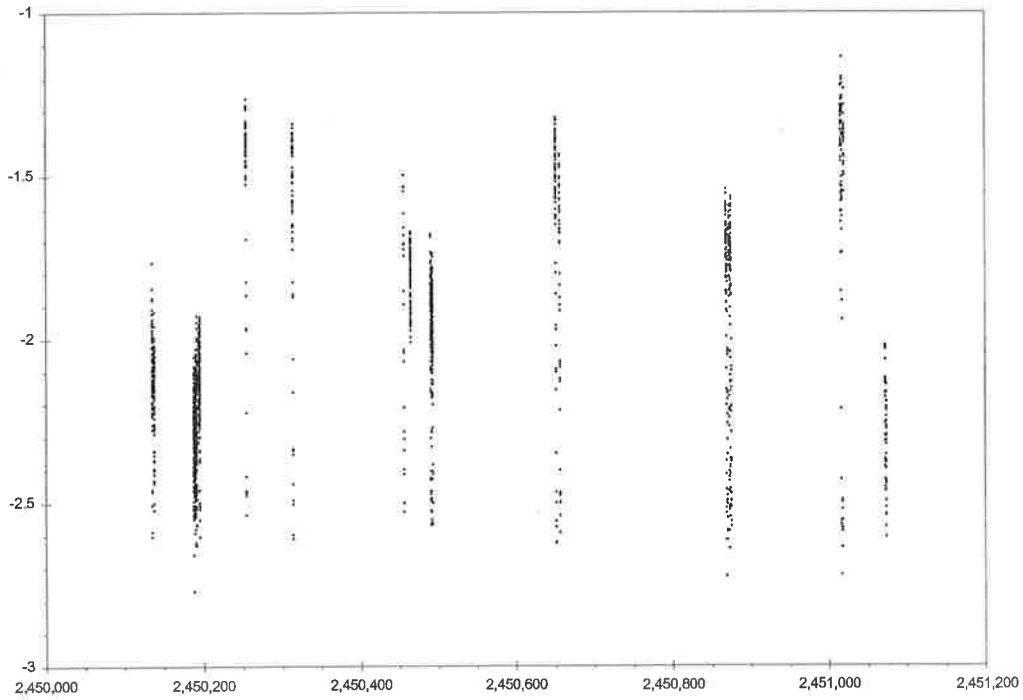

Figure 7.8

Woomera white-light photometry.
Ordinate is differential magnitude, abscissa is heliocentric Julian day (HJD).
Note: only data covering at least the eclipse portion of the orbit are included.

not sharp, with ingress and egress having considerable extent, so that the eclipsed region is somewhat extended, e.g. a disc. As much visible radiation is coming from the disc, the eclipse

is quite deep. The CTIO data show that mid-eclipse is total, so at such phases the light curve drops down to its low-state level. The presence of the optically-bright disc means that the CV is, outside eclipse, much brighter in this active state than in the low state.

In intermediate states, the accretion disc is present, but has lower luminosity as a result of reduced mass transfer rate. This leads to a lower out-of-eclipse brightness for the CV, yet with a definite eclipse. It may be possible that the diameter of the disc varies somewhat with the change in mass transfer rate, and one would expect changes to the eclipse profile in such cases.

With sufficiently dense and even observational coverage, the question of the time scale for state changes, and for staying in a given state, may be examined.

It is clear from a plot of brightness versus HJD for Cen 2 that changes are not infrequent and may occur in comparatively short times. Indeed, major changes can occur within two months (e.g. April-June 1996 or HJD 2,450,190 to 2,450,250 for the first observed low-high transition; July-September 1998 or HJD 2,451,016 to 2,451,073 for a high-low transition). Smaller transitions can occur within a week- for example, over 7^{th}-15^{th} January 1997 or HJD 2,450,456 to 2,450,464. Also, the April 1996 data shown evidence of an increase in activity from the low state to a low-intermediate state; by June 1996 Cen 2 was in a high state, so the April 1996 data may show the very beginnings of a low-high transition. In Figure 7.9 are shown the light curves for five nights of photometry in this month; it is obvious that there is significant change in the system, especially from 170496 to 200496. There is a noticeable change from 160496 to 170496, present mainly around $\phi = 0.25$. Unfortunately, for these cases there were no observations made during the transitional periods, so it is not known just how the change takes place; for example, a slow and gradual change over some weeks, or a much more rapid (days or shorter) variation.

The CTIO data (all taken with Cen 2 in high states) show that there can be fine-scale differences in the light curve from night-night.

Alas, the Woomera and CTIO data are not sufficiently exhaustive for the time scale of the state changes to be determined; thus far, it can only be said that major high-low or low-high transitions have been observed to take place within intervals of about 60 days. The actual time needed may be much shorter, as suggested by the noticeable change within a week in January 1997, or within a few days (April 1996). Similarly, the questions of possible periodicity of state changing, and preference for one state over the other, cannot be answered with these data.

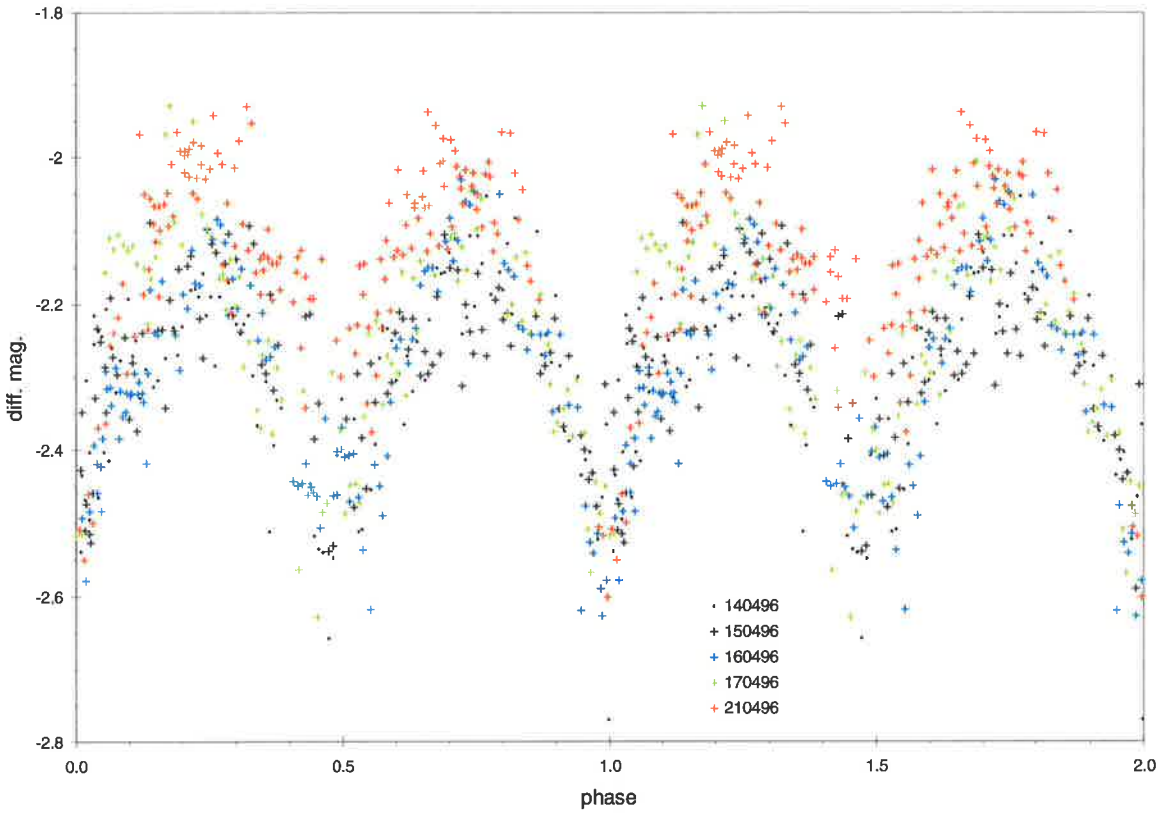

Figure 7.9

Woomera photometry from April 1996, showing changes in the light-curve over a few days. Note: error bars not included for the sake of clarity.

7.7 Eclipse profile

In an eclipsing system such as Cen 2, the limb of the secondary will hide in turn the various accretion regions and the primary star; these components will reappear in reverse order after mid-eclipse. Thus, the profile of the light curve during the eclipse phase is a source of information on the size and relative brightnesses of the various eclipsed components.

Examination of the light curve of eclipsing CV's (e.g. Barwig *et al.* 1994, Glenn *et al.* 1994, Howell *et al.* 1988, Schwope *et al.* 1993, Silber *et al.* 1994)) shows that there are a number of points at which the slope of the profile changes quite significantly and quickly. These turning points mark the times of immersion (or emersion) of system components near the primary star. Generally, the presence of one or more of the following may be discerned: accretion stream; accretion disc; hot spot at point of intersection of accretion stream and disc; primary star; accretion zone(s) on primary star. Which of these is observed depends on several factors, including

- type of CV , i.e. magnetic (polar or intermediate polar) or non-magnetic
- activity state of CV (for magnetic systems)
- inclination of the system (e.g. for a disc CV, i may be high enough for eclipse to be total, and therefore all components will be eclipsed; or, i may be such that only some of the disc is eclipsed, and the primary may be visible at all phases)
- temporal resolution and accuracy of photometry.

The phase or temporal width of a discrete portion of the profile is an indication of the physical width of the corresponding eclipsed component, whilst the magnitude or flux change exhibited at that stage measures how bright that component is. Thus, if calibrated fluxes are obtainable, we may determine the flux contributions from the various components, and if the separation of the primary and secondary stars is found, we can determine the physical widths of these components also.

For Cen 2, the greater accuracy and higher temporal resolution of the CTIO data allow the eclipse profile to be studied. It is to be noted, however, that the time resolution is not particularly high, and is in the range 30-45 seconds. To examine fully the nature of the eclipsed sources requires much higher resolution, of the order of a few seconds. The CTIO data allow us then to see the gross features of the profile, but do not allow us to examine fine features such as eclipse of the white dwarf.

Figure 7.10 shows the eclipse profile from four nights of CTIO photometry. Magnitudes have been converted to monochromatic flux via the relation given in Bessell 1979. The positions of a number of clear turning points are marked. Whilst the overall flux levels for different nights are rather variable, it is to be noted that the phase positions of these

turning points are quite stable- as is the observed brightness during total eclipse. Calling these points c1-c6 in turn (contact points), it is proposed that they define the following eclipse sections:

contact points	**eclipse section**	**possible explanation**
c1 to c2	Ingress 1	eclipse of accretion stream
c2 to c3	Ingress 2	eclipse of accretion disc (in high state)
c3 to c4	Total eclipse	eclipse of all accretion sources and primary
c4 to c5	Egress 1	egress of accretion stream
c5 to c6	Egress 2	egress of accretion disc (in high state)

and these have the following phase and temporal widths:

Table 7.5

Widths of eclipse sections in the CTIO data

	phases	**phase width**	**width** (seconds)
I(ngress)1	$0.939 < \phi < 0.945$	0.006	103
I2	$0.945 < \phi < 0.97\sim0.98$	0.025~0.035	429~600
T	$0.97\sim0.98 < \phi < 1.03$	0.06~0.05	1029~858
E(gress)1	$1.03 < \phi < 1.035\sim1.038$	0.005~0.008	86~137
E2	$1.035\sim1.038 < \phi < 1.06$	0.025~0.022	429~377

The identification of the eclipsed components was obtained as follows. I1 and E1 may be identified with the start and end of the low-state eclipse in Stobie *et al.* 1996; the total phase width (mid-I1 to mid-I2) is the same within errors, and the mid-point between these sections in

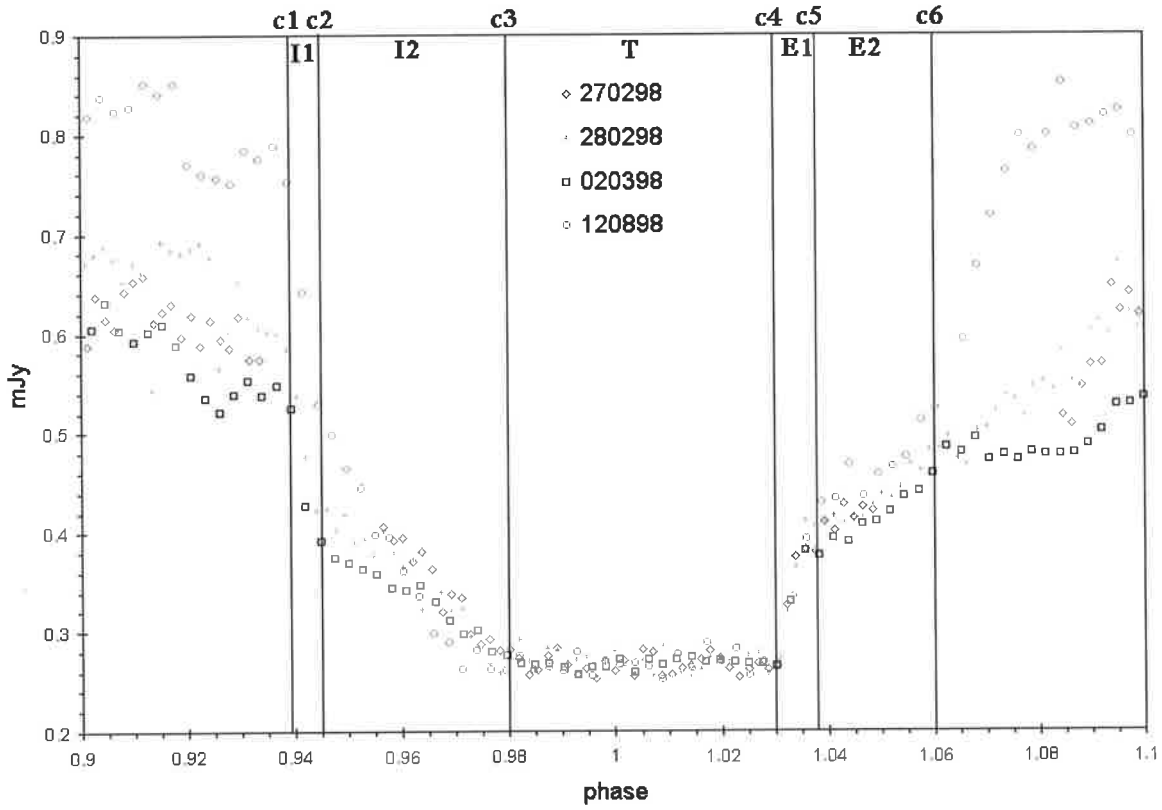

Figure 7.10

CTIO V-band data, phases 0.9 to 1.1 only. Ordinate is flux, abscissa is orbital phase. Vertical lines mark proposed phases of occlusion and reappearance of various system components (see text). These "contact points" are labelled above the lines. The sections of the eclipse profile defined by them (I1, I2, etc.) are labelled between the lines.

the CTIO data precedes phase zero by about 0.02 in phase (compared with 0.03 in Stobie *et al.* 1996, but as that paper does not give an orbital phase zero, the slight discrepancy (only about 170 seconds) cannot explicitly be accounted for, although it may well be due to different phase zeroes).

Secondly, the mid-points of I2 and E2 are symmetric about phase zero, and as this phase zero is that of secondary inferior conjunction (i.e. also an ellipsoidal minimum), the extended source responsible for these sections is symmetrically disposed about the primary. That is, it is most likely an accretion disc.

The *form* of the eclipse profile is very similar to that of eclipsing AM Her systems such as V2301 Oph (Barwig et al. 1994) and RE 2107-05 *a.k.a.* HU Aqr (Glenn et al. 1994), but the strong ellipsoidal modulation in Cen 2 allows us to fix an orbital phase zero, as defined by an ellipsoidal minimum, with the presence of both low-state and high-state eclipses easily defining which corresponds to secondary inferior conjunction. With this *orbital* phase zero, I1 and E1 are not symmetric about phase zero and their combined mid-point must precede it; thus, the corresponding source precedes the WD. In the afore-mention polars, the steep eclipse sections (identified with the eclipse of accretion zones on the surface of the primary) are symmetric about phase zero. In those systems, the shallower eclipse sections are identified with the eclipse and egress of the accretion stream (which lags the accretion spot in phase) , and these are *not* symmetrically placed about phase zero; in Cen 2, the shallow profile sections *are* symmetric about phase zero.

An accretion stream preceding an accretion disc coherently explains the profile seen for Cen 2, in spite of the similarity of form with those of the mentioned AM Her systems- it is the phasing of the profile, based on an orbital phase zero defined by the ellipsoidal modulation, which does not allow an AM Her explanation (apart from any other considerations which also point away from such a classification).

A look at the flux changes during the eclipses is of interest. These are given in Table 7.6.

Table 7.6

Flux variations (mJy) during eclipse

Nigh t	flux at phase 0.9	change in I1	change in I2	flux for T	change in E1	change in E2	flux at phase 1.1
875	0.59	0.13	0.13	0.27	0.11	0.09	0.53
872	0.62	na	na	0.27	0.11	na	0.61
873	0.67	0.18	0.15	0.27	0.14	0.08	0.6
1037	0.82	0.26	0.25	0.27	0.13	0.14	0.8

We may also consider the ratio of fluxes as follows:

Table 7.7

Flux ratios during eclipse

night	flux at $\phi = 0.9$/ flux at c1	c1/c2	c2/c3	c5/c4	c6/c5	0.1/c5
875	1.11	1.33	1.48	1.41	1.24	1.13
872	na*	na	na	1.41	na	na
873	1.17	1.43	1.56	1.52	1.20	1.22
1037	1.04	1.49	1.96	1.48	1.35	1.48

* ("na" indicates that this ratio cannot be determined due to lack of data).

A number of points are evident:

(1) As the activity state increases, the flux drop or increase associated with each section will, in general, be greater. A higher activity state results from increased accretion, and this may be expected to increase the flux from the accretion regions.

(2) The eclipse is not symmetrical in the sense that the flux change at ingress does not equal that at egress for the same section. Thus, it may be that the accretion stream is self-shadowing to some extent, and may even obscure some of the disc during egress. The stream itself may not be isotropic- the inner side may be hotter (brighter) than the outer. It could be that a bulge in the disc (presumably at the stream/disc intersection) shadows some of the disc during egress.

(3) The flux change for E1 is much more constant than that for other sections. That is, the flux increase at stream egress is much less dependent on activity state than are flux changes for

other sections. The major changes for the stream therefore must occur on the inner face of the stream, i.e. that which faces the disc. This face is seen at stream ingress, and there is significant state-dependent flux variation seen then. This asymmetry may be a result of heating of the stream's inner face from radiation from the disc or the disc/stream intersection.

(4) The stream and disc appear to contribute approximately the same flux before ingress, as the flux changes during I1 and I2 are nearly equal for the three nights of complete data.

7.8 System parameters and physical dimensions of components

By assuming $q = 1$, $M_1 = 0.6$, and using P_{orb} and Equation 2.16, Stobie *et al.* 1996 derive an initial estimate of the separation of the primary and secondary of $a = 1.06\ 10^{11}$ cm. This was further refined by use of Equations 2.1, 2.2 and 2.14 to yield final estimates of $q = 0.56$ and $a = 1.08\ 10^{11}$ cm. Furthermore, they estimate $i = 81°$.

Using these figures, and Equations 2.13-2.15, we can determine the basic system parameters as follows:

q	a cm	M_2 M_{sun}	M_1 M_{sun}	R_2 cm	R_{L1} cm	$R_{L(2)}$ cm	$R_{L(eq)}$ cm
0.56	$1.08\ 10^{11}$	0.46	0.82	$3.55\ 10^{10}$	$6.02\ 10^{10}$	$3.6\ 10^{10}$	$4.61\ 10^{10}$

It is to be expected that $R_{L1} + R_{L(eq)} = a$; this is so within 2%, and scatter in Equation 2.1 may well account for the very small discrepancy. Also, Equation 2.14 is accurate only to 2%.

P_{orb} and a can be used to determine the relative velocity of the WD and secondary in their orbits; we derive $v_{rel} = 3.96\ 10^7$ cm/s. With this and the temporal widths of the various eclipse profile sections given in the previous section, we can obtain the physical sizes of the corresponding system components. We then have:

disc diameter = $2.04\ 10^{10}$ cm for an assumed phase width of 0.03

stream width = $4.76\ 10^9$ cm for an assumed phase width of 0.007

Figures 7.11a-c are scale diagrams of the system based upon these parameters. In the plan view (i.e. from above the orbital plane) of Figure 7.11a, the line-of-sight to the observer is to the left, and the positions of system components for a few choice phases have been included.

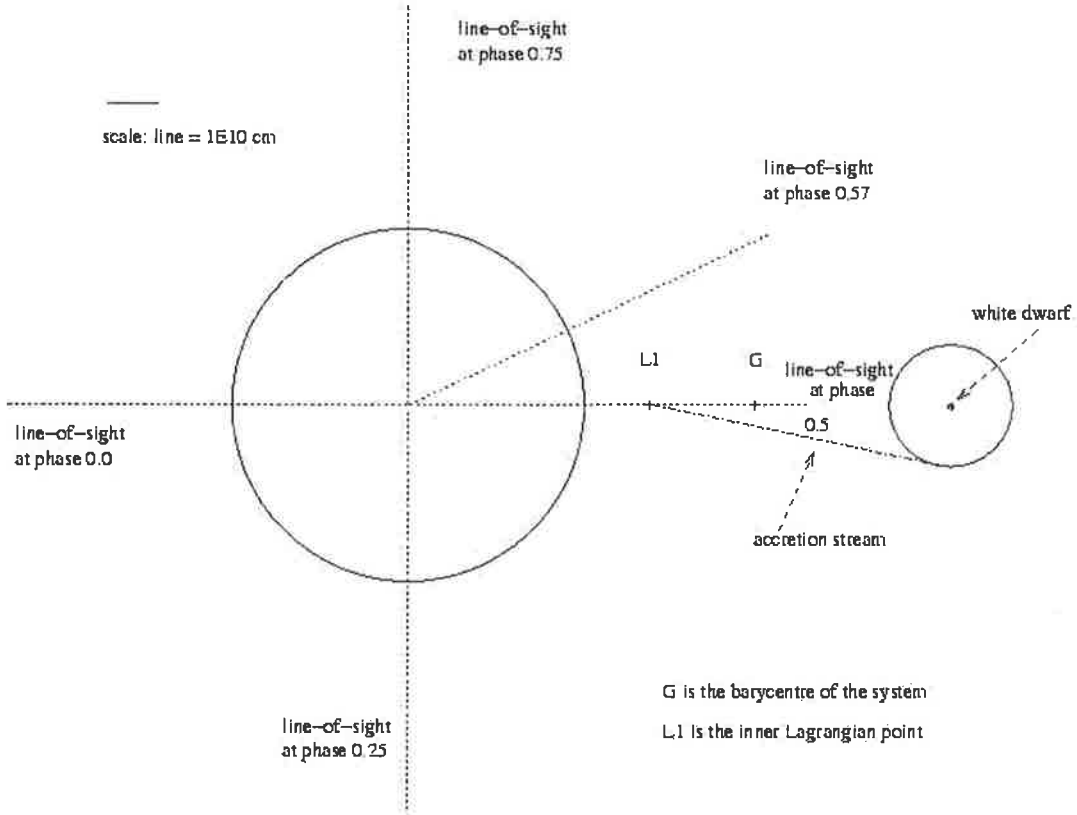

Figure 7.11a

Cen 2 system diagram (to scale), plan view, based on CTIO V-band photometry. The line-of-sight is shown for various phases. Note that in these figures, the secondary is shown as a sphere of radius R_2, and not as a tidally- or rotationally-distorted ellipsoid. The accretion stream is shown very simply as a straight tline from the inner Lagrangian point to the edge of the accretion disc (small circle to the right of the figure).
Please note also that the white dwarf primary is not shown to scale- it is too small to be seen.

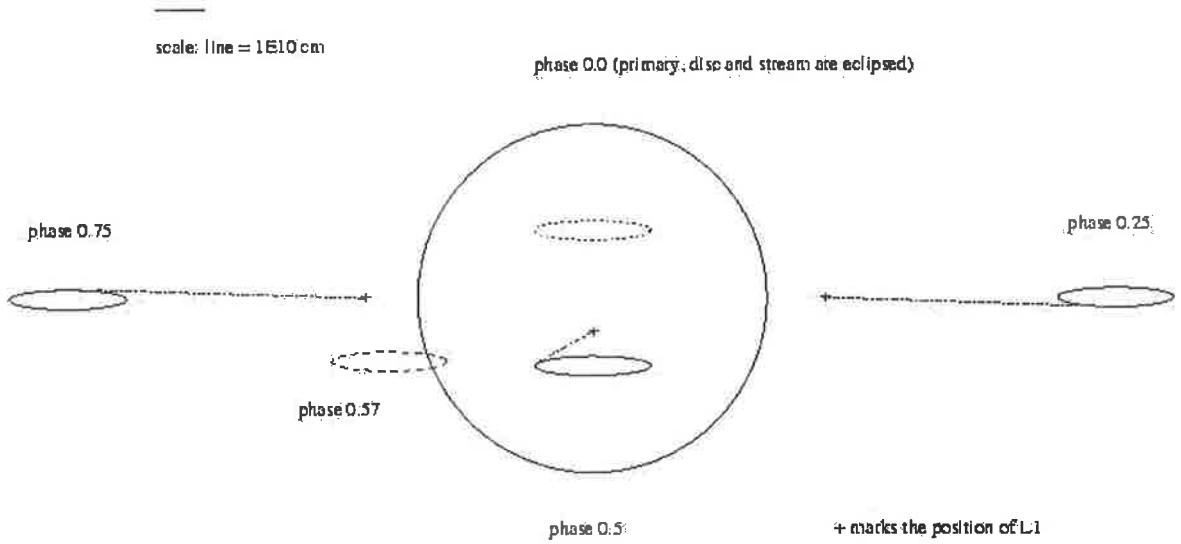

Figure 7.11b

Cen 2 system diagram (to scale), based on CTIO photometry. This is the view along the line-of-sight. The position of the accretion disc for various phases is shown.

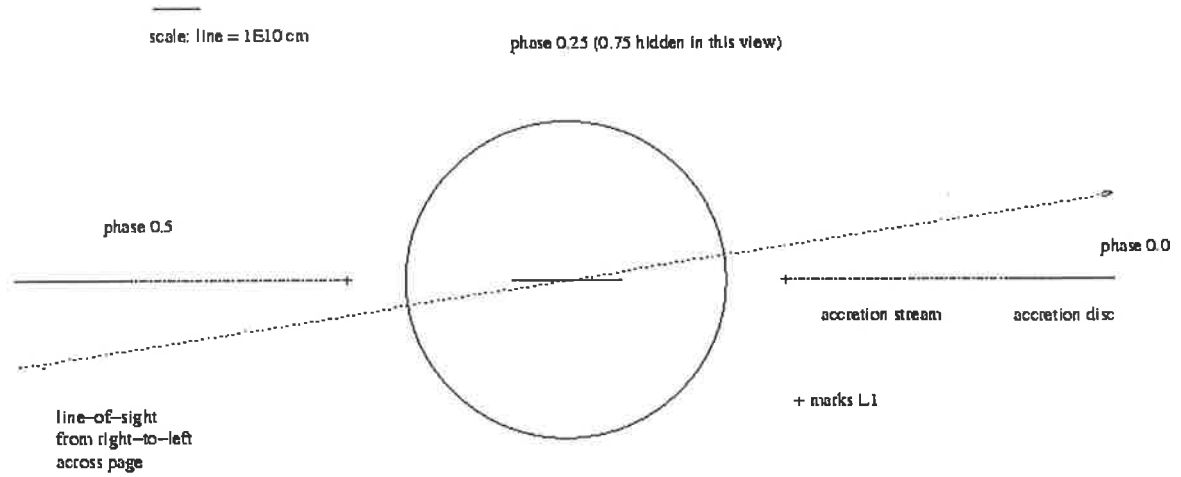

Figure 7.11c

Cen 2 system diagram (to scale), based on CTIO photometry. This view is from one side of the system; Line-of-sight is from left to right. System inclination, i, is estimated at 81°. The position of the accretion disc at phases 0.0, 0.5and 0.25 is shown.

In Figure 7.11b, the observer views the system into the page. Figure 7.11c shows the system viewed side-on.

These disc (and possibly also stream) dimensions are, strictly speaking, valid only for the V-filtered data. The disc has a radial temperature distribution; the disc temperature decreases outwards from the primary (*e.g.* WCVS Figures 2.32 and 2.33). The apparaent diameter of the disc, as determined from its eclipse width, may vary somewhat with the wavelength observed.

With regard to i, for a disc system to be fully-eclipsed, the following condition must be satisfied:

$$\cos i \leq \frac{R_2}{a + R_d} \qquad (7.1)$$

where R_d is the radius of the disc. Equating R_2 with $R_{L(2)}$, one obtains for Cen 2, $i > 73.7°$.

7.9 The light curve outside eclipse

In all activity states, the light curve of Cen 2 exhibits pronounced ellipsoidal modulation. In the simplest (admittedly hypothetical) case of an isolated star suffering tidal distortion, this modulation may be modelled by a simple cosine curve. We shall apply this simplification to the highest-quality data here.

The CTIO data for JD 2,450,875 cover a full orbit, and are shown again in Figure 7.12. The ellipsoidal modulation has been fitted as a cosine curve of half the orbital period, also shown. Subtracting this model fit from the data results in the curve shown in Figure 7.13. Outside eclipse, there appears to be a remnant wave at the orbital period. This wave will be referred to as the "orbital component", since it occurs at the orbital period. This is not to suggest that it remains fixed in phase- it is just a reference to the period at which it occurs. This wave can be modelled by another cosine wave at the orbital period, as shown. Subtracting this from the (data-ellipsoidal) curve results in the essentially flat-topped "light curve" shown. It is therefore surmised that the out-of-eclipse modulation can be well modelled by the sum of these two cosine curves. In Figure 7.14, this resultant is shown, and it is clear that it does indeed fit the observed modulation.

Whilst the ellipsoidal modulation has, by definition, a phase zero at the orbital phase zero as given in the optical ephemeris, the orbital wave must have a phase offset in order best to fit the data. For the night given, this offset is 0.07.

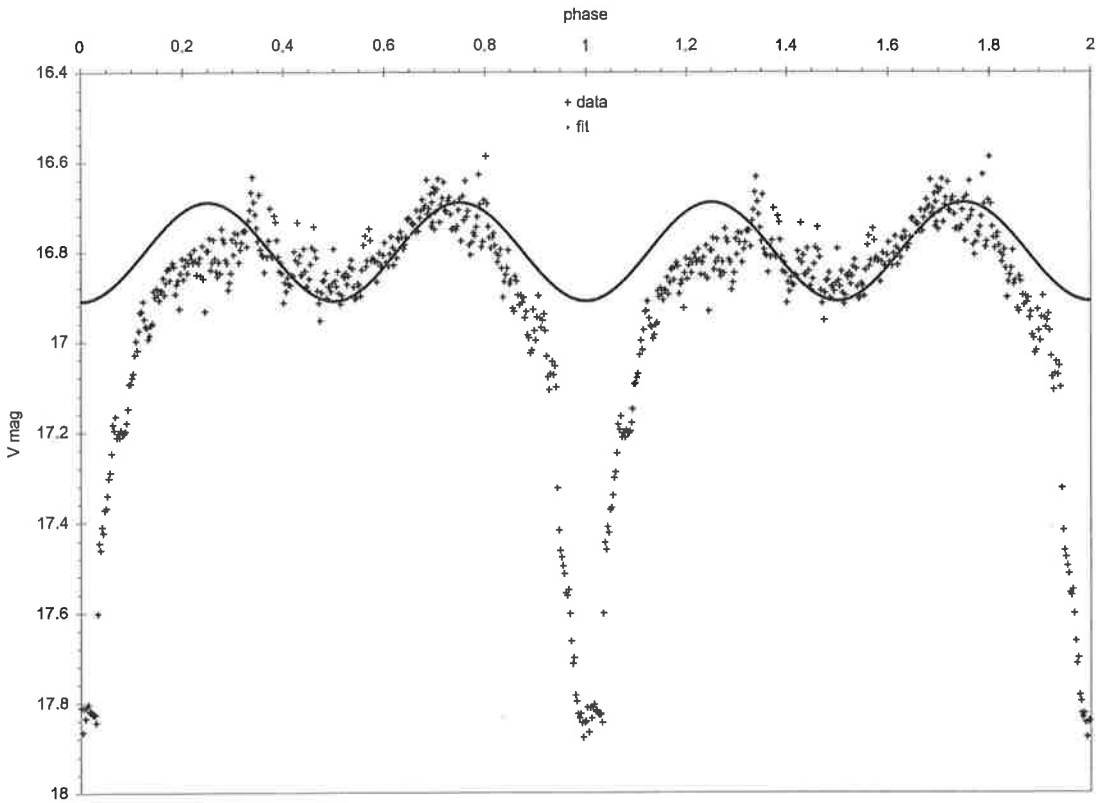

Figure 7.12

CTIO V-band data for JD 2,450,875; model fit to the ellipsoidal modulation is shown.

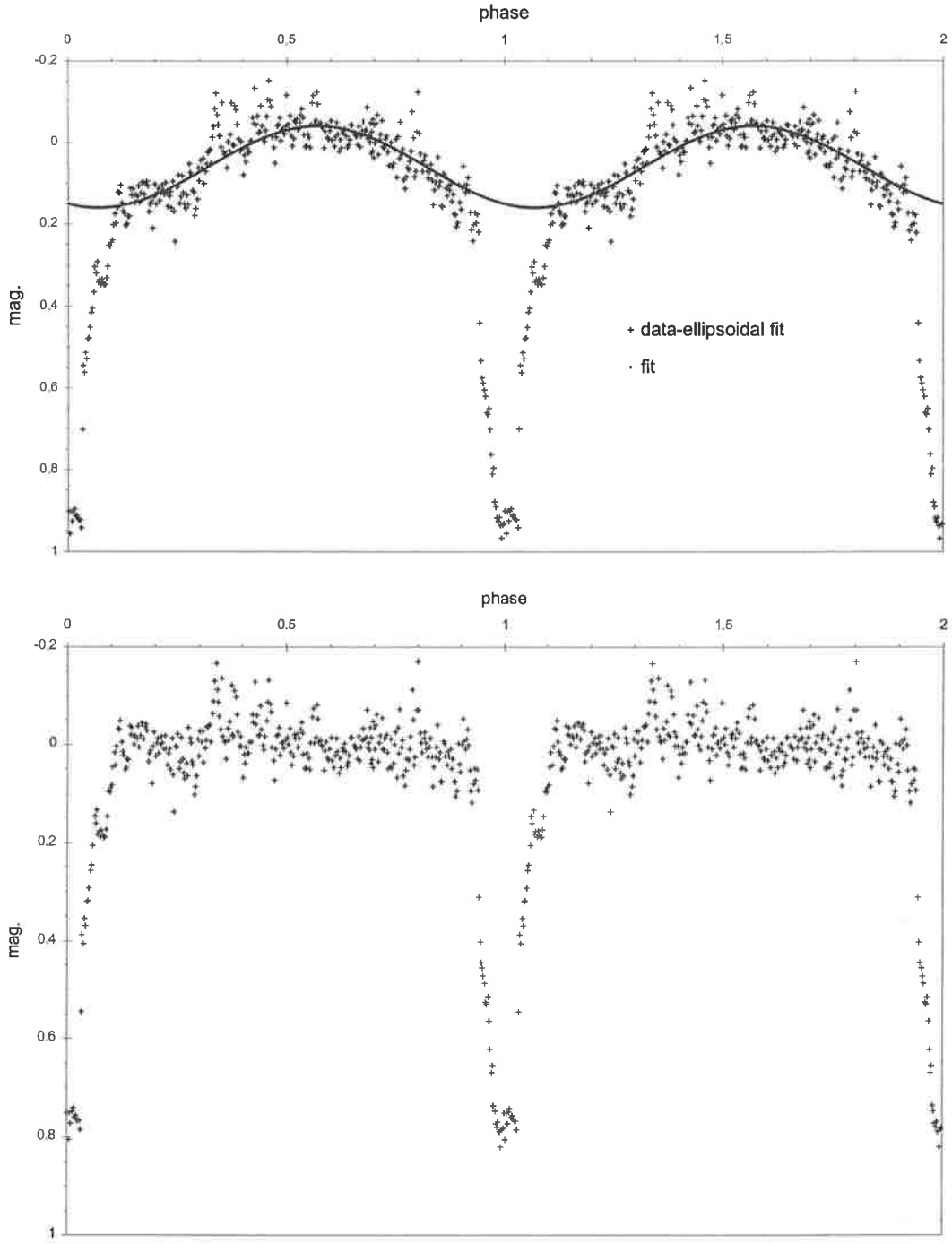

Figure 7.13

Upper panel: the remnant "orbital" modulation as a result of subtracting the model ellipsoidal modulation from the data; and the fit to this remnant.
Lower panel: result of subtracting both the ellipsoidal and orbital fits from the data. The out-of-eclipse light-curve is essentially free of long-term modulation.

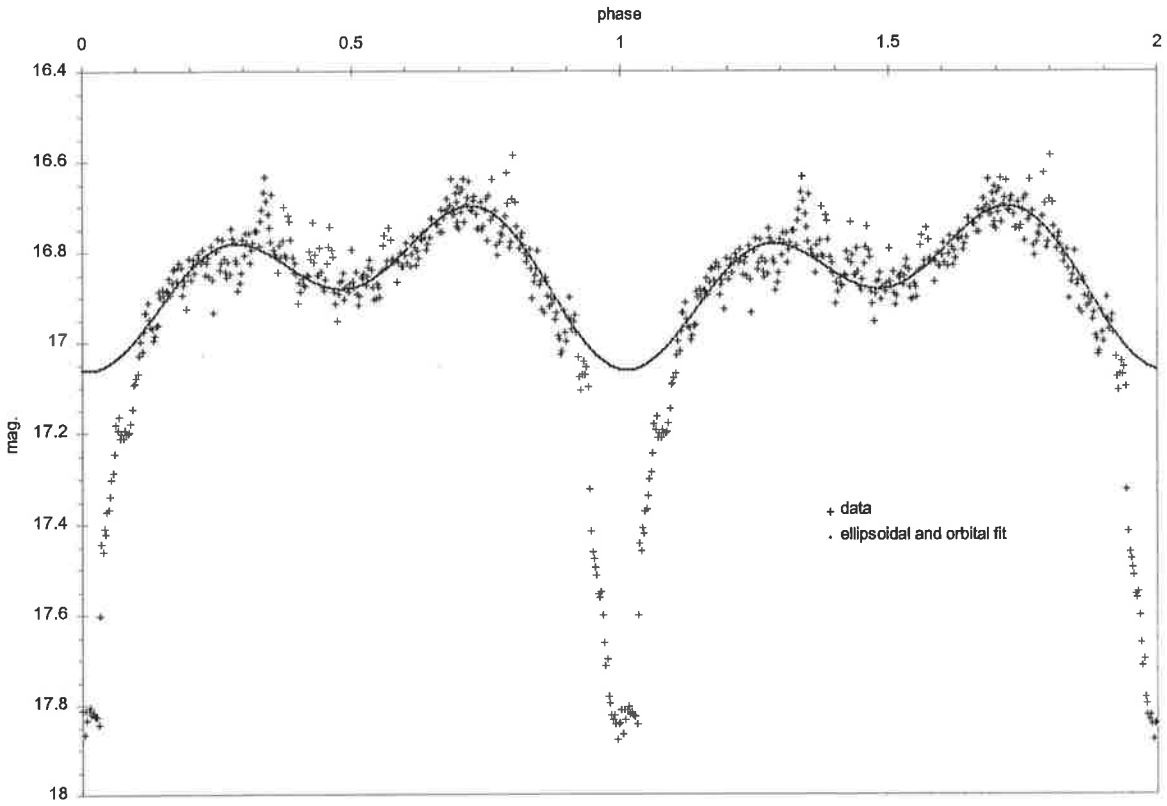

Figure 7.14

Observed light-curve, and the sum of the ellipsoidal and orbital fits.

There are some nights' data in the Woomera observations (and one night for the SSO data) for which a similar process may be undertaken. The data and the best-fit ellipsoidal-plus-orbital sum are shown in Figure 7.15. For all such nights, the required phase zero and amplitudes of the ellipsoidal and orbital fits are given in Table 7.8.

Table 7.8

Phase offsets and amplitudes for orbital component

Date	**JD**	**orb. ϕ offset**	**orb. amp. (mag.)**	**ell. amp. (mag.)**
note: CTIO	2,450,875	0.07	0.2 (V filter)	0.22 (V filter)
190696	2,450,254	-0.1	0.25	0.22
240796	2,450,289	-0.03	0.12	0.19
120297	2,450,492	-0.07	0.12	0.26
130297	2,450,493	0.07	0.17	0.25

Examination of these light curves shows that, on occasion at least, the two local maxima per cycle are of different brightness, and also that they do not occur exactly at the expected phases of 0.25 and 0.75. This is why the orbital component requires a small phase shift. Furthermore, it is clear that *which* of these minima is brighter, changes; thus, the phase shift of the orbital component swings between positive and negative values. This swing can occur from day to day (see the data for 120297 and 130297), but since Cen 2 has never been followed for a full two cycles in its high state, it is not known whether or not this so-called "orbital component" undergoes significant cycle-to-cycle phase shifts.

What is the source of this orbital component? It is seen to have a maximum in the phase range $0.4 < \phi < 0.57$ and appears to be smoothly-varying over the entire (out-of-eclipse) orbit. The hot-spot contribution (if there be such) is usually expected to be at maximum at around $\phi = 0.8$, and usually is more of a "hump" around that phase then a smooth cosine curve over all (or at least most) of the orbit. Thus, the cause is unlikely to be a hot spot.

If the cause is the heated face of the secondary which faces the primary, one would expect narrow emission lines in the high-state spectrum between phases 0.25-0.75 (i.e. when this face of the secondary is towards the observer). However, it is not known if there has been any high-resolution, phase-resolved high-state spectroscopy undertaken, so this possibility can

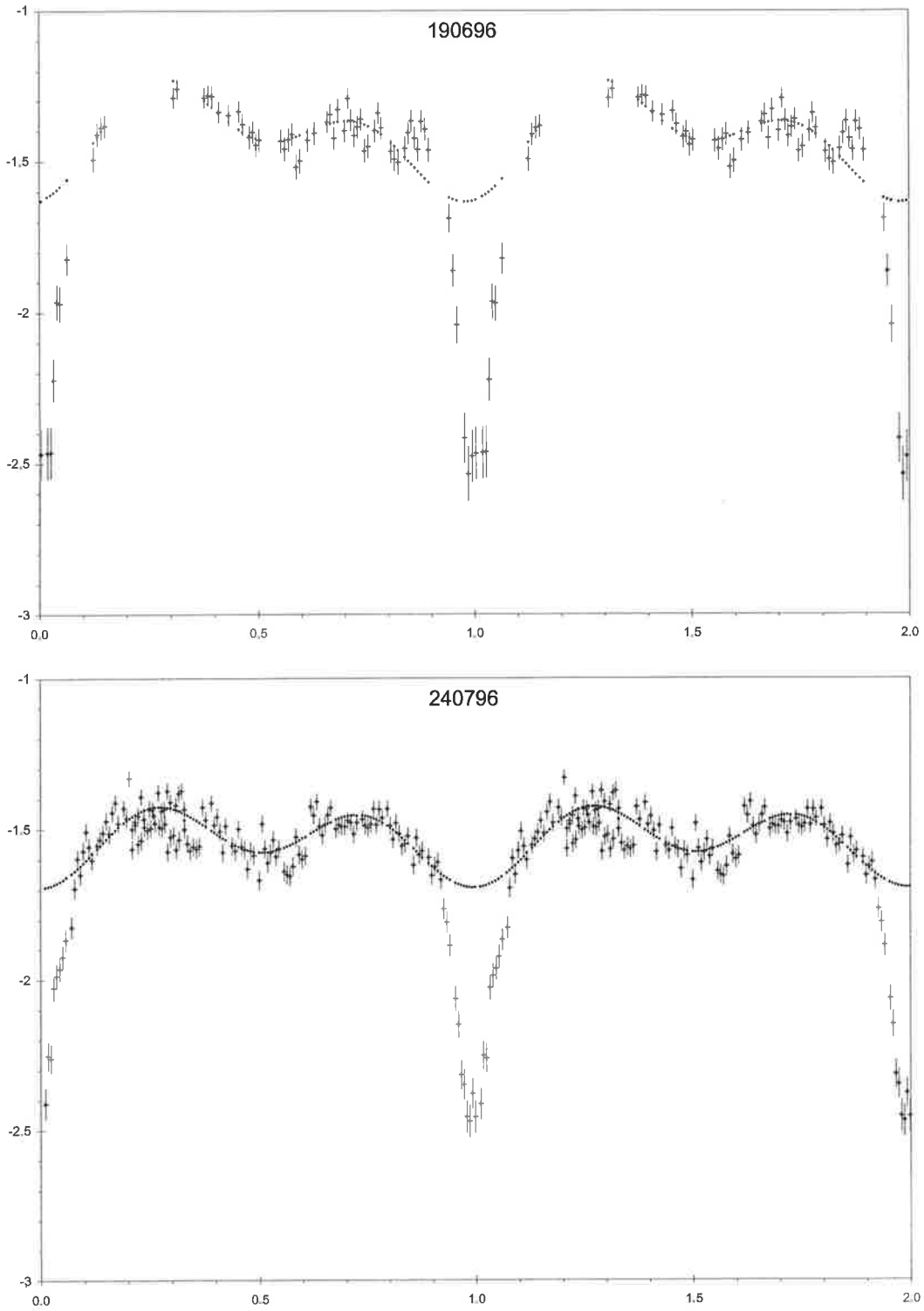

Figure 7.15

Combined ellipsoidal and orbital fits to Woomera and SSO white-light photometry. Ordinate is differential magnitude; abscissa is orbital phase.
Note: for 240796, there is some overlap of data around phases 0.2-0.4 due to the length of the observing run being greater than one orbital cycle.

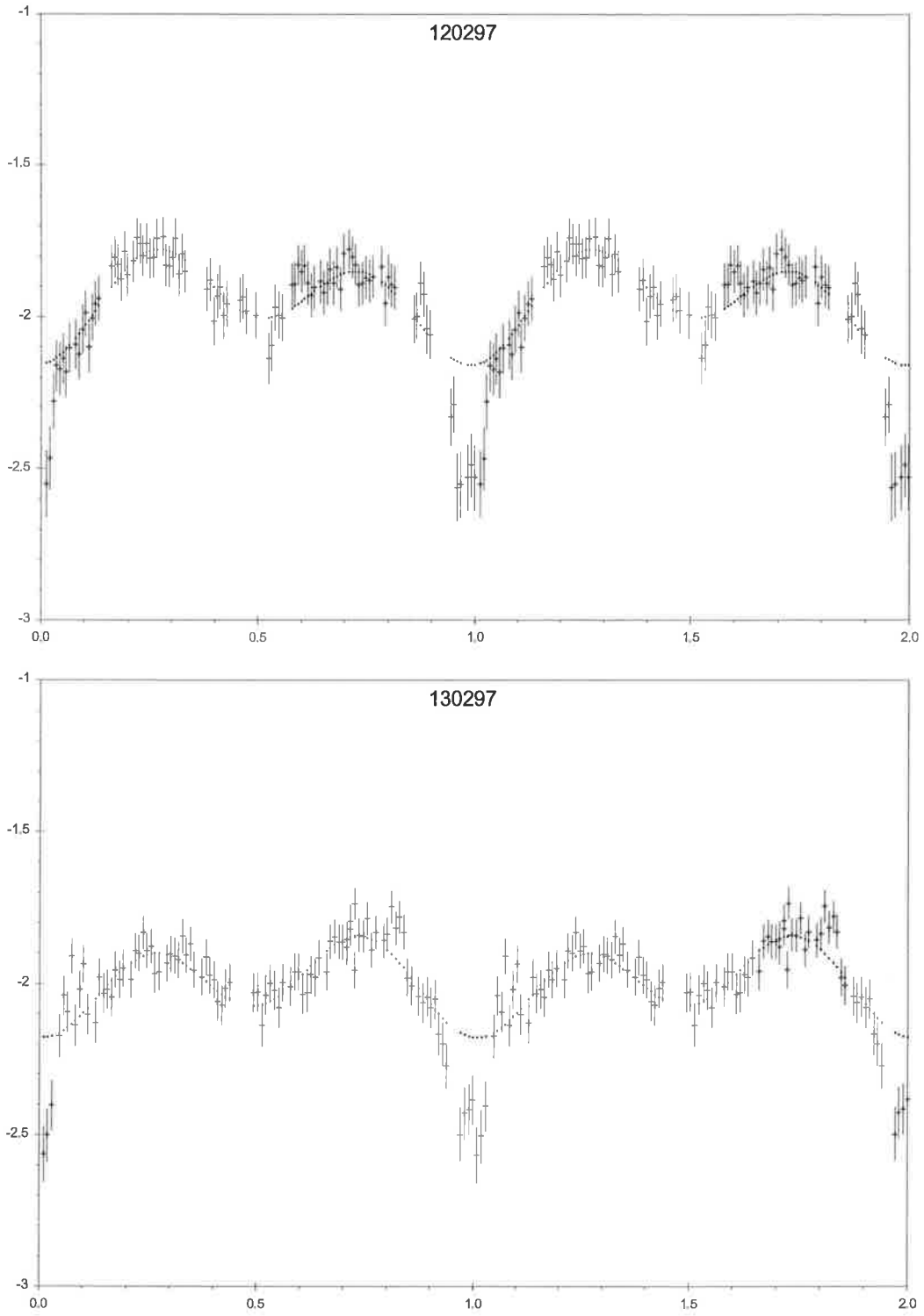

Figure 7.15 continued
Ellipsoidal and orbital fits to Woomera white-light photometry. Ordinate is differential magnitude; abscissa is orbital phase.

not be examined in detail. In any case, one would have to explain the apparent phase-wandering mentioned above.

Since Cen 2 exhibits characteristics of both polars and intermediate polars (Howell *et al.* 1997), it is possible that cyclotron emission from the primary is involved. Assuming that the primary's magnetic axis is directed somewhat towards the secondary, the line-of-sight would be most nearly transverse to the magnetic field lines near the primary's surface around orbital phase 0.5. This would lead to a maximum in the optical flux, due to cyclotron emission, at such phases. Again, the phase-wandering of the "orbital" component would have to be considered.

The CTIO data show evidence of considerable small-scale flaring for Cen 2 in its higher activity states, and also suggest the possibility of quasi-periodic oscillations. In Figure 7.16 are shown the flux-calibrated V-band data for 070898 and 140898. For 070898, a possible "flare" of approximately 86 seconds in duration is evident near time = 95 minutes, with an increase in intensity of 33% over the immediate pre-flare flux. For 140898, a flare of duration 515 seconds is seen near time = 50 minutes, with an increase of 28% over the immediate pre-flare flux. (Note, though, that this second event looks as if it could be a flare superimposed on the possible QPO's in that night's data, which would mean a shorter duration and smaller amplitude for the flare itself).

For the 140898 data, period searches on the data in the range 90-1800s, using both phase-dispersion minimisation (PDM) and the "Lancelot" neural network (both available from http://www.kusastro.kyoto-u.ac.jp/vsnet/etc/prog.html) period searching algorithms, estimate best periods of 1117-1128s. For 070898, a PDM search in the period range 600-1800s gives a best period of 1495s, with a less significant period of 962.8s.

The source of such "low-frequency" QPO's (as distinct from high-frequency QPO's of the order of 0.3-1 Hz or thereabouts) may be (King 1989) an unstable and oscillating ionisation front at the inner Lagrangian point. The period of such QPO's may be found to be (Hameury *et al.* 1986)

$$P \approx 5.5\ 10^{-2} P_{orb} \qquad (7.2)$$

which yields 944s for Cen 2. This is in not unreasonable agreement with the data for 070898, but is not supported by the 140898 data.

It is to be noted, however, that the "best period" peaks or troughs are quite broad, and that the value of the test parameter returned for such periods is much closer to the noise than is the case for clean signals at a definite period. Also, the above best estimates are not those which are immediately obvious from visual inspection of the data.

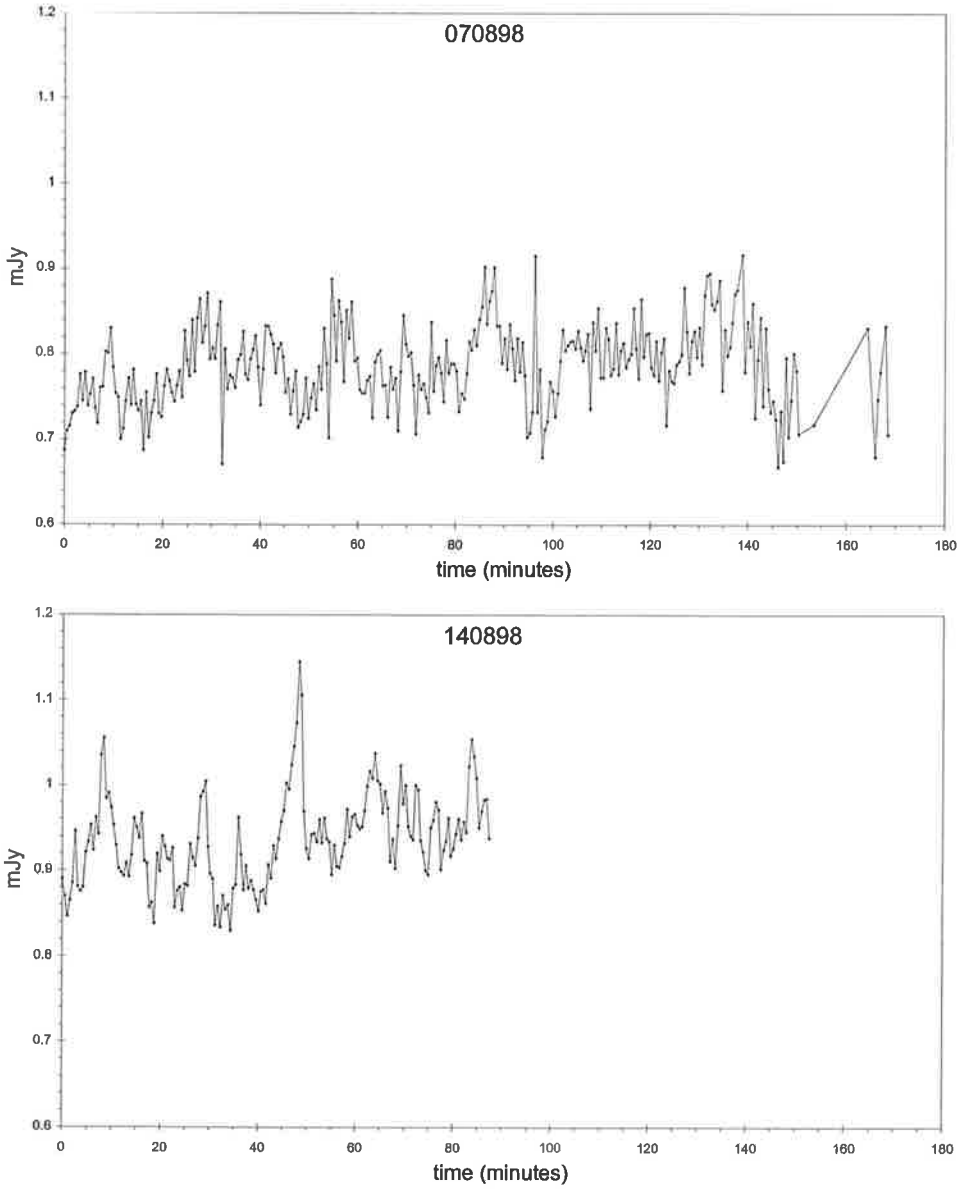

Figure 7.16

Flux-calibrated V-band CTIO photometry showing some flaring and possible quasi-periodic oscillations

7.10 General photometric variability

It is clear from all the light curves that Cen 2 is highly variable, and, within context of the experimental errors present in the photometry, is significantly variable. In Figure 7.17 is shown the scatter in the individual nights' data for Cen 2 and for all measured check stars. (For Cen 2, the eclipse was always included; those nights for which the eclipse was not measured are not included).

It is obvious (as expected) that as one measures fainter and fainter stars, the scatter in the light curves increases, this being due to increasing measurement error as a result of reducing photon (or indeed ADU) counts. For Cen 2 this is not apparent, since as the CV brightens, the eclipse deepens, and the scatter in the light curve increases. At all times, however, the scatter in the CV light curve is greater than that in check stars of similar magnitude. Thus, for the Woomera photometry, Cen 2 is always significantly variable, even when in its lowest activity state.

Figure 7.18 is based on the same data, but shows, for each star, its average (differential) magnitude and average light-curve scatter. The error bars are the standard deviation about that average magnitude or scatter, respectively. Again, it is clear that Cen 2 is very significantly variable.

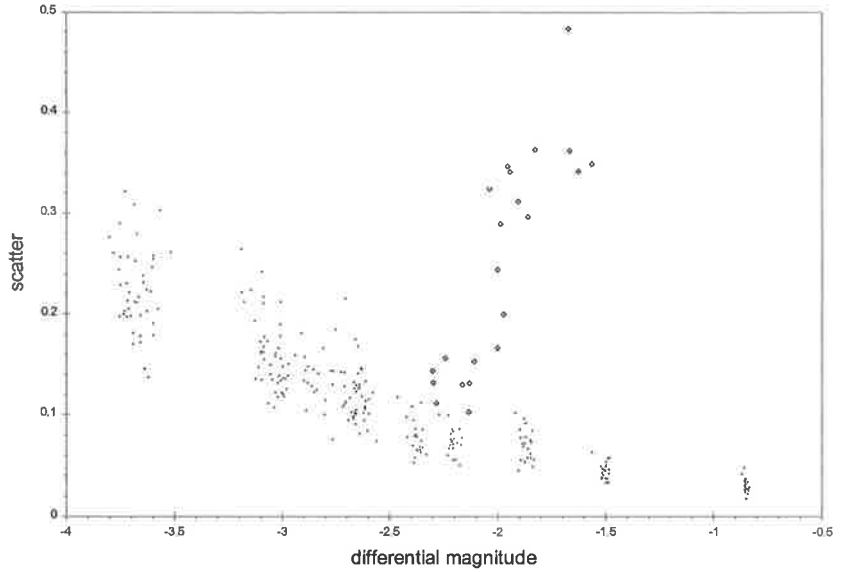

Figure 7.17

Scatter-magnitude diagram for all eclipsing Woomera data. Diamonds denote Cen 2 measurements; crosses are for field stars.

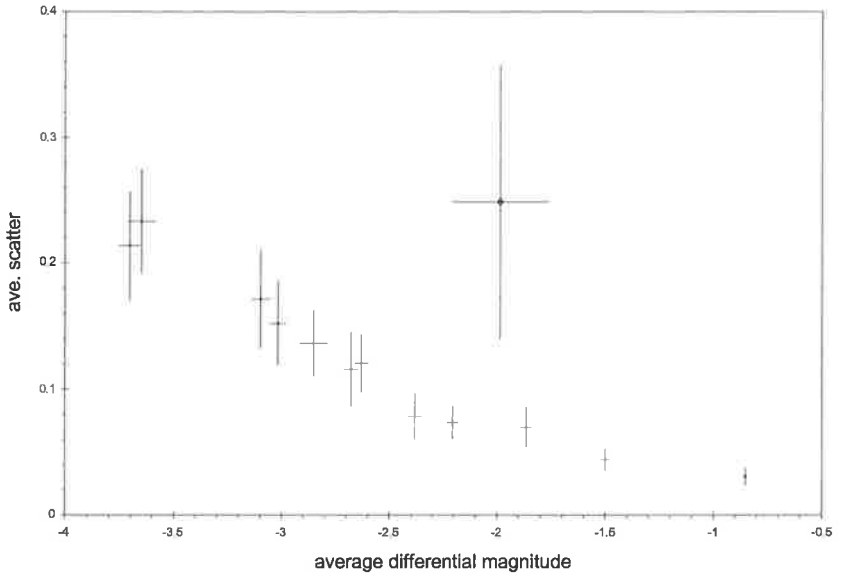

Figure 7.18

Average scatter-average magnitude plot for eclipsing Woomera data. The diamond denotes Cen 2; crosses are for field stars.

7.11 Is Cen 2 a polar or an intermediate polar? Or.....

For the data presented here, it is possible to fit a single period to *all* the data, and it is clear that this period is the orbital period of the system. This is a trait of a polar. However, there appears to be a disc during its active states. This suggests an IP classification.

So, based purely on the data here, it is not possible to say if Cen 2 is a polar or an IP.

It is seen to switch between low (inactive) and high (active) states, which is a characteristic of polars. These changes are accompanied by the formation (and loss) of a partial accretion disc around the primary, and there can be significant variation in the brightness of this disc over time scales of a few days. State changes are not infrequent, and there is the possibility of a continuum of states as the disc increases and decreases as the accretion rate changes.

Detailed spectroscopy and especially polarimetry are required, and a swag of high-accuracy, high-speed photometry capable of showing possible white dwarf rotation modulation would assist greatly. Simultaneous multi-colour photometry in an active state would also be of great interest. At this stage the question of the nature of Cen 2 remains unanswered. Indeed, this system may be a hybrid.

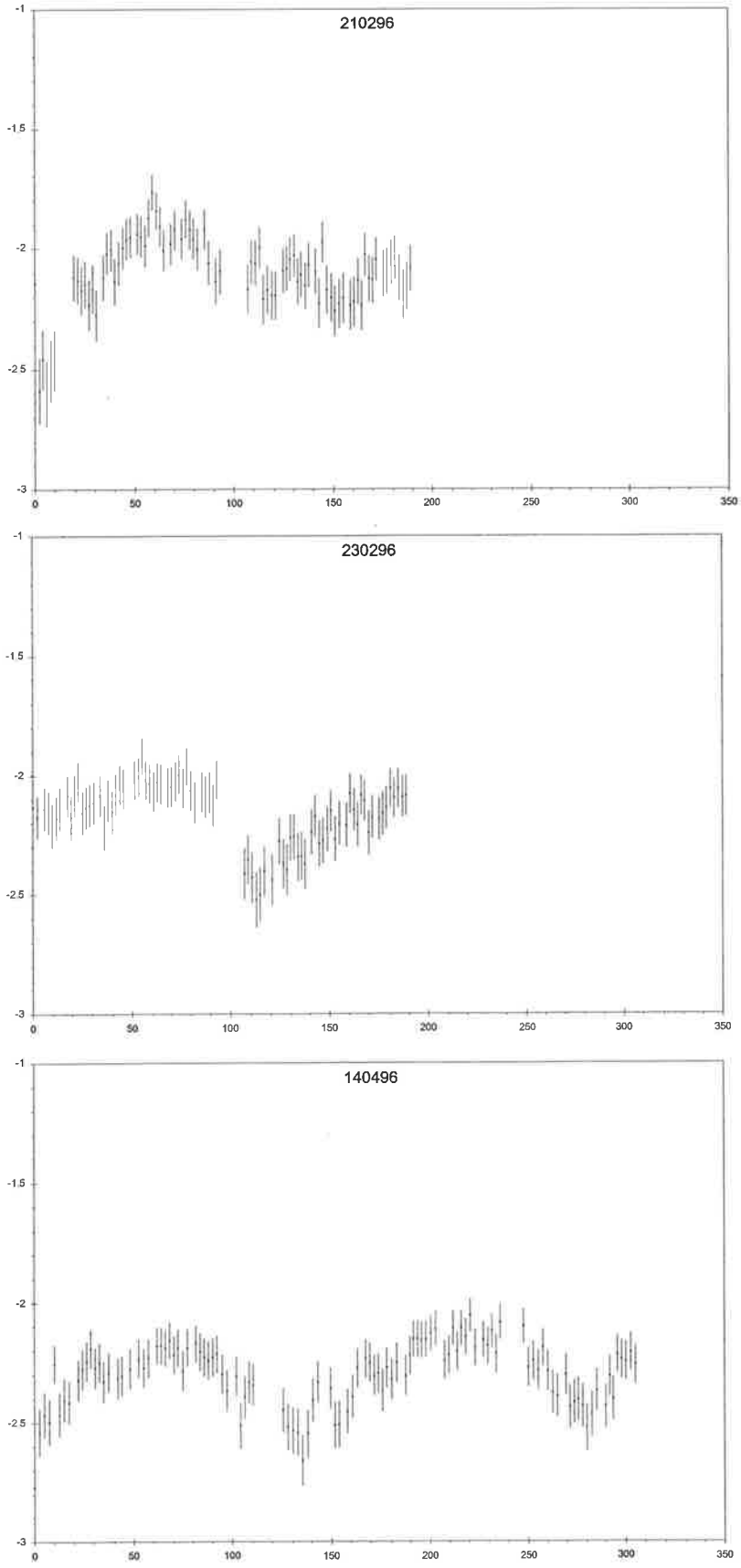

Figure 7.5

Woomera white-light photometry of Cen2.
Ordinate is differential magnitude, absissa is time (in minutes).

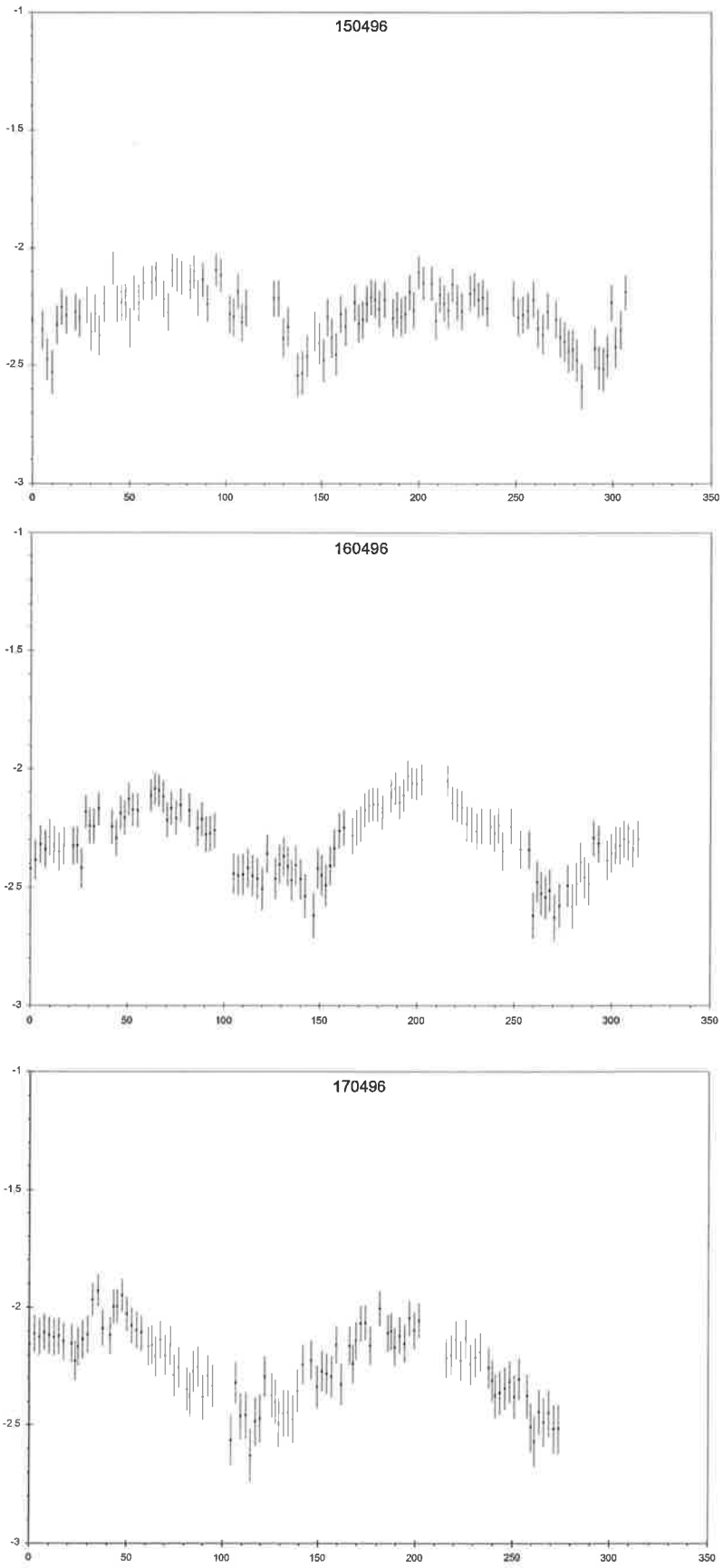

Figure 7. 5 continued

Woomera white-light photometry of Cen2.
Ordinate is differential magnitude, absissa is time (in minutes).

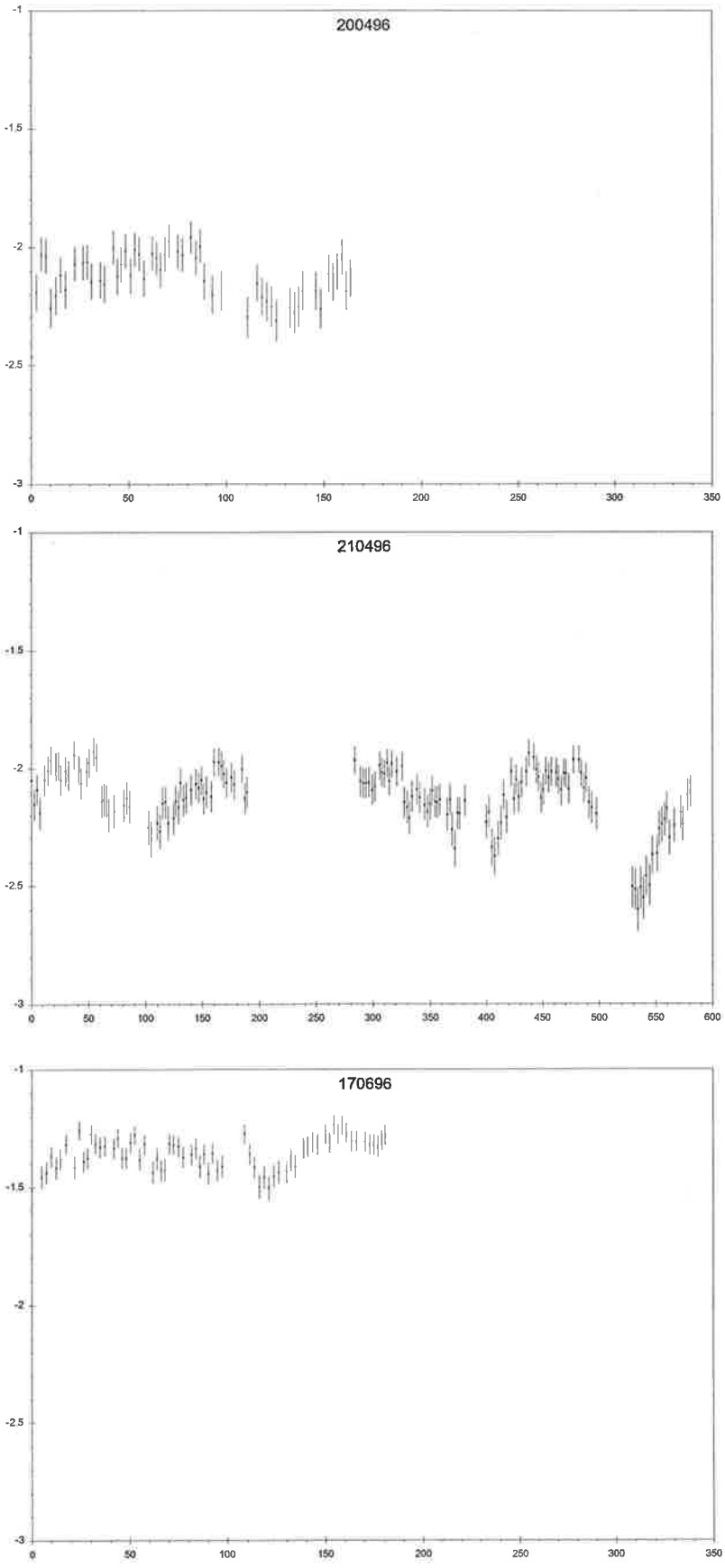

Figure 7. 5 continued

Woomera white-light photometry of Cen2.
Ordinate is differential magnitude, absissa is time (in minutes).

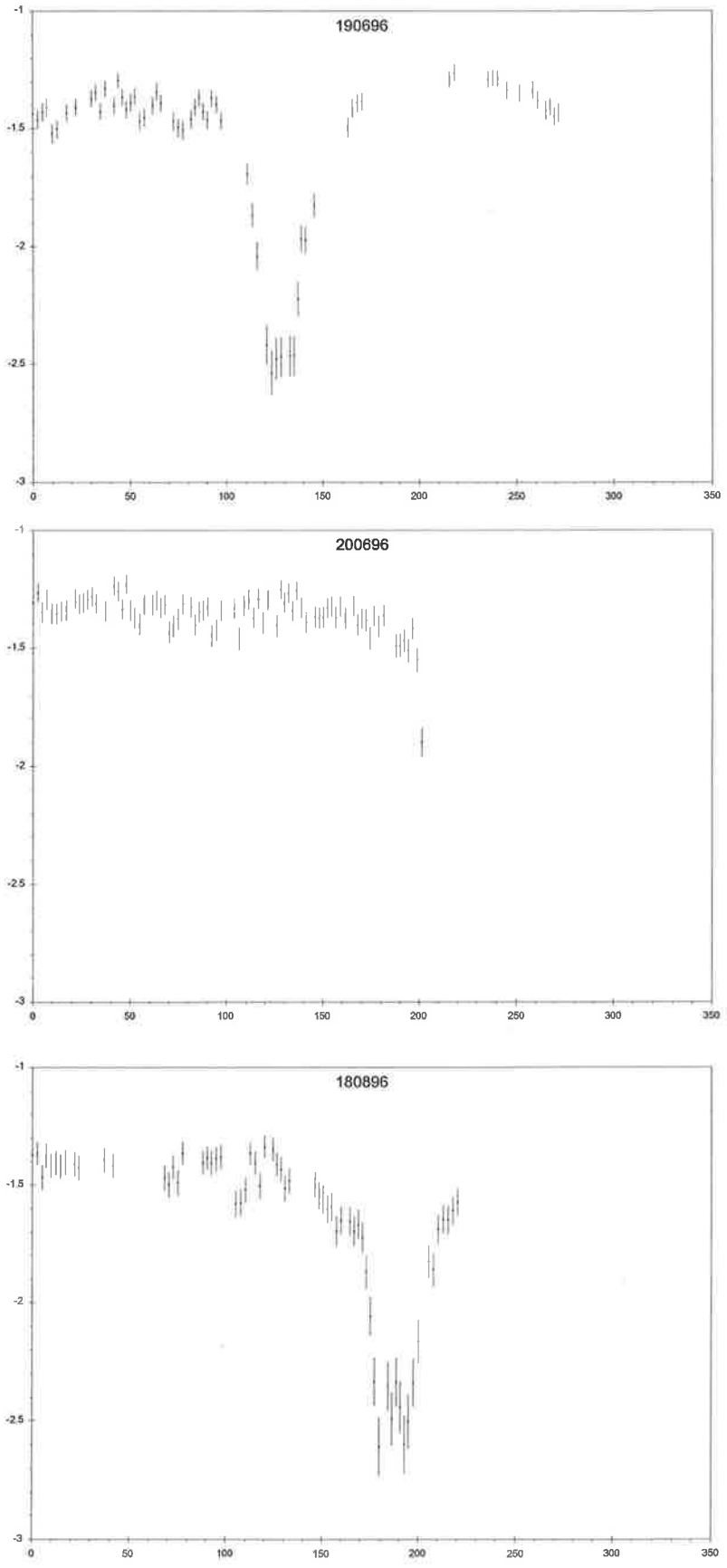

Figure 7. 5 continued

Woomera white-light photometry of Cen2.
Ordinate is differential magnitude, absissa is time (in minutes).

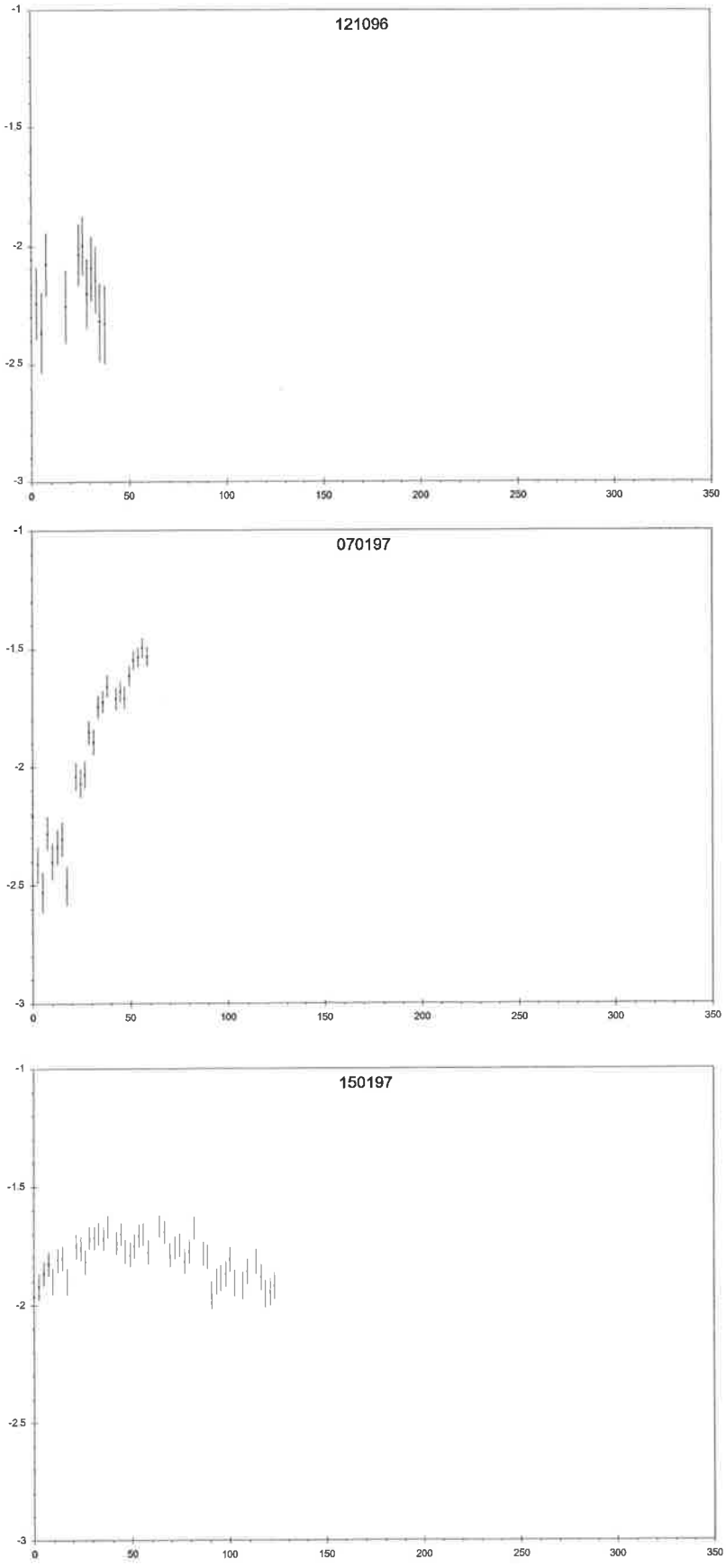

Figure 7. 5 continued

Woomera white-light photometry of Cen2.
Ordinate is differential magnitude, absissa is time (in minutes).

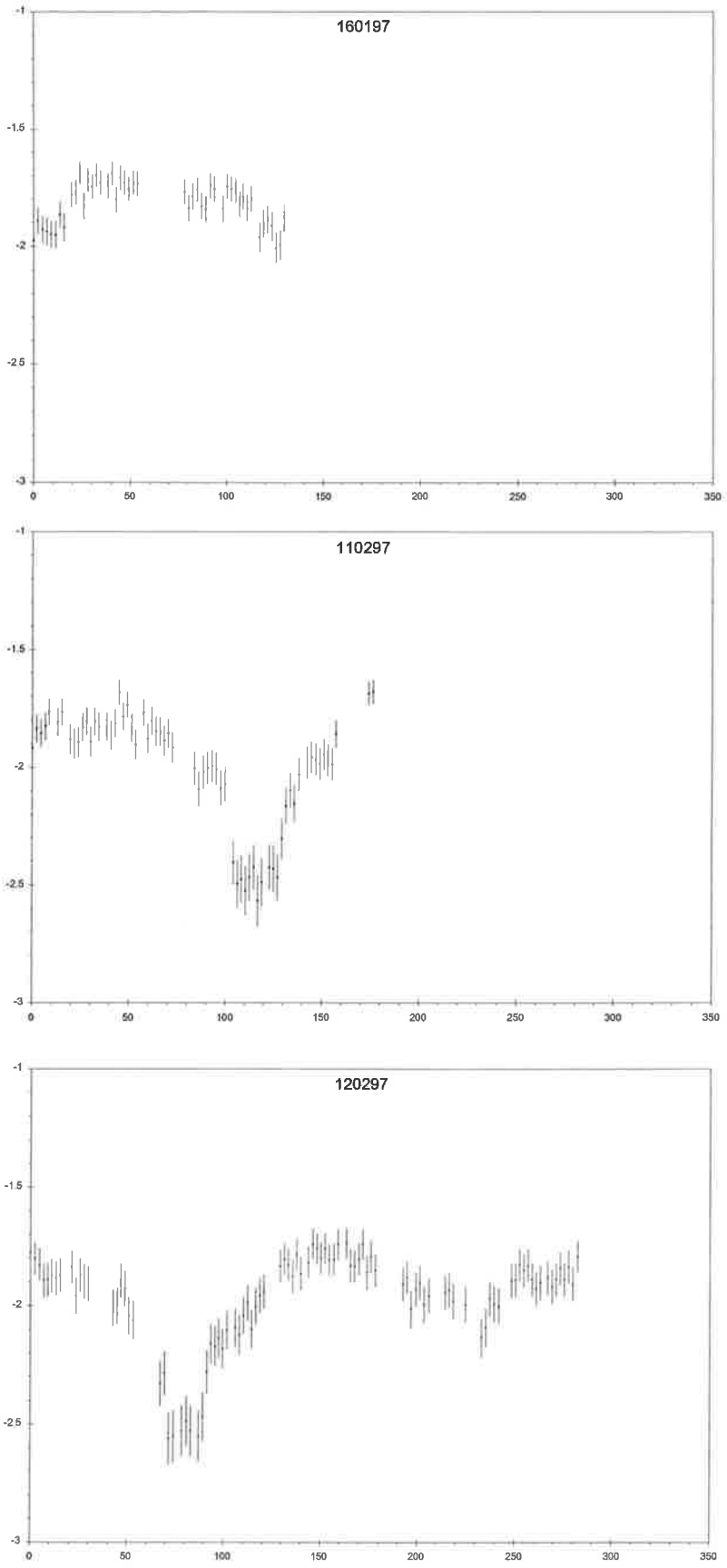

Figure 7. 5 continued

Woomera white-light photometry of Cen2.
Ordinate is differential magnitude, absissa is time (in minutes).

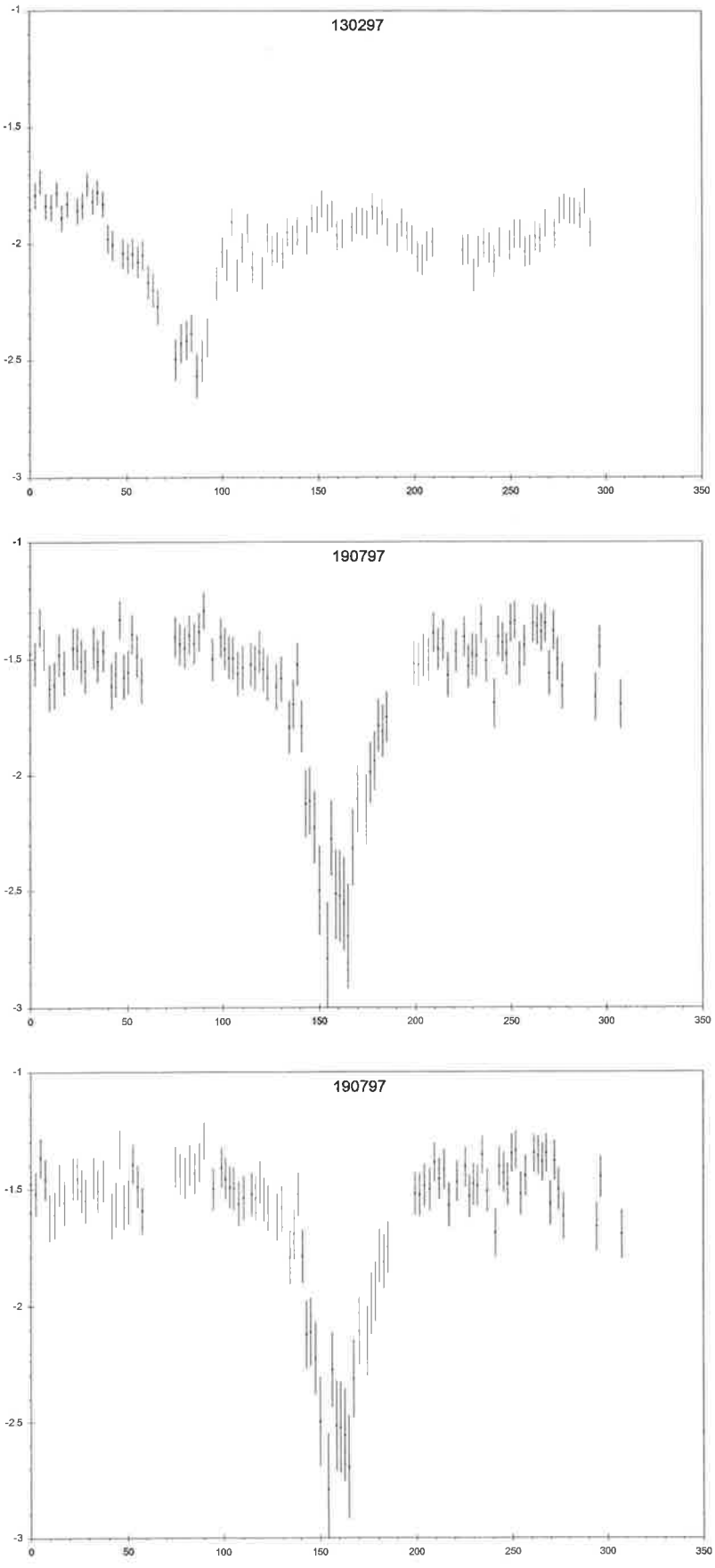

Figure 7. 5 continued

Woomera white-light photometry of Cen2.
Ordinate is differential magnitude, absissa is time (in minutes).

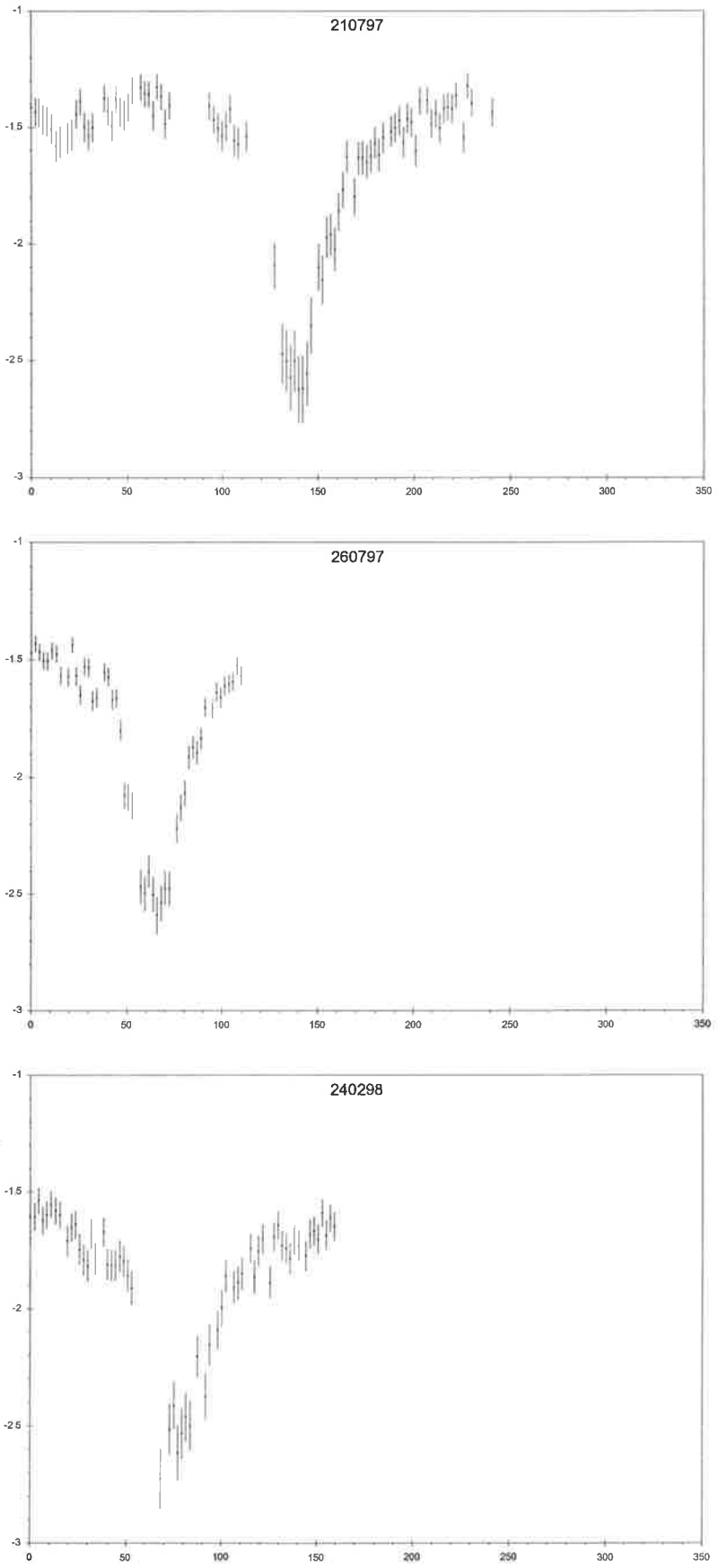

Figure 7. 5 continued

Woomera white-light photometry of Cen2.
Ordinate is differential magnitude, absissa is time (in minutes).

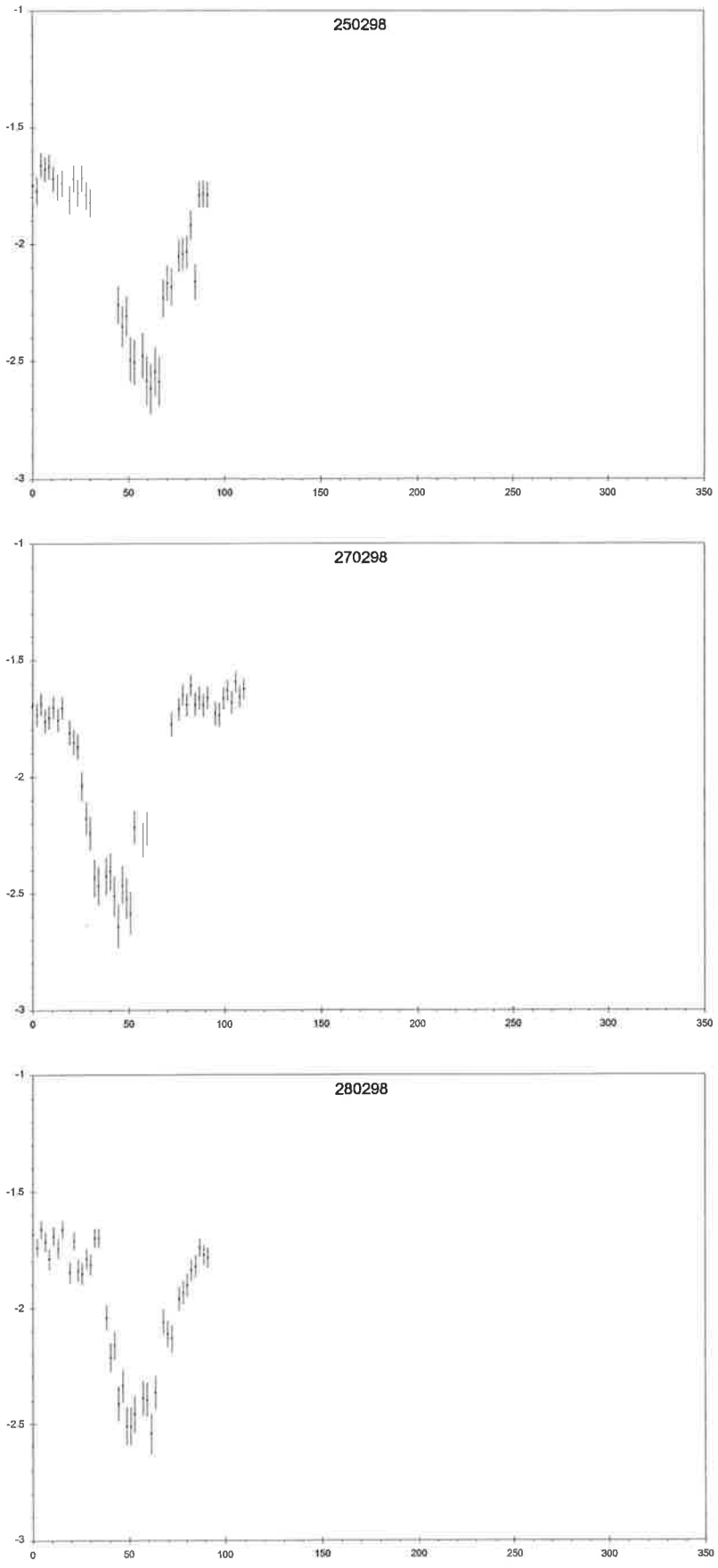

Figure 7. 5 continued

Woomera white-light photometry of Cen2.
Ordinate is differential magnitude, absissa is time (in minutes).

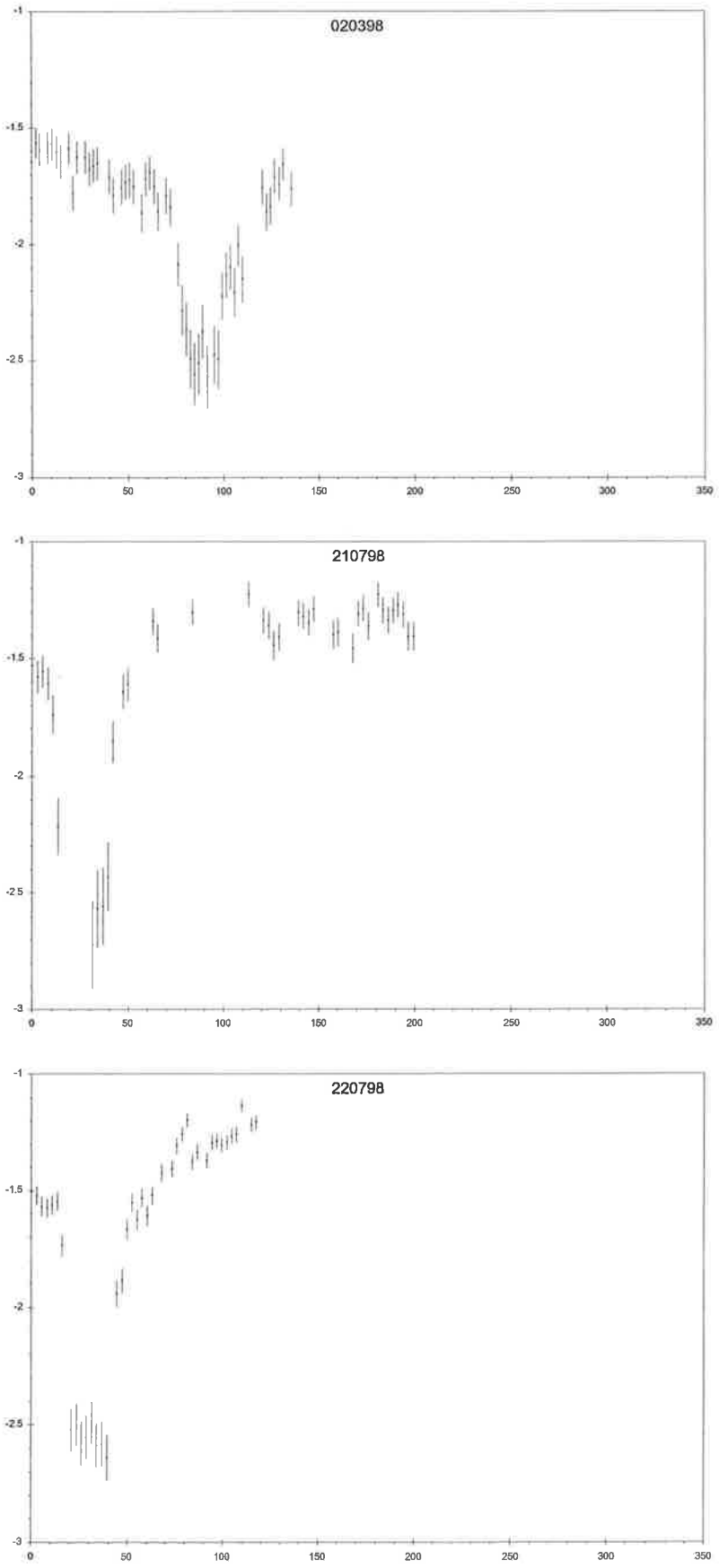

Figure 7. 5 continued

Woomera white-light photometry of Cen2.
Ordinate is differential magnitude, absissa is time (in minutes).

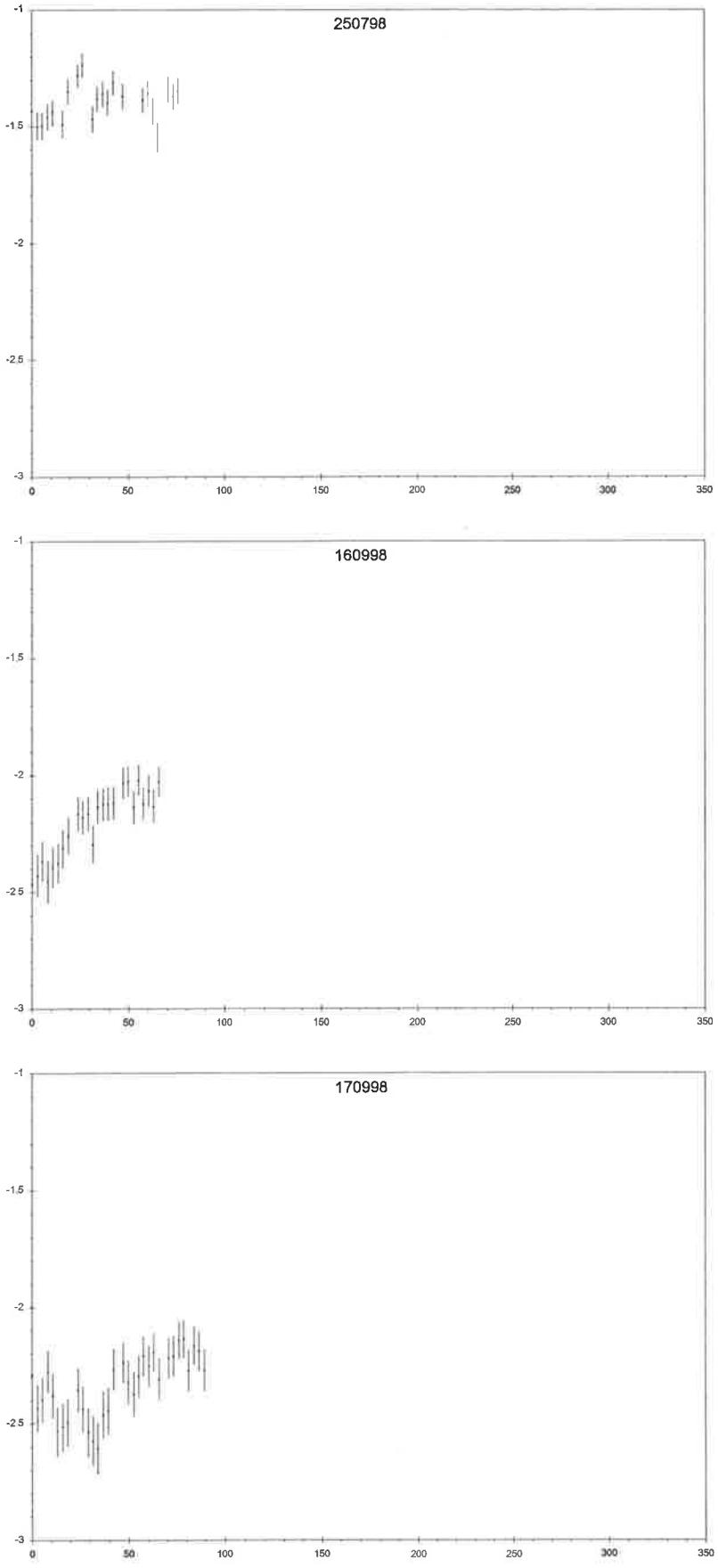

Figure 7. 5 continued

Woomera white-light photometry of Cen2.
Ordinate is differential magnitude, absissa is time (in minutes).

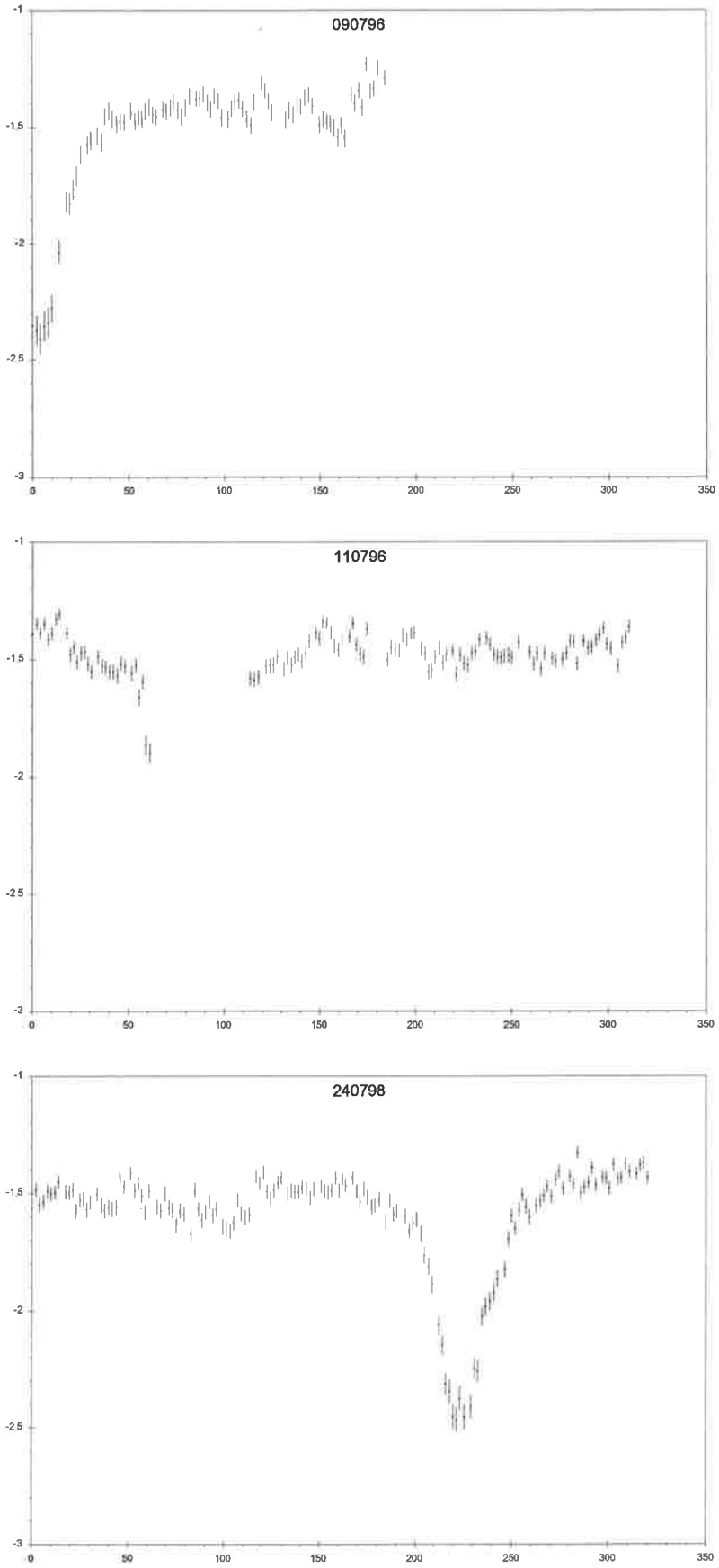

Figure 7. 5 continued

SSO white-light photometry of Cen2.
Ordinate is differential magnitude, absissa is time (in minutes).

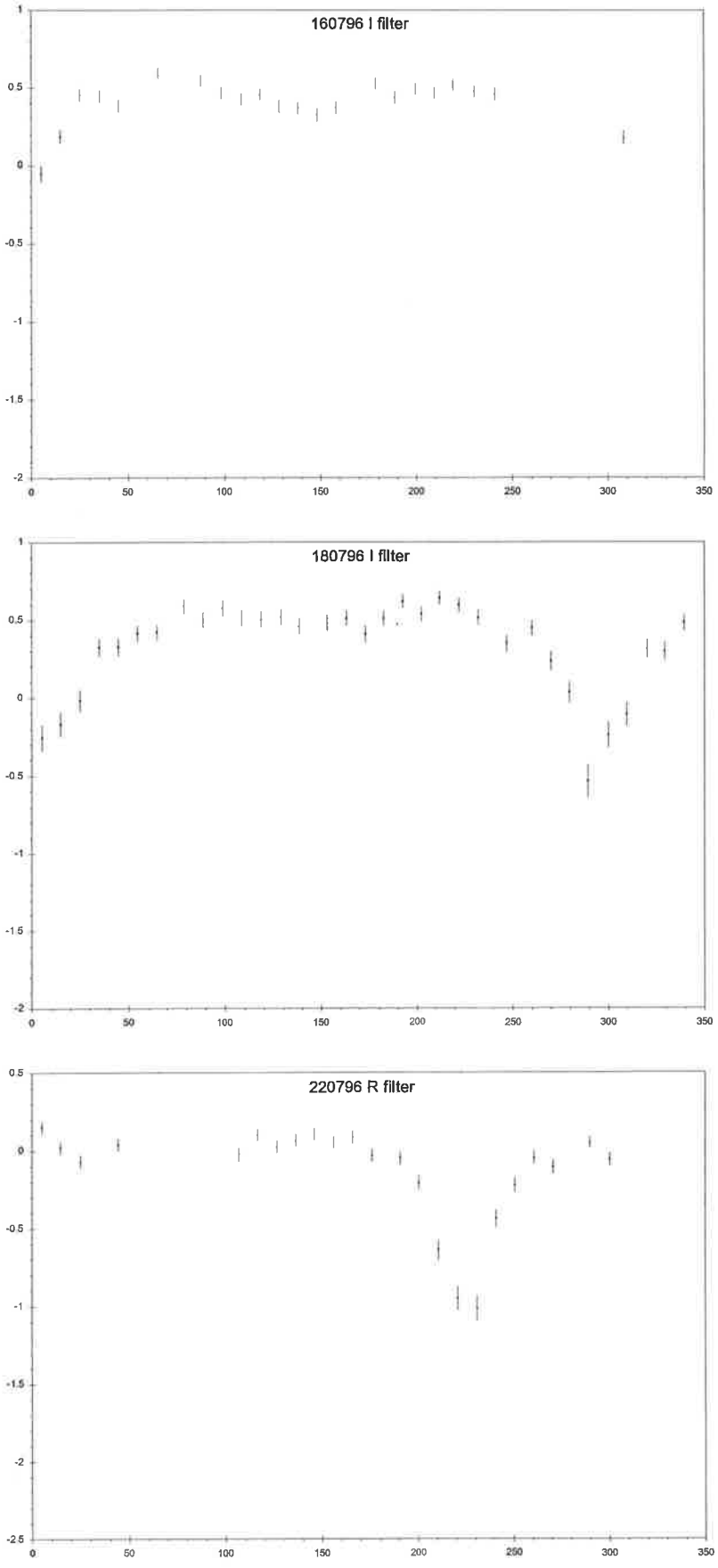

Figure 7. 5 continued

SSO filtered photometry of Cen2.
Ordinate is differential magnitude, absissa is time (in minutes).

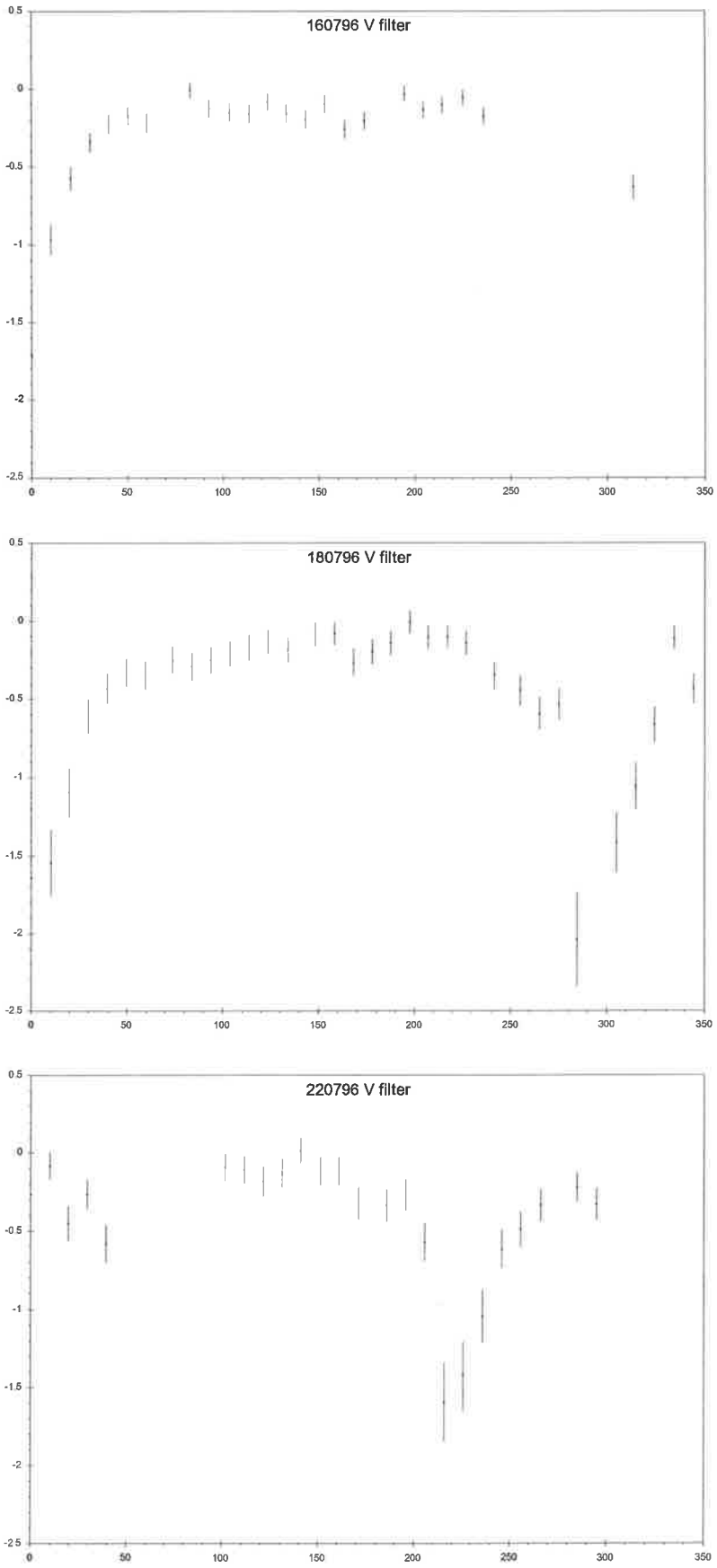

Figure 7. 5 continued

SSO filtered photometry of Cen2.
Ordinate is differential magnitude, absissa is time (in minutes).

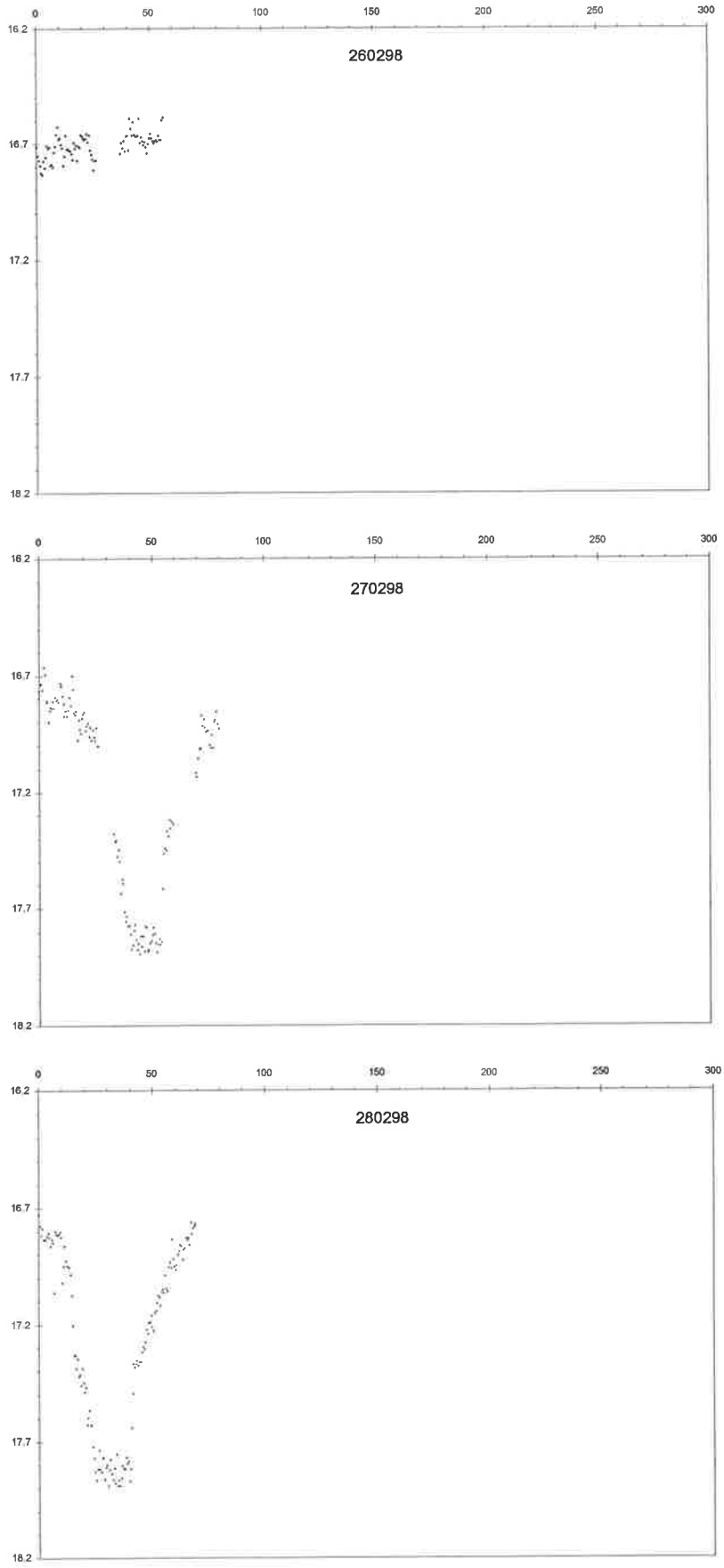

Figure 7. 5 continued

CTIO V-band photometry of Cen2.
Ordinate is calibrated magnitude, absissa is time (in minutes).
Note: no error estimates.

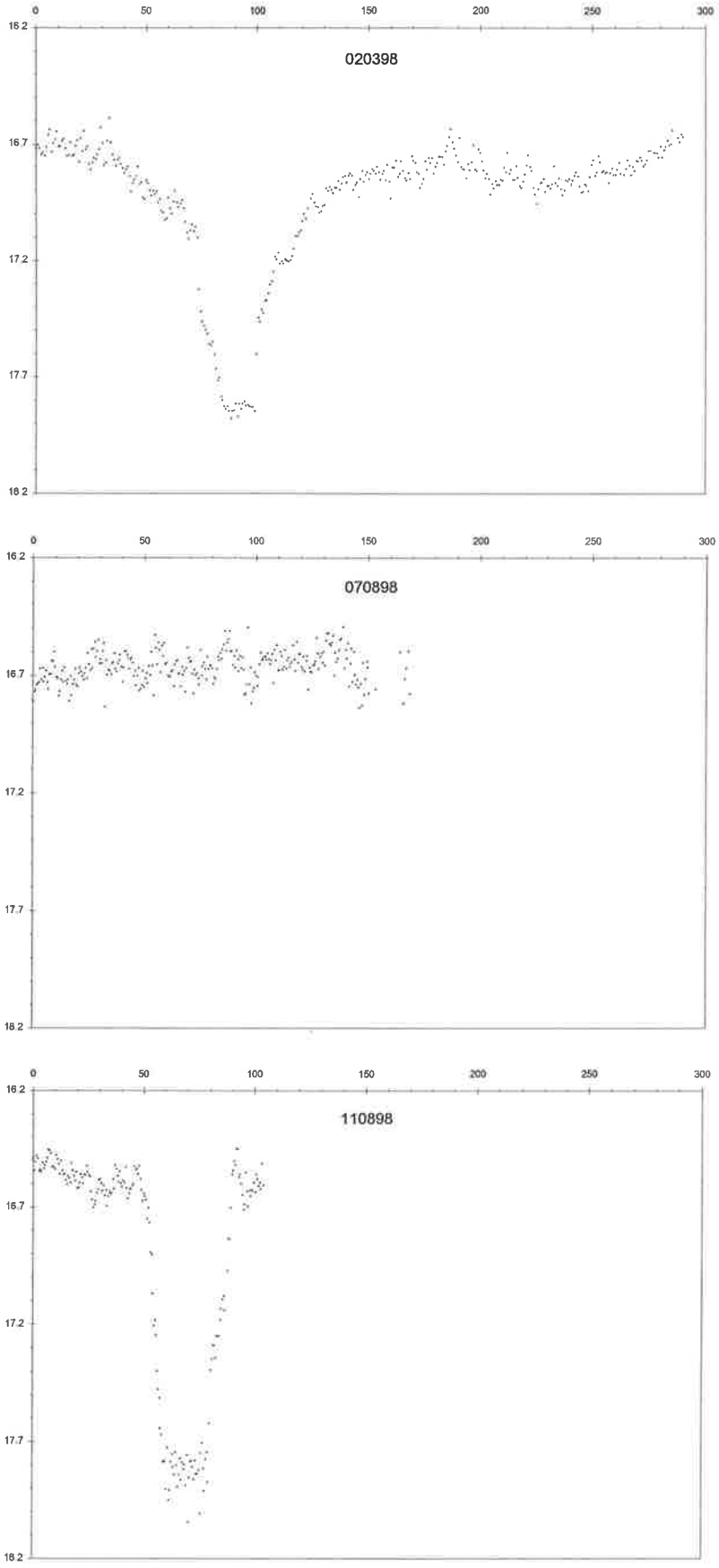

Figure 7.5 continued

CTIO V-band photometry of Cen2.
Ordinate is calibrated magnitude, absissa is time (in minutes).
Note: no error estimates.

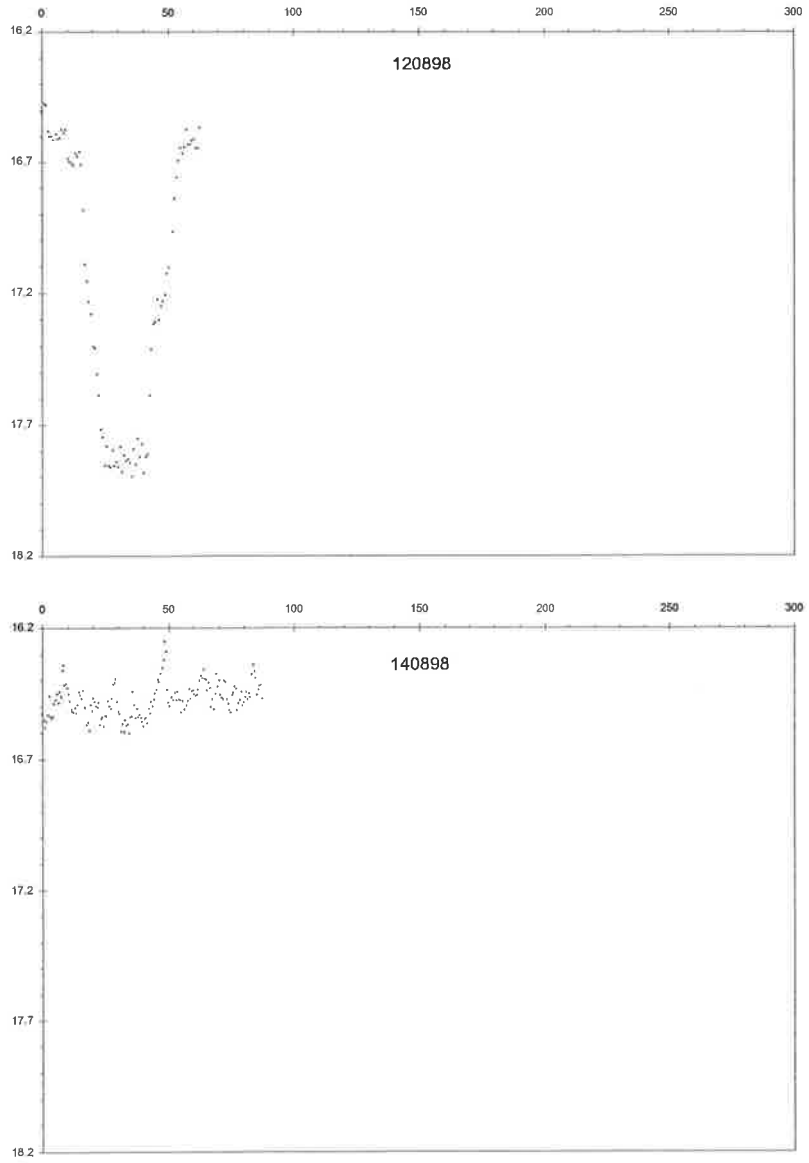

Figure 7.5 continued

CTIO V-band photometry of Cen2.
Ordinate is calibrated magnitude, absissa is time (in minutes).
Note: no error estimates.

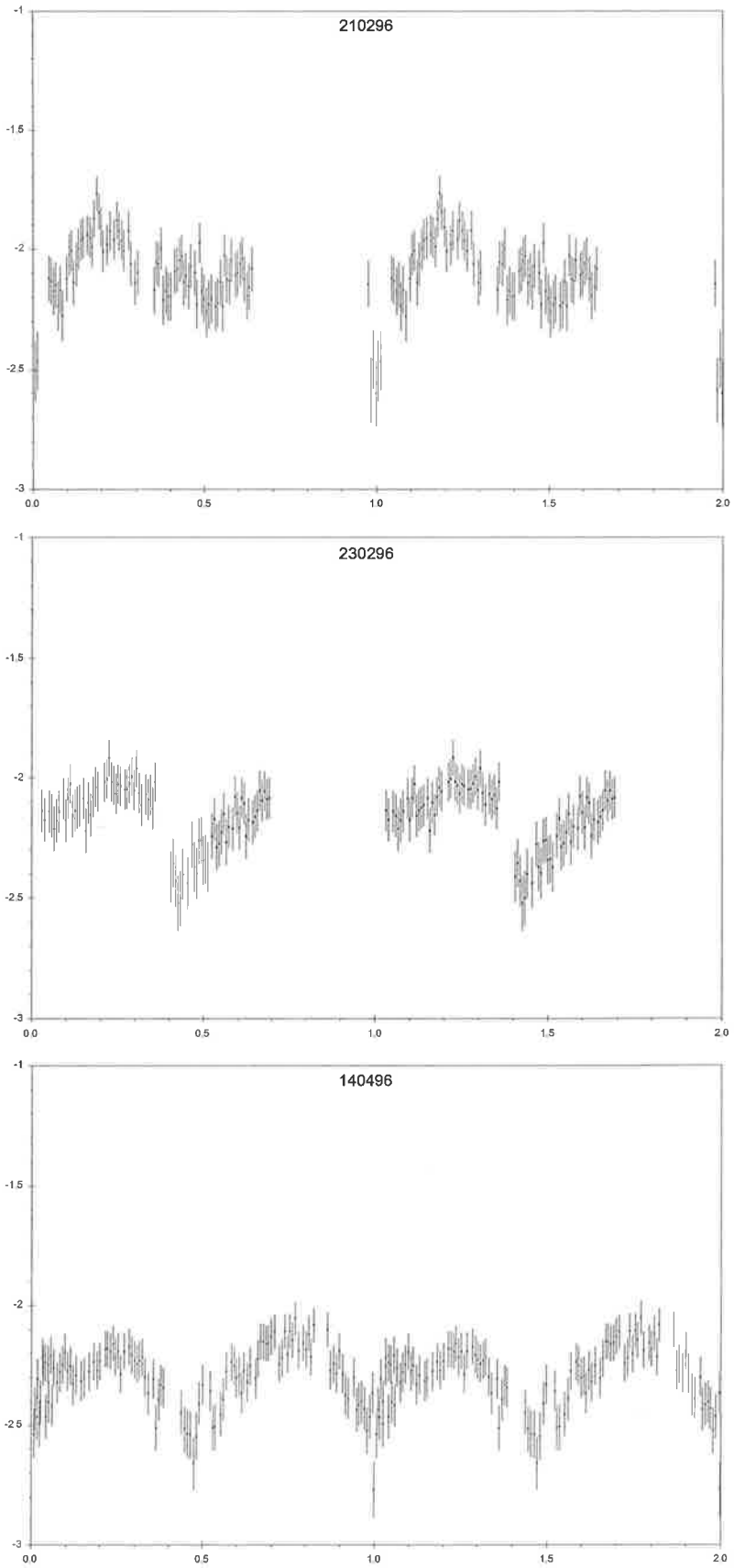

Figure 7.6
Woomera white-light photometry of Cen 2.
Ordinate is differential magnitude, abscissa is orbital phase.

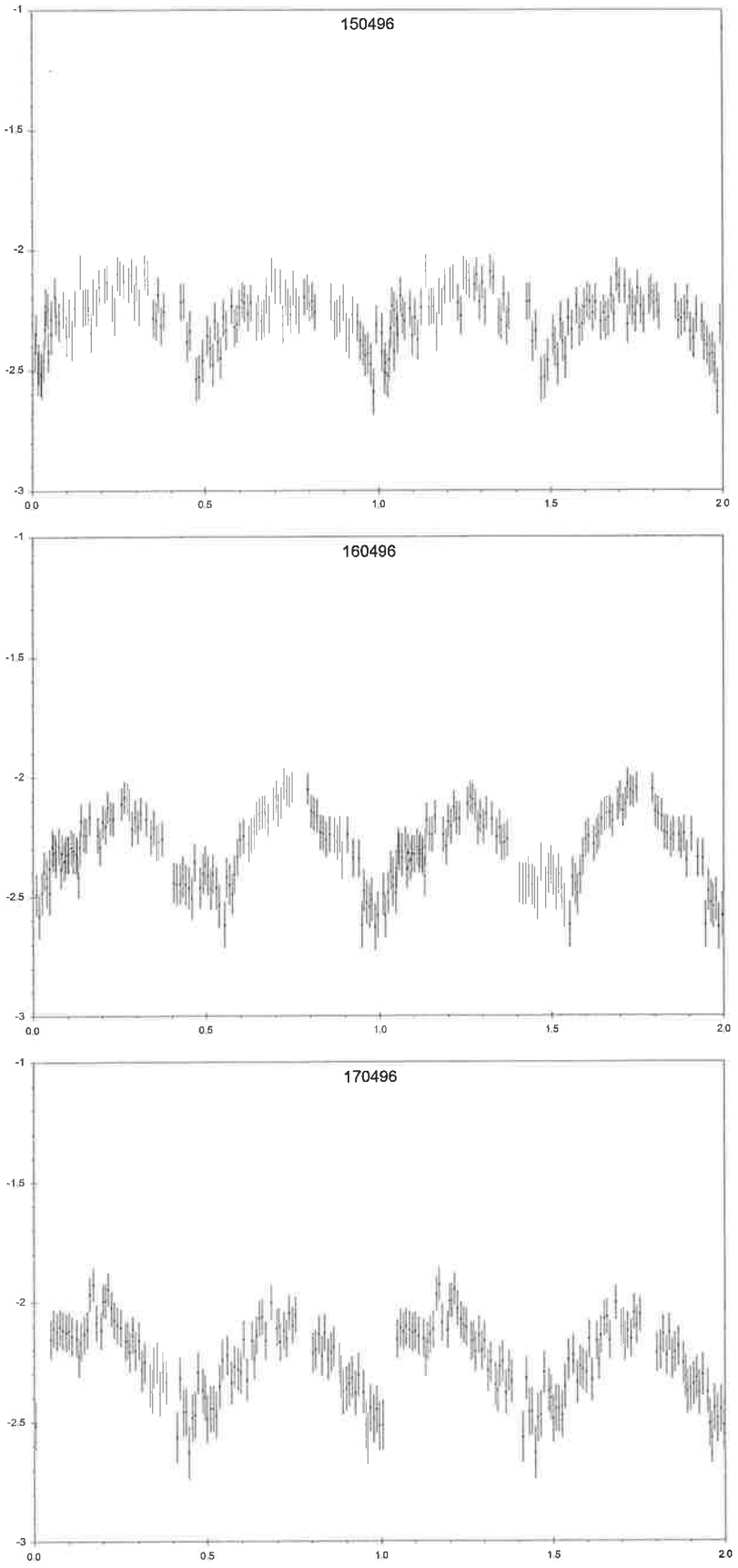

Figure 7.6 continued
Woomera white-light photometry of Cen 2.
Ordinate is differential magnitude, abscissa is orbital phase.

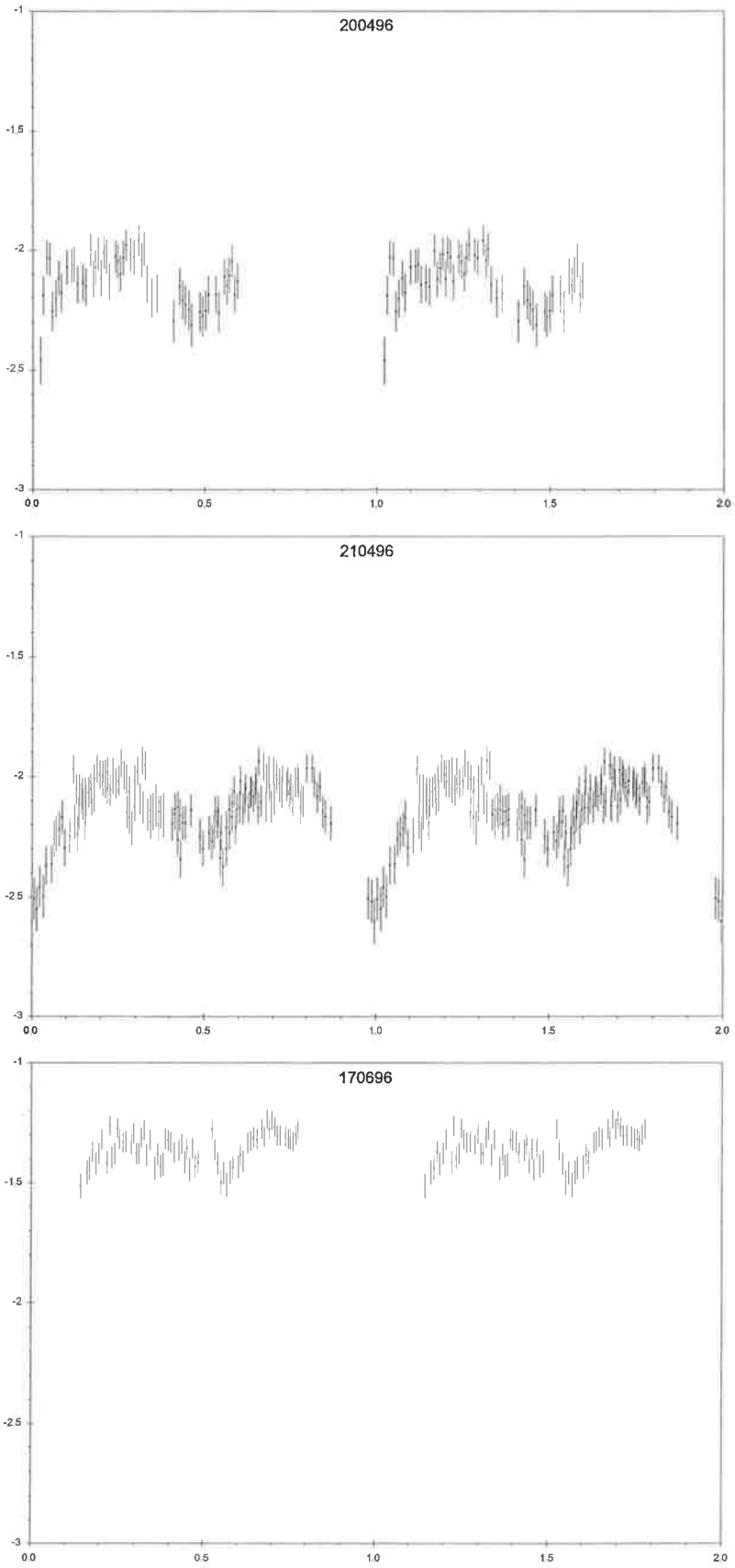

Figure 7.6 continued
Woomera white-light photometry of Cen 2.
Ordinate is differential magnitude, abscissa is orbital phase.

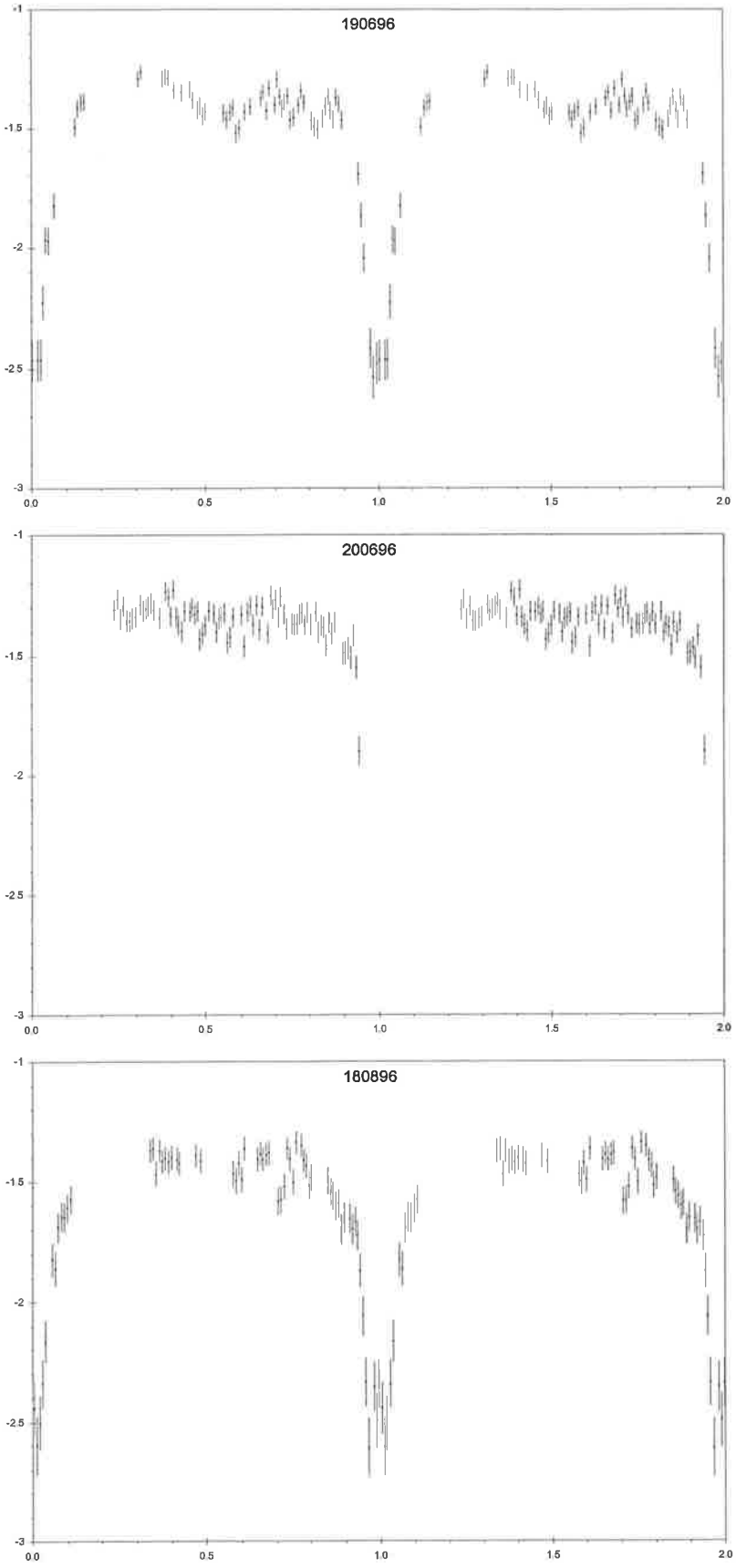

Figure 7.6 continued
Woomera white-light photometry of Cen 2.
Ordinate is differential magnitude, abscissa is orbital phase.

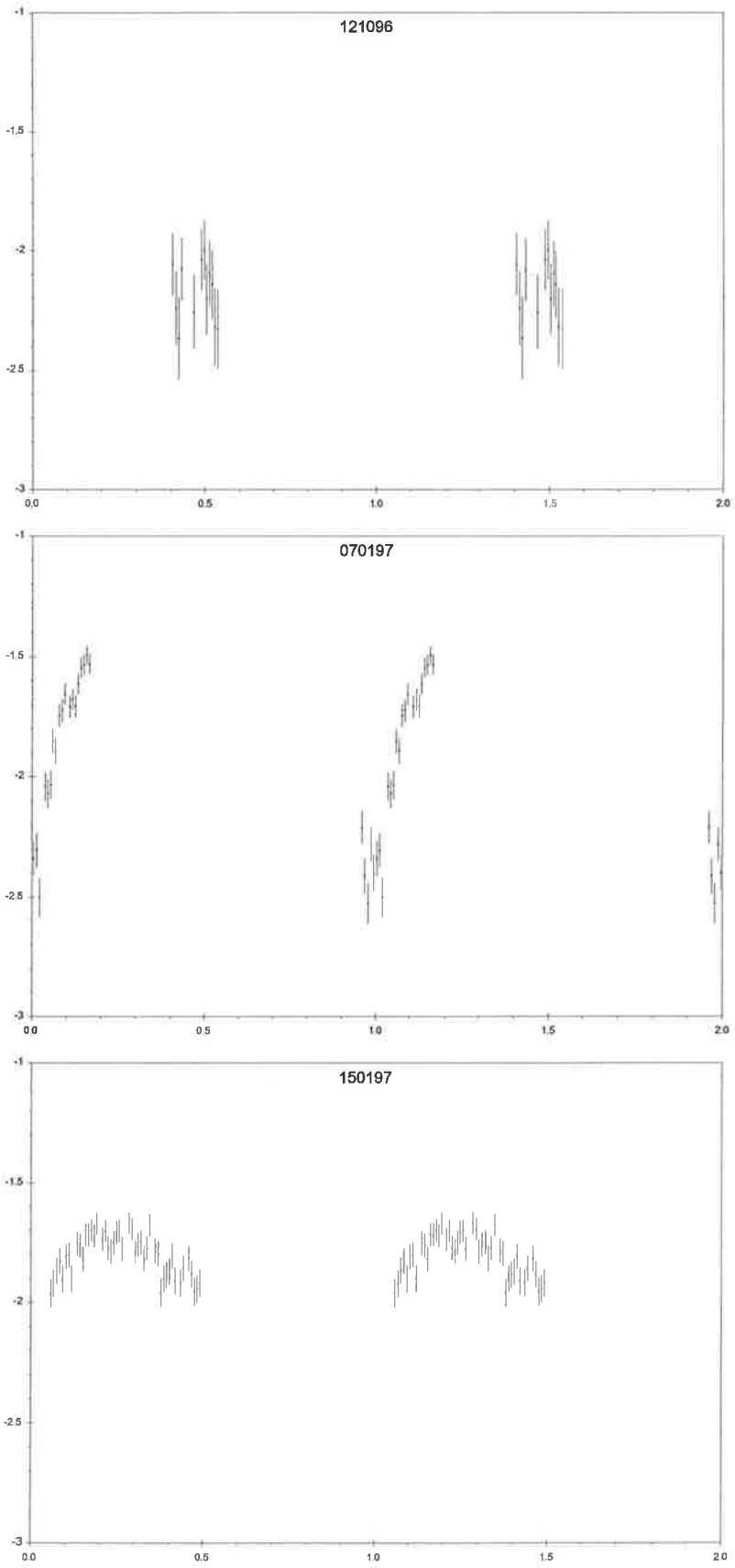

Figure 7.6 continued
Woomera white-light photometry of Cen 2.
Ordinate is differential magnitude, abscissa is orbital phase.

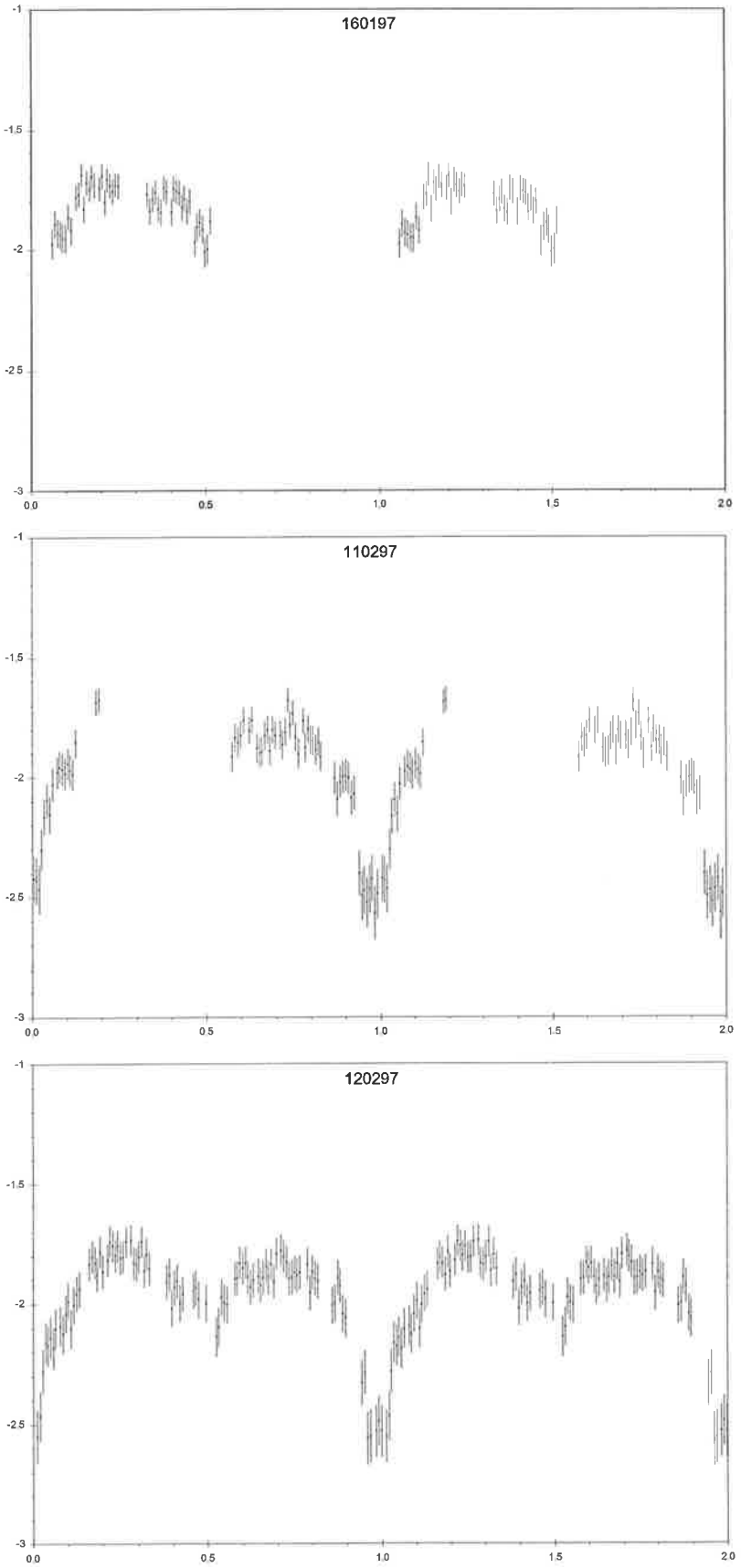

Figure 7.6 continued
Woomera white-light photometry of Cen 2.
Ordinate is differential magnitude, abscissa is orbital phase.

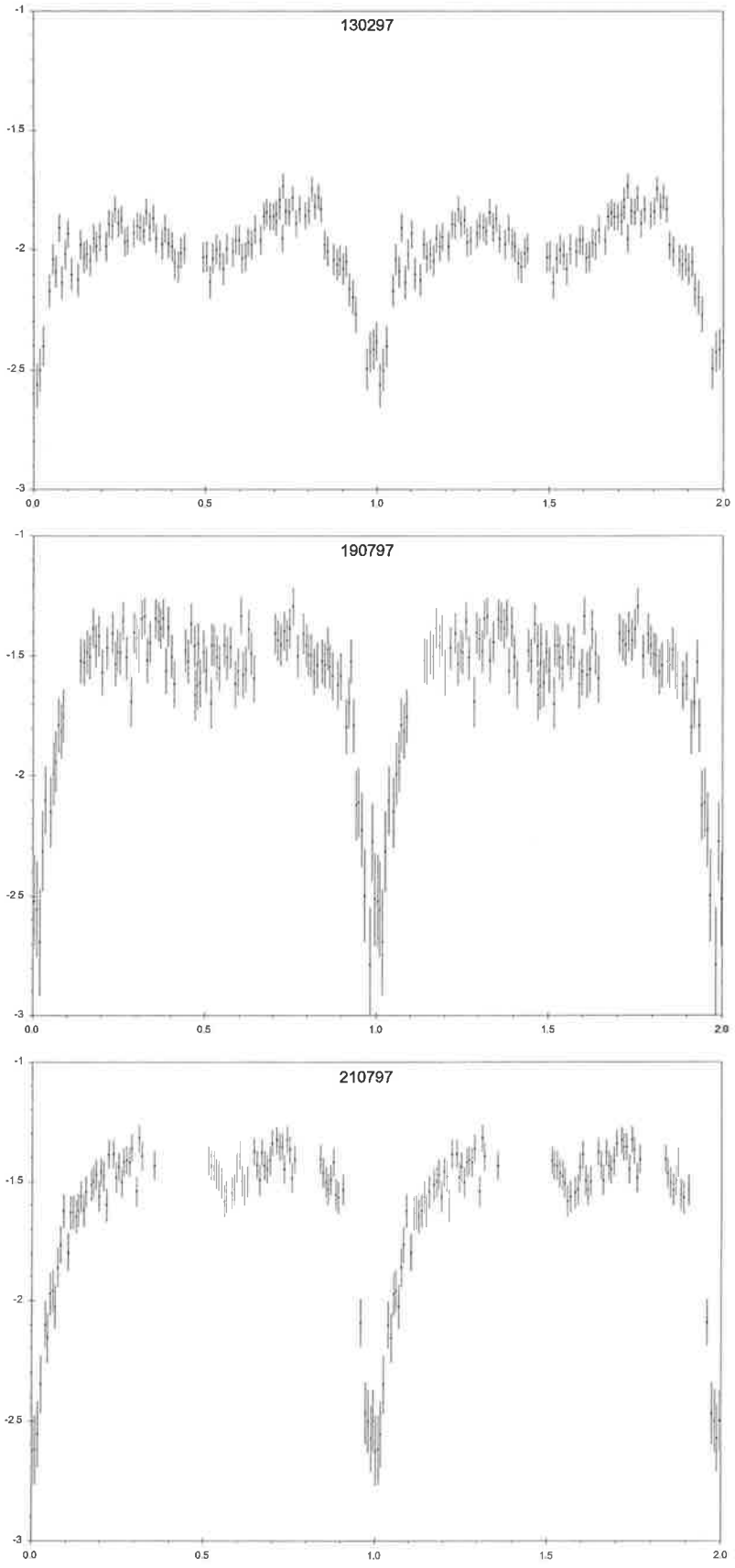

Figure 7.6 continued
Woomera white-light photometry of Cen 2.
Ordinate is differential magnitude, abscissa is orbital phase.

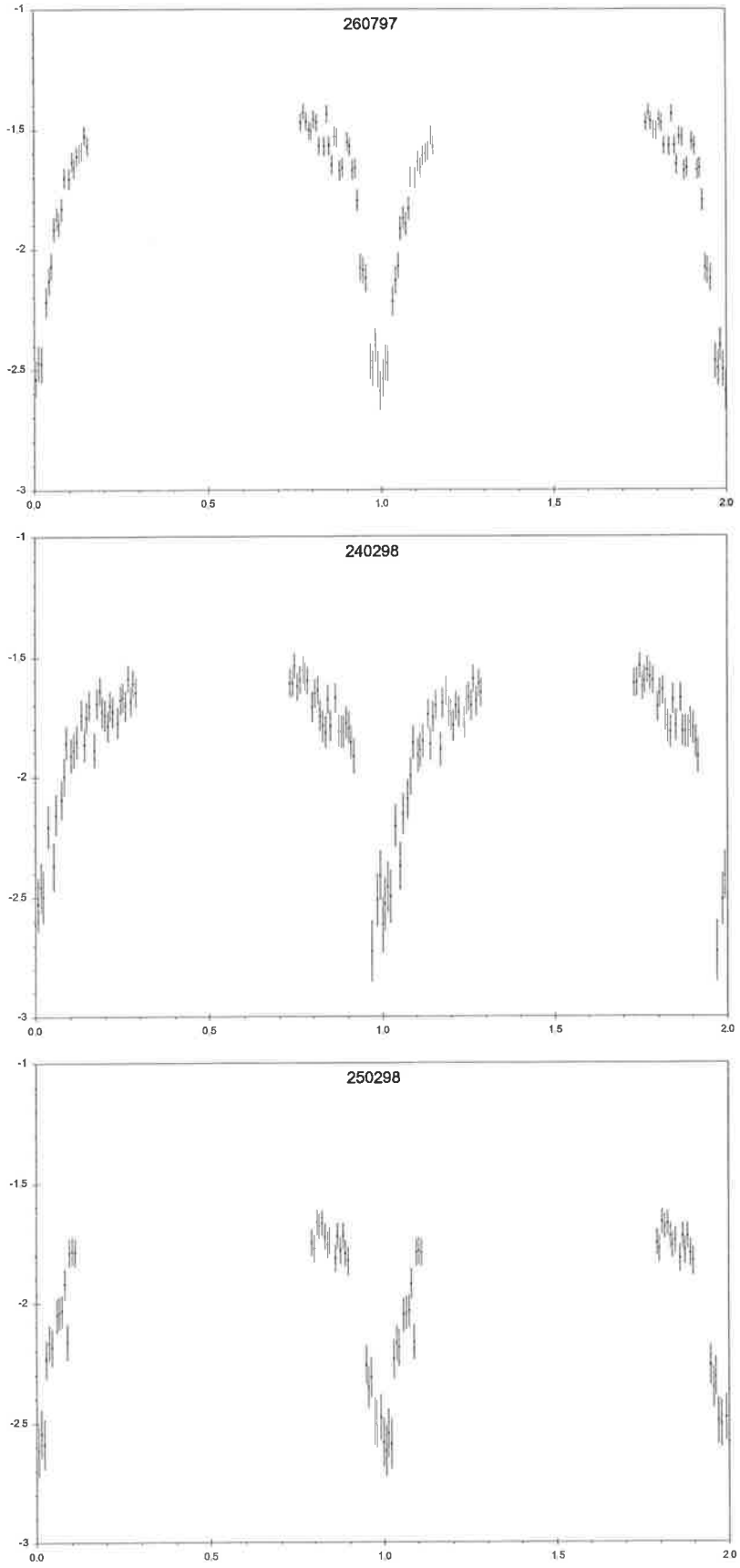

Figure 7.6 continued
Woomera white-light photometry of Cen 2.
Ordinate is differential magnitude, abscissa is orbital phase.

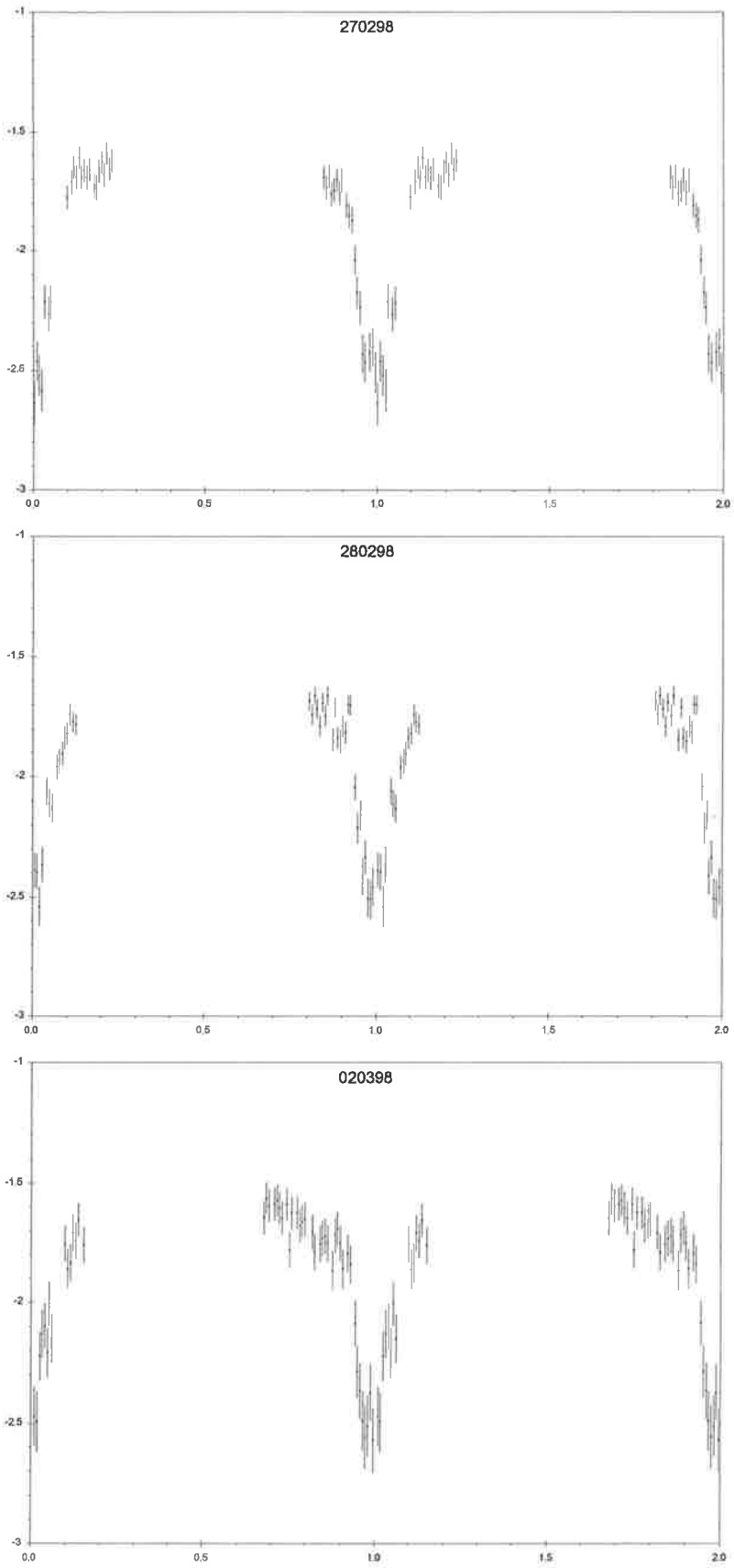

Figure 7.6 continued
Woomera white-light photometry of Cen 2.
Ordinate is differential magnitude, abscissa is orbital phase.

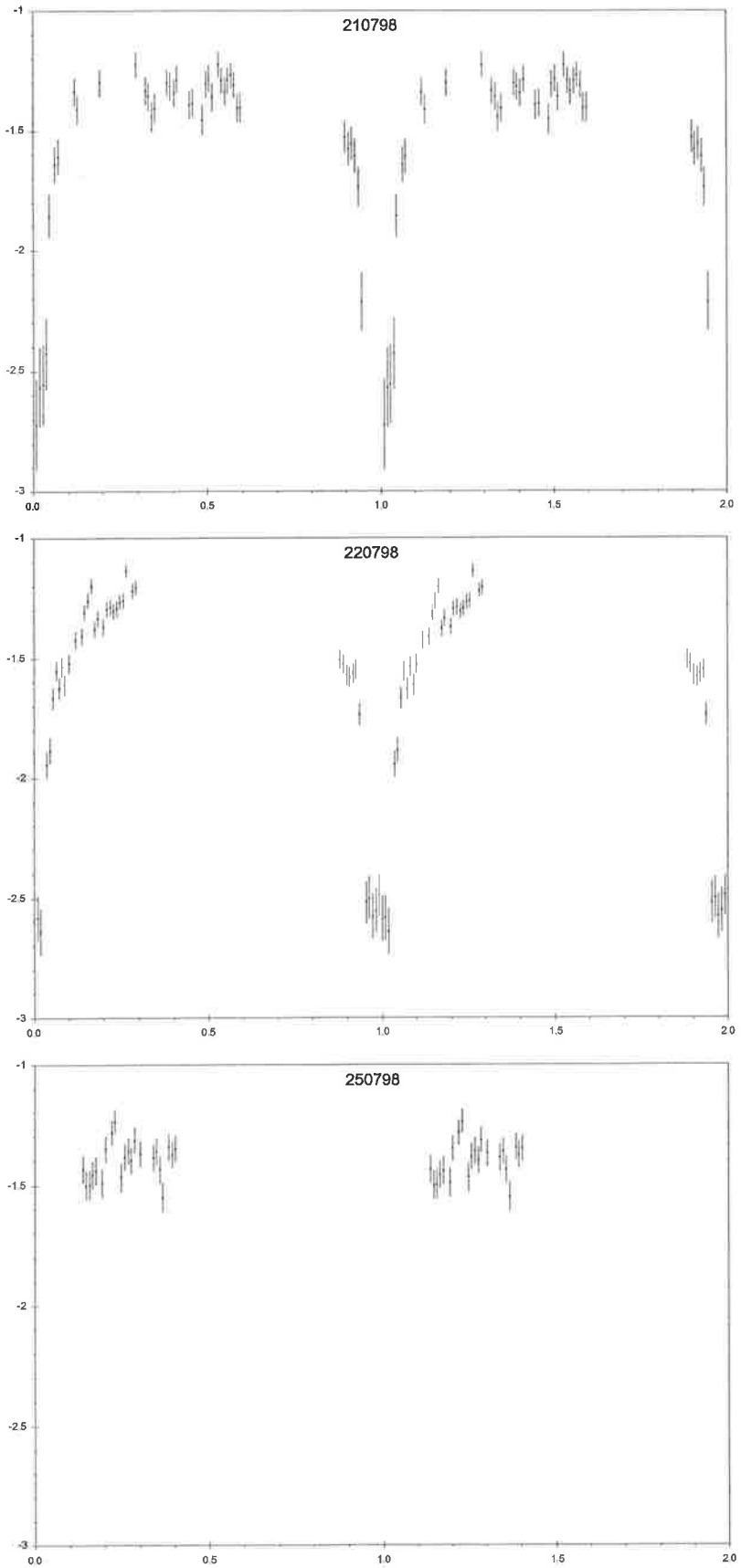

Figure 7.6 continued
Woomera white-light photometry of Cen 2.
Ordinate is differential magnitude, abscissa is orbital phase.

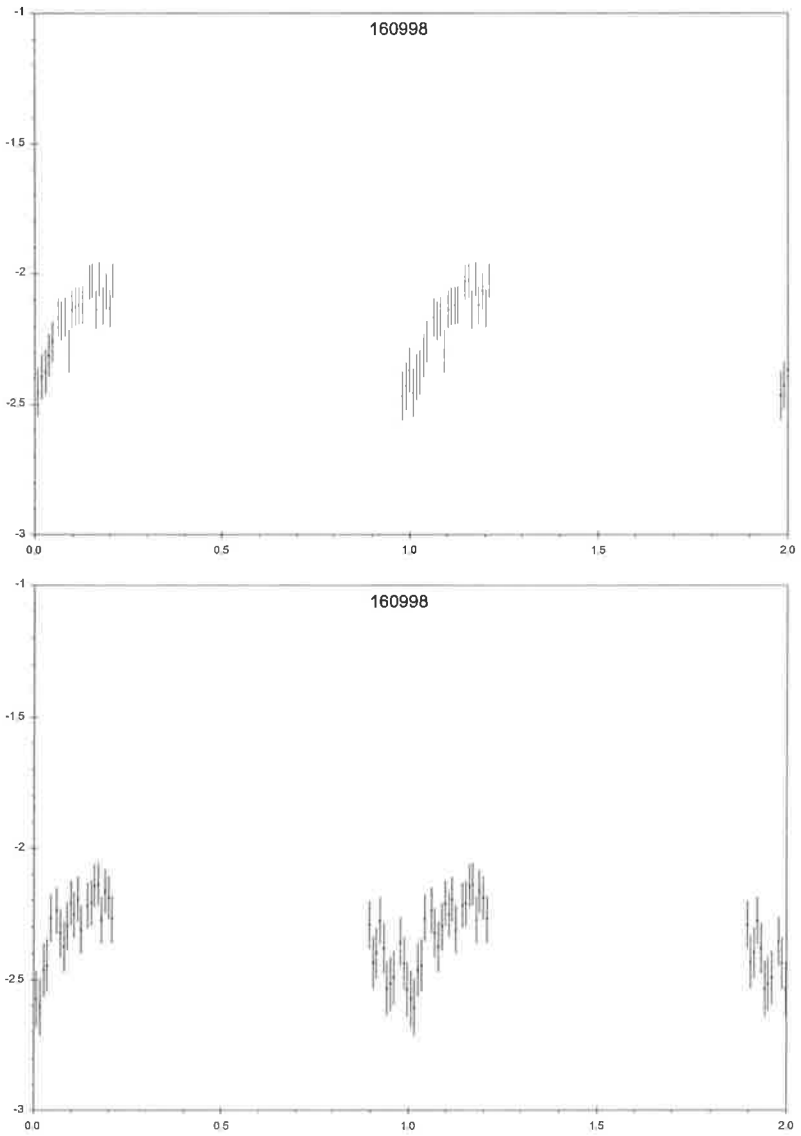

Figure 7.6 continued
Woomera white-light photometry of Cen 2.
Ordinate is differential magnitude, abscissa is orbital phase.

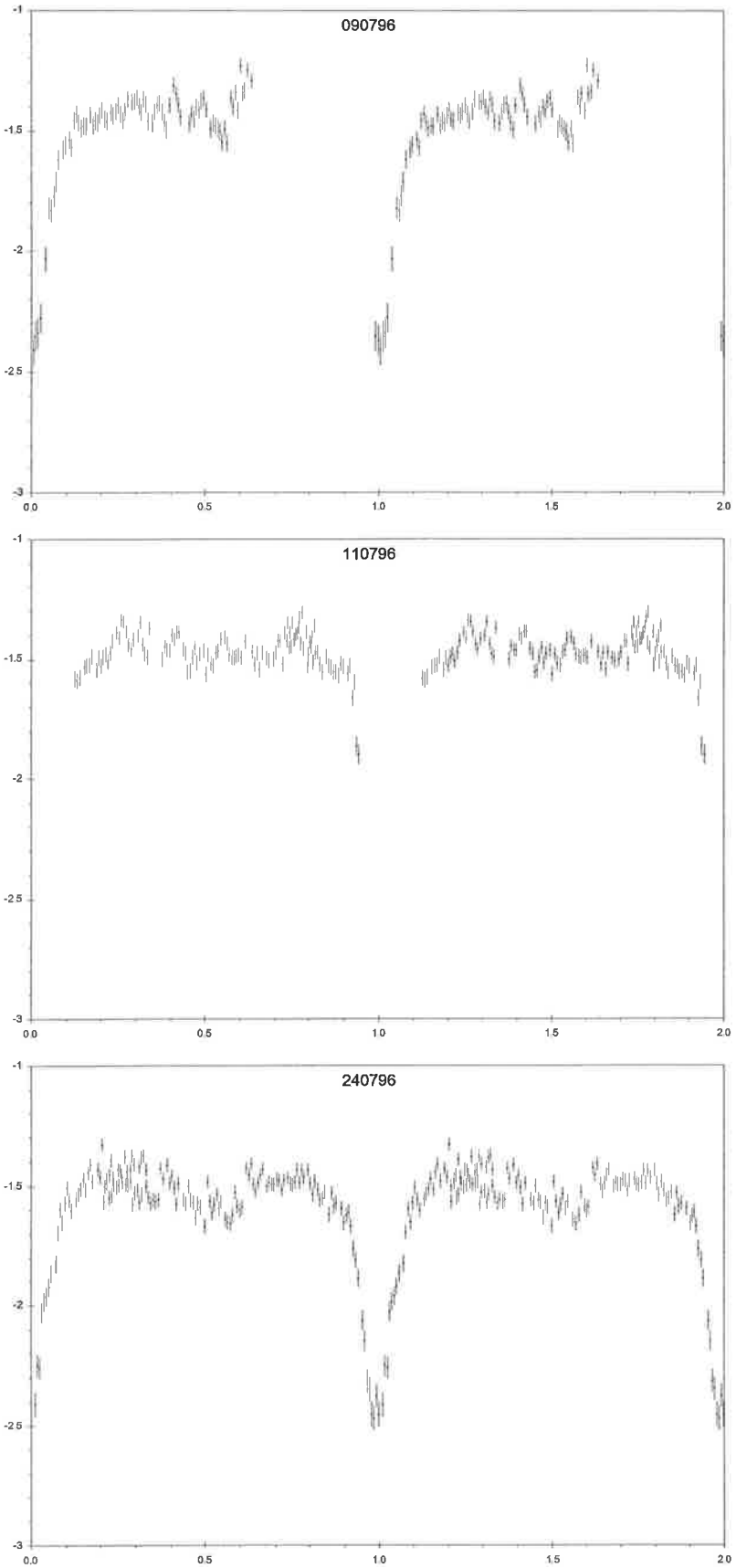

Figure 7.6 continued
SSO white-light photometry of Cen 2.
Ordinate is differential magnitude, abscissa is orbital phase.

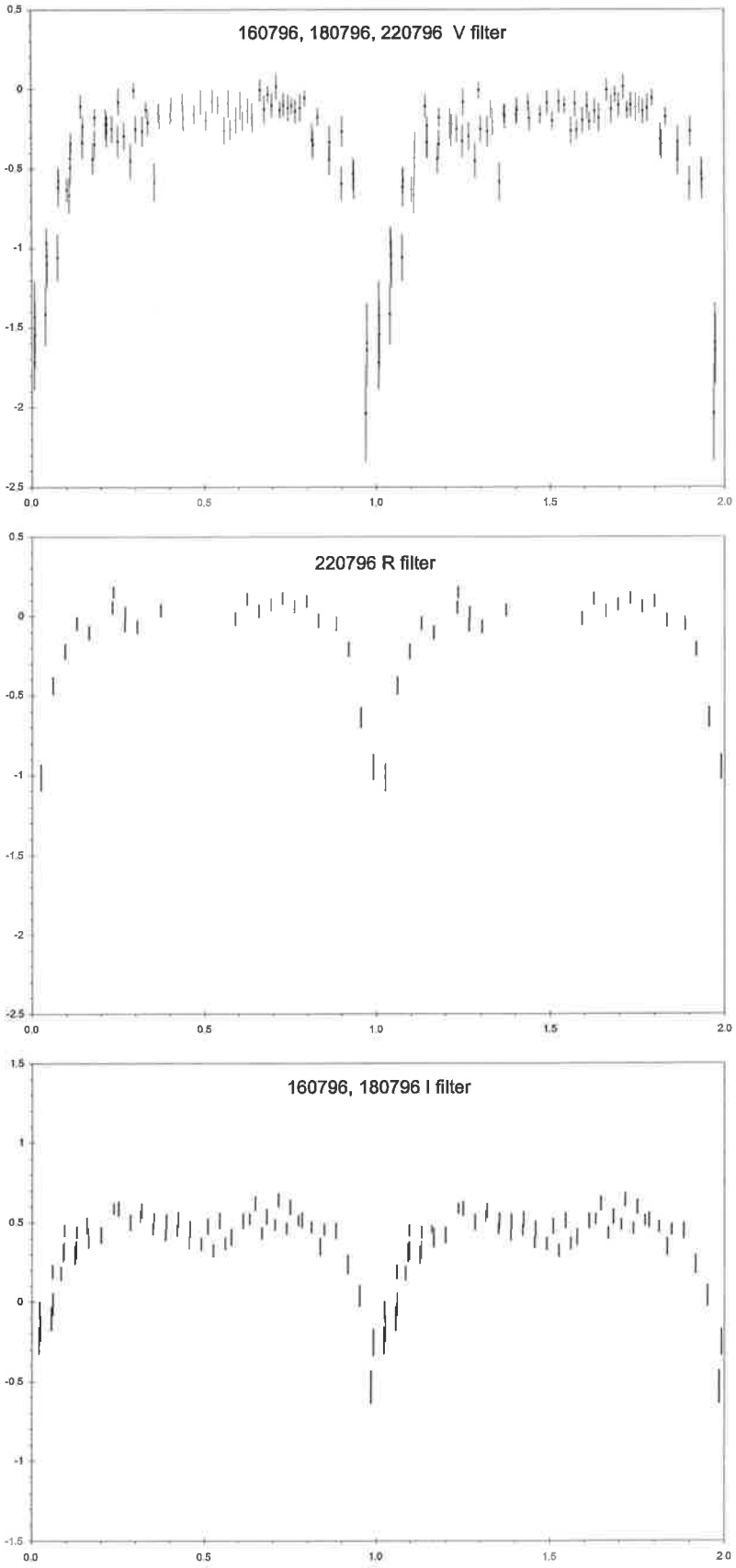

Figure 7.6 continued
SSO filtered photometry of Cen 2.
Ordinate is differential magnitude, abscissa is orbital phase.

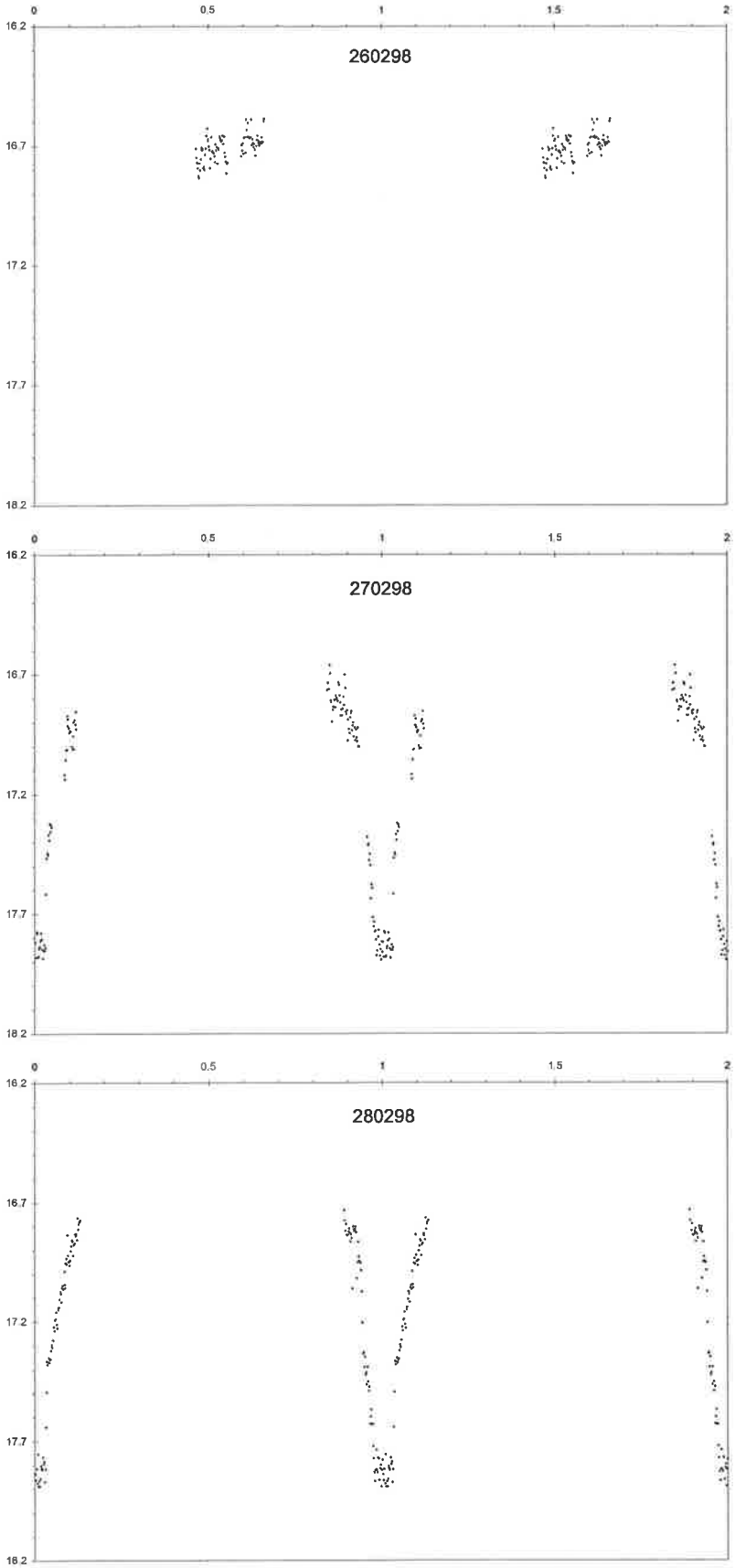

Figure 7.6 continued
CTIO V-band photometry of Cen 2.
Ordinate is calibrated magnitude, abscissa is orbital phase.
Note: no error estimates.

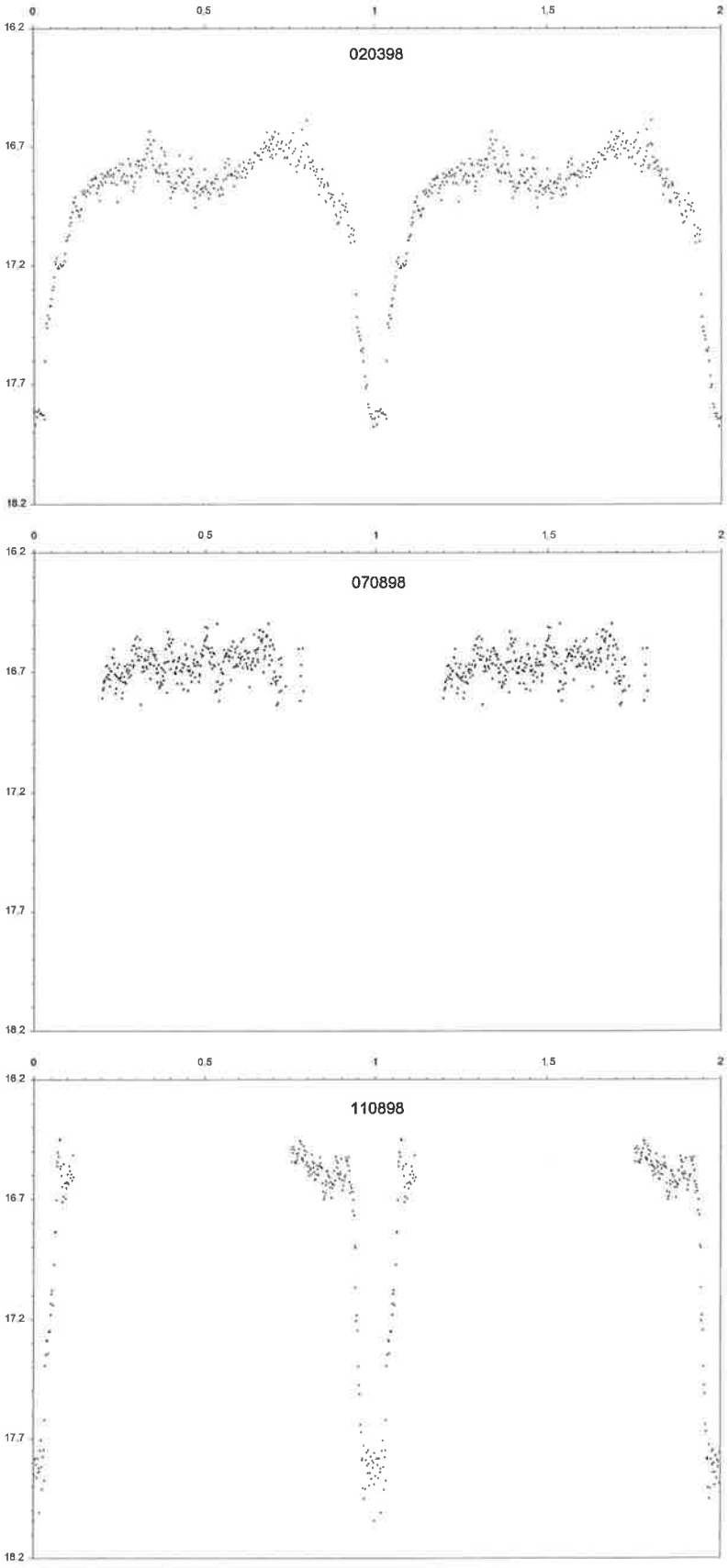

Figure 7.6 continued
CTIO V-band photometry of Cen 2.
Ordinate is calibrated magnitude, abscissa is orbital phase.
Note: no error estimates.

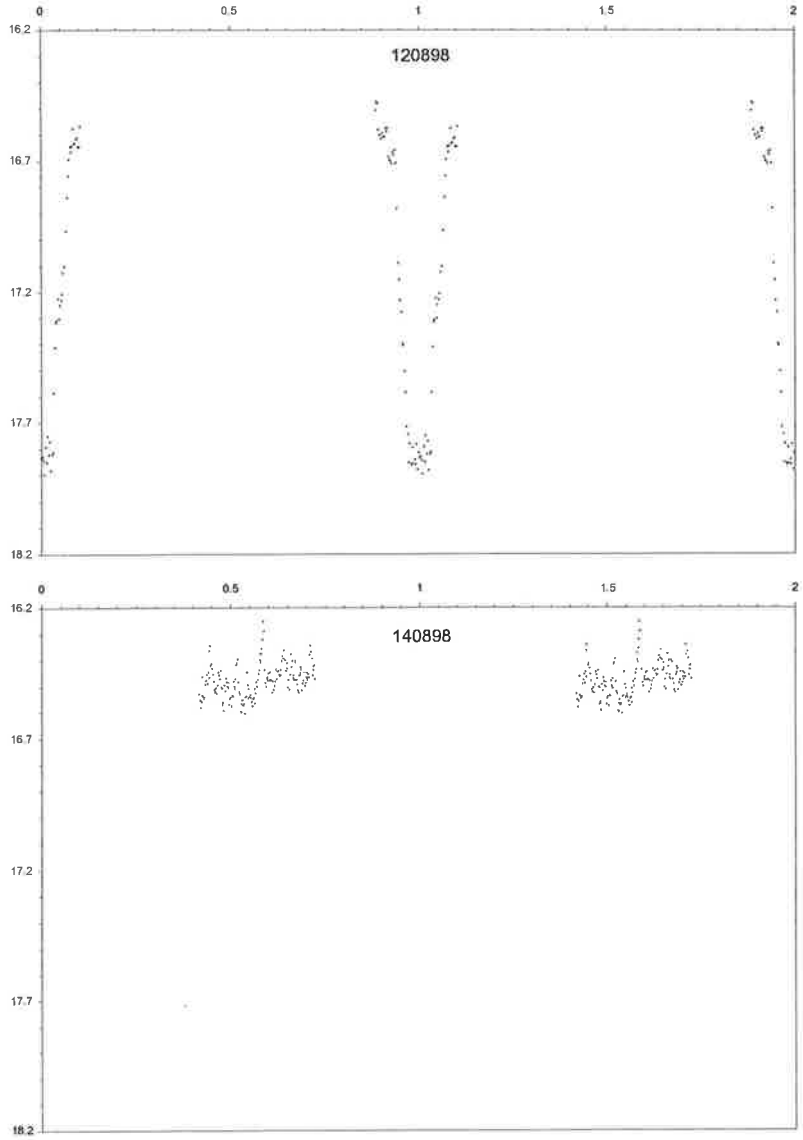

Figure 7.6 continued
CTIO V-band photometry of Cen 2.
Ordinate is calibrated magnitude, abscissa is orbital phase.
Note: no error estimates.

CHAPTER 8. EXPERIMENTAL RESULTS: PHOTOMETRY OF AX J2315-592

8.1 Discovery and X-ray behaviour

AX J2315-592 (also known as CP Tuc) was discovered serendipitously during ASCA observations of the galaxy IRAS 23128-5919, on UT 13:20 2/11/1995 to 20:50 3/11/1995 (Misaki *et al.*, IAUC 6260). At that time, it was detected at a flux of approximately 1.5 mCrab in the energy range 2-10 keV by the Gas Imaging Spectrometers aboard ASCA. Figure 8.0 shows satellite images of the field (from heasarc.gsfc.nasa.gov).

The 34 ksec of observations analysed showed clear periodicity besides that due to the 96-minute orbital period of the satellite, and the consequent interference with observations due to presence of the Earth. A prominent period of 89.34 ± 0.8 minutes (5360.4 ± 47 s) was found. Phasing of the X-ray data gave a roughly sinusoidal waveform in all energy bands, with the amplitude decreasing towards higher energies- the reverse of the usual case for AM Her types (Misaki *et al.* 1996). The 1'-radius error circle was centred at 23:15:18.4 -59:10:27 (J2000.0).

8.2 Optical identification and spectroscopy

Thomas and Reinsch (IAUC 6261) observed the two brightest stars (each about 16^{th}-17^{th} mag.) in the ASCA error circle, and, via spectroscopy, determined the northernmost of the pair to be the optical counterpart. The optical position was found to be 23:15:18 -59:10:42 (J2000.0).

Further time-resolved spectroscopy was obtained at the ESO/MPI 2.2-m telescope (Thomas and Reinsch 1996, hereafter TR96). These data cover 380nm-912nm and show typical magnetic CV emission lines and allow RV determinations for both the broad and narrow components of the Hα emission line to be obtained, from which the orbital period of the system may be derived. Also obtained were two nights of Gunn i-band photometry. In the faint portion of the light curve, a rising red continuum is seen, although no features of a late-type star are seen.

8.3 Woomera photometry

AX J2315-592 was first observed at Woomera on the night of 20-21/11/1995 (local dates). The C14 and ST-6 were used, with all time-series data being taken with the clear filter,

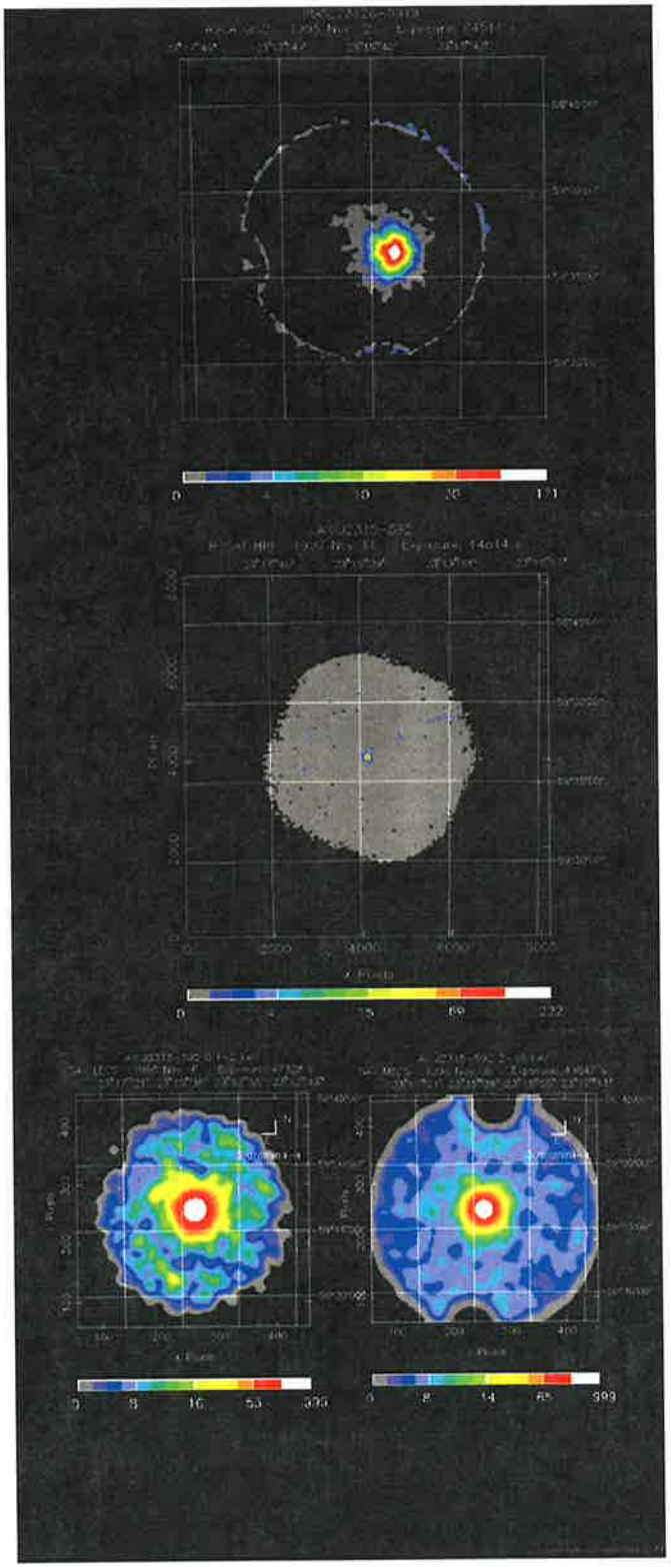

Figure 8.0

Satellite images of the CP Tuc field.
Top: IRAS image, showing the source IRAS 23128-5919 (a galaxy). This is an infra-red view of the region, and the galaxy is the dominant source.
Middle: ROSAT High-Resolution Imager (HRI) view. The CV dominates this extreme ultra-violet image.
Bottom: BeppoSAX views at two energies. The CV is the main source, and was discovered during an earlier ASCA observation of the IRAS galaxy seen in the top panel.

and with integration times in the range 75-120s in general. Temporal resolution may be taken to be 120-160s. Table 8.1 is log of the Woomera photometry.

Figure 8.1 (from co-added ST-6 images) shows the field, and the C and K stars used in the differential reduction are marked. It is to be noted that a different set of C and K stars were used for the low-state data, since several images were co-added in order to improve the signal on the now-faint CV. Figure 8.2 shows the individual nights' data as time-series, allowing one to see cycle-cycle variations when present. The same data are presented again in Figure 8.3, this time phased with the best-fit ephemeris as described in Section 8.4.

Of interest is the occasional quite significant change, from one orbital cycle to the next, of maximum or minimum brightness, and amplitude, of the light curve (see especially data for 171295 and 181295). This may be due to short-term accretion rate variations, or perhaps slight wandering of the accretion region in magnetic latitude (the latter causing slight variation in the viewing angle to the magnetic field lines near the accretion region, with a resultant change in optical intensity without change in phase of the maximum of this intensity). These two may be related, since the eventual location in magnetic latitude of the accretion region depends somewhat on the extent of penetration of the WD field by the accretion stream, and this will be affected by the accretion rate.

In both these cases, the error bars are obtained from the scatter in a given night's C-K_n data. Figure 8.4 is a phase plot of all the Woomera data. Included in Figure 8.4 is a plot of the low-state data binned in phase with bins of width 0.1. The plot *may* show the effect of ellipsoidal modulation of the secondary star. However, the data are quite noisy and rather more data would be preferred in order to examine this further. It must be noted that the phase bin around 0.25 is anomalously low (it should be a local maximum if the variation is due to ellipsoidal modulation), but since there are only four data points in that bin, this may not be a major problem. Indeed, with the small number of data used to prepare that plot, the choice of position of bin centres will somewhat influence the shape of the binned phase plot.

The scatters in individual night's C-K_n time-series were used to prepare Figure 8.5, which demonstrates the expected decrease in photometric accuracy with the measurement of increasingly faint stars. Further, it shows that the CV is significantly variable (with respect to measurement errors), except when in the low state. However, note that there are likely to be intermediate brightness states for the CV which were not observed. Figure 8.6 is a plot of all Woomera data versus HJD.

Table 8.1

Log of Woomera photometry

date	**HJD start**	**duration (mins)**	**exposures (s)**
201195	2450042.0034	90	75
211195	2450043.0376	125	75
121295	2450063.9759	130	75
151295	2450066.9998	130	75
181295	2450069.9745	190	75
160196	2450098.9777	130	75
180196	2450100.9779	130	75
170696	2450252.2625	130	90
131096	2450370.1896	130	100
141096	2450370.9815	380	100
291097	2450751.0552	90	120
311097	2450753.0108	135	120
021197	2450755.0556	90	150
051197	2450758.0680	95	150
170998	2451074.1667	210	480
200998	2451077.0996	240	480
230998	2451080.0998	230	480
240998	2451081.0573	90	480

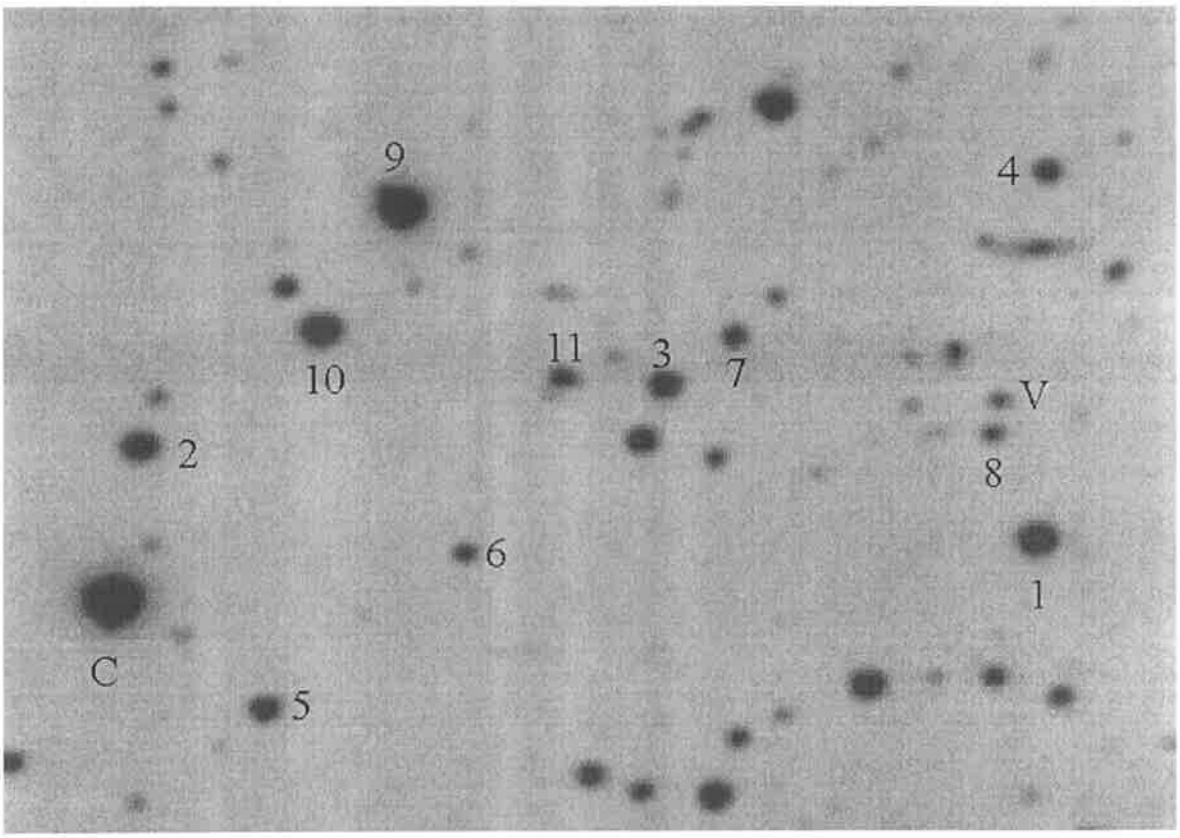

Figure 8.1a

Cropped Woomera ST-6 image showing the stars used in the active-state differential reduction.

V = variable star; C = comparison star; check stars are numbered.

North is to the top, east is to the left.

(Note that the CV was in its low state when the source images were taken).

Approximate field centre and size: (J2000.0) 23:15:40 -59:10:42 6.5' wide 5.5' high.

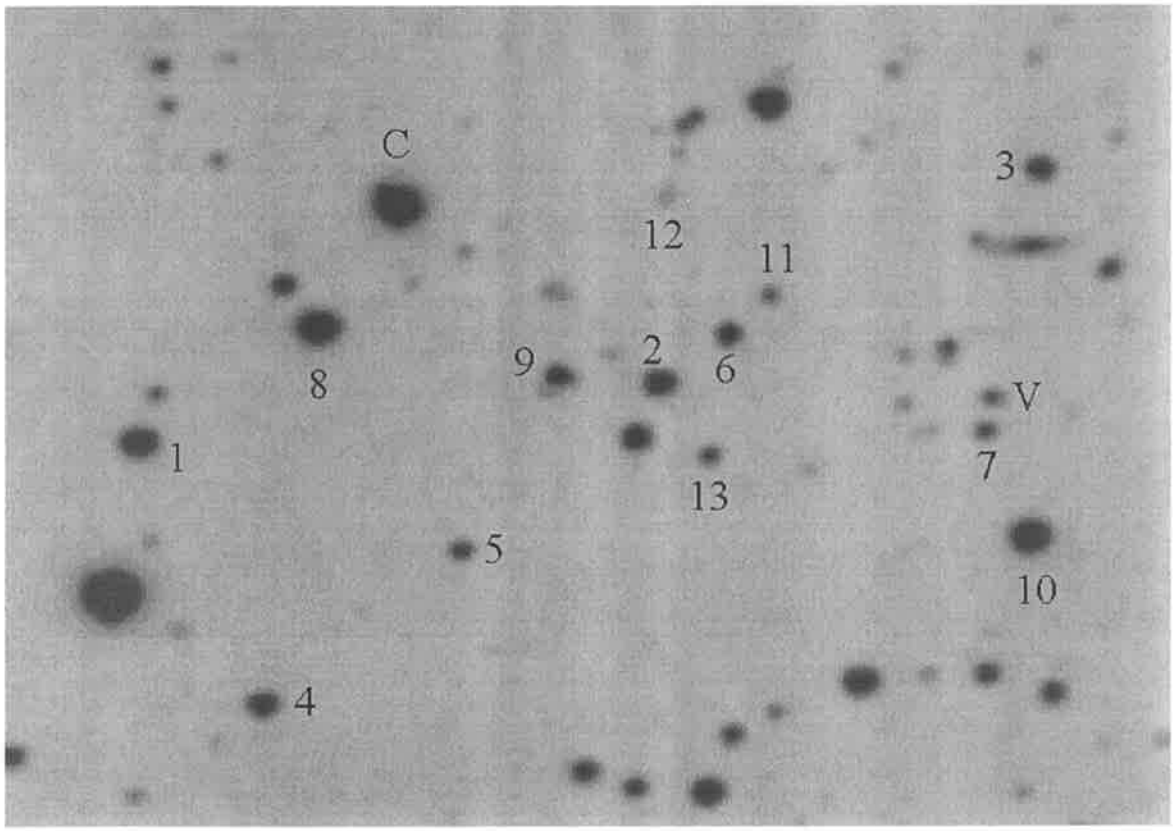

Figure 8.1b

Cropped Woomera ST-6 image showing the stars used in the low-state differential reduction.
V = variable star; C = comparison star; check stars are numbered.
North is to the top, east is to the left.
(Note that the CV was in its low state when the source images were taken).

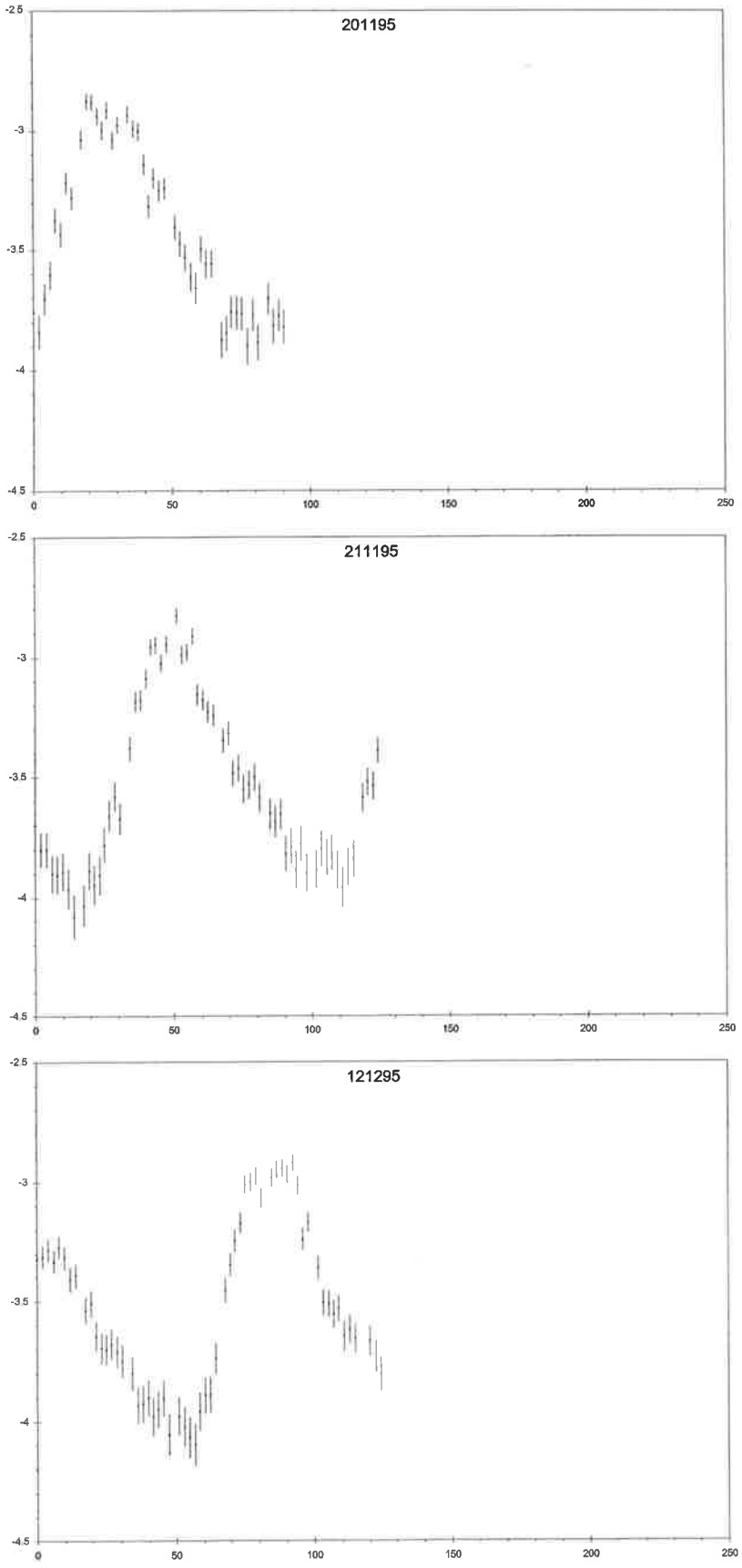

Figure 8.2

Woomera white-light photometry;
ordinate is differential magnitude, abscissa is time (in minutes).

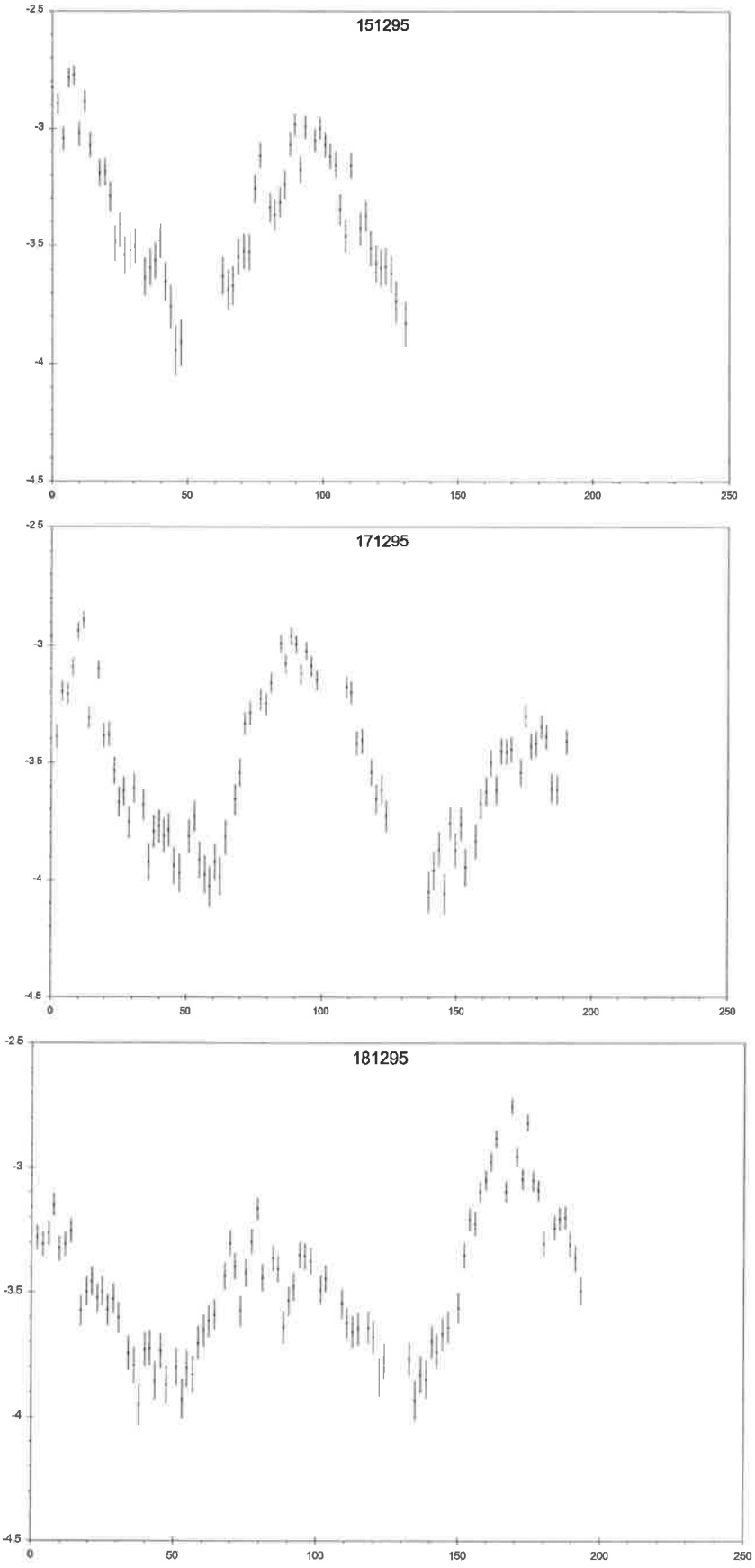

Figure 8.2 continued
Woomera white-light photometry;
ordinate is differential magnitude, abscissa is time (in minutes).

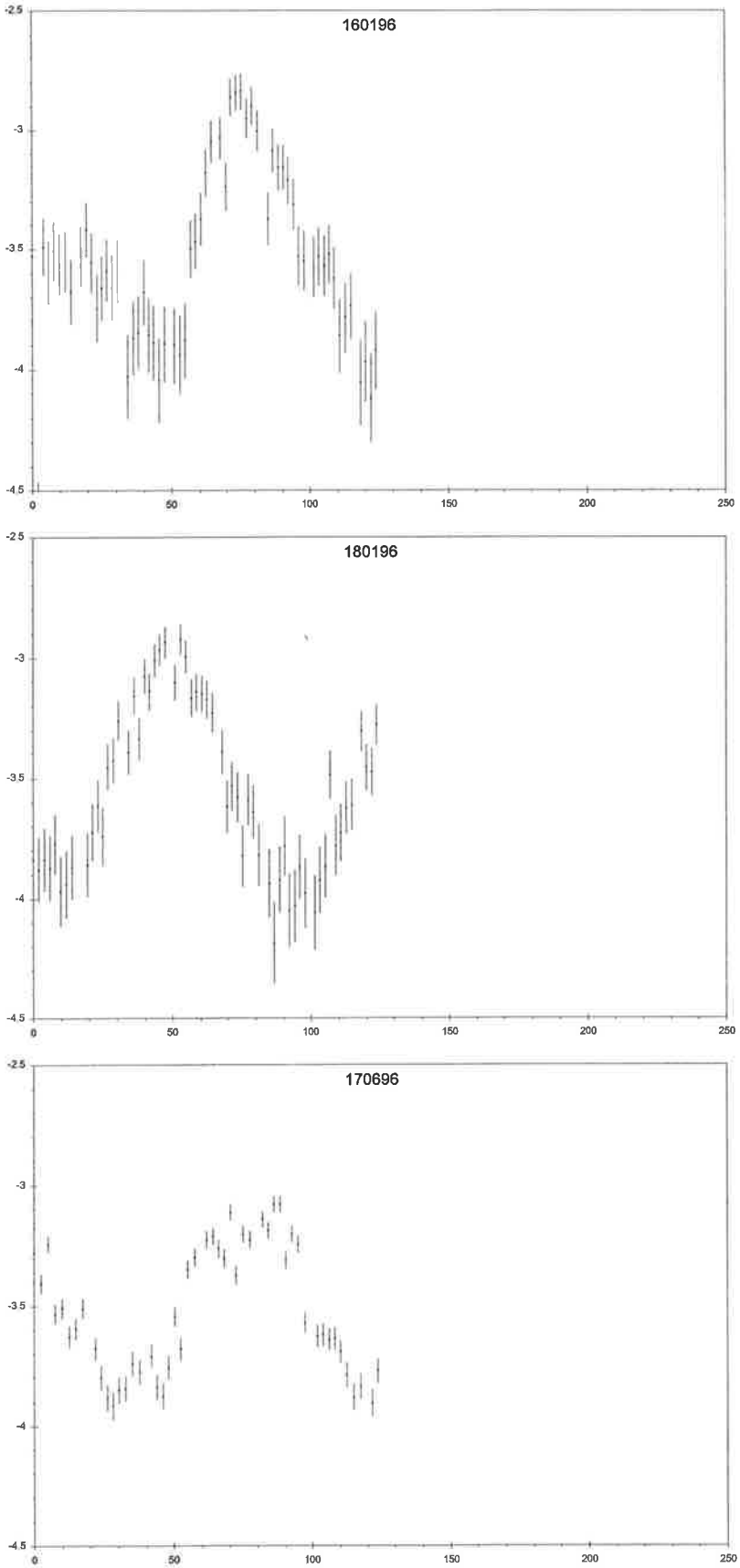

Figure 8.2 continued
Woomera white-light photometry;
ordinate is differential magnitude, abscissa is time (in minutes).

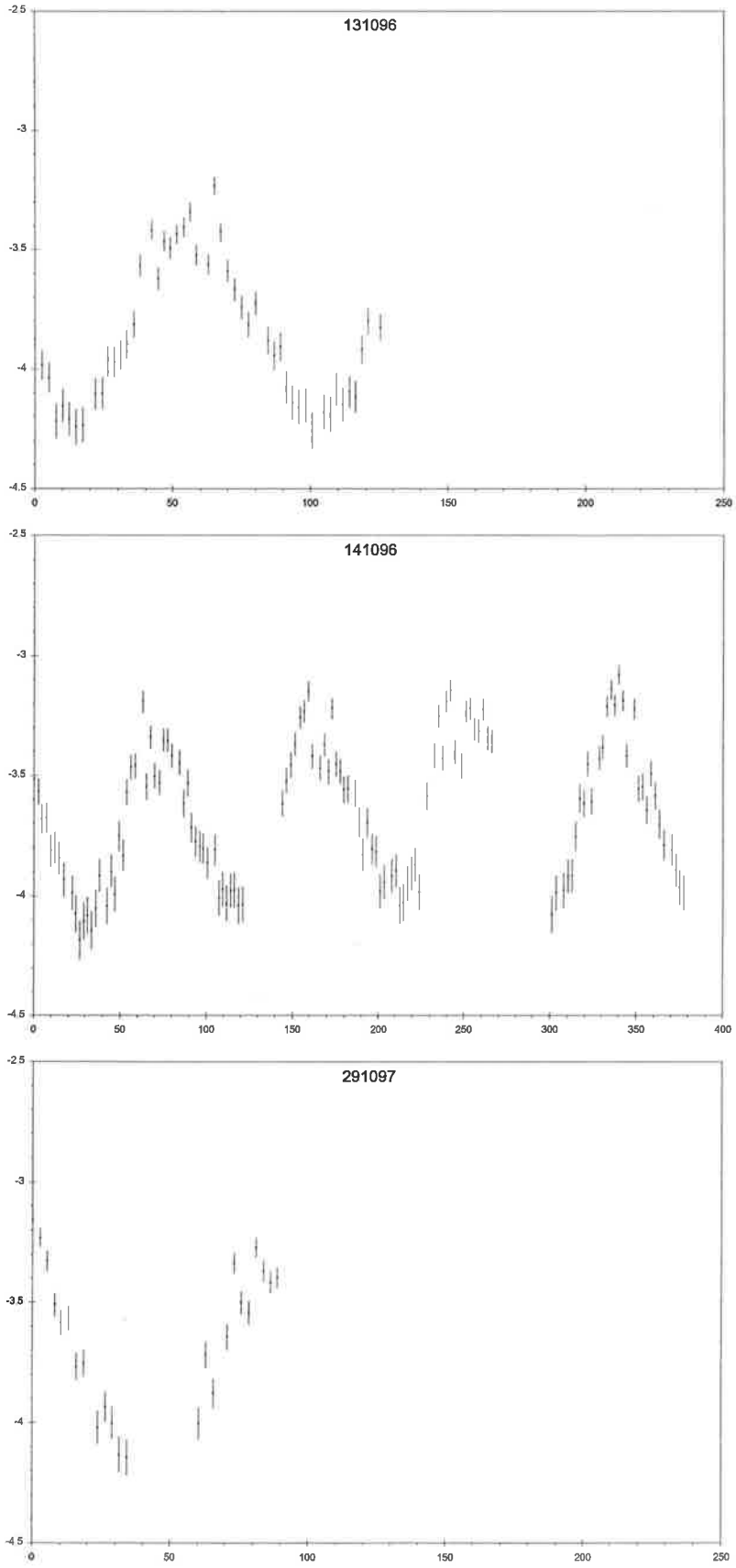

Figure 8.2 continued
Woomera white-light photoametry;
ordinate is differential magnitude, abscissa is time (in minutes).

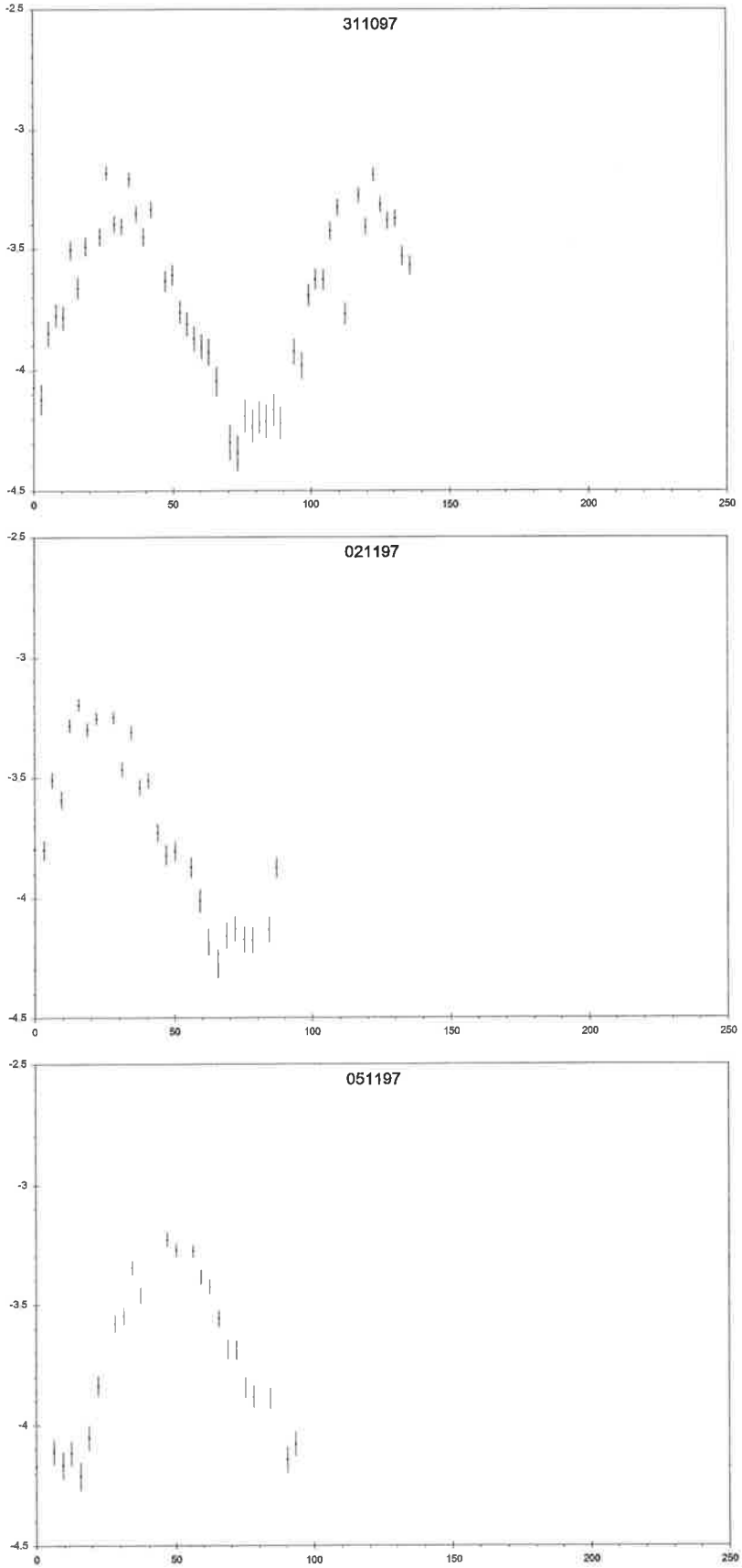

Figure 8.2 continued
Woomera white-light photometry;
ordinate is differential magnitude, abscissa is time (in minutes).

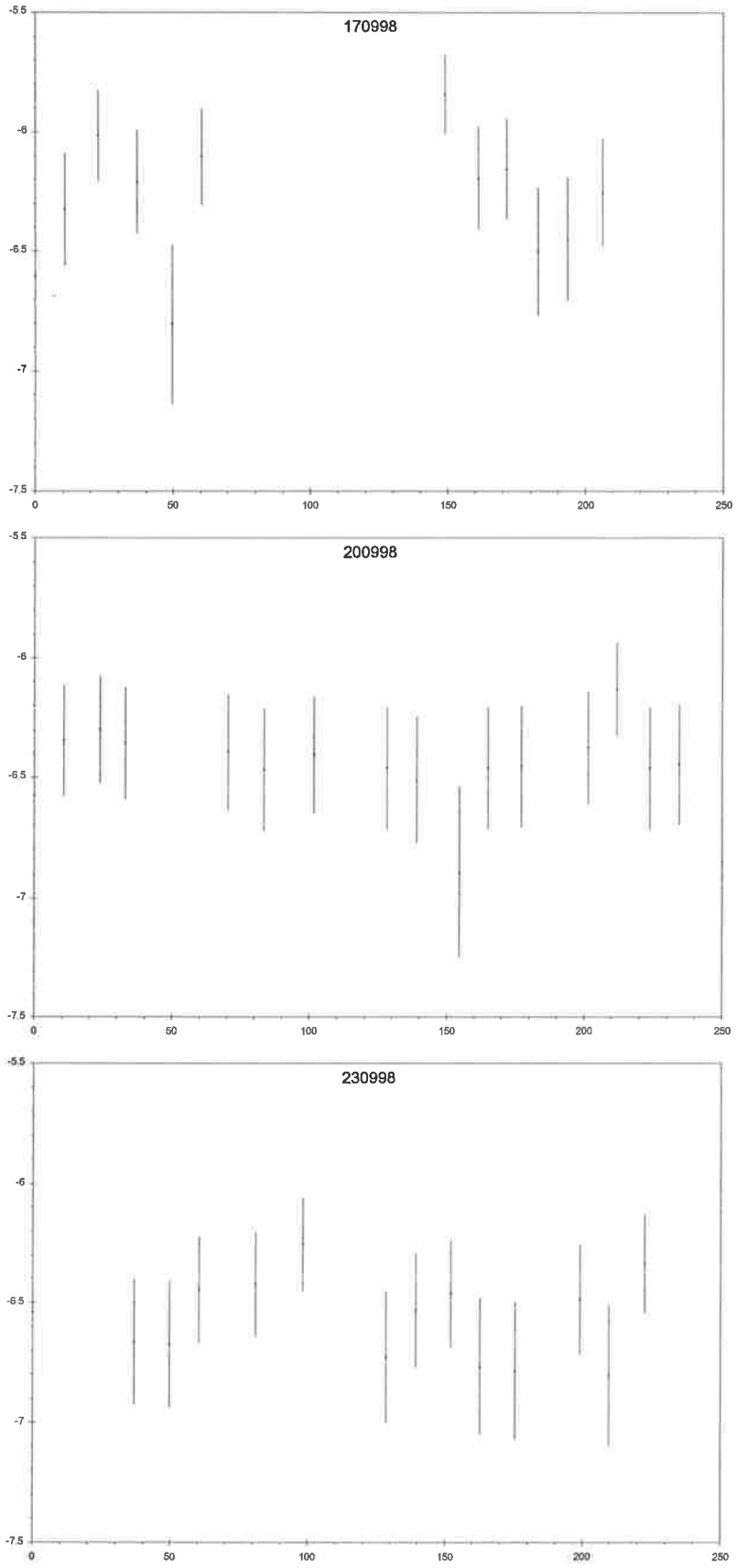

Figure 8.2 continued
Woomera white-light photometry;
ordinate is differential magnitude, abscissa is time (in minutes).

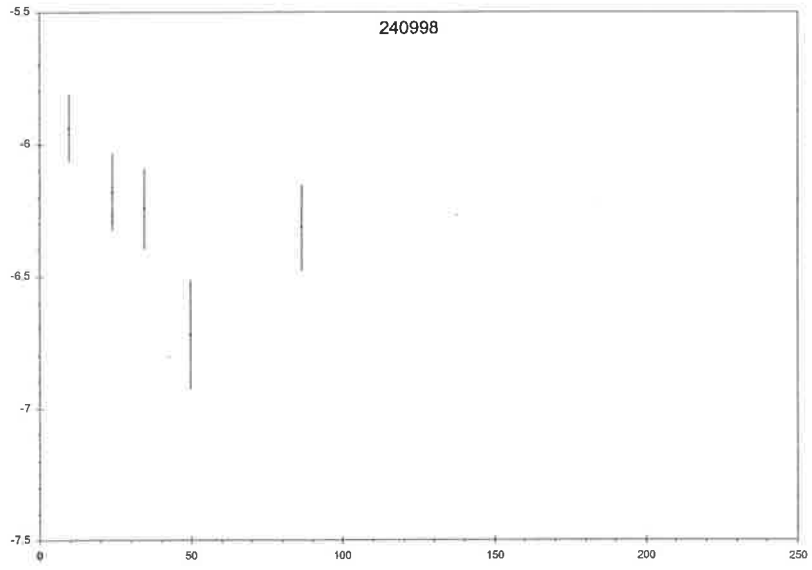

Figure 8.2 continued
Woomera white-light photometry;
ordinate is differential magnitude, abscissa is time (in minutes).

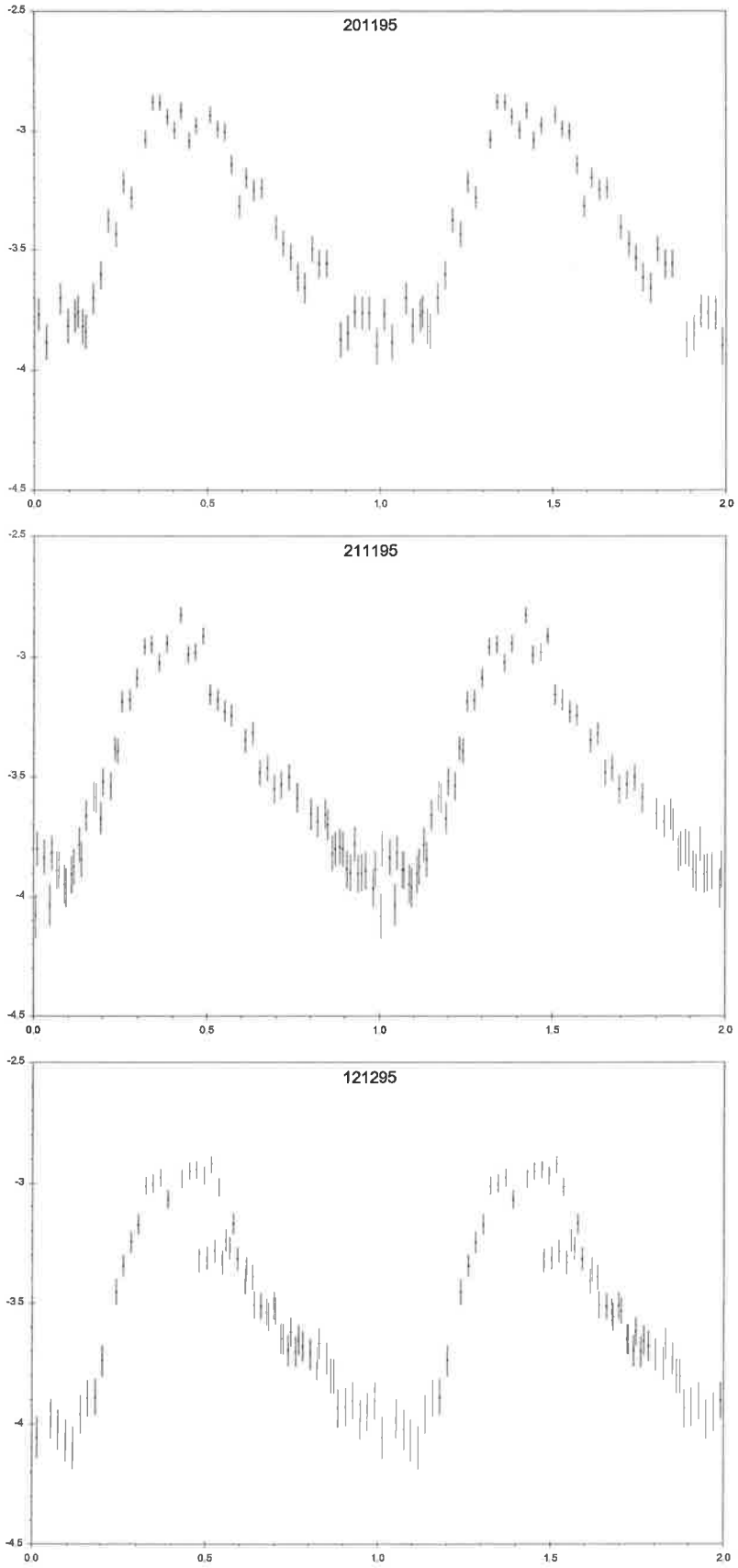

Figure 8.3
Woomera white-light photometry;
ordinate is differential magnitude, abscissa is orbital phase.

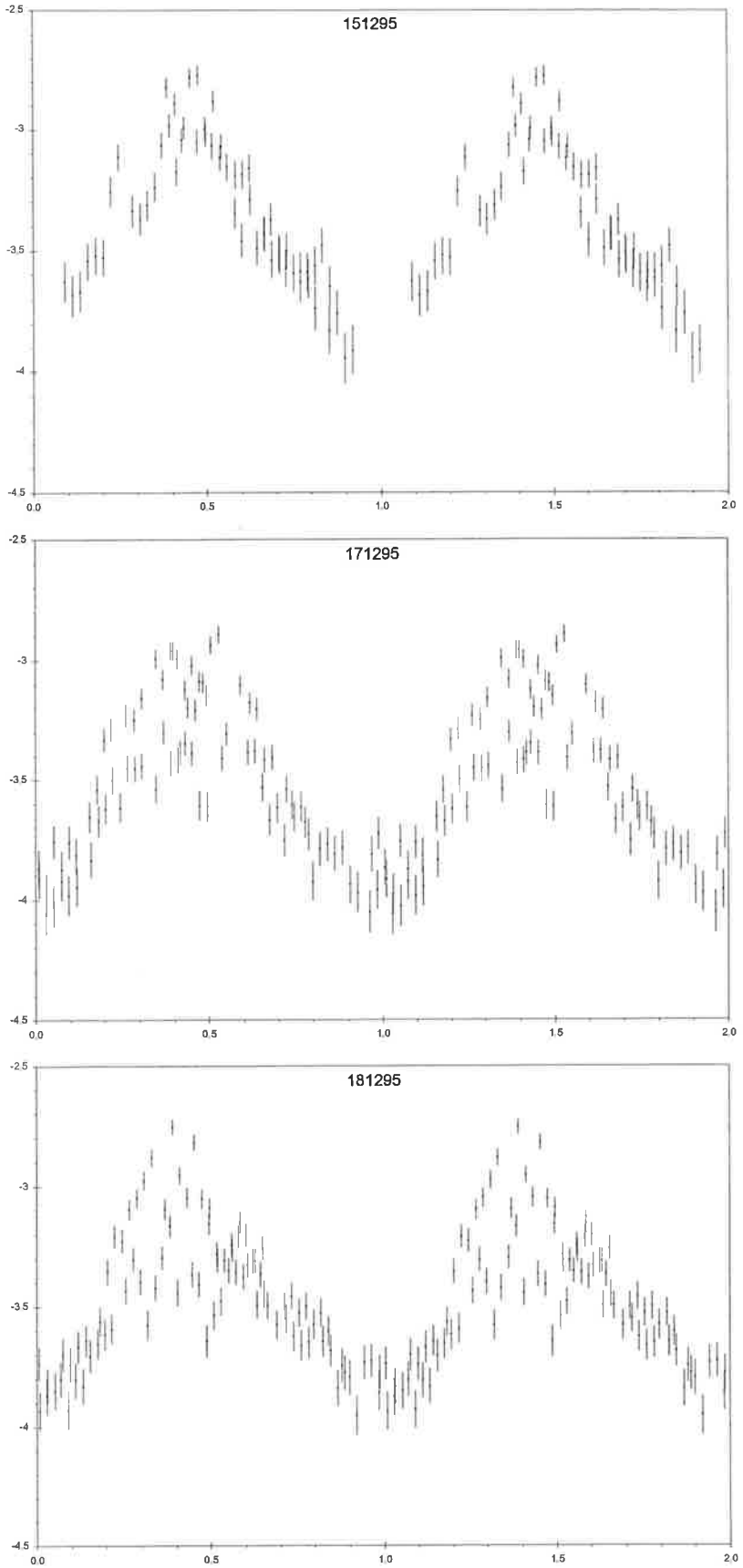

Figure 8.3 continued
Woomera white-light photometry;
ordinate is differential magnitude, abscissa is orbital phase.

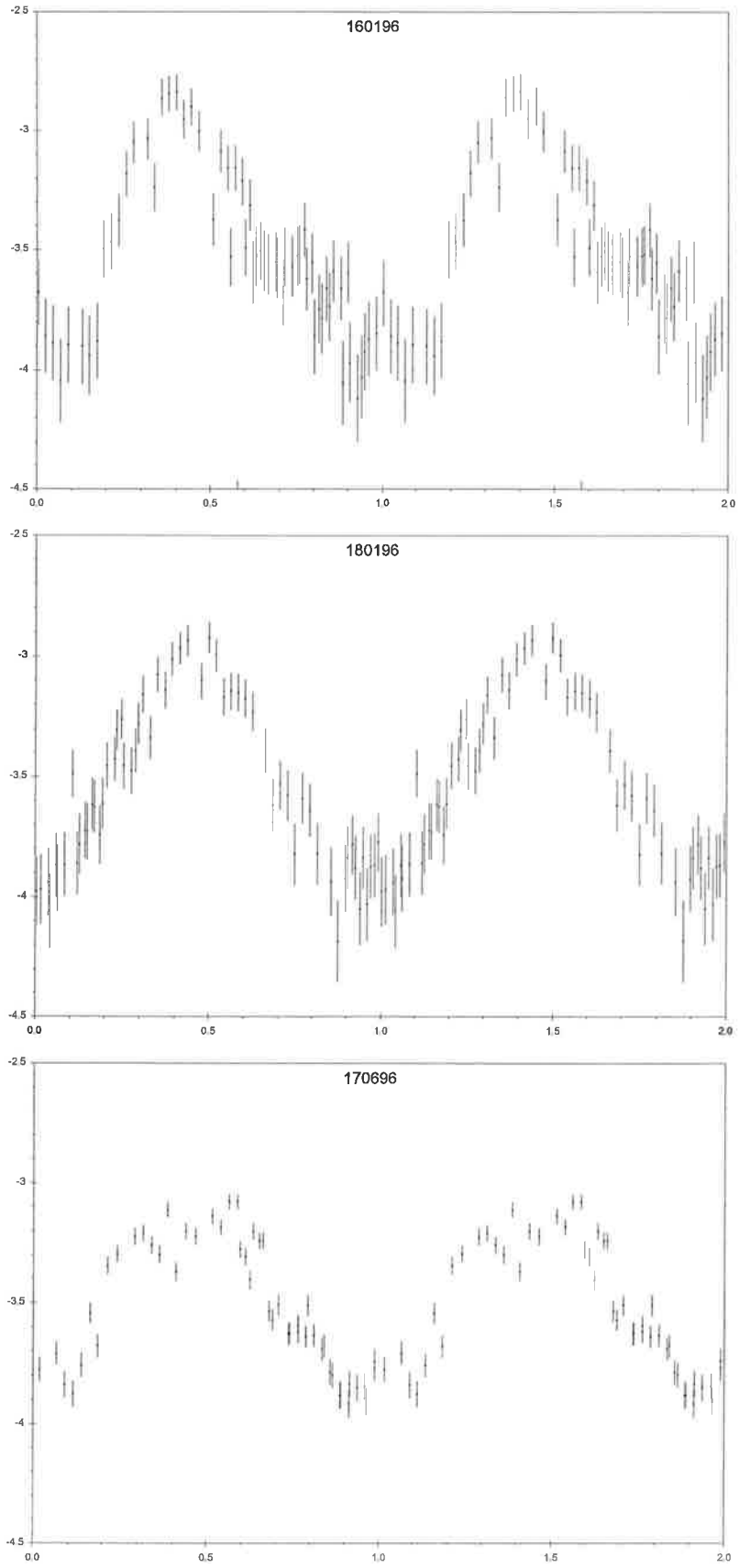

Figure 8.3 continued
Woomera white-light photometry;
ordinate is differential magnitude, abscissa is orbital phase.

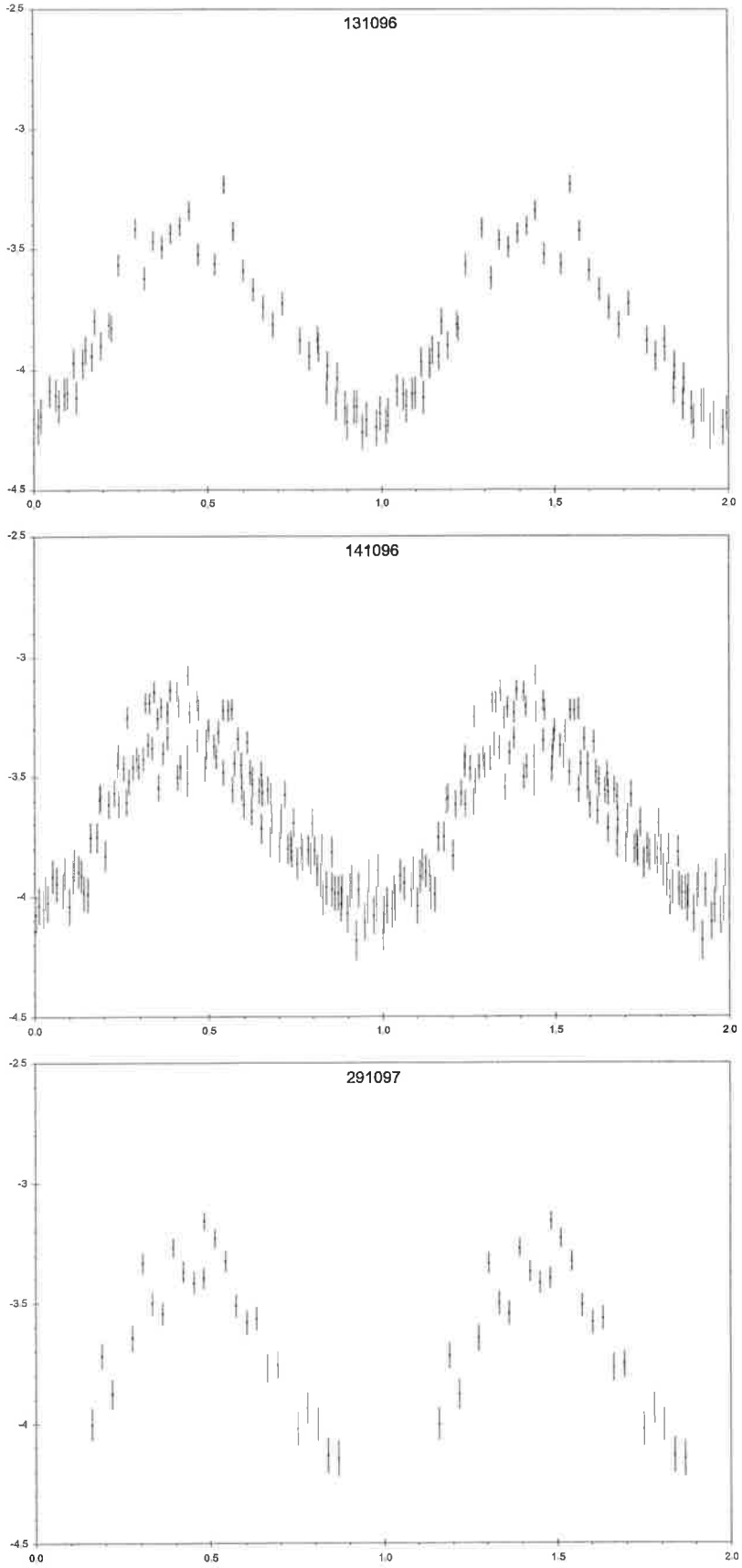

Figure 8.3 continued
Woomera white-light photometry;
ordinate is differential magnitude, abscissa is orbital phase.

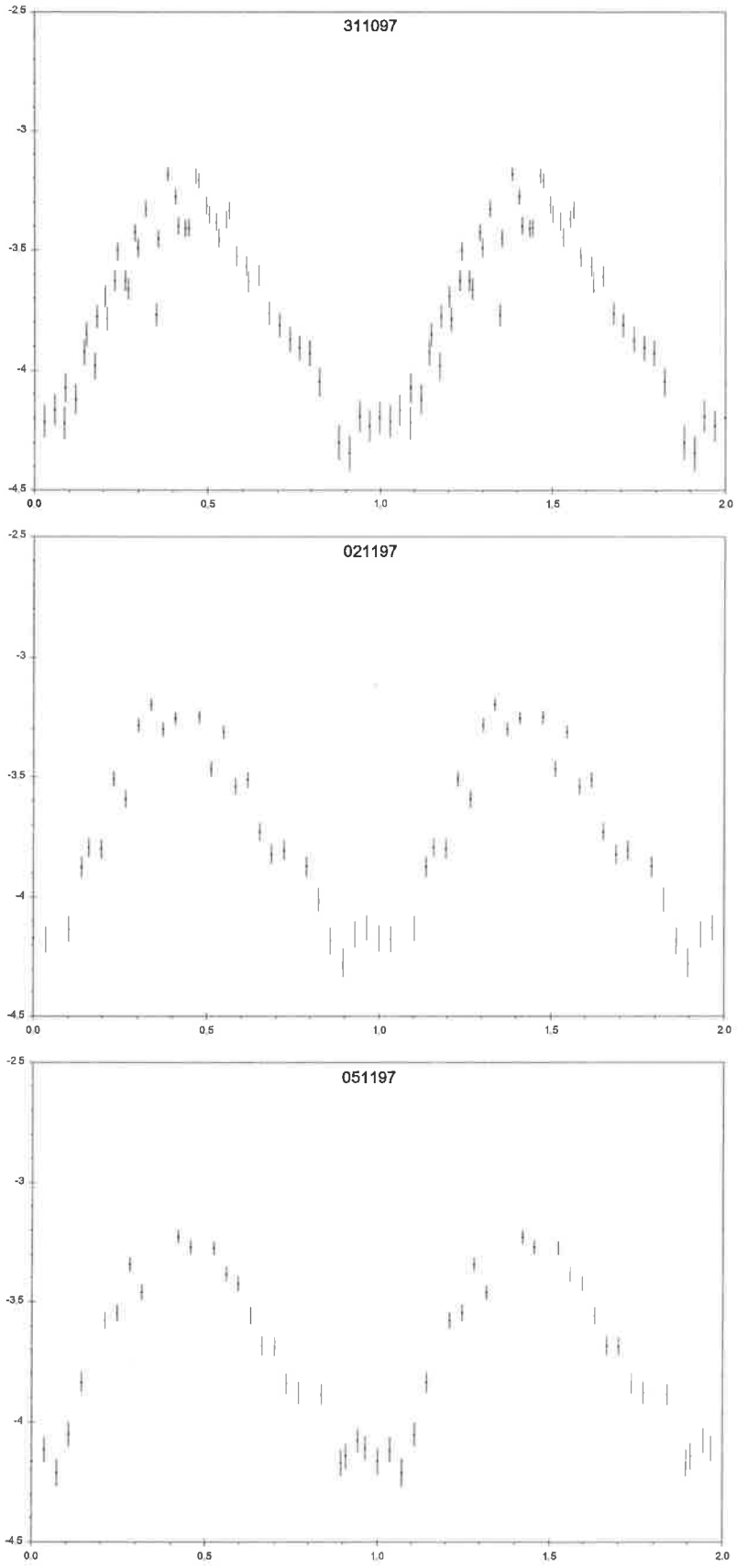

Figure 8.3 continued
Woomera white-light photometry;
ordinate is differential magnitude, abscissa is orbital phase.

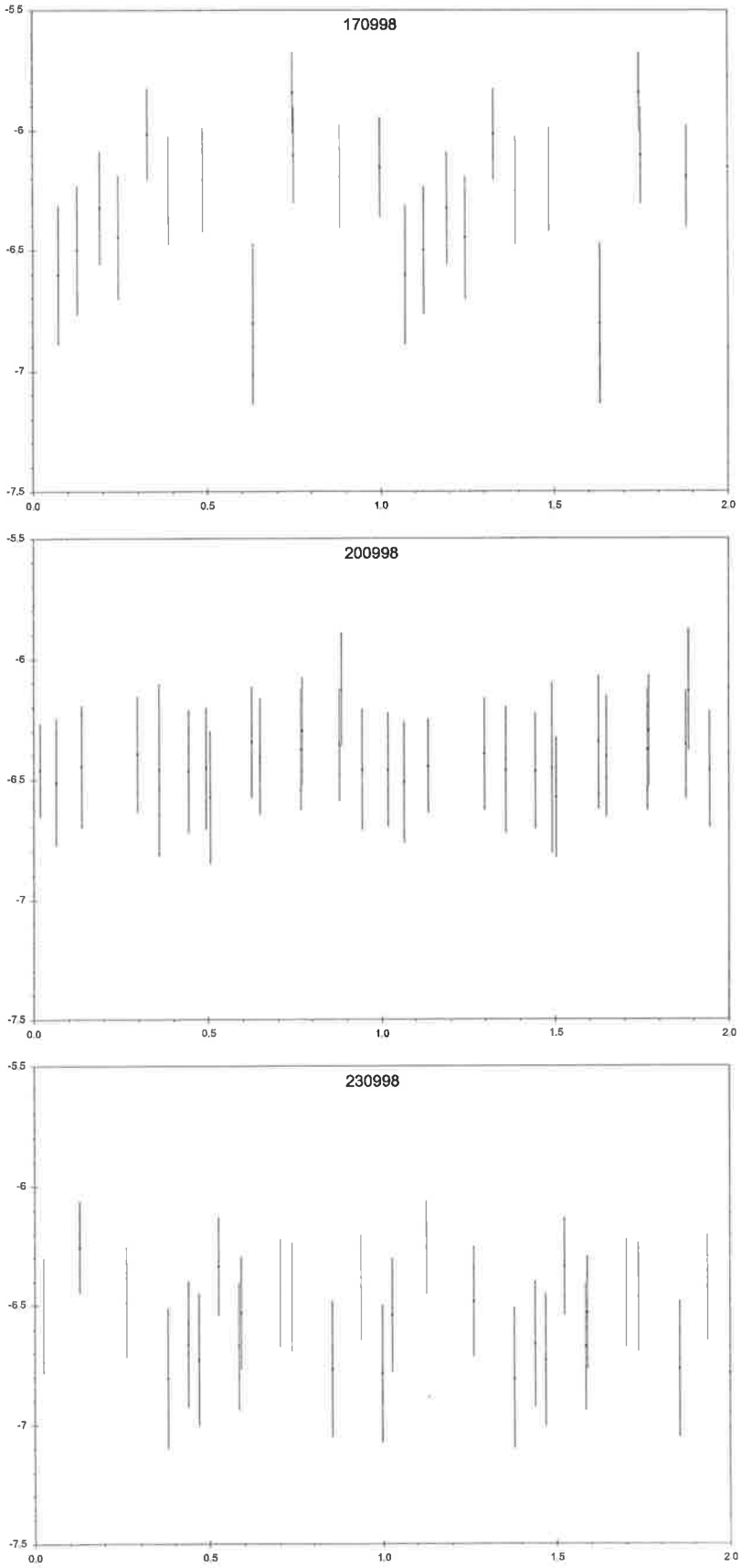

Figure 8.3 continued
Woomera white-light photometry;
ordinate is differential magnitude, abscissa is orbital phase.

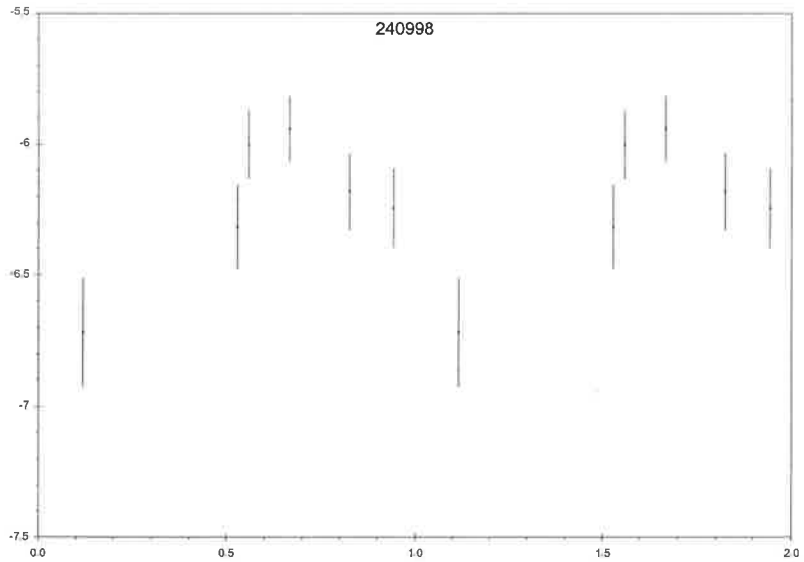

Figure 8.3 continued
Woomera white-light photometry;
ordinate is differential magnitude, abscissa is orbital phase.

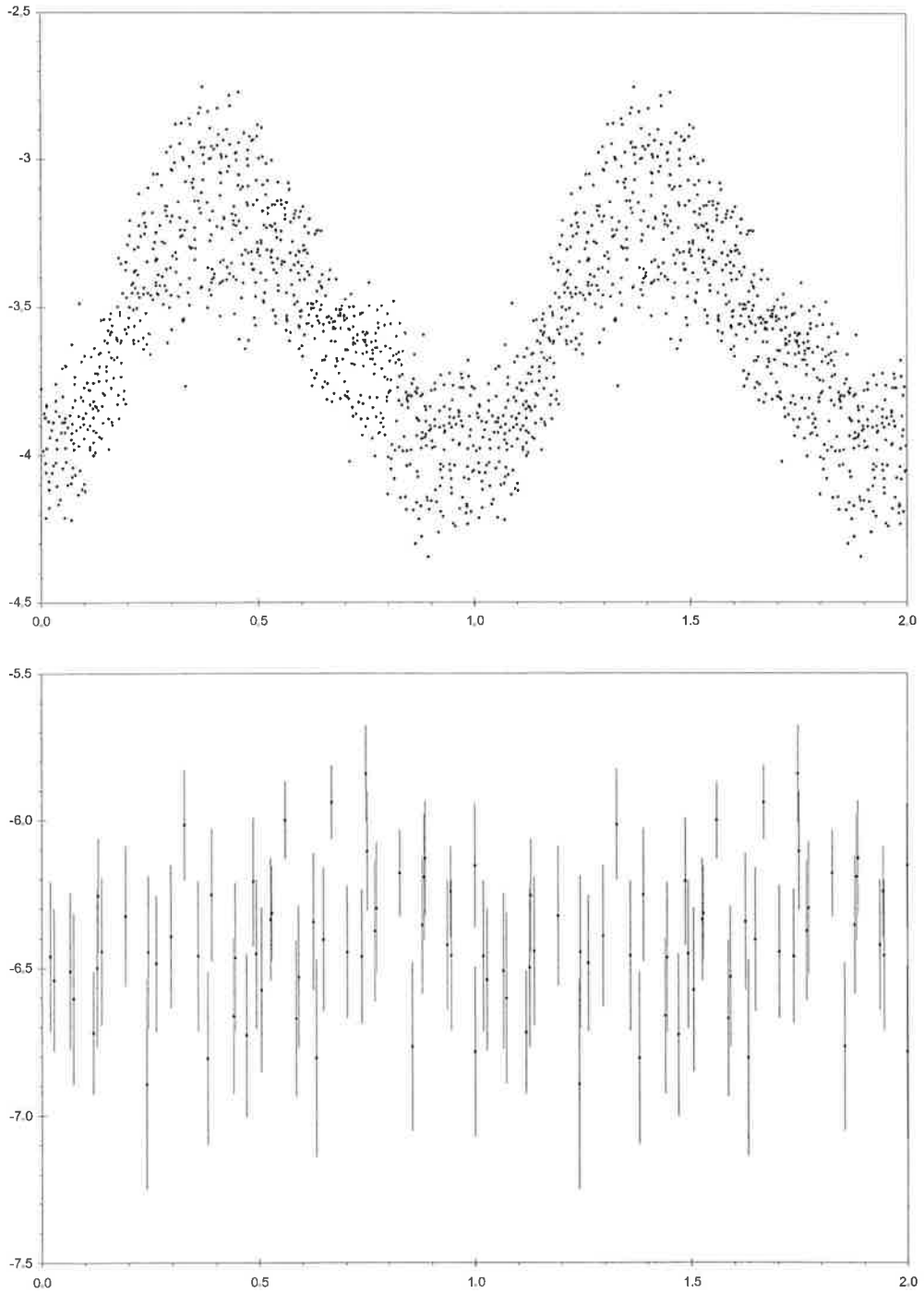

Figure 8.4

Woomera data phased at P_{orb} = 5342.31s.
Ordinate is differential magnitude, abscissa is orbital phase.
Upper panel: high-state data only. Lower panel: low-state data only.
Error bars are included for the latter to emphasise that the low-state data are much noisier than the active-state data.

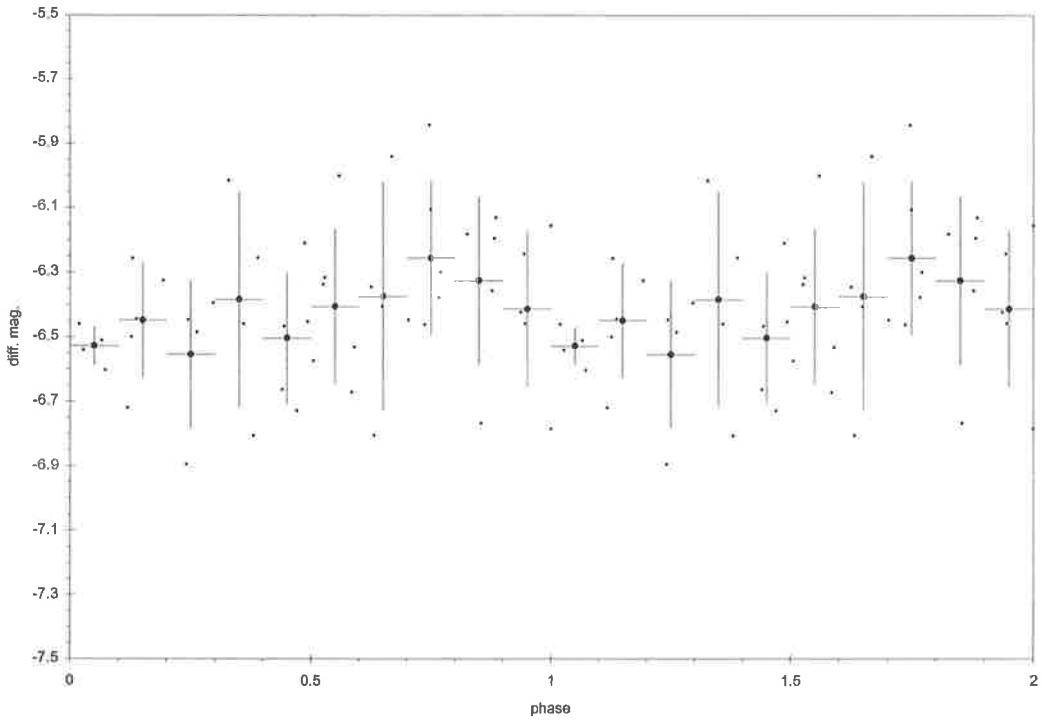

Figure 8.4 continued
Woomera low-state data phased at P_{orb} = 5342.31, and with the spectroscopic phase zero of TR96.
Ordinate is differential magnitude, abscissa is orbital phase.
The low-state data have been binned in phase-bins of width 0.1 (dots).
The crosses show the low-state data without error bars.
The binned data may show the effects of ellipsoidal modulation from the secondary star.

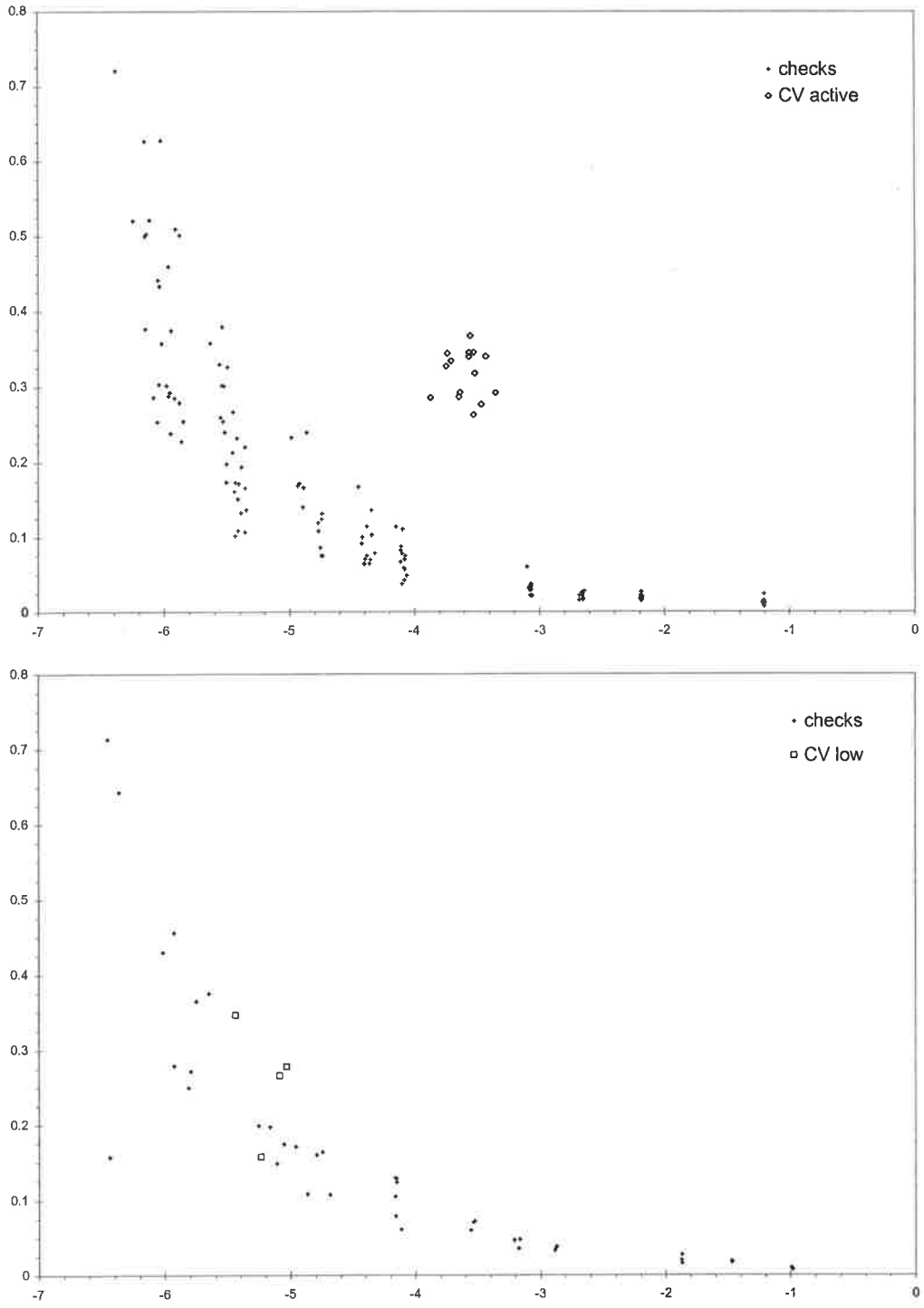

Figure 8.5

Magnitude-scatter plots for Woomera photometry.
Abscissa is scatter (in mags); ordinate is (average) differential magnitude for each night.
Upper panel: for CV in its active state. Lower panel: CV in its low state.
Note that different sets of C and K stars were used. The C star for the low-state data is 1.207 mags fainter than that for the high-state data.
In its active state, the CV always is significantly variable. In the low state, this was not so on the four nights of observations. This is mainly a result of the limitations of the small telescope used, since it is likely that ellipsoidal modulation from the secondary should then be visible.

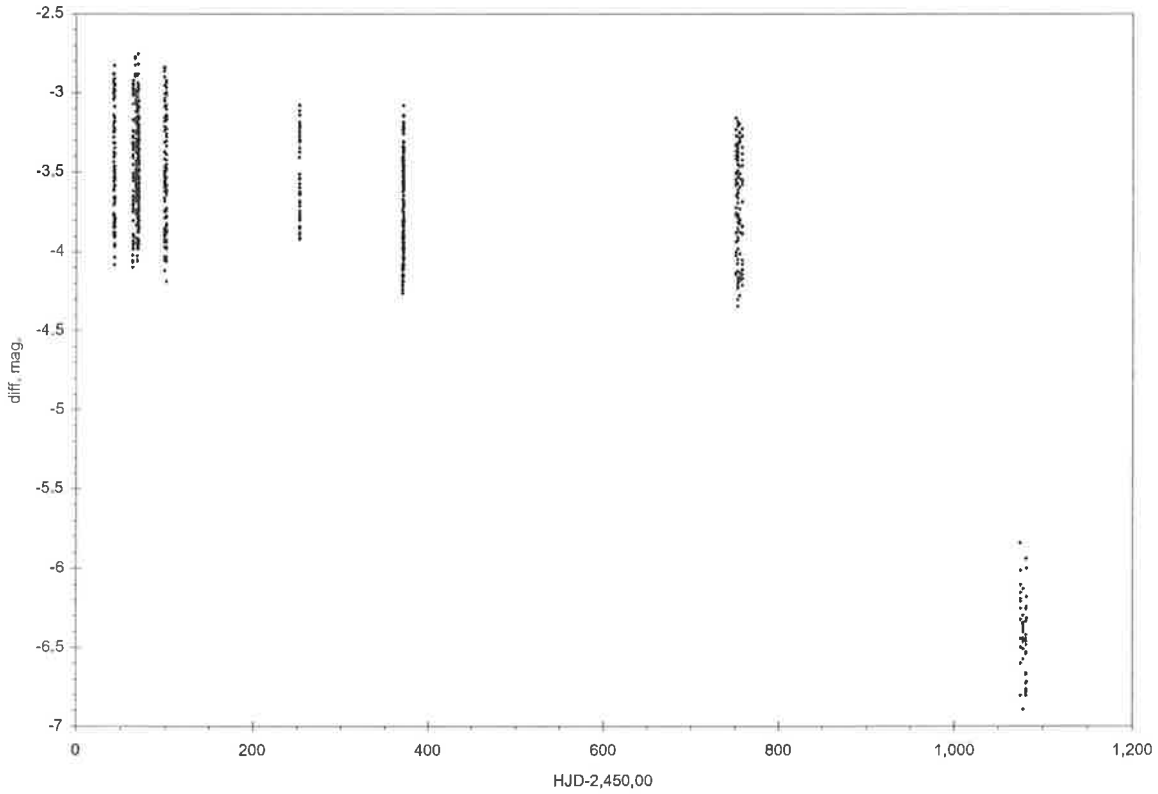

Figure 8.6
Woomera white-light photometry vs. HJD.

8.4 Orbital period

From their Hα narrow component (i.e. from the heated face of the secondary star) RV measurements, TR96 derive an orbital period of 5343.0624 ± 0.86s. Modelling of their initial two nights of Gunn i photometry yields P_{orb} = 5342.4576s; these two estimates are self-consistent.

However, neither of these periods directly is consistent with the Woomera photometry. These data cover HJD 2,450, 042 to 2,450,751 for the CV in its active state and to HJD 2,451,081 in total. That is, the active-state data cover some 11,467 orbits. Therefore, in the assumed absence of any change in phase zero or P_{orb}, phasing these data will be very sensitive to any error in the period employed. Adoption of the above periods leads to significant smearing within the phase plot, and this is taken to signify that these periods are not correct. Figure 8.7 shows the Woomera data phased with both these periods from TR96.

Examination of the phase plot for trial periods around 5342-5343s suggests that the best period is 5342.31 ± 0.02s (0.06183229 ± 0.0000002 d), which is that period which gives best agreement in phase between *all* high-state data. This period is, however, within the error limits of the TR96 spectroscopic period. It is better defined, though, due to the much greater time base of the Woomera photometric data. The phase zero is taken to be that from TR96, namely HJD 2,450,033.6495.

Figure 8.8 shows the results of period searches using both phase-dispersion minimisation (PDM) and neural-network (NN) methods (available from http://www.kusastro.kyoto-u.ac.jp/vsnet/etc/prog.html). Most of the structure in these plots is due to the sampling, in time, of the data. That is, it is not due to true periodic signals within the light from the CV, but is due to the discrete nature of the observations, and the various temporal spacings between individual exposures, between nights, and between months.

If we simulate the entire photometric data-set by a sinusoid of period P_{orb} and amplitude equal to the average observed amplitude, we can examine the effect of such sampling on a "pure signal". It is to be noted that a pure sine wave, if continuously sampled for an infinite time, would yield a periodogram showing a single, narrow signal at P_{orb}. Sampling a sine wave, then, as per the observed data, will show the effect of the discrete sampling on the periodogram.

Figure 8.9 shows a portion of the synthetic light curve, along with the related observed data. Figure 8.10 shows periododgrams for the real data and the synthetic data, and the difference between the two. In the last plot, it is seen that there are no significant peaks at any *new* periods. That is, all "periods" present in the observed data are present also in the model

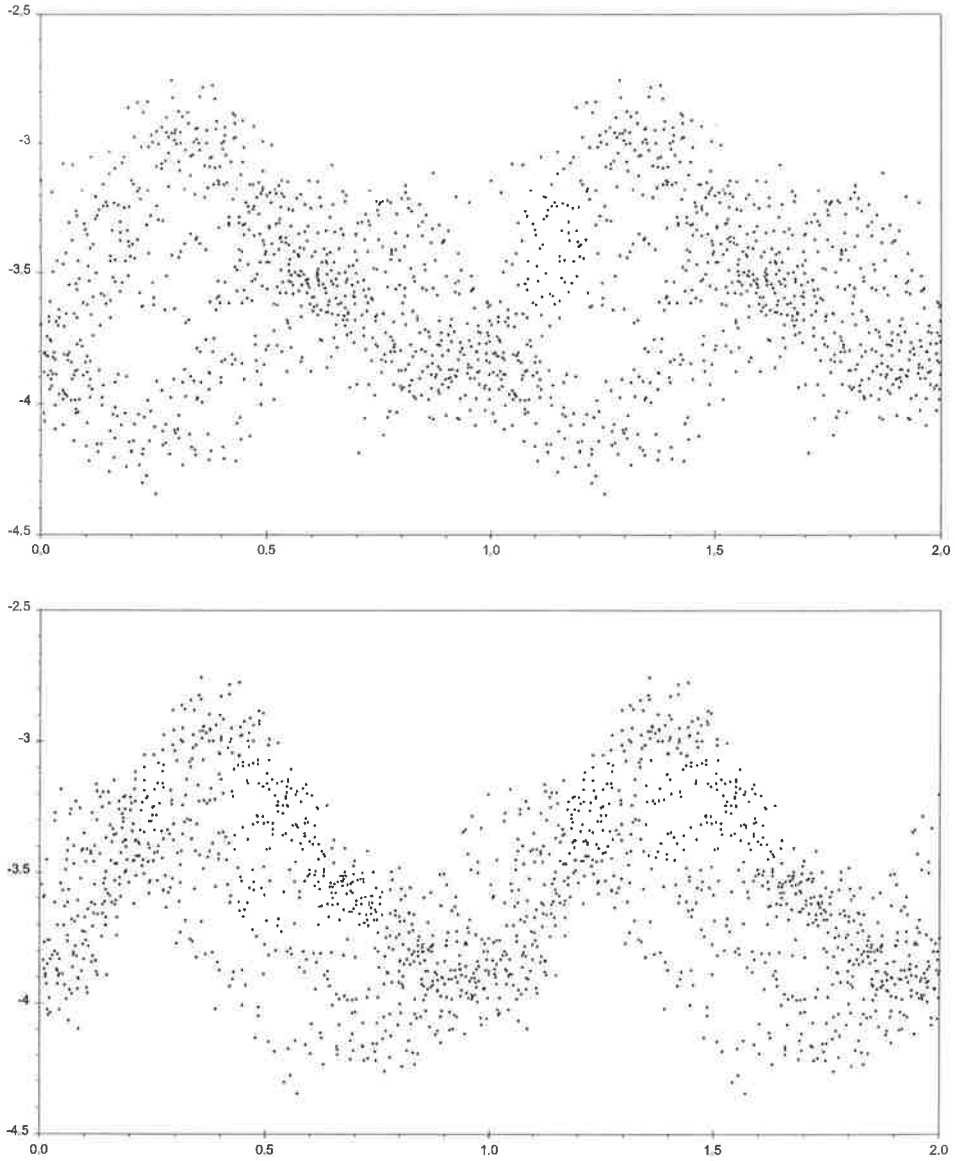

Figure 8.7

Woomera active-state data phased with orbital periods of
upper panel: 5343.0624s (from TR96 spectroscopy), and
lower panel: 5342.4576s (from TR96 photometry).
Ordinate is differential magnitude; abscissa is orbital phase.
These periods do not fit the entire data set,
although they may phase individual nights quite well.

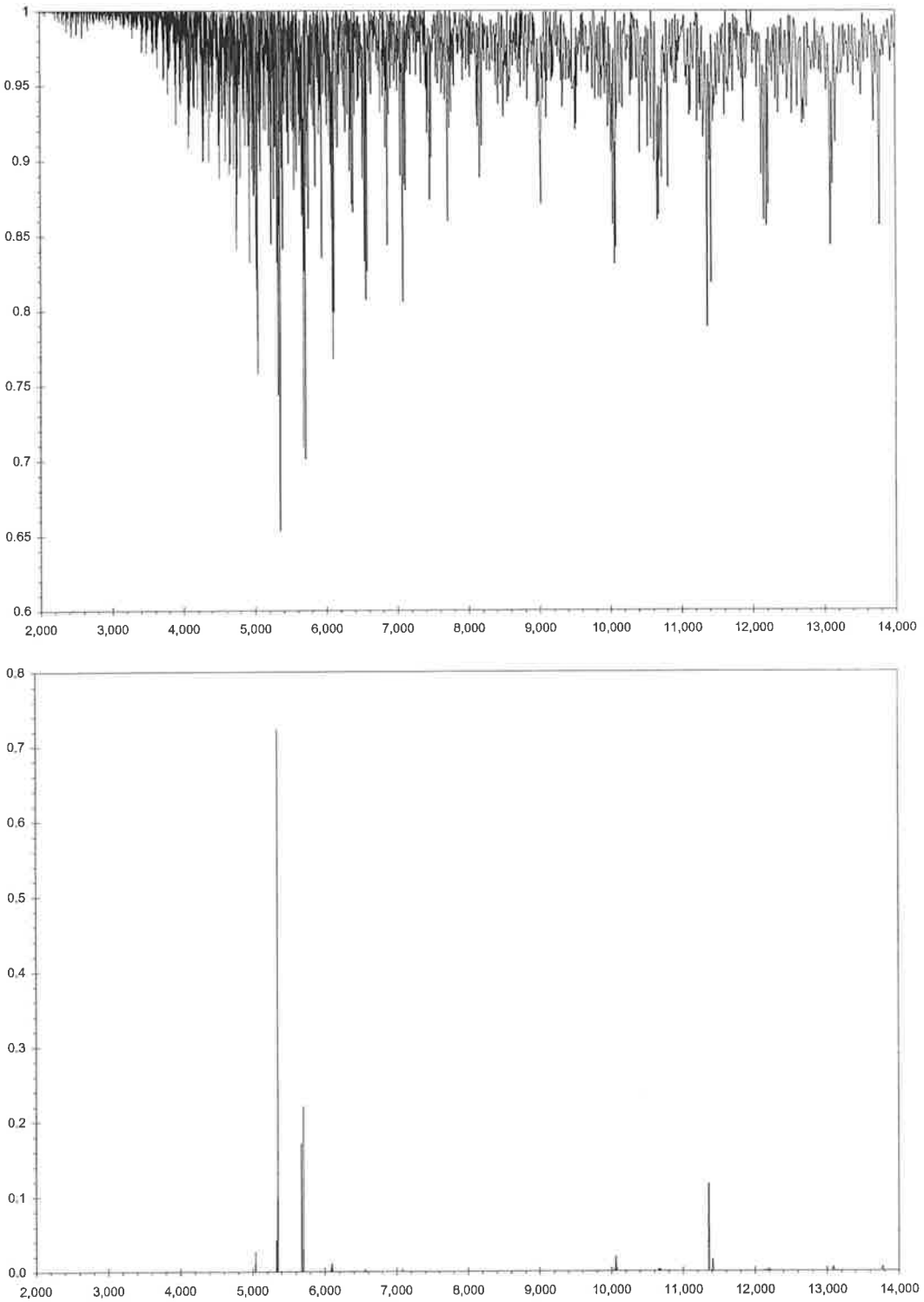

Figure 8.8

Period searches on active-state data only.
Upper panel is via PDM; lower, via neural-network methods.
Ordinate is significance of trial period; abscissa is period (in seconds).

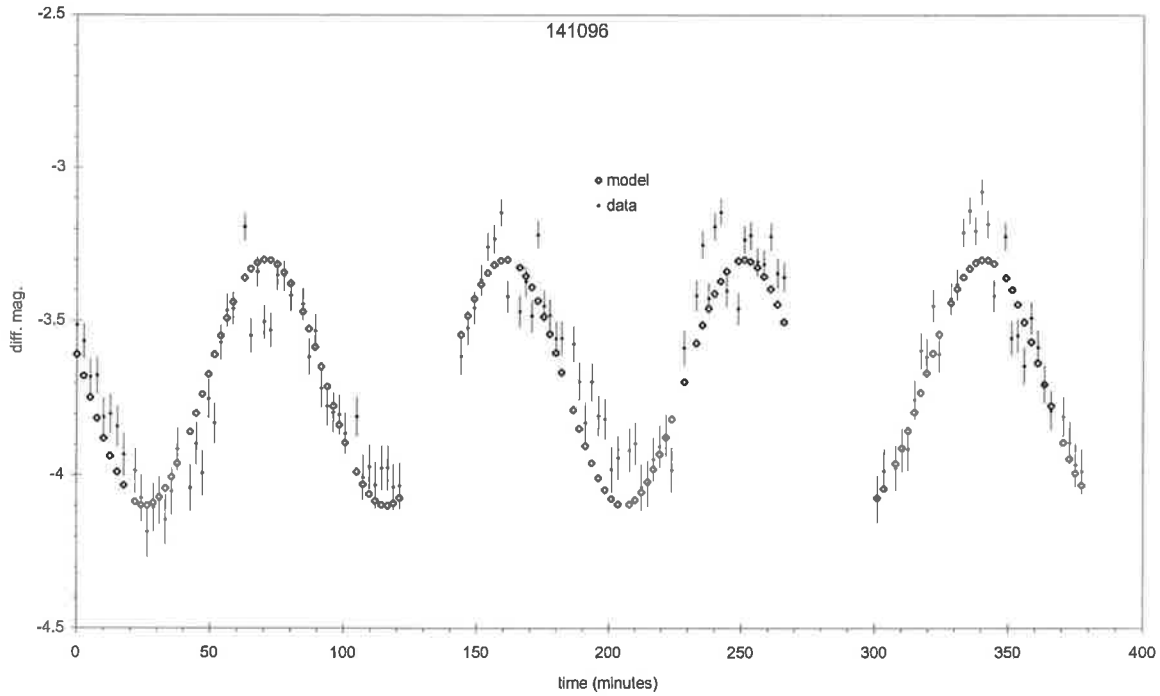

Figure 8.9
Woomera white-light photometry with sinusoidal fit to the data.

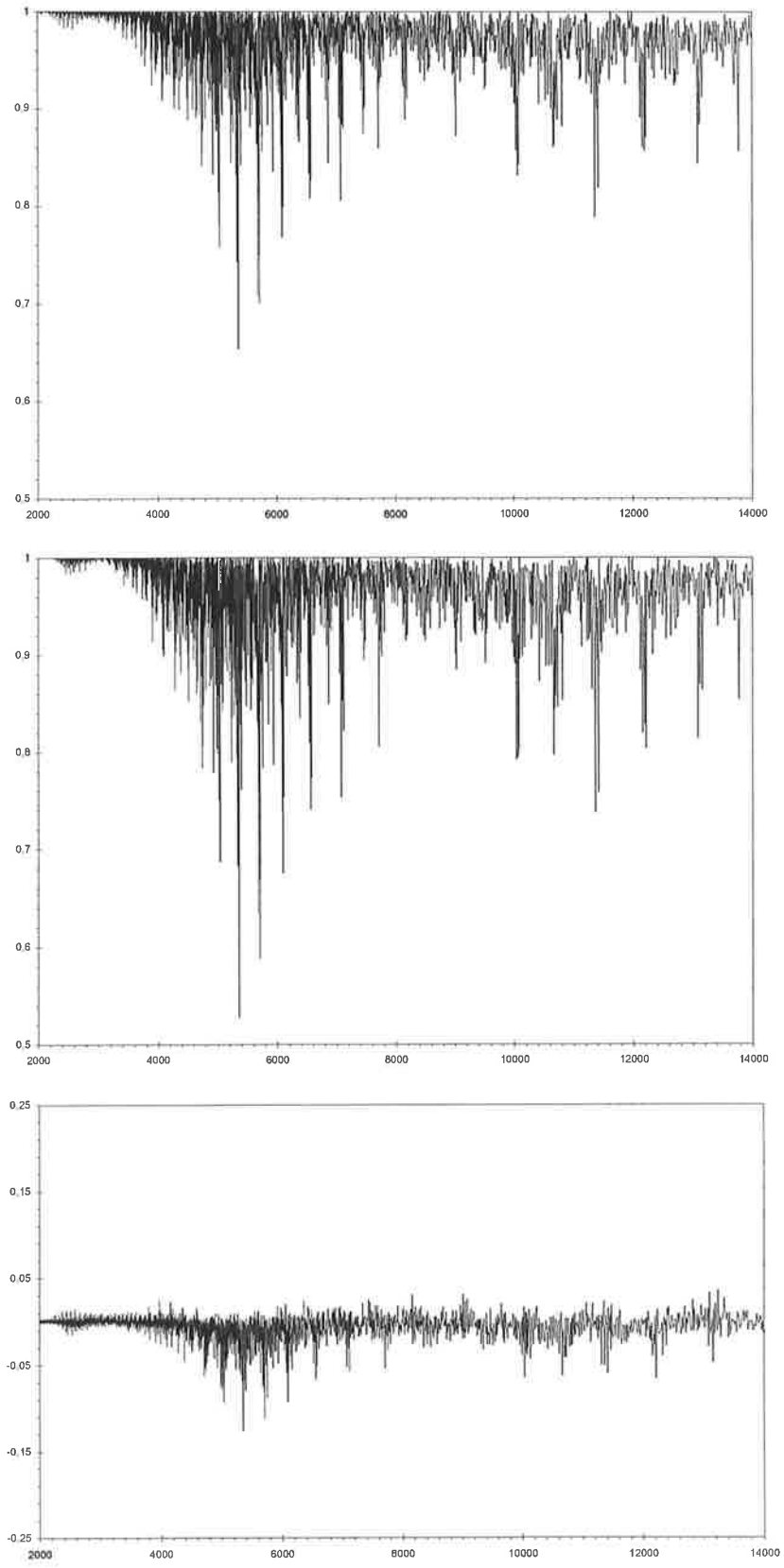

Figure 8.10

PDM period searches on (top) data, and (middle) sinusoidal fit to data. Lowest panel shows the difference between these. Ordinate is strength of signal, abscissa is period (in seconds). Most of the structure is due to the temporal sampling of the data, and not to actual periodic signals.

data (represented by a pure sine wave), and the difference between the observed and model PDM plots is due to changes in the amplitudes of these plots. That is, the structure in the obseved PDM is due overwhelmingly to the temporal sampling of the data. Of course, since the actual light curve is not exactly sinusoidal, exhibits changes in amplitude over various time scales, and *may* exhibit quasi-periodic flickering, a simple sinusoid will not perfectly model the data. This alone will result in differences between the two periodograms; but the gross similarities are evident.

The orbital period derived from the Woomera data will be taken as the correct one. Using this period, and the relations given in Section 2.2.2, the following parameters may be obtained:

M_2	R_2	T_2	ρ_2	$M_V(2)$	$M_V(2)$	$\dot{M}$
0.106	0.144	2870	48.6	16	15.8	$>1.6\ 10^{-11}$ $<2.8\ 10^{-11}$
M_{sun}	R_{sun}	K	g cm^{-3}			$M_{sun}\ yr^{-1}$

and the spectral type of the secondary star being about M4-M6 from the Sp(2)-P_{orb} relation in Figure 2.5.

From modelling of *RXTE* data, Ramsay (Ramsay 2000) finds the mass of the WD to be in the range 0.65-0.78 M_{sun}, with a best estimate of 0.68. Using the secondary mass of 0.106 M_{sun} obtained above, we then have an estimate of the mass ratio, $q = 0.16$.

8.5 Activity (state) changes

It is clear from the time series and phase plots that this CV undergoes drastic state changes, involving variations in both overall intensity and, presumably at least, waveform. The latter is not clear from the Woomera data due to the large scatter in the low-state data. However, since most of the high-state light comes from the accretion region(s), it may be expected that in the low state- when accretion is minimal or negligible- that the form of the light curve also changes. Indeed, ellipsoidal modulation of the secondary star may be visible in sufficiently accurate photometry, as it is likely that light from the secondary will dominate.

The HJD plot in Figure 8.6 shows perhaps three distinct states:

(i) a high state from HJD 2,450,000 to about 2,450,150;

(ii) a slightly lower active state from HJD 2,450,250 to 2,450,750 (where there begins a long gap in the data);

(iii) a low, presumably inactive, state around HJD 2,451,080.

Due to the incompleteness of the data, it is not possible to give close estimates of the durations of these states, or of the transitions between them. It is expected, however, that since this source is a polar, it will tend to spend most of its time in a higher state (Cropper 1990).

The decrease in flux in the second stage suggests a decrease in accretion rate. The system is not eclipsing (see Sections 8.6-8.8), so we may expect a decrease in both maximum and minimum light during an orbit. This is so since the accretion region is always visible, and a decrease in accretion-based flux results in a reduction in intensity during the entire orbit (cf Cen 2 where there is a stable minimum flux, due to there being a total eclipse of the primary and its accretion regions(s) in all states). There also is a slight reduction in amplitude (from about 0.9mag to 0.7mag in the unfiltered Woomera data).

The last data show the CV in a much reduced activity state. The drop in average magnitudes from the first stage is about 3mag, corresponding to an intensity drop of around a factor of 16 over the broad Woomera CCD wavelength response. Note that TR96 estimate m_V = 17 in the high state. Assuming $\Delta V = 2.5$ mag for this decrease, it is estimated that the low-state $m_V = 19.5$. It is to be noted that from spectroscopy, TR96 derive a *minimum* distance of 175 pc. These together suggest the total system $M_V < 13.28$.

For the white dwarf L1512-34 B (Allen, Section 111), we have $M_1 = 0.81$ (within the expected range for CP Tuc; see next section), $R_1 = 0.0126$ and $M_V = 11.3$. It will be assumed that the properties of this star can be compared with the properties of the primary in CP Tuc. We then have M_V estimates for both stars in the CV, namely 11.3 and 16. Together, they yield a combined M_V magnitude of 11.29. It is evident that there is very little contribution (about $1/75^{th}$) to the V-band flux from the secondary considering just the light from the two stars alone (i.e. ignoring accretion- largely equivalent to the low state of this system); this may explain why TR96 found little evidence of a late-M spectrum in the (active state) faint phase spectrum.

With an estimated low-state $m_V = 19.5$, the distance to CP Tuc now becomes 439 pc (or 348 pc for $m_V = 19$, 277 pc for $m_V = 18.5$). Of course, of paramount importance here is an accurate m_V, preferably in both active and inactive states.

Historically, CP Tuc has shown activity-state transitions. Figure 8.11 shows three SuperCOSMOS images of the CV, and the change in activity state is clear. During the 1996 SSO observing trip, Polaroid copies of survey plates of the field (and others) were obtained at the UKST building. Examination of these (which include the two UKST images in Figure 8.11) yields the following:

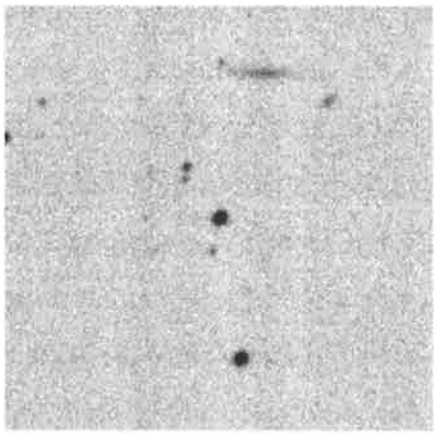

UKST plate B5152; IIIaJ + GG395; 7/7/1979
CV is in an active state

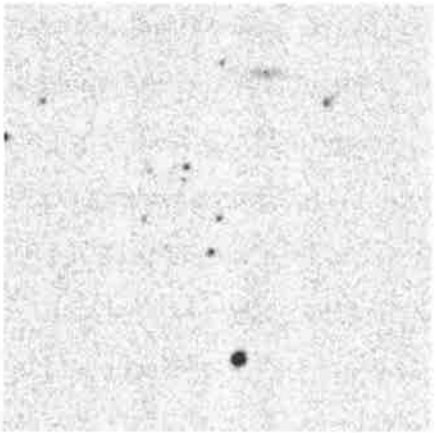

ESO plate R5371; IIIaF + RG630; 1/11/1983
CV is in a low state

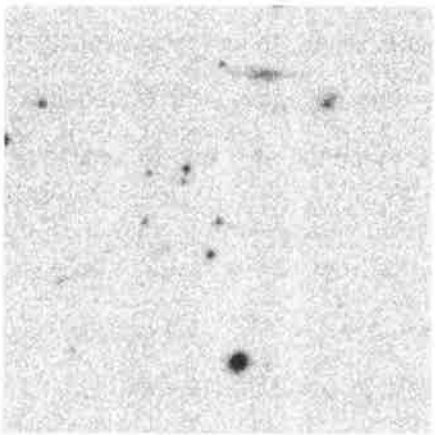

UKST plate OR16181; IIIaF+OG590; 7/7/1994
CV is in a low state

Figure 8.11
Archival Schmidt survey images of a 3'-square field centred on CP Tuc.
North is up, east is to the left.
Included is plate name, emulsion and filter used, and UT date.

Date	State	Approx. mag.	Plate
9/6/1975	high	16.9 (blue)	J1579
9/8/1975	high	"	J1808
7/7/1979	high	"	J5152
24/8/1979	middle-high	17.5 (red)	R5310
10/10/1980	low-middle	18 (blue)	J6490
1/11/1983	low	19 (red)	ESO R5371
7/7/1994	low	"	OR16181
28/8/1995	low	"	OR16755

The approximate magnitudes for CP Tuc were estimated by comparison with magnitudes given by SuperCOSMOS (http://www-wfau.roe.ac.uk/sss/obj.html) for nearby field stars of similar diameter on the images.

It is possible that July-August 1979 saw a high-low state transition, but one can't say from the above just how long the low state lasted. A more thorough search of all available plates at ESO and UKST would be required.

Since the source was first detected by satellite in November 1995, it was likely in a high state at that time. From plate OR16755, we know it was in a low state in late August 1995, so it is possible that a low-high transition may occur in about two months (or shorter).

8.6 Models

There is not enough information within the Woomera data alone to determine all system parameters. We shall now consider the models described to date in the literature. TR96 find the following system parameters:

$M_2 = 0.11$

$0.7 < M_1 < 0.9$ (0.83 ± 0.1 for B = 15MG and 0.79 for B = 10MG)

B = 17MG

$38° < i < 49°$

and therefore also $0.12 < q < 0.16$. This is consistent with that derived in Section 8.4.

Equating R_2 with the volume radius of the Roche lobe of the secondary R_{L2} from Equation 2.14, we can estimate the separation of the centres, a, of the primary and secondary, to be $4.54\ 10^{10} < a(\text{cm}) < 5.12\ 10^{10}$.

They determine that the accretion region is not eclipsed by the WD surface at any phase, and that the modulation in intensity during the orbital cycle- especially in the Gunn i

band in which their photometry was undertaken- is due to angular dependence of cyclotron opacity.

As a phase zero, TR96 take the blue-red crossing of the narrow Hα emission component (this being from the hated face of the secondary), and specify HJD 2,450,033.6495(8). This is superior conjunction of the secondary. With this phase zero, the Woomera data (phased with a period of 5342.31s) show a minimum near $\phi = 0.0$ (perhaps 0.95), and a maximum near 0.4. This phasing appears to be consistent throughout both high states observed here; i.e. there is no significant phase shift associated with the slightly lower activity state. This would suggest that the azimuthal location of the accretion region did not change significantly with the (presumed) slight lowering in accretion rate responsible for the slight drop in activity level.

Ramsay *et al.* 1999 (hereafter RPBW99) propose a model in which the accretion region is in fact far removed from the magnetic pole. One best fit to their polarimetric observations yields $i = 42°$ and $\beta = 50°$. Here, β is the angle between the rotational axis and the magnetic axis. In this case, the broad X-ray minimum is due to eclipse of the accretion region by the WD itself. From R and I photometry and RXTE X-ray data, they find that the centre of the X-ray minimum coincides with the optical minimum. There is no change in sign of the circular polarisation, and this suggests that only a single accreting pole only is present (if there were two, a change in sign for approximately half the orbit would be expected).

From combined ASCA, SAX and RXTE data, the following ephemeris was found:

$$T = \text{HJD } 2{,}450{,}024.8015(7) + 0.06183207(8) * E$$

i.e. period = 5342.2908 ± 0.007s. This period is consistent with that derived from the Woomera photometry. When the Woomera data are phased with this phase zero, the optical minimum is found at phase 1.05 and maximum near 0.5. The location of the accretion region(s) is shown in Figure 8.12; it is seen that optical maximum corresponds to the accretion region being most nearly transverse to the line-of-sight, but with the main accretion region directed to the observer. Having no spectroscopic observations, RPBW99 do not attempt to give an orbital definition of their phase zero; it is based on the centre of the X-ray minimum, and is therefore defined in terms of the visibility of the accretion region on the WD. (It is to be noted that there is a considerable displacement in longitude between the magnetic pole and the main accretion region). The high-state light-curve of this system was modelled successfully using their model as found from their polarimetric data.

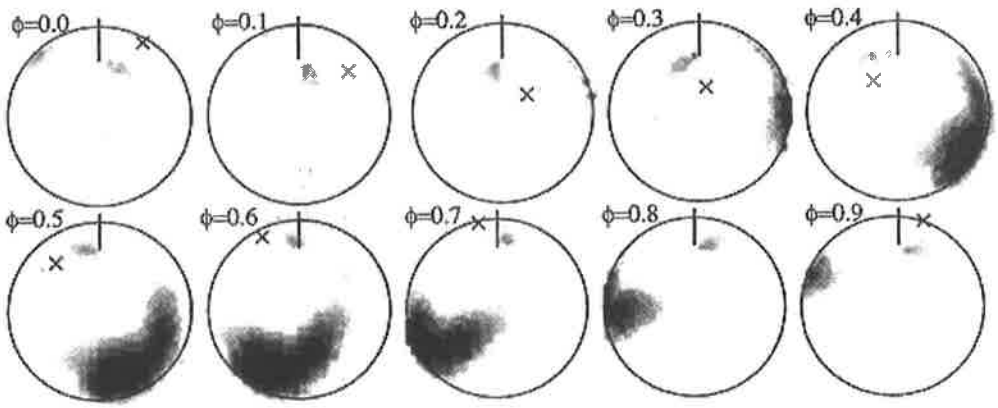

Figure 8.12

Position of magnetic pole (cross), rotation axis, and accretion regions as found from Stokes modelling of polarimetric data (reproduced from RPBWW 99).
Phases are as per the ephemeris in that paper.
For these results, it was assumed that i *= 42° and* β *= 50°. Note that the accretion region is far removed from the magnetic axis.*
These values of i *and* β *are not supported by the Woomera photometry, especially since this model has the main accretion fully eclipsed every orbit, which is not seen in the photometry.*

8.7 Simple modelling of the optical light curve

Much of the high-state optical flux in a polar comes from cyclotron harmonics, and these are most prominent in the infra-red part of the optical spectrum. The modulation in intensity is due to the varying angles between the observer's line-of-sight and the magnetic filed lines as the CV rotates. Therefore, for a polar having $i = 0°$ (i.e. its orbital plane in the plane of the sky), there should be no modulation in the optical flux, since this angle will be constant throughout the orbit.

TR96 model their filtered optical flux (using a Gunn *i* filter) from CP Tuc using the relation

$$f = f_0 \sin^6\theta + f_1 \qquad (8.1)$$

where

f_0 and f_1 are constants, and

θ is the angle between the line-of-sight and the magnetic field direction.

The value of θ may be approximated using the following relation (Thomas *et al.* 1996)

$$\cos\theta = \cos i \cos\beta + \sin i \sin\beta \cos 2\pi(\phi - \phi_c) \qquad (8.2)$$

where

ϕ is orbital phase, and ϕ_c is the centre of the bright portion of the light curve.

Figure 8.13 (upper panel) shows the Woomera data for CP Tuc in its *highest* activity state, as a flux ratio for (CP Tuc)/(comparison star), and have been normalised. Figure 8.13 (lower panel) shows the same data binned with phase widths 0.05; the vertical error bars give the scatter in each phase bin. Included is the model light curve for a single accretion spot, as given by Equations 8.1 & 8.2, and with the constants adjusted as required.

The accretion spot has no extension in latitude, longitude or height, and is co-incident with the magnetic pole. As simple as this model is, the fit to the data is very good. Whilst good fits are obtained with $i = 40°$ and $\beta = 31°$ or 26° (as found in TR96), it must be noted that a range of *i* and β values are not inconsistent with these data.

There is a deficit in the model curve for $0.7 < \phi < 0.9$ (evident also in the RPBW99 white-light and TR96 I data). This may signify a weak longitudinal extension to the accretion region, in the sense of a slight trailing edge. There may also be some influence due to the

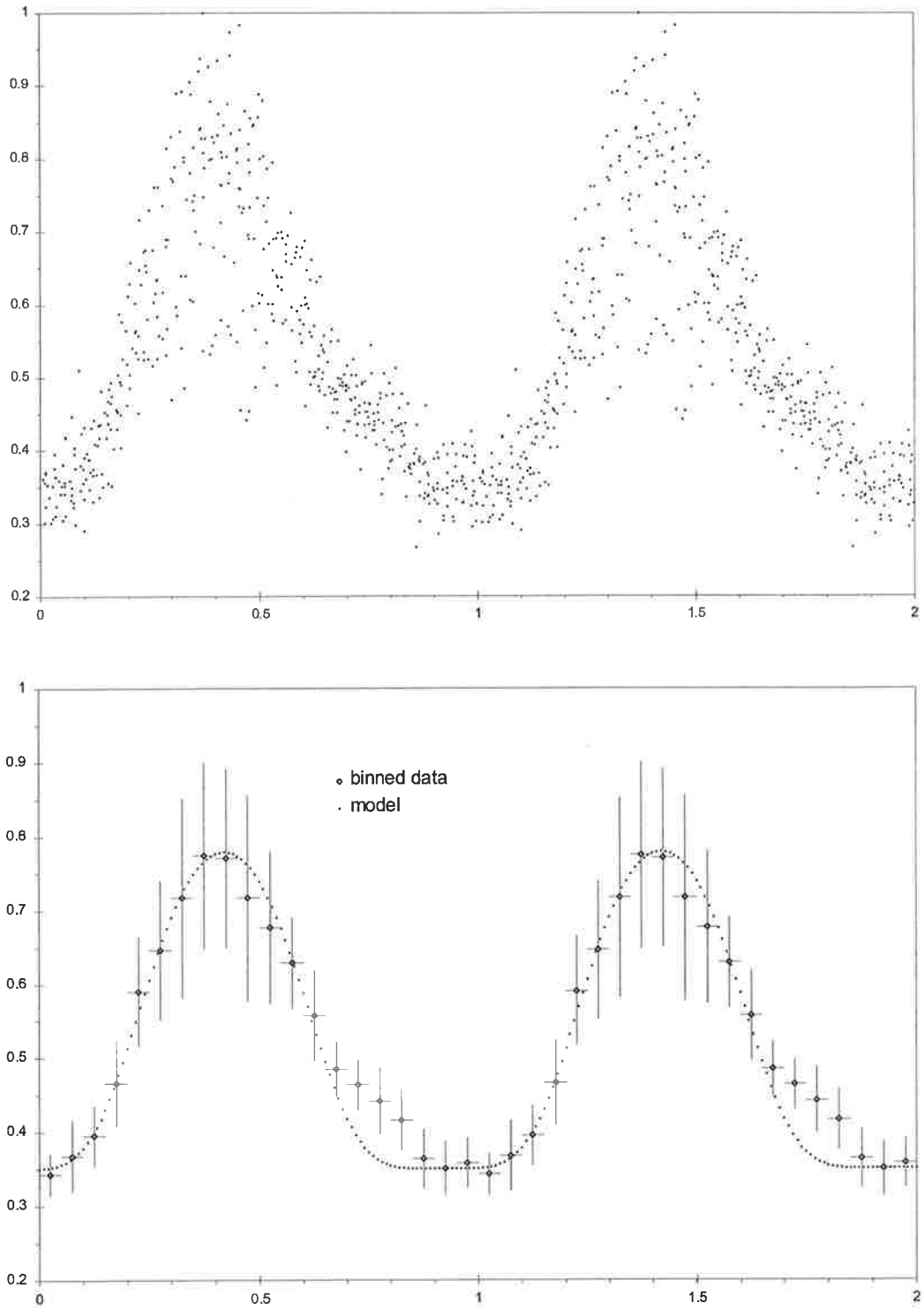

Figure 8.13

Ordinate is normalised flux; abscissa is orbital phase. Phase zero as per TR96 spectroscopy; period as derived from Woomera data.
Upper panel: Woomera highest-state data, presented as normalised flux
Lower panel: the same data shown binned with phase width 0.025, and with a model light curve for $i = 40^\circ$ *and* $\beta = 31^\circ$.

differing spectral response of the unfiltered CCD used for the Woomera data, and the infra-red filter pass-band assumed in the application of Equation 8.1 by TR96.

Applying i and β as found by RPBW99, one obtains the model light curve as shown in Figure 8.14. It is clear that the fit is not as good as before. In this regard, the Woomera data do not support the latter model. It must be noted, however, that RPBW99 have the main accretion region somewhat displaced from the magnetic pole, which is not the case in the simple model here. Thus, there are differences between the two models, so this point may not be relied upon too heavily.

For the slightly lower-activity high-state data (i.e. HJD 2,450,300-2,450,800), reasonable fits to the binned Woomera data are obtained with $i = 40°$ and $\beta = 26°$ or 31°. However, a slightly better fit is obtained for $i = 40°$ and $\beta = 36°$ to 40°; Figure 8.15 shows these, and that $i = 42°$ and $\beta = 50°$ is still not a good fit to the data.

Is this change in β significant? Figure 8.16 shows the highest-state data fitted with $i = 40°$ and $\beta = 40°$. Whilst this fit is consistent within the scatter present in the phase bins (excluding approximately $0.7 < \phi < 0.9$, and this feature is present for all i and β checked so far), there is a noticeable discrepancy for the two phase bins around $\phi = 0.5$; the model peak is broader than that observed. This suggests that the change in β may be significant.

It is noted that the shape of the model light curve depends on the values of both i and β, and that the slight but noticeable changes in the light curve could be produced by changing both of these parameters. However, I have chosen to fix i and then to vary β in order to fit the data. This allows one to say that, given an assumed i, the observed changes in the light curve may be explained by a change in the latitude of the accretion region.

Of course, this simple model has it that the accretion spot is co-incident with the magnetic pole. Since the orientation of the magnetic pole cannot actually change, β itself cannot change physically. For the sake of this model, β may be interpreted as the angle between the WD rotation axis and the accretion region (spot), *including* the inclination of the magnetic axis to the rotation axis. Thus, change in the model β-parameter actually represents a slight wandering in latitude of the accretion spot with respect to the magnetic pole.

Since the reduced flux in the lower active state is presumably due to a reduction in the mass-transfer rate, the increase in "β" (i.e. movement of the accretion spot towards the WD equator), may be due to reduced penetration of the primary's magnetic field by the less-vigorous accretion stream. The stream will be captured by the WD's field further out from its

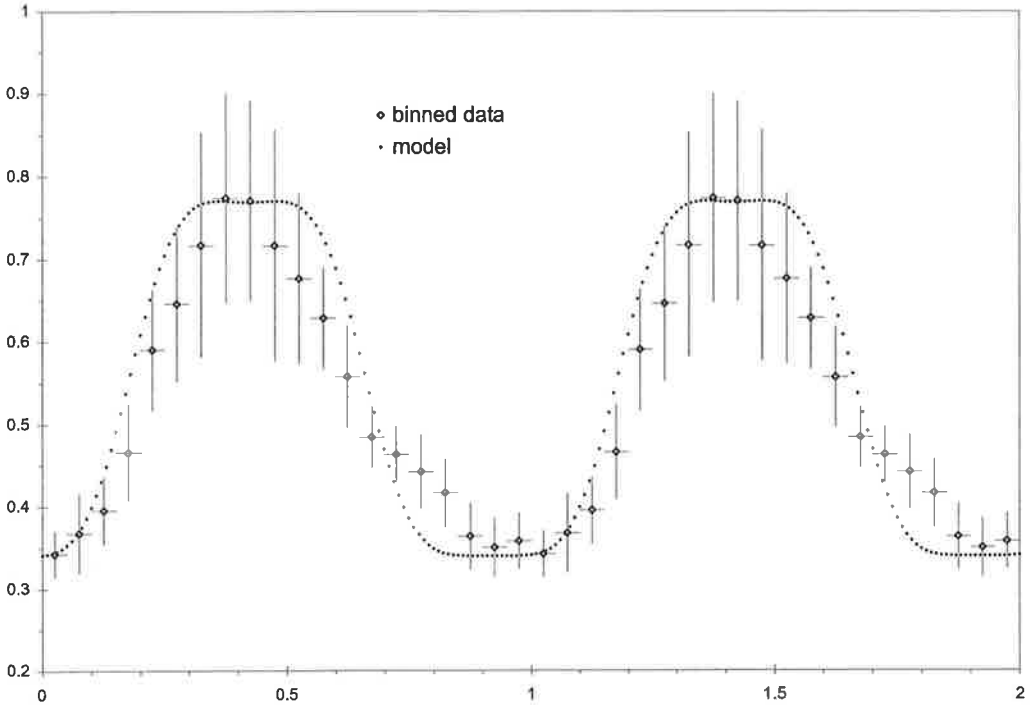

Figure 8.14

Ordinate is normalised flux, abscissa is orbital phase. Binned Woomera highest-state data, with model fit for $i = 42^\circ$ *and* $\beta = 50^\circ$*. The model light curve is significantly broader than the observed light curve.*

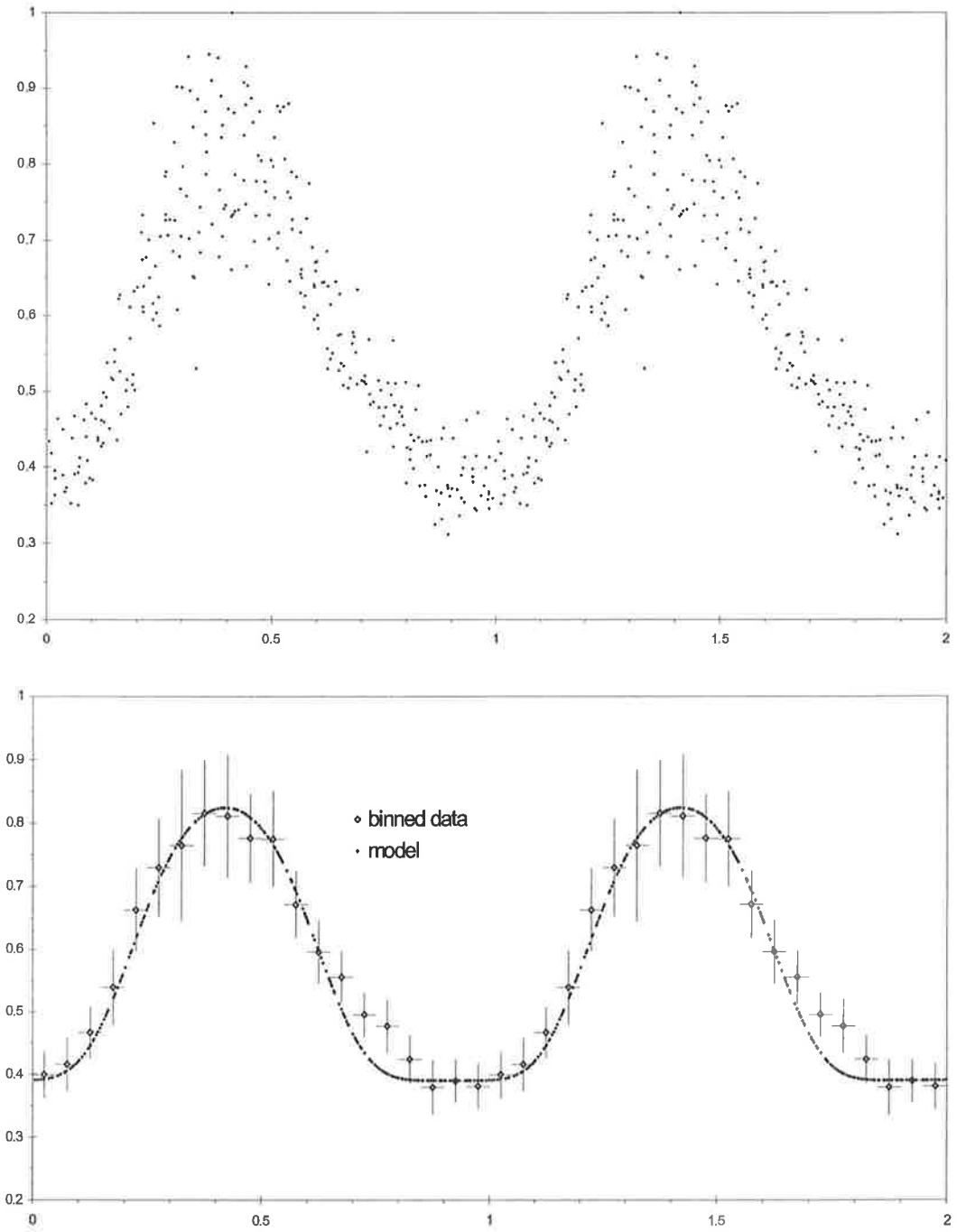

Figure 8.15
Ordinate is normalised flux; abscissa is orbital phase.
Upper panel: Woomera mid-state data, presented as normalised flux.
Lower panel: the same data showed binned with phase width 0.025, and with a model light-curve for $i = 40^{\circ}$ *and* $\beta = 36^{\circ}$.

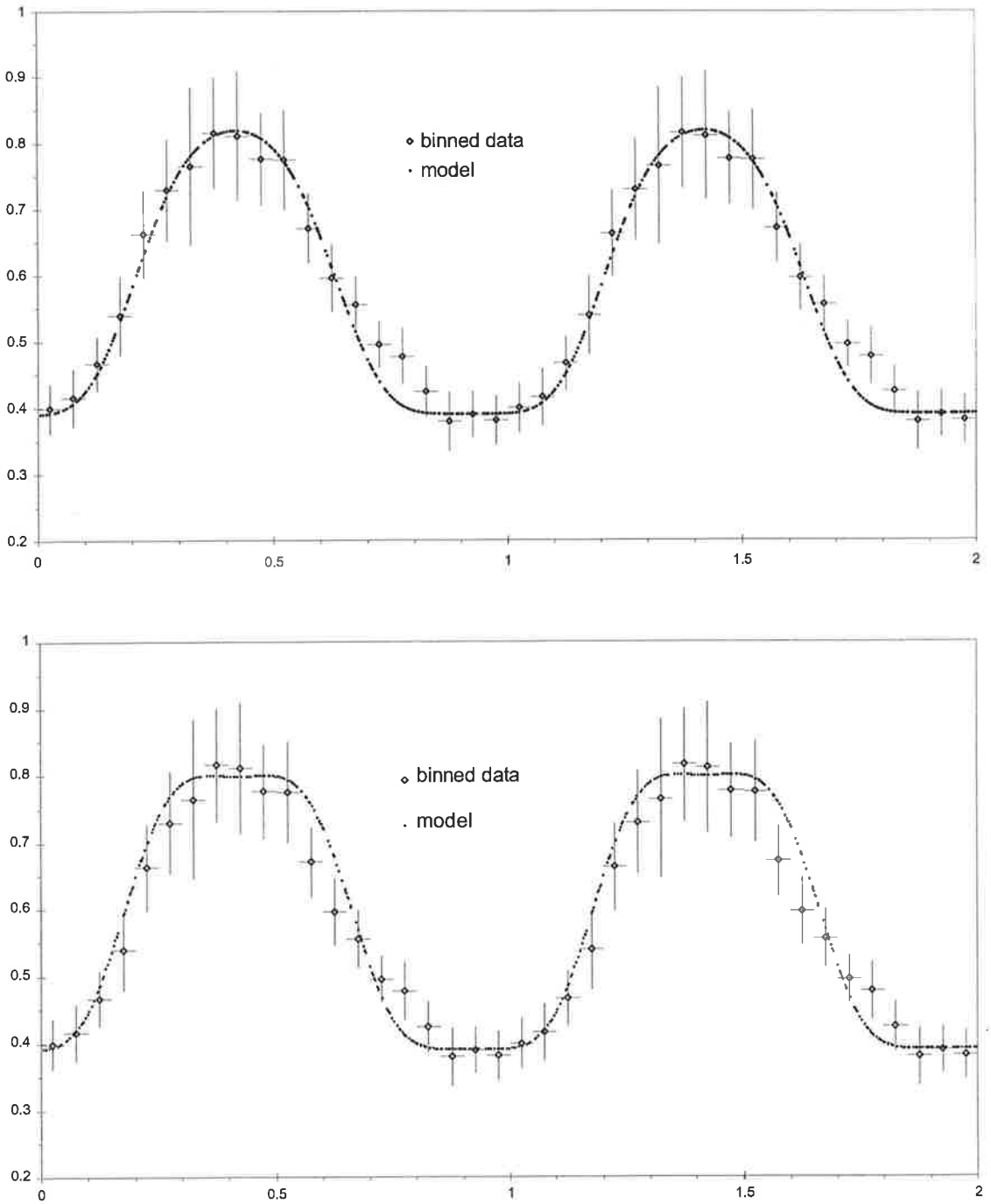

Figure 8.15 continued
Ordinate is normalised flux; abscissa is orbital phase.
Upper panel: binned data and model for $i = 40^\circ$ *and* $\beta = 40^\circ$.
Lower panel: binned data and model for $i = 42^\circ$ *and* $\beta = 50^\circ$.

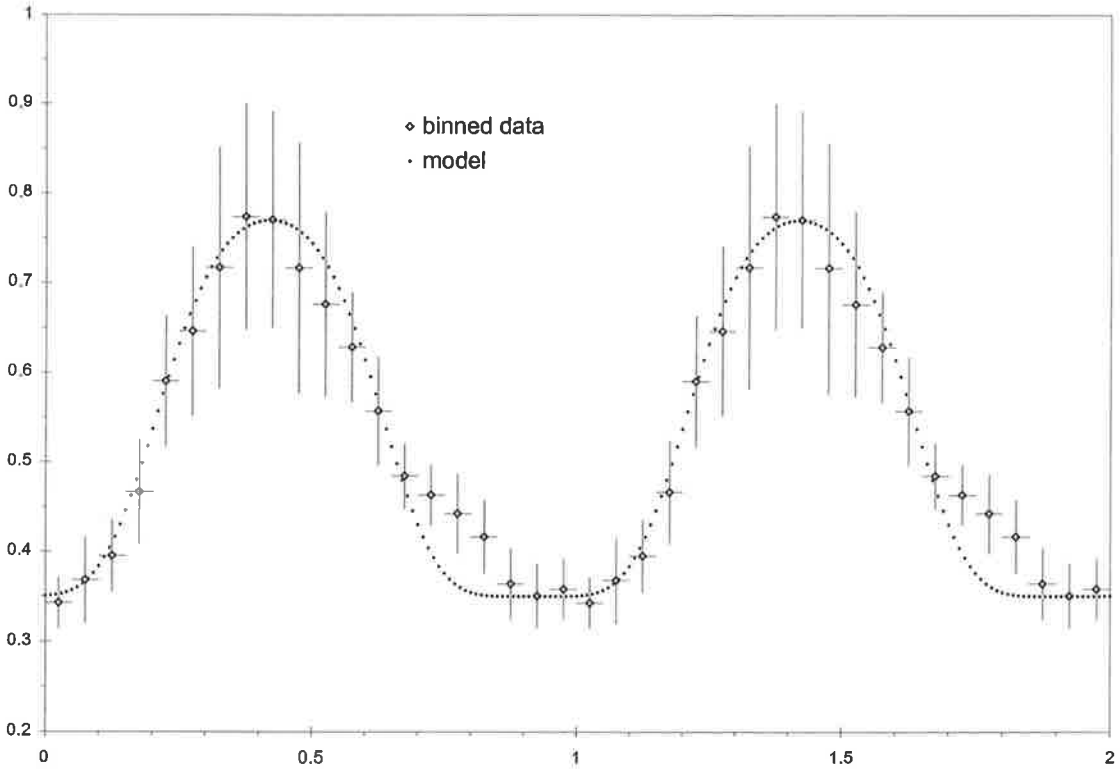

Figure 8.16
Ordinate is normalised flux, abscissa is orbital phase. Binned Woomera highest-state data, with model light-curve for $i = 40^\circ$ *and* $\beta = 40^\circ$.

surface, and may be channelled along field lines which have their foot-print at a lower magnetic latitude.

8.8 Which model?

The models given in TR96 and RPBW99 are somewhat contradictory. In the former, the accretion region always is visible; in the latter, it is eclipsed for roughly half the orbital cycle by the WD itself. The Woomera data may be modelled by the simple equation given in TR96, assuming no eclipse of the primary accretion region at all. Yet, RPBW99 model the observed optical intensity variations successfully based upon their self-eclipsing model.

It is clear that CP Tuc is not an eclipsing system in the sense of eclipse by the secondary star. In such systems (e.g. E114+18 (Biermann *et al.* 1985), EP Draconis (Schwope & Mengel 1997), HU Aqu (Schwope *et al.* 1997), RX J0515.6+0105 (Shafter *et al.* 1995), 1H 1752+081 (Barwig *et al.* 1994), EXO 033319-2554.2 (Beurmann *et al.* 1988), LB1800 (Buckley *et al.* 1990), RX J2107.9-0518 (Schwope *et al.* 1993) and others), the light curve exhibits a deep and narrow optical eclipse when the stream, WD and accretion regions are totally hidden by the secondary. In the case of a partial eclipse, the dip will not be flat-bottomed.

The low-field polar RX J1957.1-5738 (Thomas *et al.* 1996) is self-eclipsing; that is, the accretion region is eclipsed by the WD surface, but the WD is not eclipsed by the secondary. This CV shows a flat-bottomed light-curve in both ROSAT X-ray and in optical photometry, lasting for very close to half the orbit. The X-ray count-rate in this portion of the light-curve is near zero.

Outside this eclipse region, the optical light-curve is not dissimilar to that for CP Tuc. However, the main point is that the CP Tuc optical light-curves do not show such a flat region for any significant time, and certainly not for the 0.2-0.3 of an orbit suggested by the RPBW99 model. CP Tuc's X-ray light curve also does not show such a feature. Admittedly, the RPBW99 best-fit model has the magnetic pole only marginally self-eclipsing ($i + \beta = 92°$); but the main accretion region is somewhat displaced in both latitude and longitude and is virtually totally eclipsed.

The Woomera low-state data show that when accretion is "off", the system is nearly 3 magnitudes fainter. This suggests that the contribution of accretion to the optical luminosity of the system is very significant. In the TR96 model, the accretion region on the primary, and the stream, are both always visible. In the RPBW99 model, the main accretion region is hidden for around half the orbit, although the stream remains visible.

Unless the stream itself provides much of the high-state luminosity, and/or the minor accretion regions of the RPBW99 model contribute some optical intensity, it is not clear how a fully-self-eclipsed main accretion region in CP Tuc cannot give rise to a flat-bottomed light-curve. Perhaps the longitudinal extent of the accretion region in the RPBW99 model is sufficient to "even out" the light curve.

Whatever the case, there had been no low-state observations of CP Tuc prior to the publication of those papers. Whilst it is not possible to decide between the two models discussed above using the Woomera data alone (although they are supportive of the TR96 model), the influence of low-state observations on these remains to be seen.

CHAPTER 9. EXPERIMENTAL RESULTS: PHOTOMETRY OF EUVE J2115-58.6

9.1 Discovery

EUVE J2115-58.6 (also known as RX J2115-5840, RX J2115.7-5840, Ind 1 or CD Ind), was detected in the EUVE All-sky Survey during 20-23/10/1992. The source was observed by the same satellite again over the period 19-25/4/1993. Total exposure was around 1200s, with a total of only some 40 photons finally accepted from the source. Detection was only in the 100-Ångstrom wavelength band.

The nominal EUVE position was α = 21:15:46 δ = -58:39:48 (2000.0), with an error circle 1' in diameter.

This source also was seen in the ROSAT All-Sky Survey (1990-1991). Total observation time was 294s, yielding an average count rate of 0.38 $\pm$ 0.19s^{-1}. It was detected in the ROSAT soft (0.1 - 0.4 keV) and hard (0.4 - 2.4 keV) bands. In total, 102 photons were accepted during these observations. Satellite image are shown in Figure 9.0 (from heasarc.gsfc.nasa.gov).

9.2 Optical identification and initial spectroscopy

As part of an optical ID programme for EUVE sources, Craig (IAUC 6297 and private e-mails) examined the EUVE error circle. Optical spectra of candidate stars within the source error circle were obtained in 1995 December 10^{th}-12^{th} with the 1.5-metre telescope at CTIO. The Cassegrain spectrograph and LORAL (1200x800) CCD were used with a 300 line/mm grating and a 4.5 arc-second entrance slit to yield a resolution of 9Å over the wavelength range 3700-6750Å. A He-Ar lamp was used for wavelength calibration (errors about 0.1 Å), and the standard stars Feige 110 and LTT3218 were used for flux calibration. Standard IRAF procedures were used to reduce the data. A spectroscopic observing log is given in Table 9.1.

Table 9.1
CTIO spectroscopy log

Run number	UT date	UT time (start)	exposure (s)
281	10/12/1995	01:01:09	2700
282	10/12/1995	01:57:36	2700
379	11/12/1995	10:23:02	2700
381	11/12/1995	11:11:39	3600
478	12/12/1995	00:29:27	3000
479	12/12/1995	01:20:29	3000

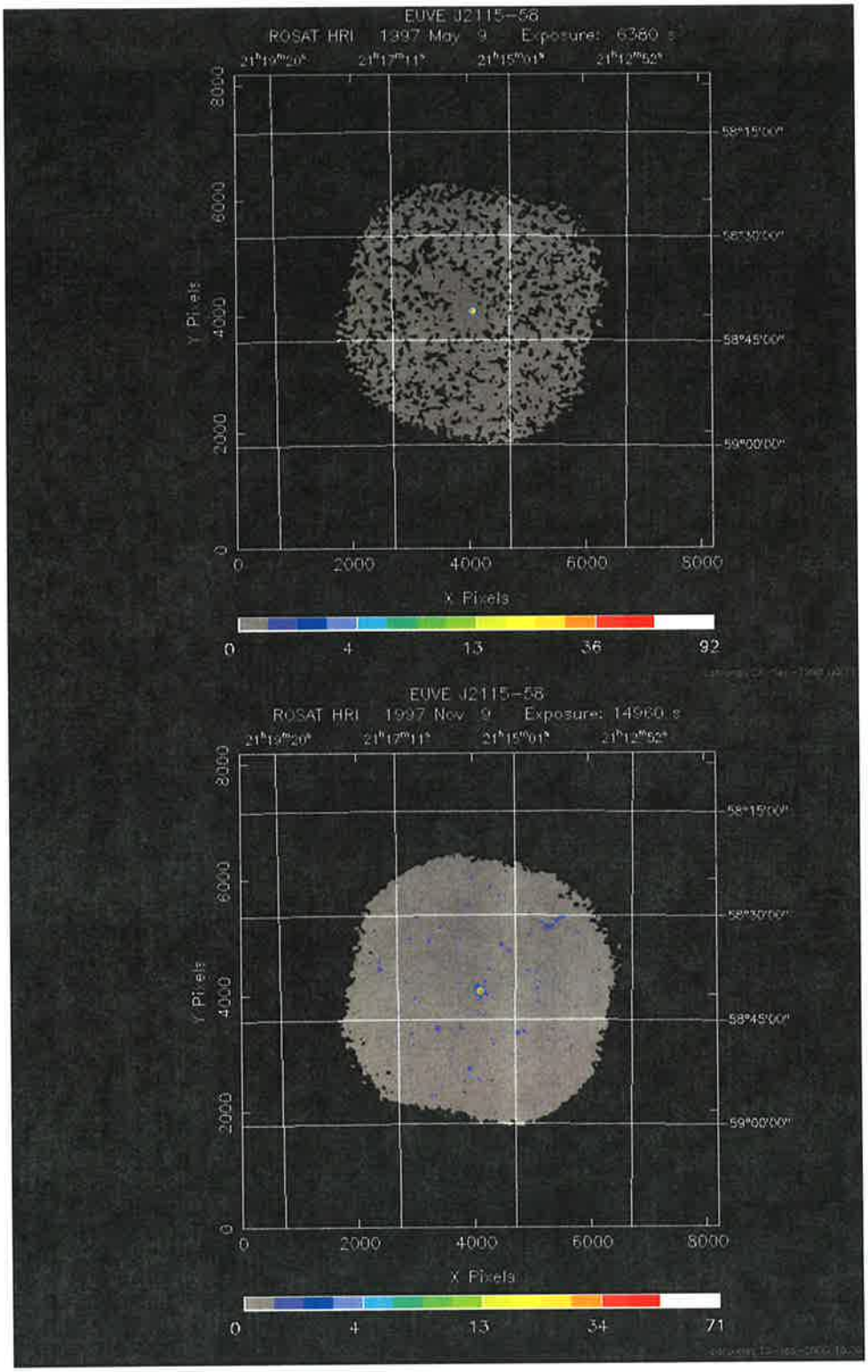

Figure 9.0

ROSAT HRI images of the Ind 1 field.
Top panel: a 6,380-second observation on May 9th 1997.
Lower panel: a 14,960-second observation on November 9th 1997.
The source is brighter in the earlier image, since the intensity scale (coloured bar) has a greater range than in the later image. But note that the later data-run was much longer, indicating that the CV was much more active at the time of the earlier observation.

One of the candidates exhibited strong H Balmer lines, as well as HeII 4686- typical of magnetic cataclysmic variables. Furthermore, significant variability was seen in the spectra obtained, suggesting that this candidate was the EUVE source, and indeed most likely an AM Her type CV.

The discovery spectra are shown in Figure 9.1. There are clear changes in both continuum and emission-line levels, as well as wavelength shifts in the emission lines (i.e. radial velocity variations). Thus, the CV was in a variety of different activity levels when these various data were obtained. Figure 9.2 shows the region of Hβ and HeII 4686; the RV and flux variations are evident. The optical position is (J2000.0) 21:15:41 -58:40:54.

9.3 Woomera and SSO photometry

Indus 1 was first observed from Woomera on the night of 15-16/04/1996 (local dates). Table 9.2 is an observing log for these data. Exposures ranged from 90 seconds to 180 seconds for the clear filter. As usual, the ST-6 was used with the C14, with the ST-4 and C5 providing auto-guiding. Error estimates for each time-series data point were derived from an exponential fit to each night's scatter-average magnitude plot for the check stars. Figure 9.3 shows the stars used in the clear-filtered differential photometry; Figure 9.4 shows the total set of scatter-magnitude data for these observations.

Some V and I data were obtained at the SSO 0.6-m telescope in July 1996.

Figure 9.5 shows the time-series data as differential magnitude vs. time. Scales on both axes are common to all plots. It is immediately seen that there is considerable variation in both the average magnitude of the CV, and of the form of the light-curve. There are times when a hump, recurring at approximately 110 minutes, is prominent; at other times, the light curve is essentially flat. There also are occasions when an underlying, longer-term trend is present, upon which the "hump" may or may not be superimposed.

Figure 9.6 shows these data *vs.* HJD. Figure 9.7 shows the two main groups of data, but with an expanded HJD scale such that day-to-day and month-scale variations are more readily seen.

The filtered SSO data are shown in Figure 9.8. It is clear that the amplitude of modulation increases toward longer wavelengths, as is expected from the shifted cyclotron emission from the accreting region(s) in polars. This effect may also be influenced by ellipsoidal modulation of the secondary. However, since there are times when the light curve is essentially flat, even in the "red" Woomera unfiltered photometry, it may be surmised that ellipsoidal modulation might not contribute much (if any) to this amplitude.

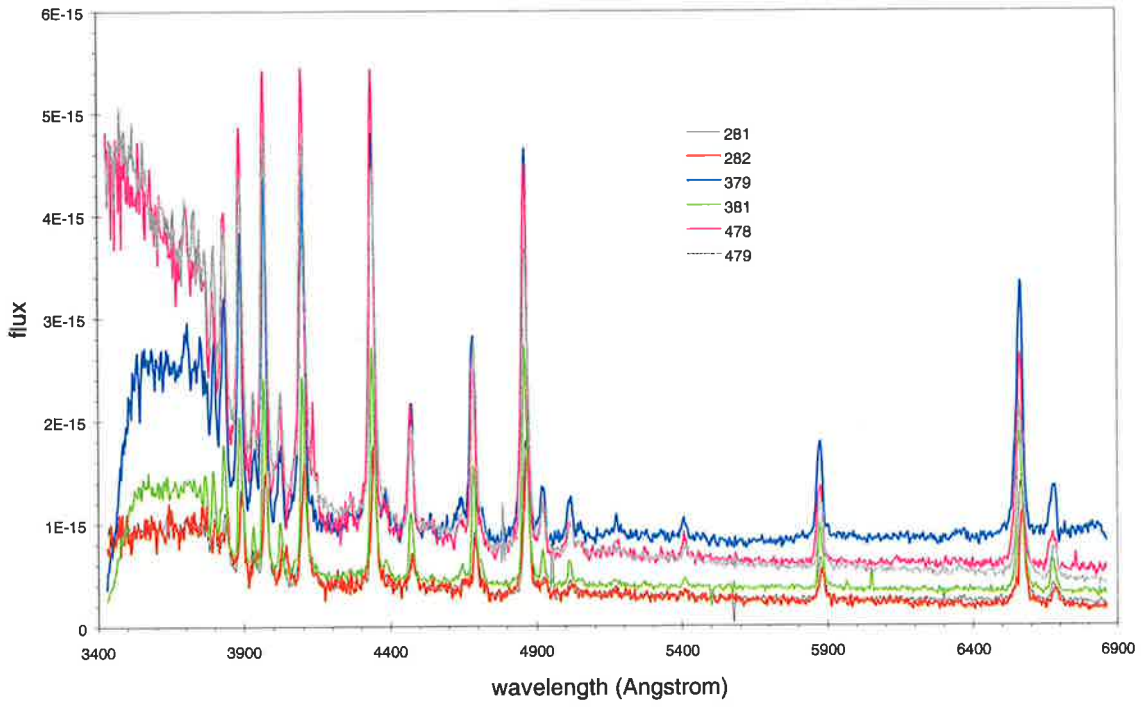

Figure 9.1

CTIO discovery spectra. Ordinate is flux (erg/cm^2/s/Å); abscissa is wavelength. Of note is the changing continuum level, but especially interesting is the change in line intensities.

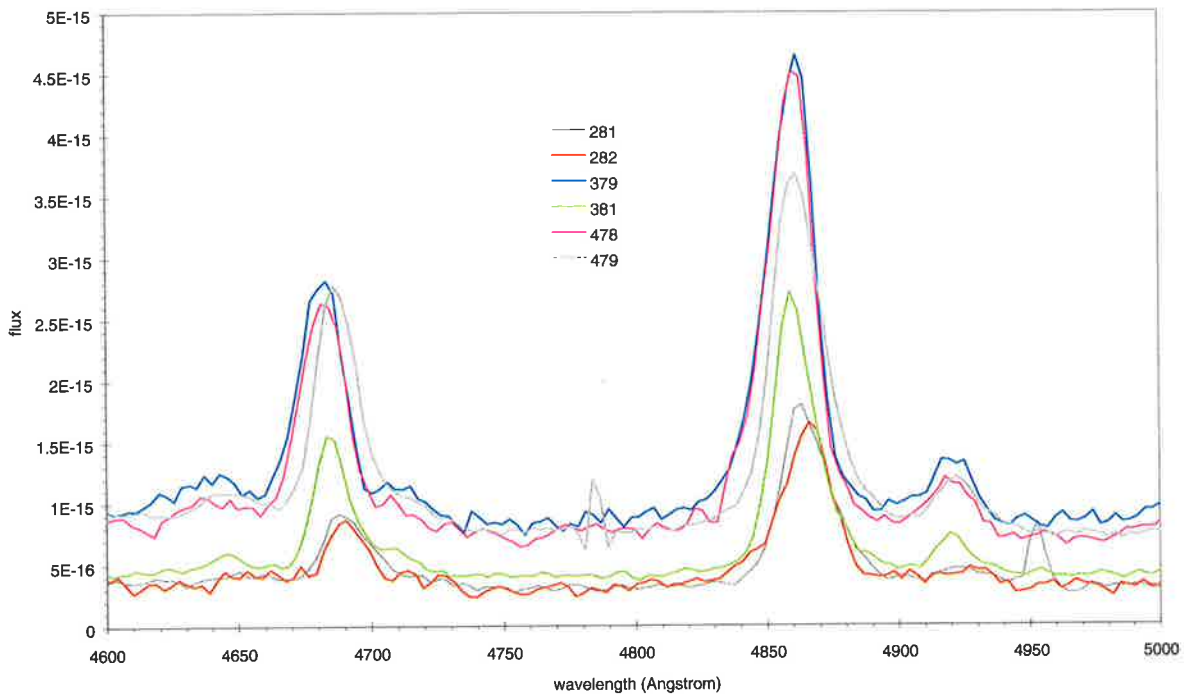

Figure 9.2

Radial velocity and flux changes near Hβ (near 4860 Å) and HeII 4686. Ordinate is flux (erg/cm^2/s/Å); abscissa is wavelength.

Table 9.2

Indus 1 photometry observing log

Date	Duration (mins)	Exposure (s)	HJD start (-2,450,000)	Filter	Site
150496	125	90	189.2422	clear	Woomera
160496	180	90	190.1882	"	"
170496	175	90	191.1948	"	"
190496	210	90	193.1658	"	"
170696	180	90	252.1132	"	"
200696	150	90	255.1278	"	"
220796	160	240	287.1768	V and I	SSO
150896	390	90	311.0090	clear	Woomera
190896	90	120	315.1788	"	"
200797	260	120	650.1090	"	"
210797	260	90	651.1038	"	"
230797	360	150	652.9315	"	"
260797	405	120	656.0337	"	"
270797	550	120	656.9541	"	"
290797	260	120	659.1247	"	"
300797	265	120	660.1135	"	"
310797	290	150	660.9768	"	"
281097	200	150	749.9617	"	"
291097	120	150	750.9487	"	"
011197	215	150	753.9489	"	"
021197	120	150	754.9588	"	"
031197	135	150	755.9695	"	"
041197	150	150	756.9528	"	"
240798	105	150	1019.0796	"	"

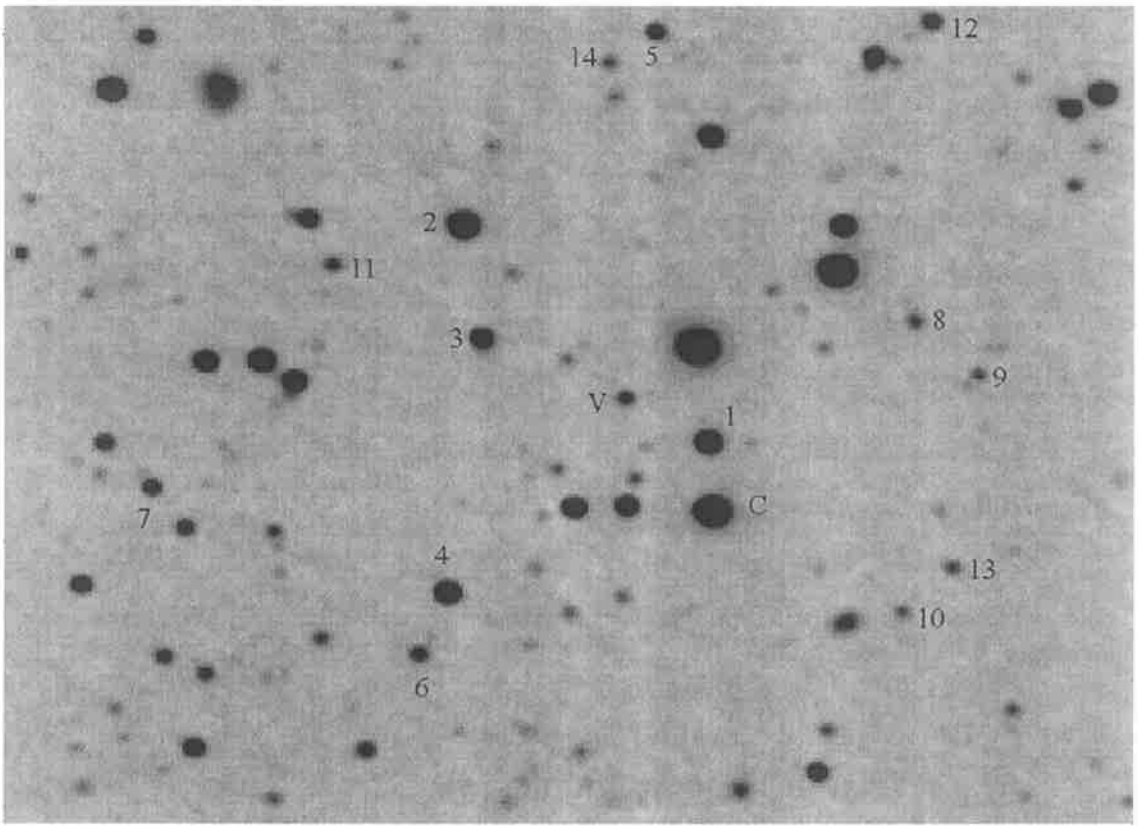

Figure 9.3

Cropped Woomera ST-6 image showing stars used in the differential reduction.
V = variable star; C = comparison star; check stars are numbered.
North is to the top, east to the left.
Approximate field centre and size: (J2000.0) 21:15:44 -58:40:54 8' wide 6.7' high.

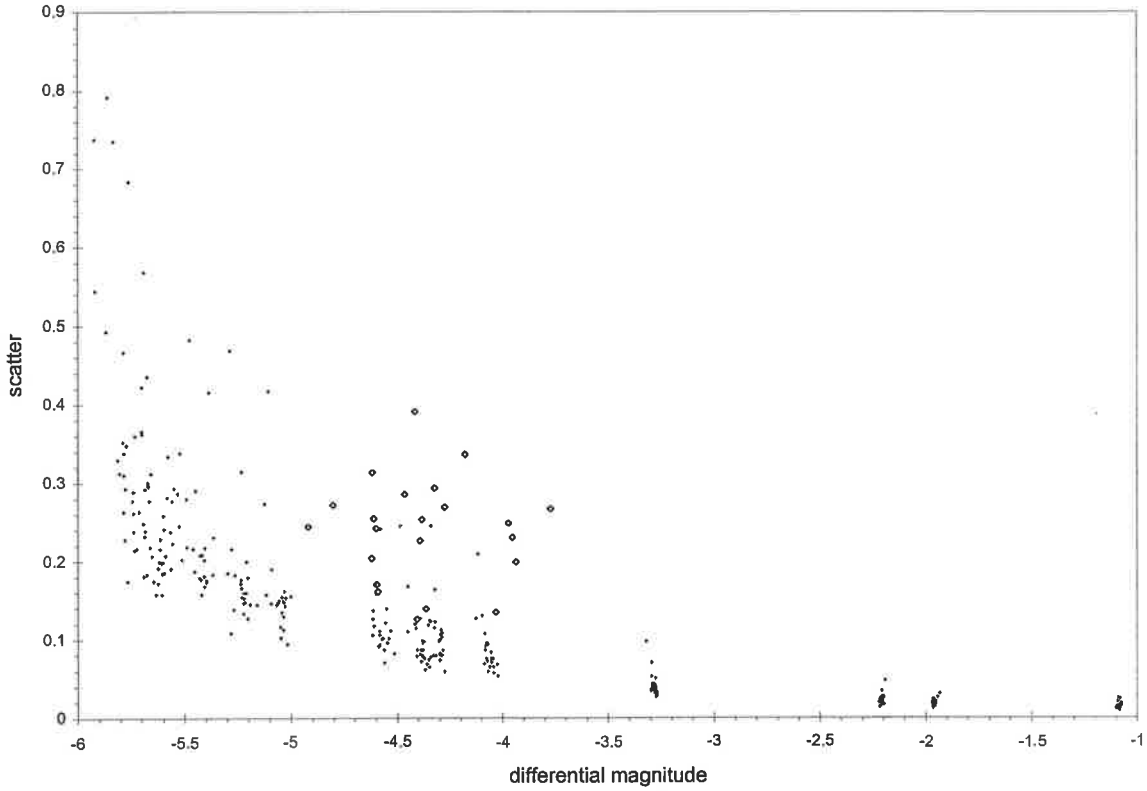

Figure 9.4

Scatter-magnitude diagram for Woomera white-light data.
Crosses denote K stars; diamonds are for the CV.
Note that a couple of poor-quality nights are evident by increases in the K scatter values above the general trend for most nights.

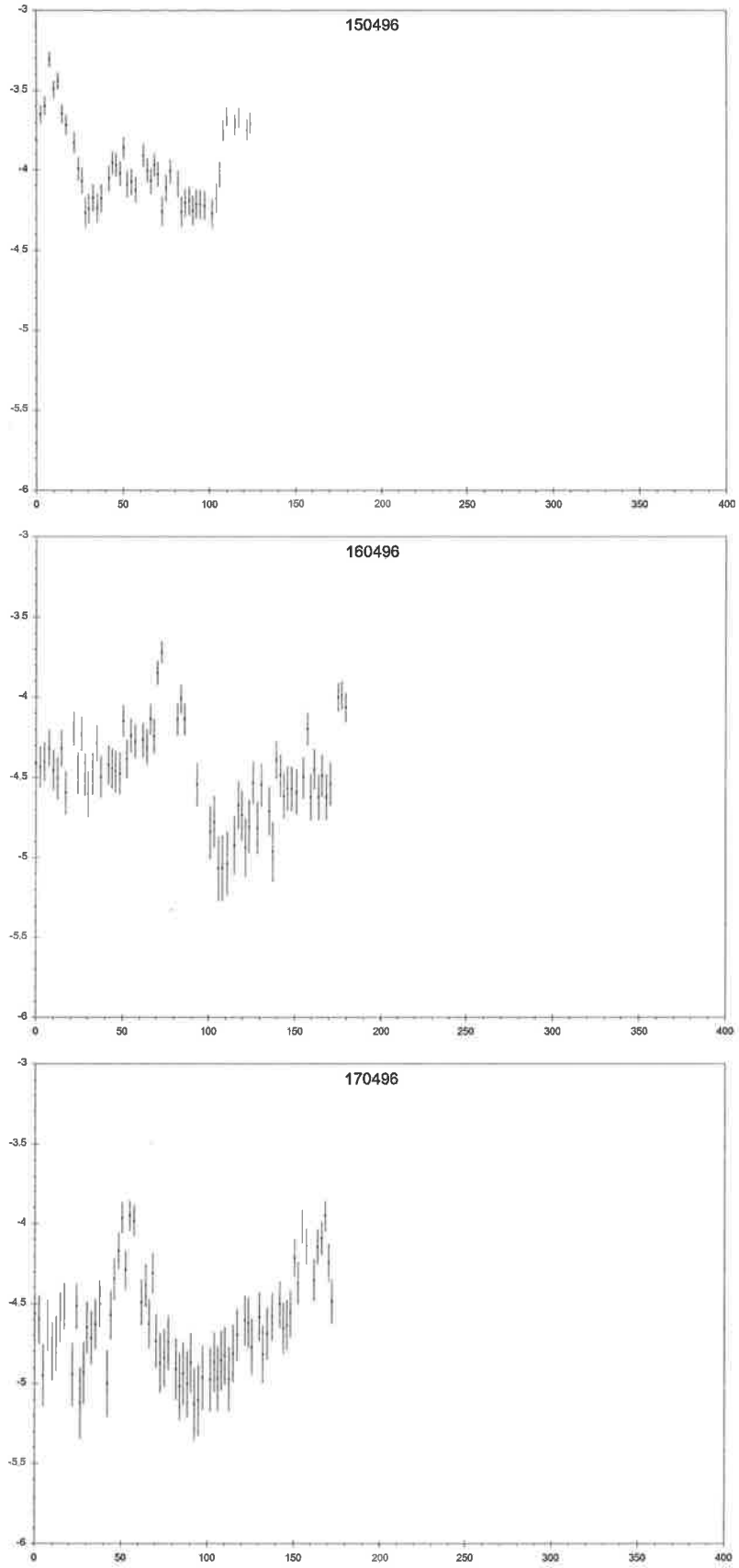

Figure 9.5
Woomera white-light photometry;
ordinate is differential magnitude, abscissa is time (in minutes).

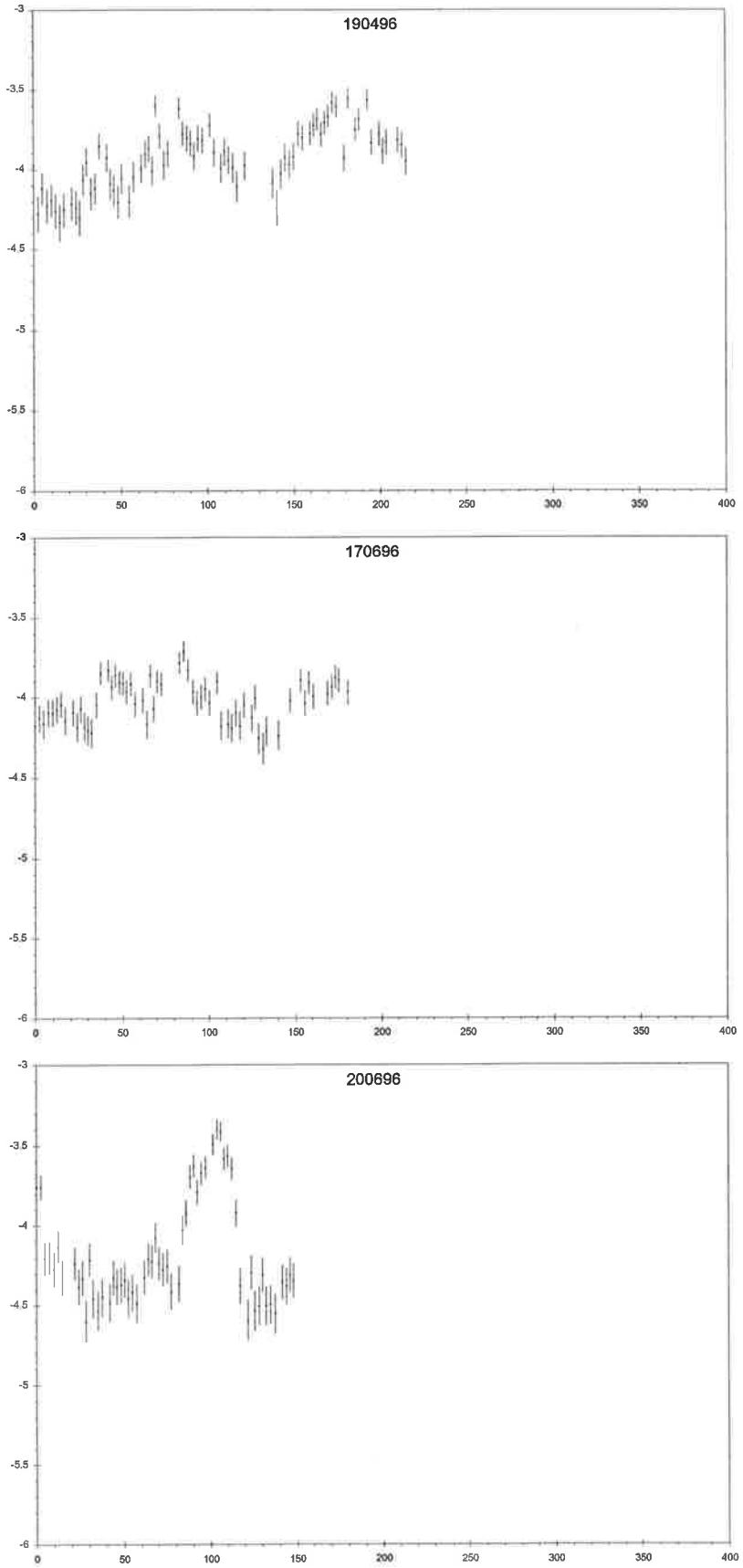

Figure 9.5 continued
Woomera white-light photometry;
ordinate is differential magnitude, abscissa is time (in minutes).

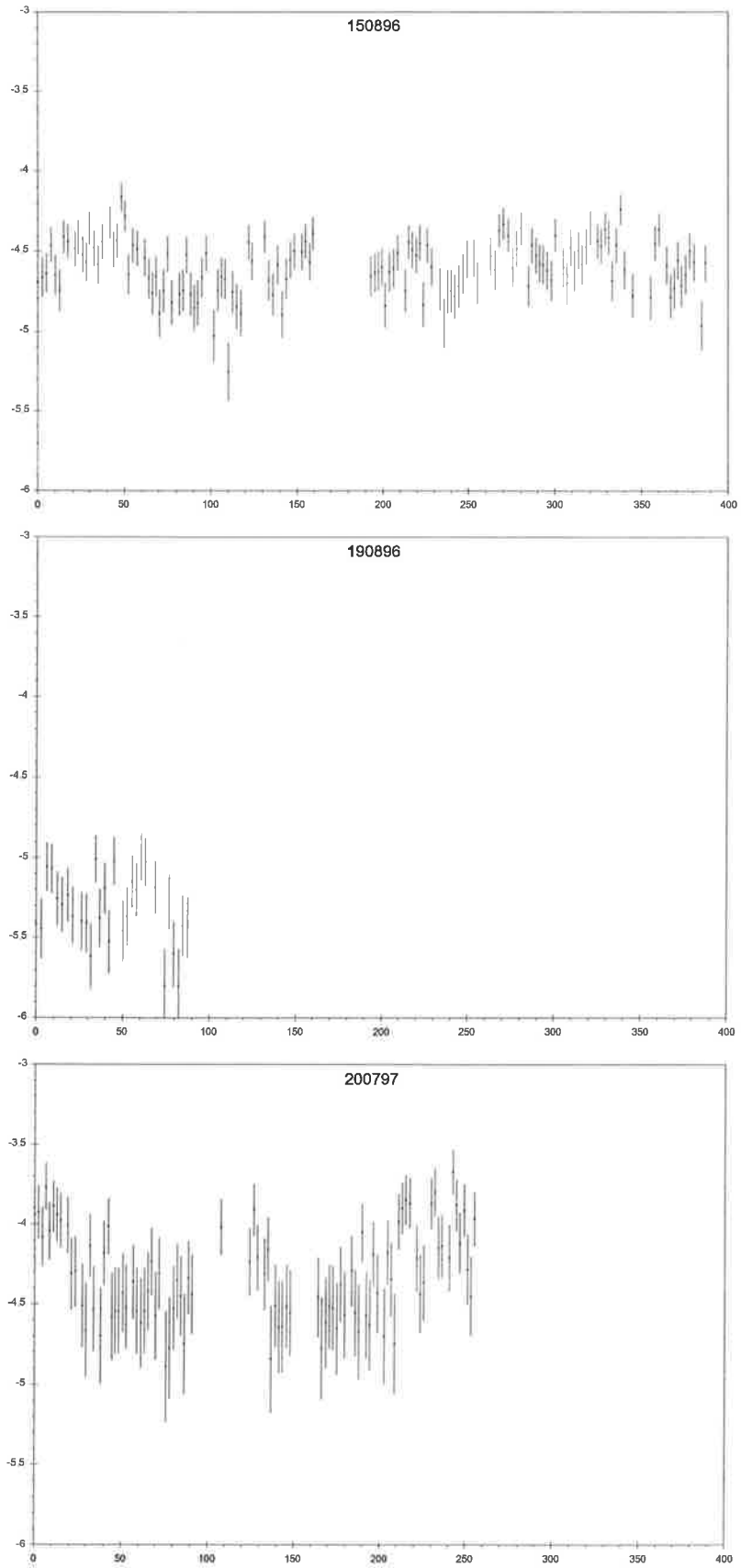

Figure 9.5 continued
Woomera white-light photometry;
ordinate is differential magnitude, abscissa is time (in minutes).

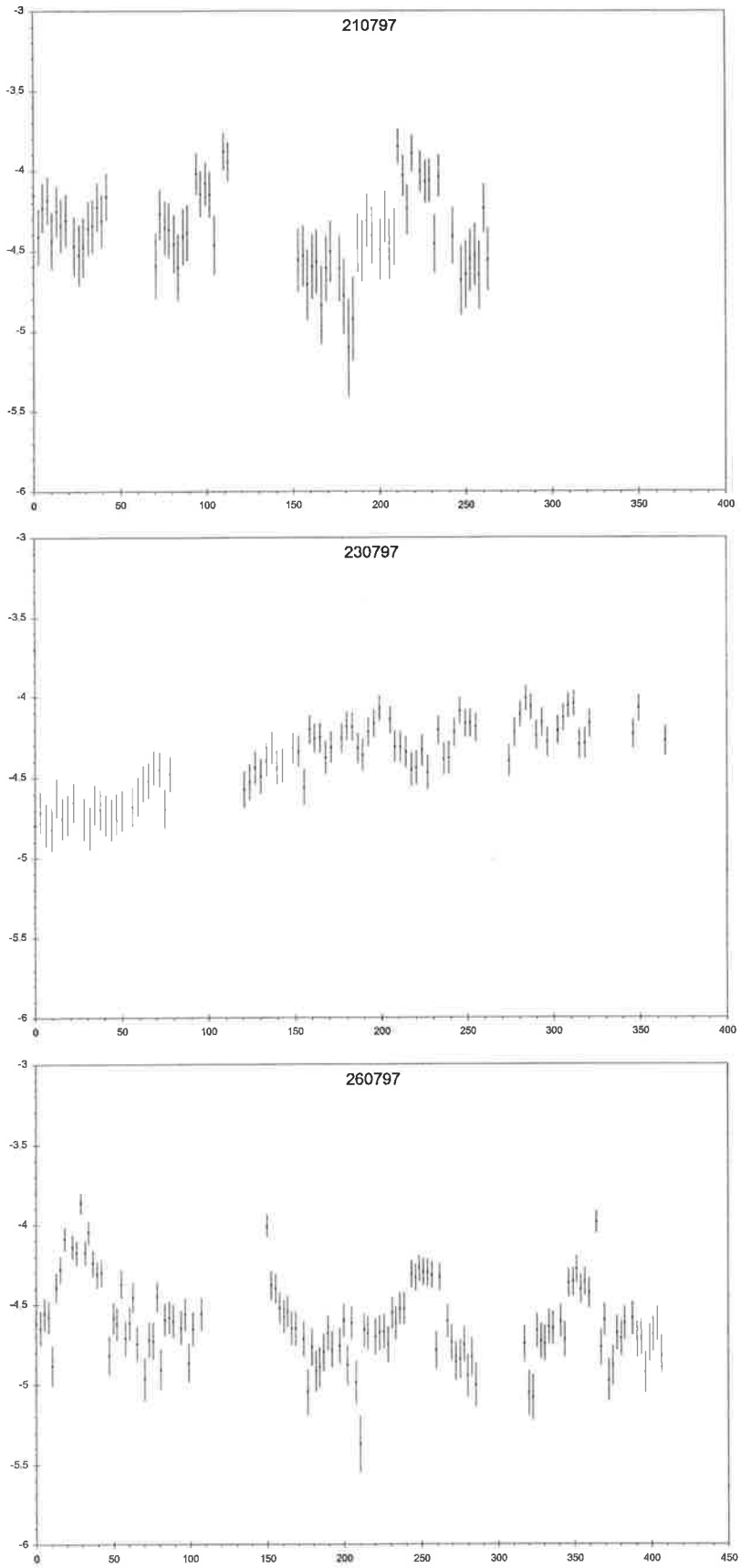

Figure 9.5 continued
Woomera white-light photometry;
ordinate is differential magnitude, abscissa is time (in minutes).

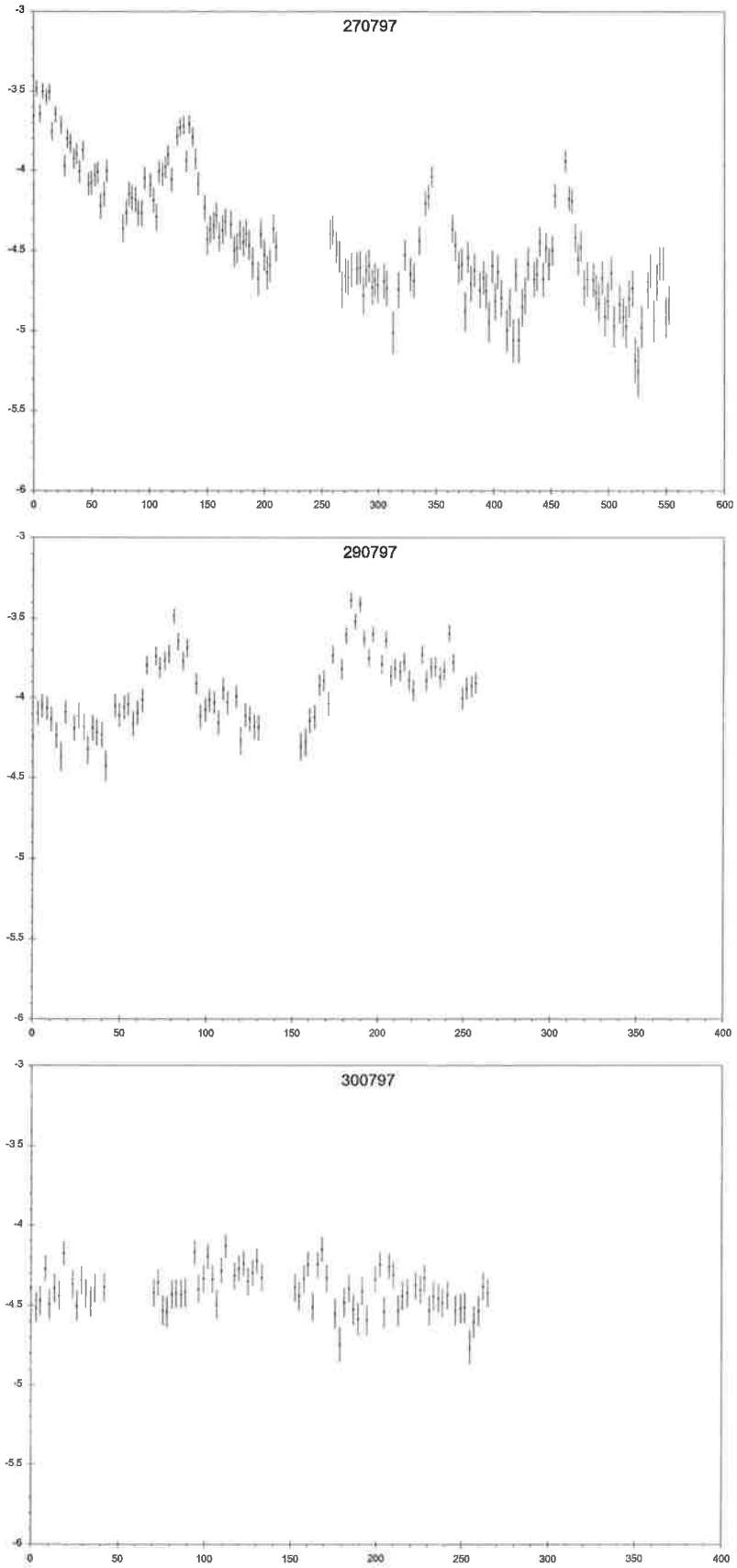

Figure 9.5 continued
Woomera white-light photometry;
ordinate is differential magnitude, abscissa is time (in minutes).

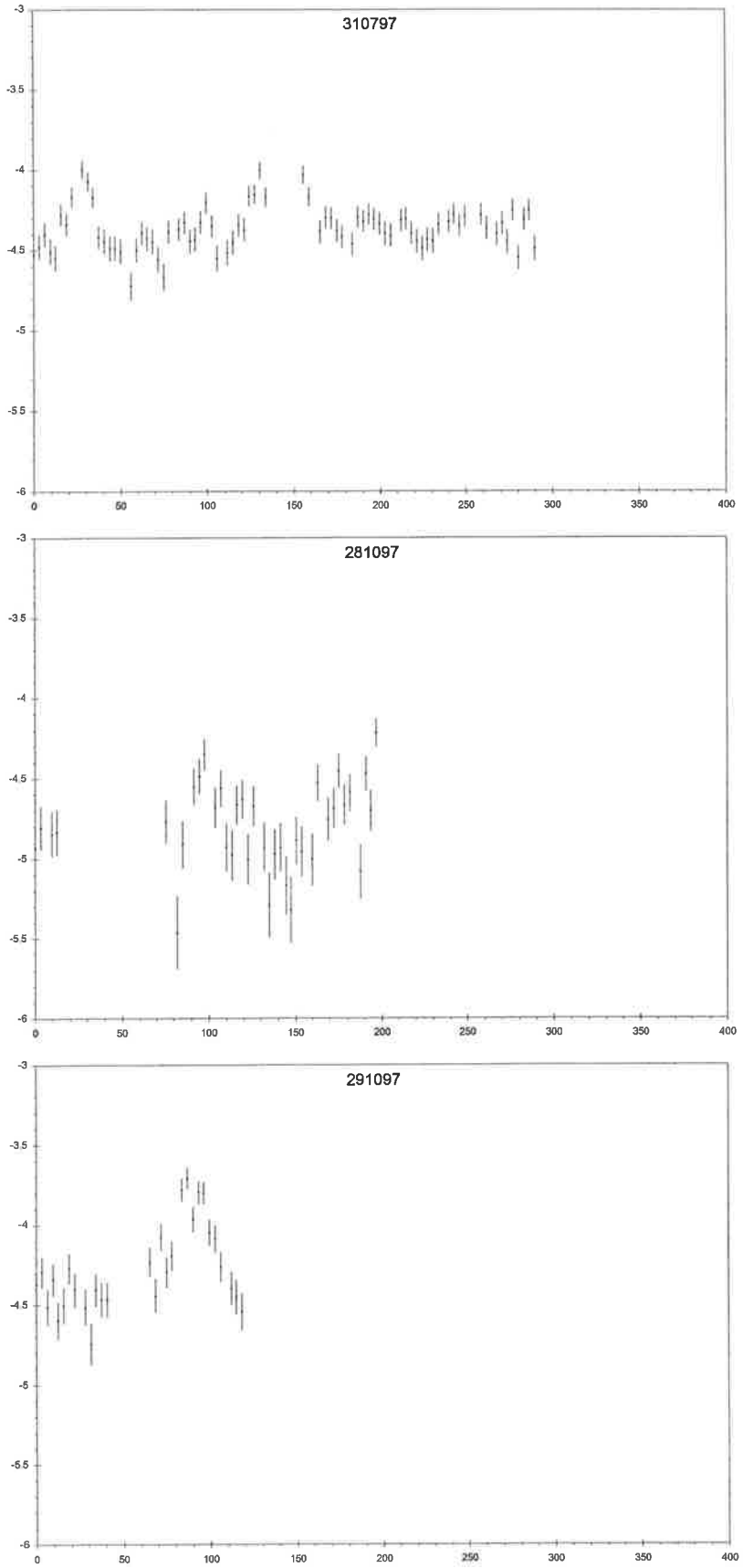

Figure 9.5 continued
Woomera white-light photometry;
ordinate is differential magnitude, abscissa is time (in minutes).

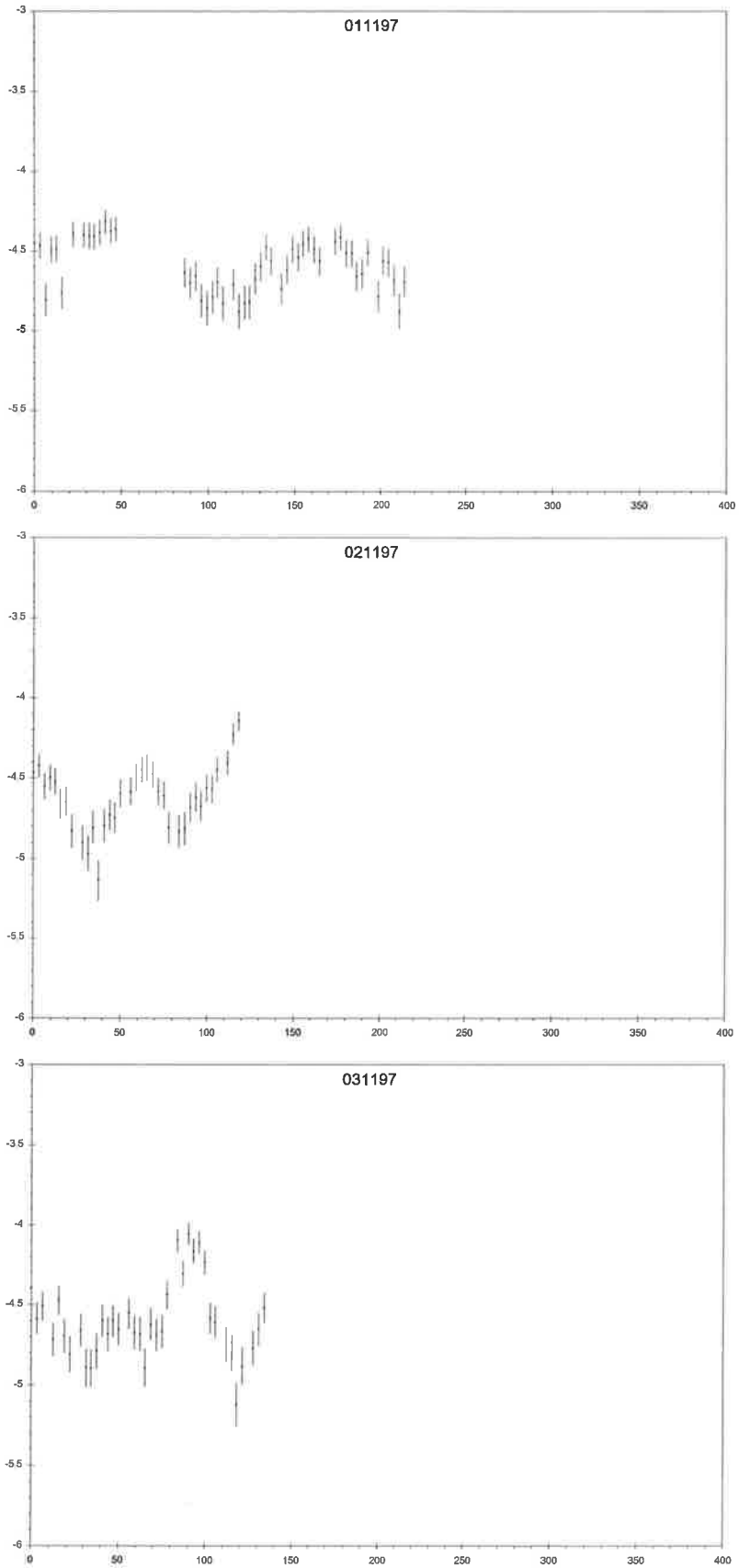

Figure 9.5 continued
Woomera white-light photometry;
ordinate is differential magnitude, abscissa is time (in minutes).

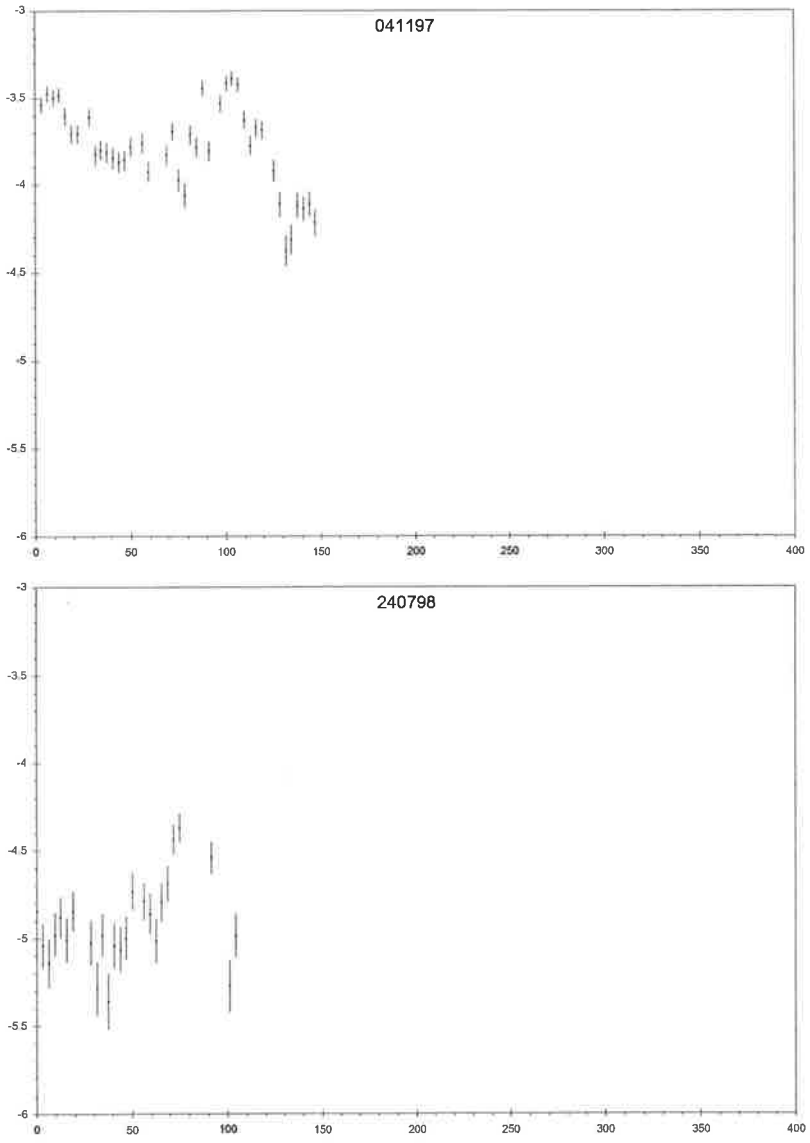

Figure 9.5 continued
Woomera white-light photometry;
ordinate is differential magnitude, abscissa is time (in minutes).

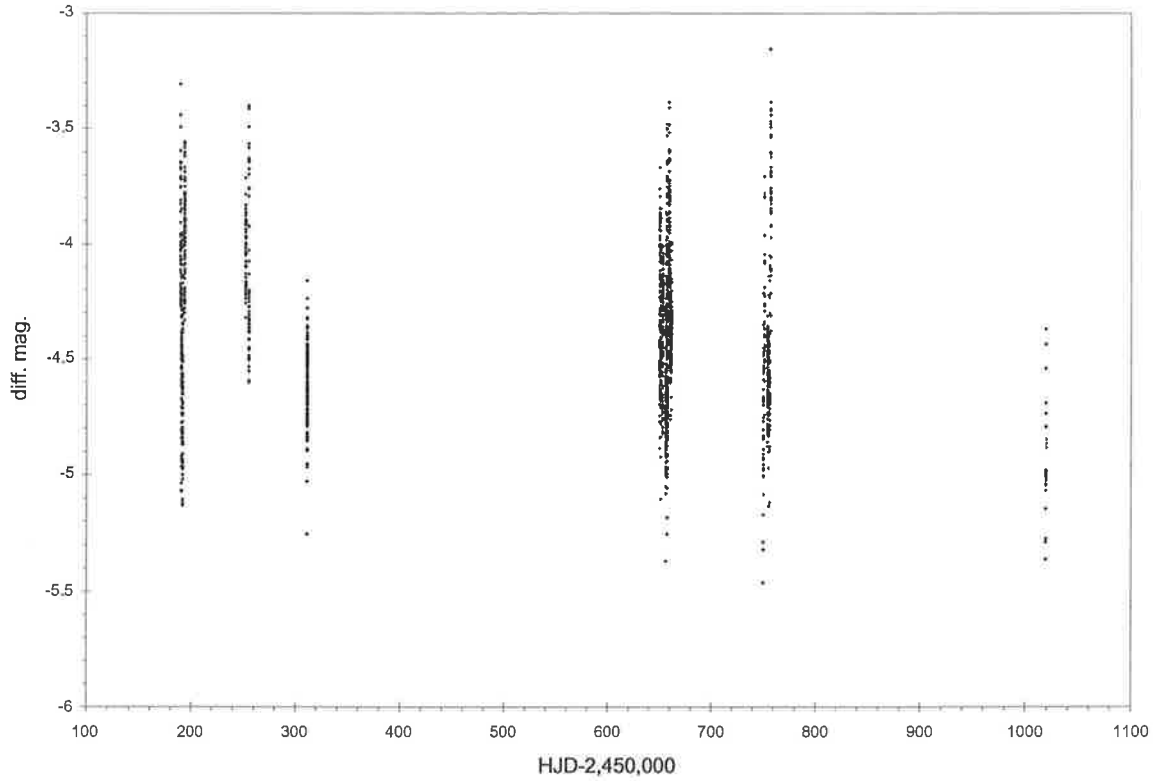

Figure 9.6
Woomera white-light photometry vs. HJD.

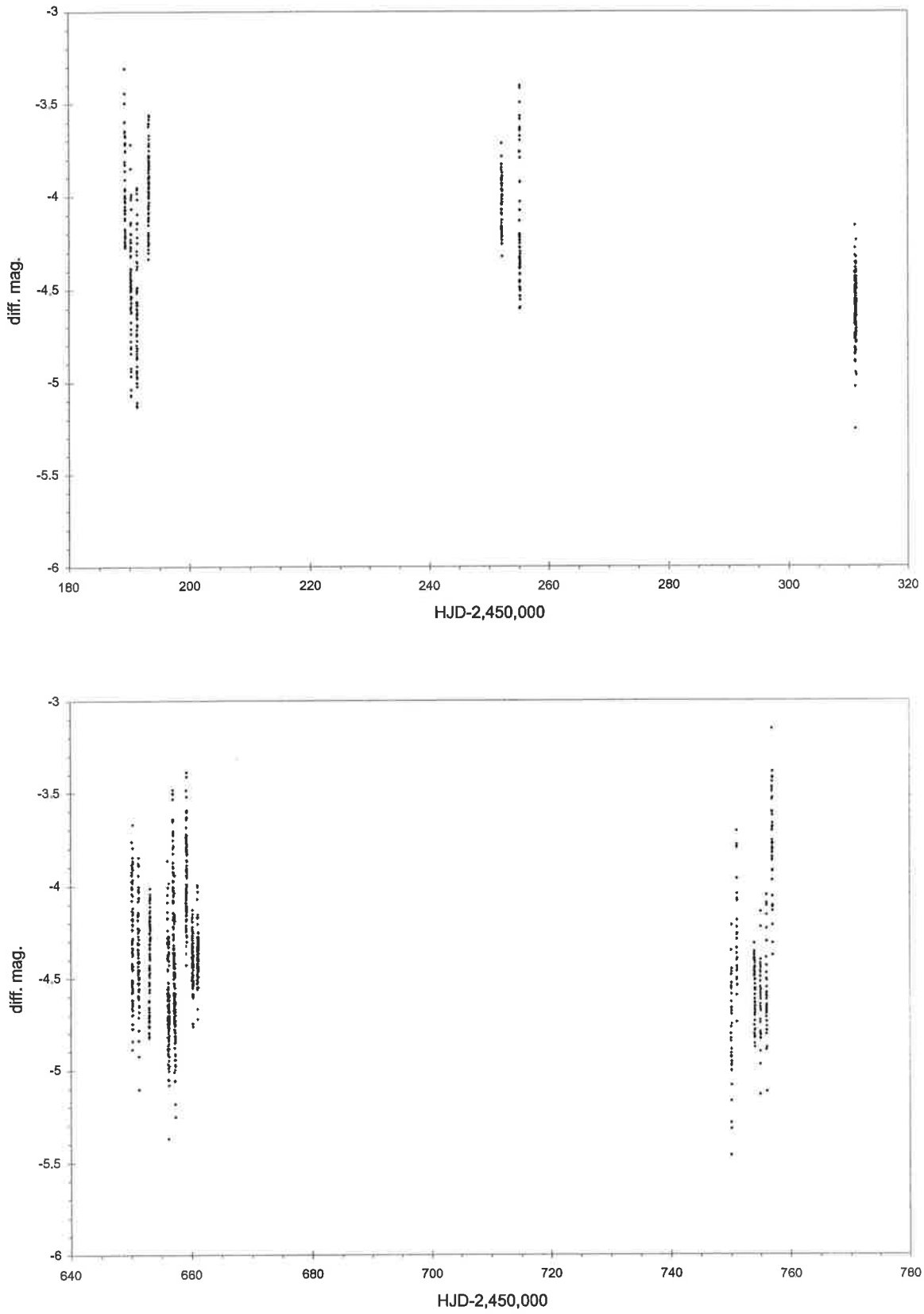

Figure 9.7
Woomera white-light photometry vs. HJD.

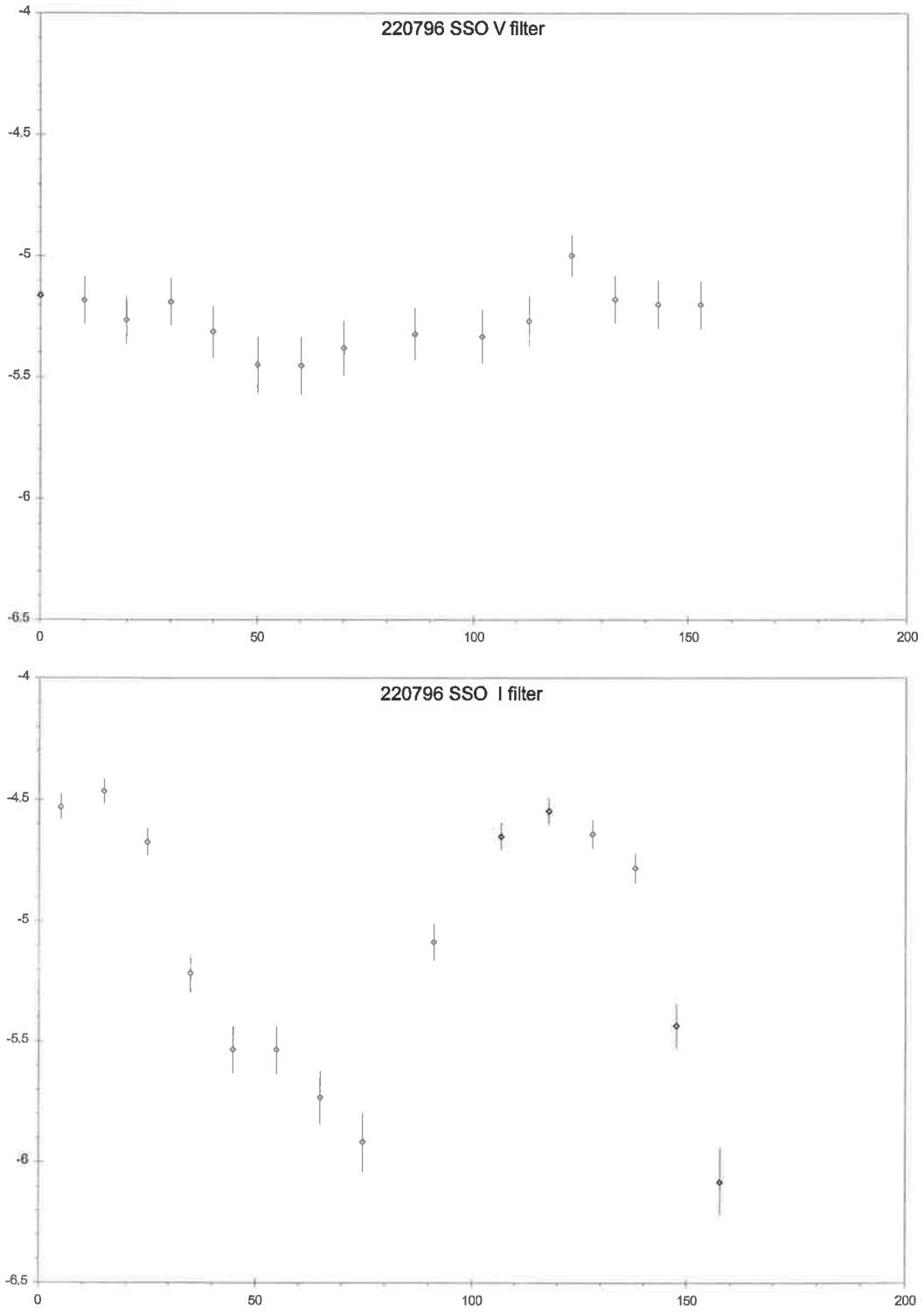

Figure 9.8

Quasi-simultaneous SSO filtered photometry; top plot is V, lower is I. Ordinate is differential magnitude, abscissa is time (in minutes).

On occasions, sequential VRI frames were obtained before or after clear-filtered time-series observations. Some of these have been co-added to produce tri-colour images of this field; the results are shown in Figure 9.9. These demonstrate that the CV reddens as it brightens, supportive of the suggestion of increased cyclotron emission in more-active states (cf. the case of an IP, which would be bluer in higher-activity states).

9.4 Data from other observers

Let us first consider observations reported in the literature. These cover optical spectroscopy, polarimetry, photometry and X-ray/EUVE data.

9.4.1 Spectroscopy

Vennes *et al.* 1996 (hereafter V96) report phase-resolved spectroscopy sufficient for estimation of the orbital period from RV variations of both line bases and peaks; they employ Hβ and HeII 4686. A likely $P_{orb} = 110.75 \pm 0.06$ min (with a one-day alias of 102.8 min) is found. A lack of cyclotron harmonics in their blue spectra suggests B<20MG for the primary. Schwope *et al.* 1997 (hereafter S97) derive $P_{orb} = 114 \pm 4$ mins from their single night of spectroscopy.

Whilst Craig's 1995 discovery spectra do show RV variations, the duration of the exposures used is too great to allow their use in examining the question of P_{orb}.

9.4.2 Polarimetry

S97 found circular polarisation variable from -15% to +15%, a strong indication of an AM Her classification. Changes in the form of the circular polarisation (CP) "light curves" suggest changes in the accretion geometry within the time-scale of the observations, and the change in sign suggests that pole-swapping is occurring. They find that P_{orb} from V96 is inconsistent with their polarimetry, and suggest that the CV is slightly asynchronous. They take their CP period to be the period of rotation of the primary, and give $P_{wd} = 109.84$ min or 109.65 min.

Ramsay *et al.* 1999 (hereafter R99) obtained polarimetry on 10 nights from 29/7 - 11/8/1997 at SAAO. Both positive and negative CP were seen, with positive being more common. Period searches on the data yield $P_{orb} = 110.889$ mins, $P_{wd} = 109.547$ min and $P_{beat} = 6.28$ days. They suggest that the accretion stream may wrap around the primary at some beat phases, so that accretion occurs on footprints of the same field line, rather than on diametrically-opposed footprints. It is also suggested that one pole may be significantly

Figure 9.9
Woomera VRI composite images of the field.
North is to the top, east to the left.
From top to bottom, CV is in faint, medium and bright states.
Note that the CV reddens as it brightens, suggesting its classification as an AM Her (i.e. polar) type. This is due to increasing red/IR emission from cyclotron harmonics in the more-active states.

stronger than the other, consistent with S97's noting that both hard (ROSAT) and soft (EUVE) emission is found at different epochs.

Ramsay *et al.* 2000 (hereafter R00) find the CP data more variable than those for R99. For example, on one night a CP peak did not repeat when expected. This suggests that the accretion geometry may vary on a cycle-cycle basis. The CP data were modelled using Stokes imaging, with this giving the form and position of accreting regions on the primary. Assuming B=15MG, best fits to the data were obtained for large i and small β; specifically, $i = 70°$ and $\beta = 10°$. Accretion on the upper hemisphere of the primary yields negative CP (rare); on the lower, it is positive (common).

9.4.3 Photometry

S97 obtained unfiltered, B- and I-band photometry at SAAO over 3-9/9/1996. Alternate B and I frames on the night of 7-8/9/1996 show little modulation in B (<0.4mag) but ΔI around 1.4mag, with mag_B around 18, and mag_I approximately 17 for the flat portion of the modulated light curve. The white-light data show both modulated and unmodulated light curves.

R00 show some intensity data obtained during their polarimetry; again, the light curve varies between exhibiting little modulation to significant modulation. Intensity peaks occur at the same WD spin phases as do CP peaks.

9.4.4 X-ray/EUVE data

R00 obtained simultaneous RXTE data with their optical observations. Ind 1 was detected in the 2-15 keV range by RXTE, over 21-27/7/1998. A discrete Fourier transform of the data yielded a peak at the spin period of the primary, i.e. at P_{wd}. Assuming the source of the X-rays to be located at the sites of CP emission, the X-ray light curves were well modelled. It was found that some X-ray intensity peaks corresponded to (unfiltered) optical intensity and positive CP peaks.

The resulting consensus is that Ind 1 is a slightly asynchronous polar, in fact the fourth such CV (the other known examples being V1432 Aql, BY Cam and V1500 Cyg). The difference between P_{orb} and P_{wd} is of the order of 1%. It is this asynchronism that varies the accretion geometry on the time-scale of P_{beat}, and is responsible for the changing form of the photometric light curve (and of the CP data, also).

At some beat phases, accretion occurs dominantly on the eclipsing, lower pole, yielding "humped" photometric data, as well as pulsed, positive CP. At other beat phases, the poles are fed more or less equally. The optical intensity is slightly modulated, and there is both positive and negative CP; these will cancel, and leave a "flat" CP waveform. At others, the upper pole is dominant, and there is negative CP, with the optical intensity being nearly constant.

The Woomera data reflect these findings. There are nights when a clear modulation is present; at others, the light curve is essentially flat. Unfortunately, there are no CP data simultaneous with the Woomera data.

9.5 Woomera data- photometric periods and phase zero

The data immediately reveal a photometric period around 109-110 minutes, as reported by other researchers. Modulation also is present on other time-scales, ranging from cycle-cycle brightening or fading trends, to day-scale changes in overall system intensity. The first is due to rotation of the white dwarf primary; the others may be related to the beat period between P_{orb} and P_{wd}, and its effect on the accretion geometry of the system.

In order to estimate P_{wd}, we shall examine only those data exhibiting the photometric hump, i.e. when the CV is accreting mainly at the far, eclipsing pole. Further, since Ind 1 displays this behaviour for a range of overall CV brightness, each night's data were shifted by the average intensity for that night. (It is to be noted that the differential magnitudes were converted to relative intensities (variable/comparison) for the following discussion).

Figure 9.10 shows the results of neural-network period searches on these data. The best period found is 6579.383s (resolution = 0.015s); Figure 9.11 shows *all* the (pulsed) data phased with this period. It is found that a change of 0.1-0.15s from this period yields a noticeable smearing in the phase plot. Figure 9.12 shows the unpulsed data thus phased. Since only those nights showing the *greatest* pulse amplitude were included in the pulsed data, there are indeed some nights with minor amounts of modulation in the "non-pulsed" data; this leads to the slight bump present in this figure.

Initially, phase zero was taken to be one of the spectroscopic phase zeroes from V96 for their assumed period of P_{orb} = 110.75 minutes. It was seen that the peak of the Woomera photometric data was then somewhat displaced from $\phi = 0$ using such a phase zero. As this system is asynchronous, there is not necessarily any correlation between a spectroscopic phase zero (related to P_{orb} and found from spectroscopy of emission regions on or near the secondary

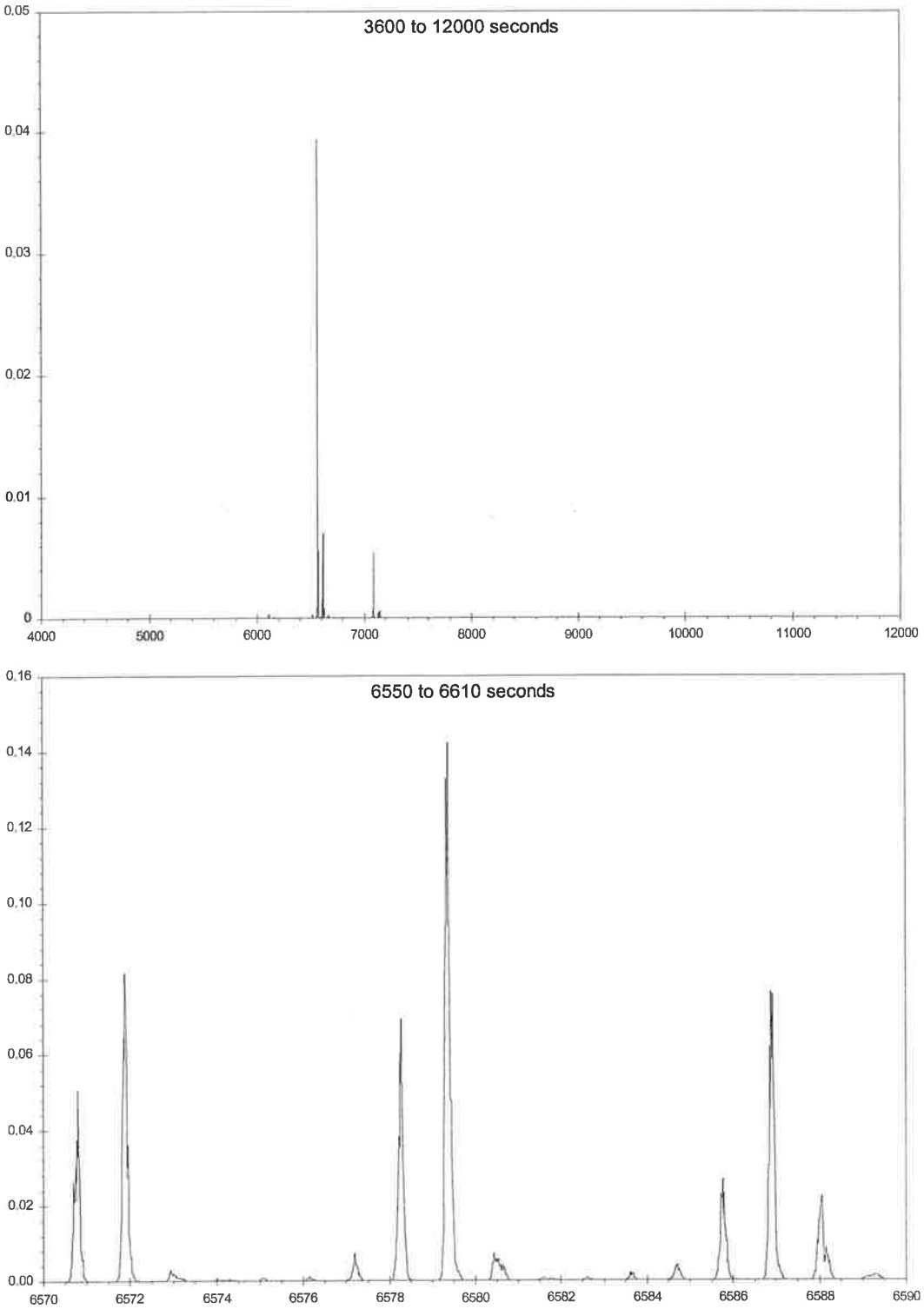

Figure 9.10

Neural-network period searches on pulsed and shifted Woomera data.
Ordinate is strength of trial period; abscissa is period (in seconds).
Top: wide-range search.
Bottom: expanded view, near best frequency, from a narrow-range search.

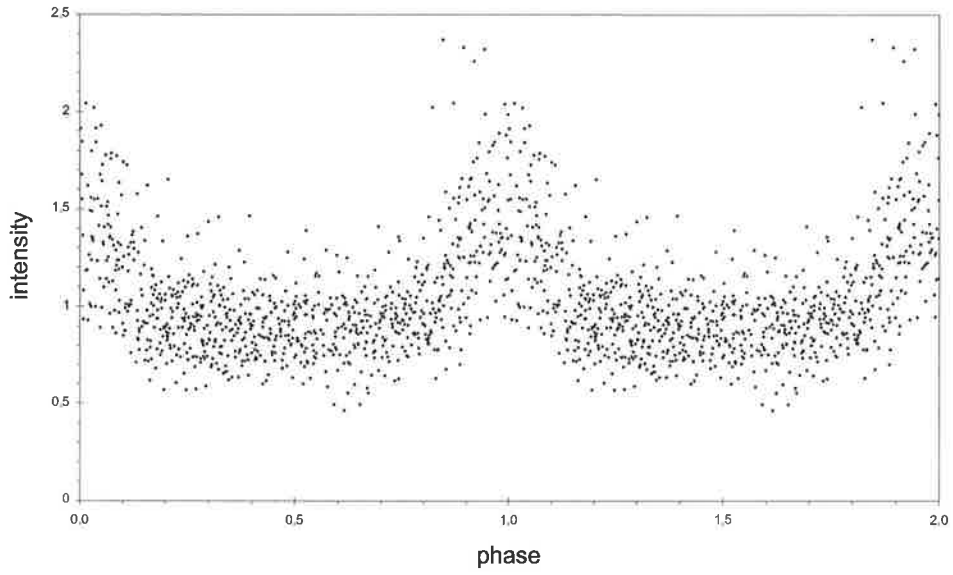

Figure 9.11
Pulsed Woomera white-light data, phased at 6579.383 seconds.

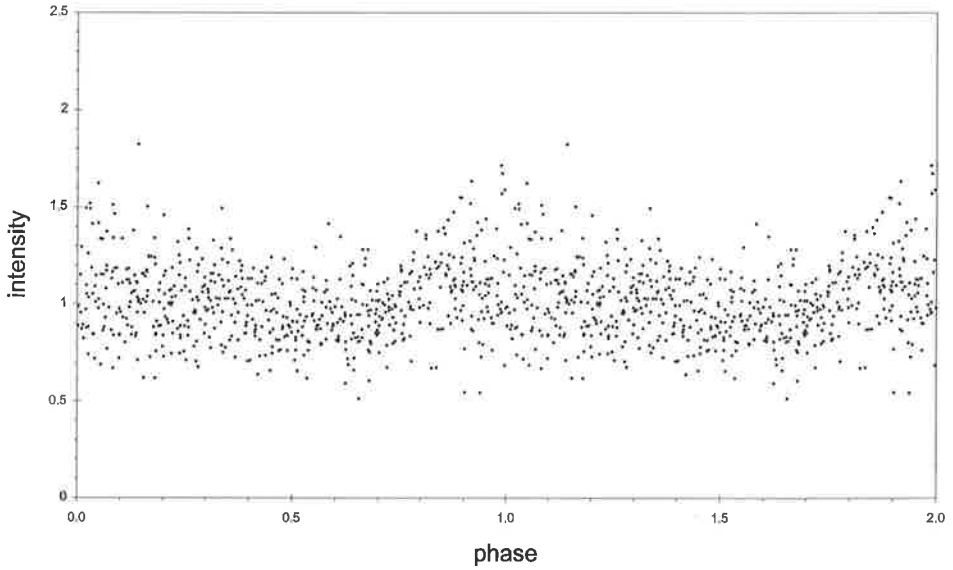

Figure 9.12
Unpulsed Woomera white-light data, phased at 6579.383 seconds.

star) and a photometric phase zero (related to P_{wd} and found from photometry of accretion regions on the primary). We are quite free to chose a different photometric phase zero.

A phase plot of the shifted and pulsed Woomera data (excluding the night of 270797 for which a significant fading trend was present in the data) was examined by eye. The phase zero was adjusted from the V96 values until the photometric peak was centred about $\phi = 0$. The resulting zero was found to be HJD 2,450,198.2385. It was noted that a shift of ± 0.0005 days away from this produced a just-noticeable movement of the peak away from $\phi = 0$, and a shift of ± 0.001 days produced a very evident shift. Thus, a photometic phase zero of HJD $2,450,198.2385 \pm 0.0005$ was adopted.

We may phase the Woomera pulsed data with the values of P_{wd} listed in Section 9.4. The resulting plots are given in Figure 9.13. It is seen that none of these fits the Woomera data as well as the period derived therefrom. It is therefore proposed that a more accurate value of the white dwarf spin period is

$P_{wd} = 6579.383$ seconds, or 109.656 minutes.

As noted above, a change of 0.1-0.15s in this period produces smearing in the phase plot, and may therefore be considered as an approximate upper bound for the error in the period estimate.

We may now examine the question of the beat period. Having no estimate of P_{orb} from Woomera, we must rely on those given in V96 and R99. The resulting beat periods are shown in Table 9.3, and use P_{wd} as given above.

Table 9.3

Beat periods for various P_{orb}

	P_{orb}(s)			
	6641.4	6645	6648.5	6653.4
P_{beat} (s)	704551.67	666259.98	632856.02	591397.55
P_{beat} (d)	8.1545332	7.7113423	7.3247225	6.8448791

Is any of these apparent in the photometry? Figure 9.14 shows the unshifted intensity data phased with each of these periods; none shows particularly great evidence of clear modulation at these periods, although $P_{orb} = 6645$s appears to impart some structure to the phase plot.

A neural network (NN) period search on these data in the range 6-8 days results in Figure 9.15. A best period of 649369.68s (7.5158528d) is found, and this implies a P_{orb} of 6626.724s (110.779min). This is consistent with results in V96 and R99. Figure 9.16 shows the data phased with this beat period; however, there is no clear pattern evident. Checks also

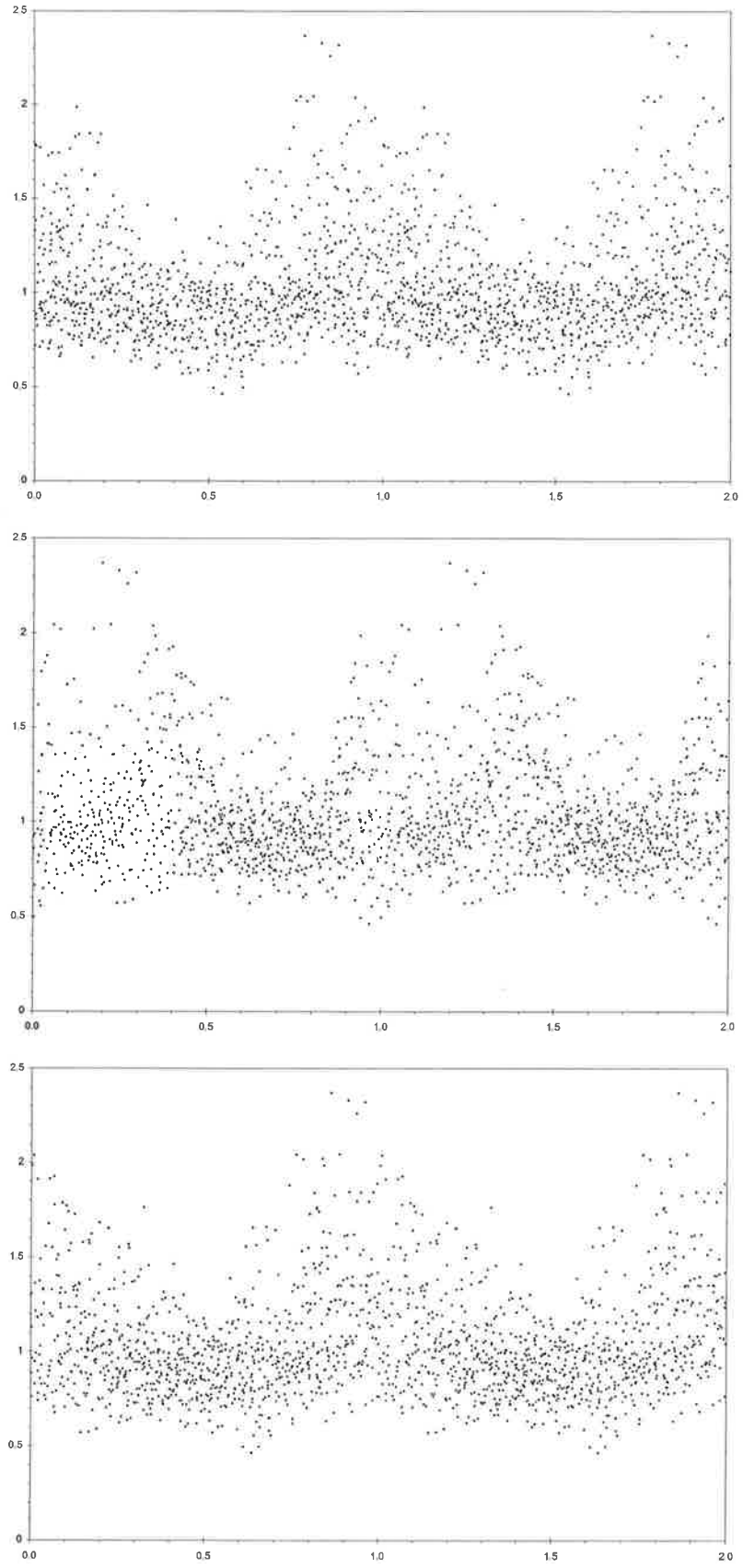

Figure 9.13

Pulsed Woomera data phased at (top to bottom) 109.84 minutes, 109.65 minutes and 109.547 minutes. Ordinate is relative intensity, abscissa is WD phase.

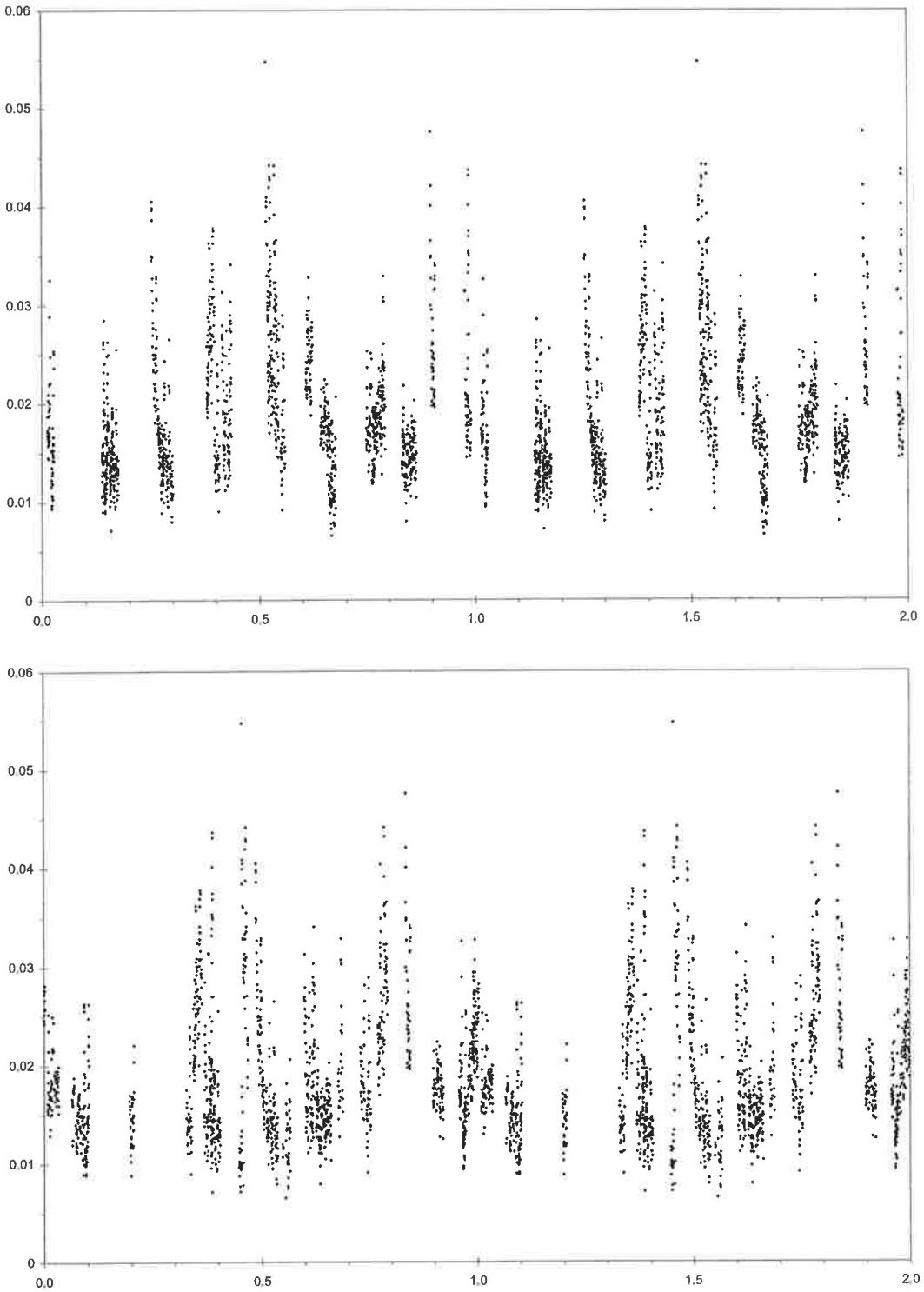

Figure 9.14

Unshifted Woomera white-light data phased with the beat periods associated with P_{orb} of 6641.4s and 6645s respectively. Ordinate is relative intensity, abscissa is beat phase.

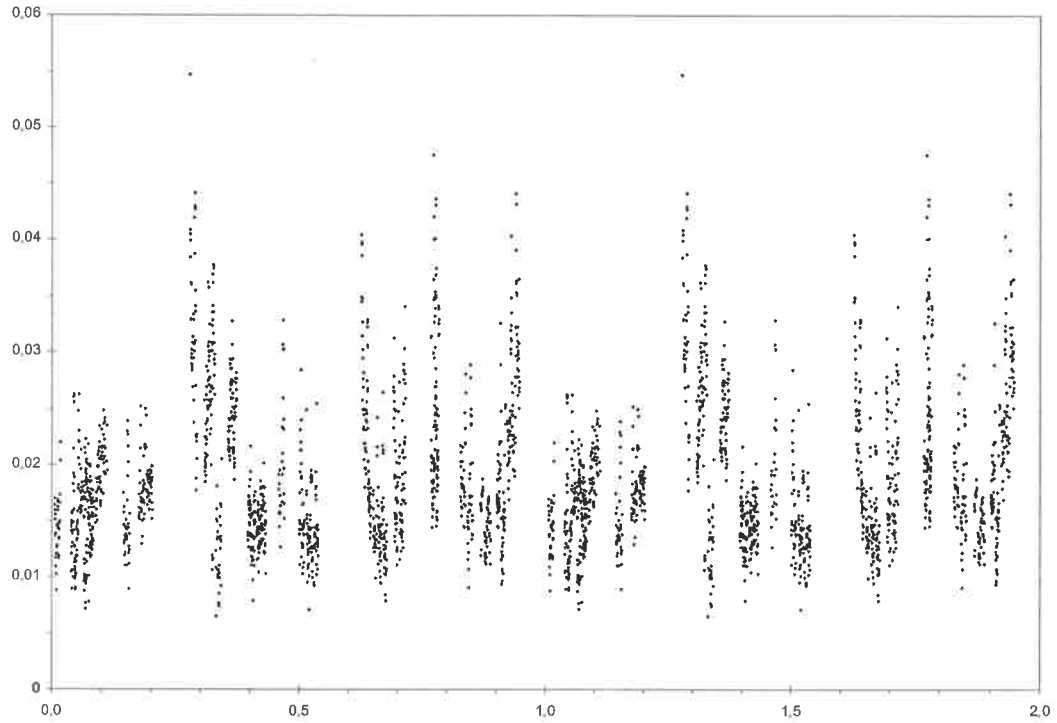

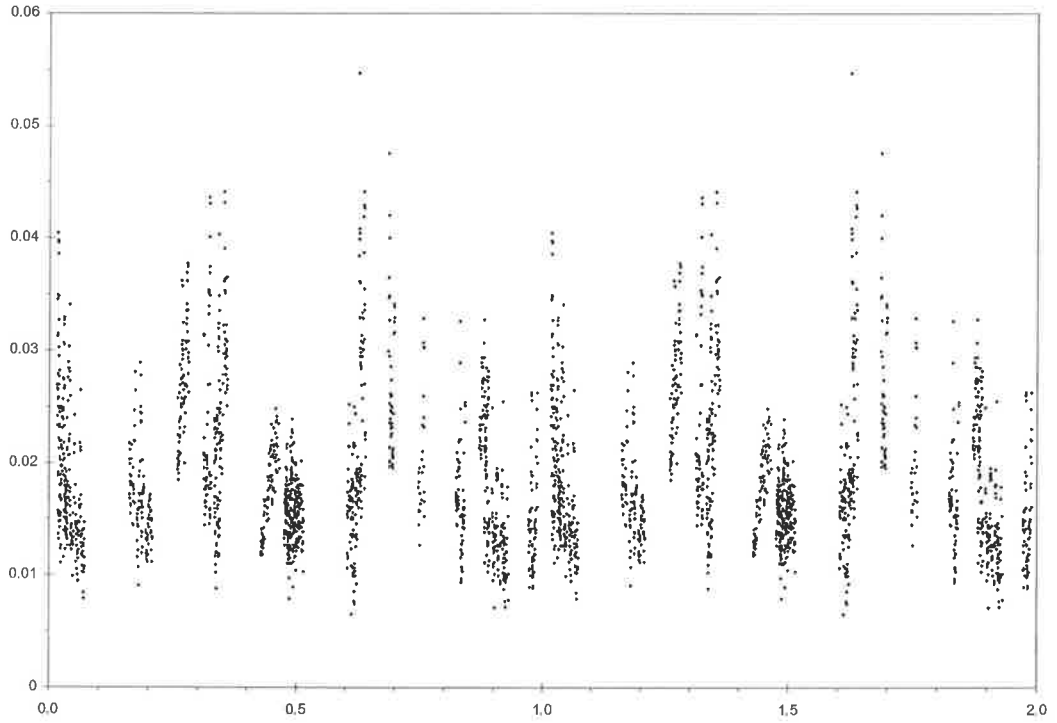

Figure 9.14 continued
Unshifted Woomera white-light data phased with the beat periods associated with P_{orb} of 6648.5s and 6653.4s respectively. Ordinate is relative intensity, abscissa is beat phase.

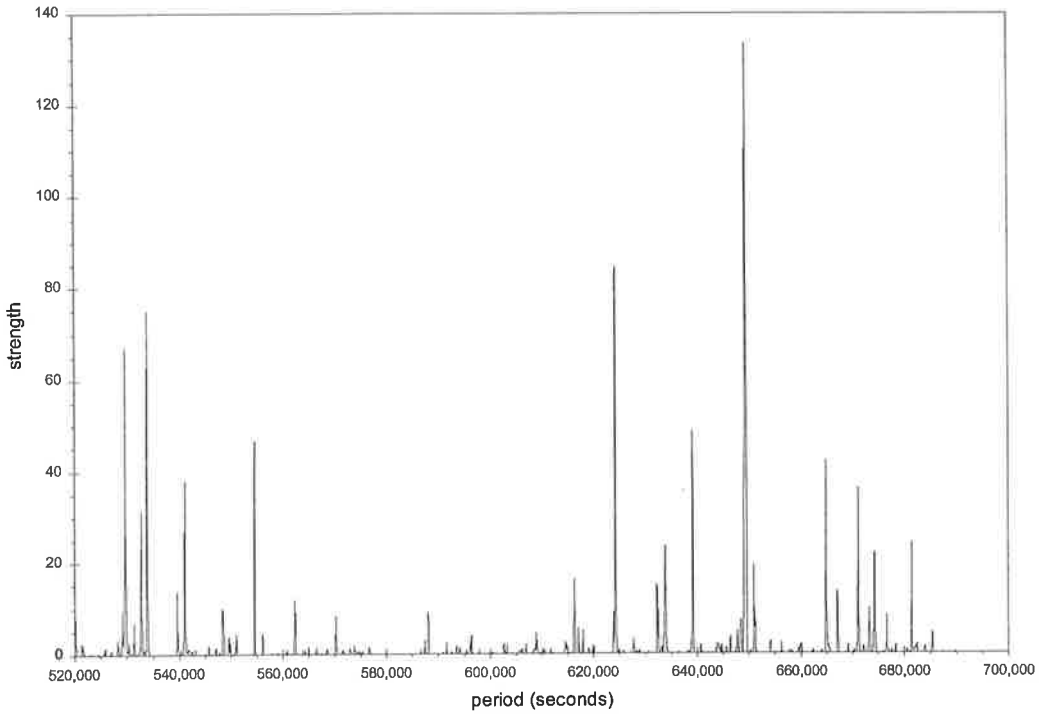

Figure 9.15
Neural-network search on all Woomera data.
Periods searched for in the range 6-8 days.

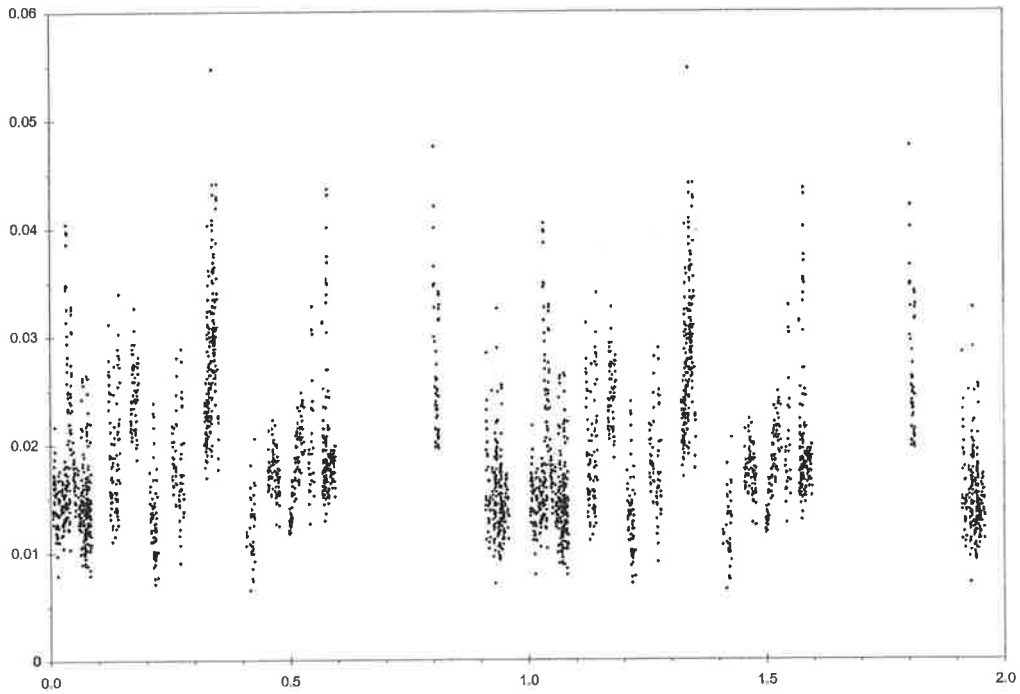

Figure 9.16
Unshifted Woomera white-light data phased with the beat period associated with a P_{orb} of 6626.724s.
Ordinate is relative intensity, abscissa is beat phase

were carried out using only each night's average HJD and brightness; this yielded a different, and similarly poor, best fit period. It would appear that the data are not sufficient to examine the question of P_{orb} significantly from consideration of the beat period.

It is clear that there exist consistent trends in the brightness of this system over several days. Figure 9.17 shows three examples of multi-night data where this is seen. However, just what the associated periodicity is (if any), is not easily ascertained. Of course, it may be that the amplitude of the photometric hump is modulated at the beat period. It is felt that investigation of this would require data of a higher accuracy than is presented here.

9.6 Woomera data- some interesting nights

9.6.1 150596 to 190596

These nights' data show a definite long-term trend (see Figure 9.17), and it is to be noted that a clear photometric hump is seen in spite of the different average brightness for different nights. Also, the brightness before and after a hump can be significantly different (see 160496 and 170496 data). This may suggest change to the accretion geometry (and rate, at least local to the accretion region(s)) on a sub-orbital time-scale.

9.6.2 170696 and 200696

The 170696 light-curve is nearly flat, with only small-scale variation over about one-and-a-half orbits. The 200696 light-curve, however, shows a prominent hump, with the flat section being about 0.5mag fainter than the average magnitude for 170696. This suggests that in the intervening time, accretion switched from the upper pole (even light curve) to the lower pole (eclipsing, and with hump present). It is noted that the mid-hump brightness for 200696 is about the same as the average for 170696.

9.6.3 230797 to 310797

These nights provide as nearly a continuous data set over the expected P_{beat} as was obtained in the Woomera data.

230797: a rise of about 1mag (intensity factor of 2.5) over some three orbits. No modulation evident.

260797: Clear humps over three orbits, but possibly with the amplitude of the hump decreasing.

270797: A most interesting night. Firstly, the CV starts about 1.2mag (intensity factor of 3) brighter than at the end of 260797. Over five orbits, the "flat" portion of the light curve drops

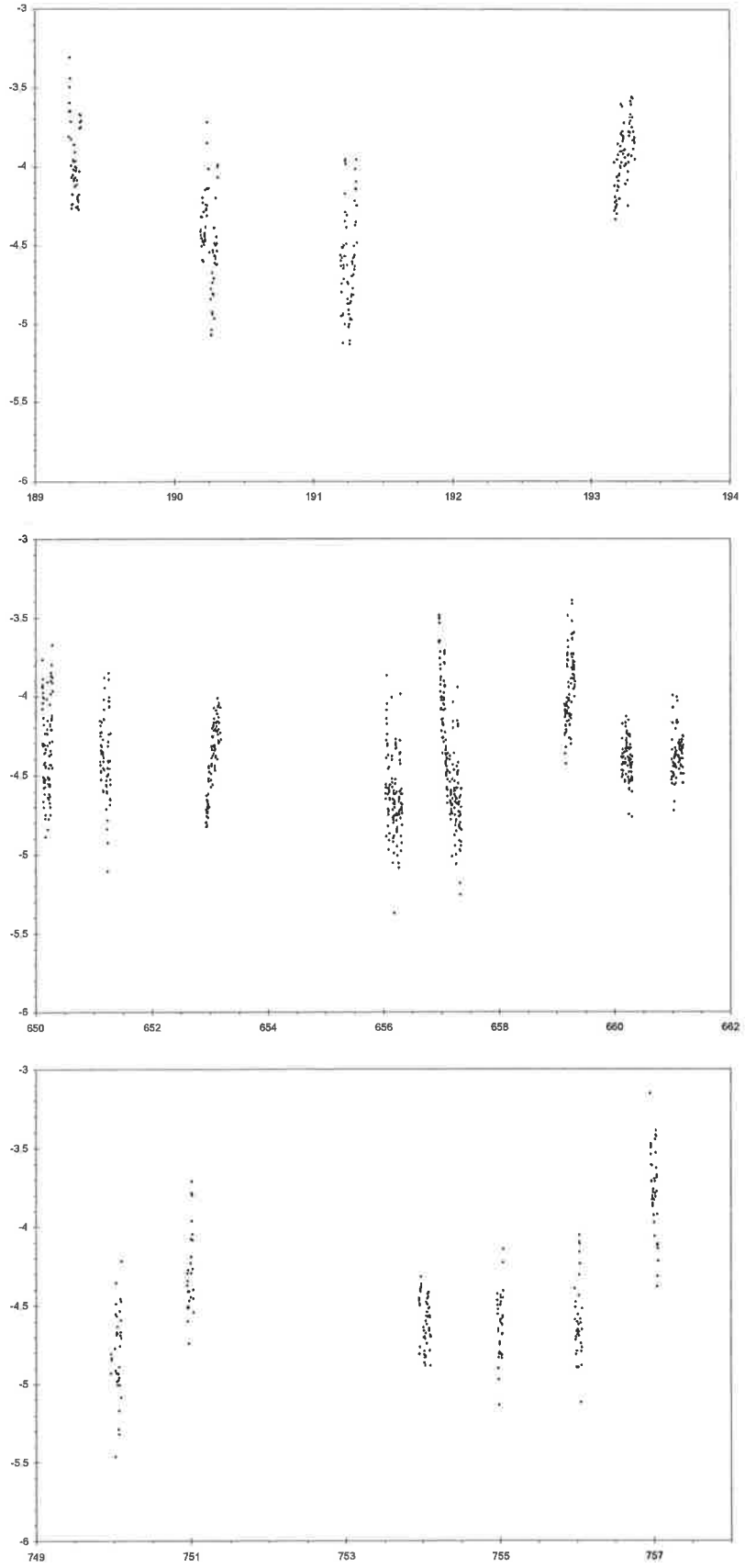

Figure 9.17
Woomera white-light data showing diurnal-scale variations. Ordinate is differential magnitude, abscissa is HJD-2,450,000.

by about 0.5mag, as does the peak of the hump. The hump amplitude does not appear to change significantly. The presence of the hump suggests that accretion is at the far pole.

Figure 9.18 shows the results of a polynomial fit to the "non-hump" sections of the night's data, and the subtraction of this fit from the data. It is confirmed that the hump amplitude is approximately constant (with the hump being superimposed on a decreasing trend) so that the decrease in intensity is global, and is not limited to a decrease in light only from the accreting pole; there must be changes elsewhere, too.

290797: CV slightly brighter, and with modulation still present.

300797: around 0.5mag fainter than the previous night, but with no modulation present over two orbital cycles. Light-curve is essentially flat.

310797: same general brightness as for 300797, but with two humps (the second incompletely observed). However, there is no third hump seen at the expected time. This confirms rapid, cycle-cycle changes in the accretion geometry as noted in R00 when a CP pulse did not repeat as expected.

9.6.4 031197 and 041197

A decrease of 1mag between nights is noted, with modulation being more notable on the second, fainter night.

The observation that both the level of modulation in the light curve and the average brightness of the CV change suggests at least the possibility of correlation between the two. Is this seen in the data so far obtained?

Quite apart from the scatter in magnitudes due solely to measurement error, the observed scatter in a night's light curve for the CV will be proportional to its amplitude. In the scatter-magnitude plot, we have both the average magnitude of the CV for each night, and the observed scatter for that night. These are shown in the upper panel of Figure 9.19, along with the expected scatter for the CV based on the fit to each night's K star data, and the average magnitude of the CV on each night. The effect of increasing measurement error on the CV scatters may be eliminated by removing, in quadrature, the expected scatter from the observed scatter.

The result of this is shown in the lower panel of Figure 9.19. There is no apparent trend in the plot, and this suggests that there is no evident correlation between CV scatter (that is to say, amplitude of the light curve) and average magnitude. As always, more data (and of higher accuracy) would assist in the examination of this question.

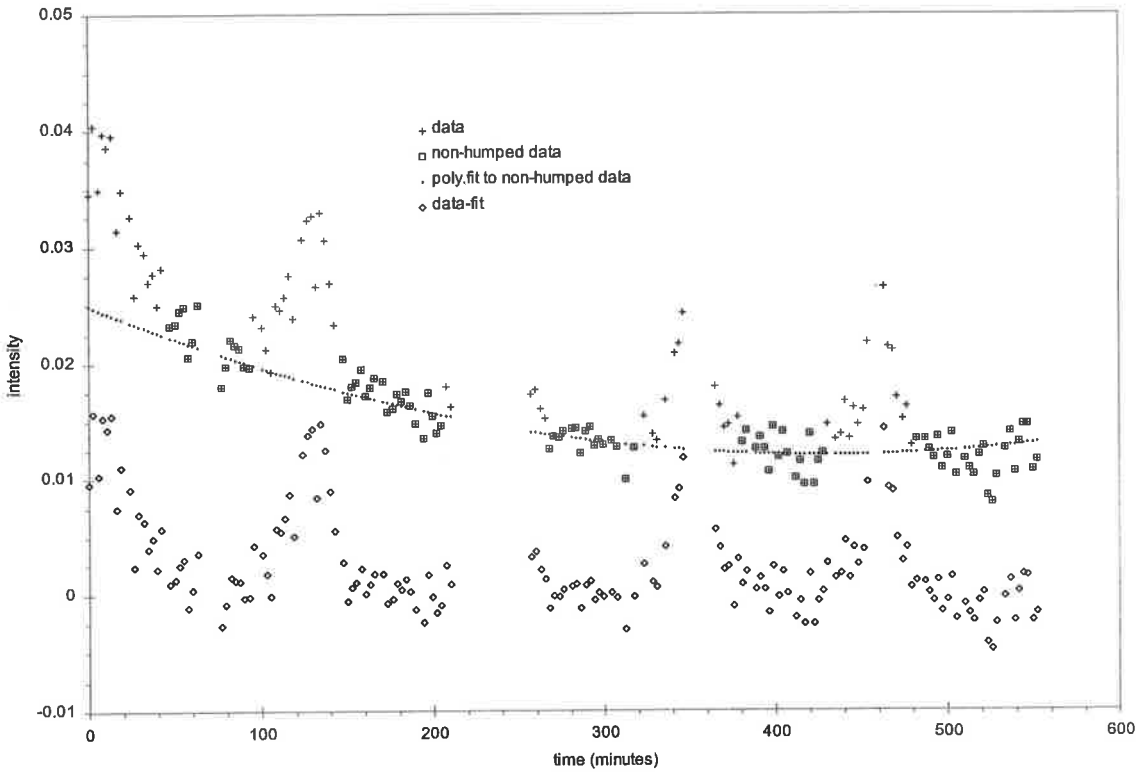

Figure 9.18

Woomera data from 270797, showing a continual fading over five orbits. A polynomial was fitted to the non-humped sections of the light curve, and subtracted from the data.

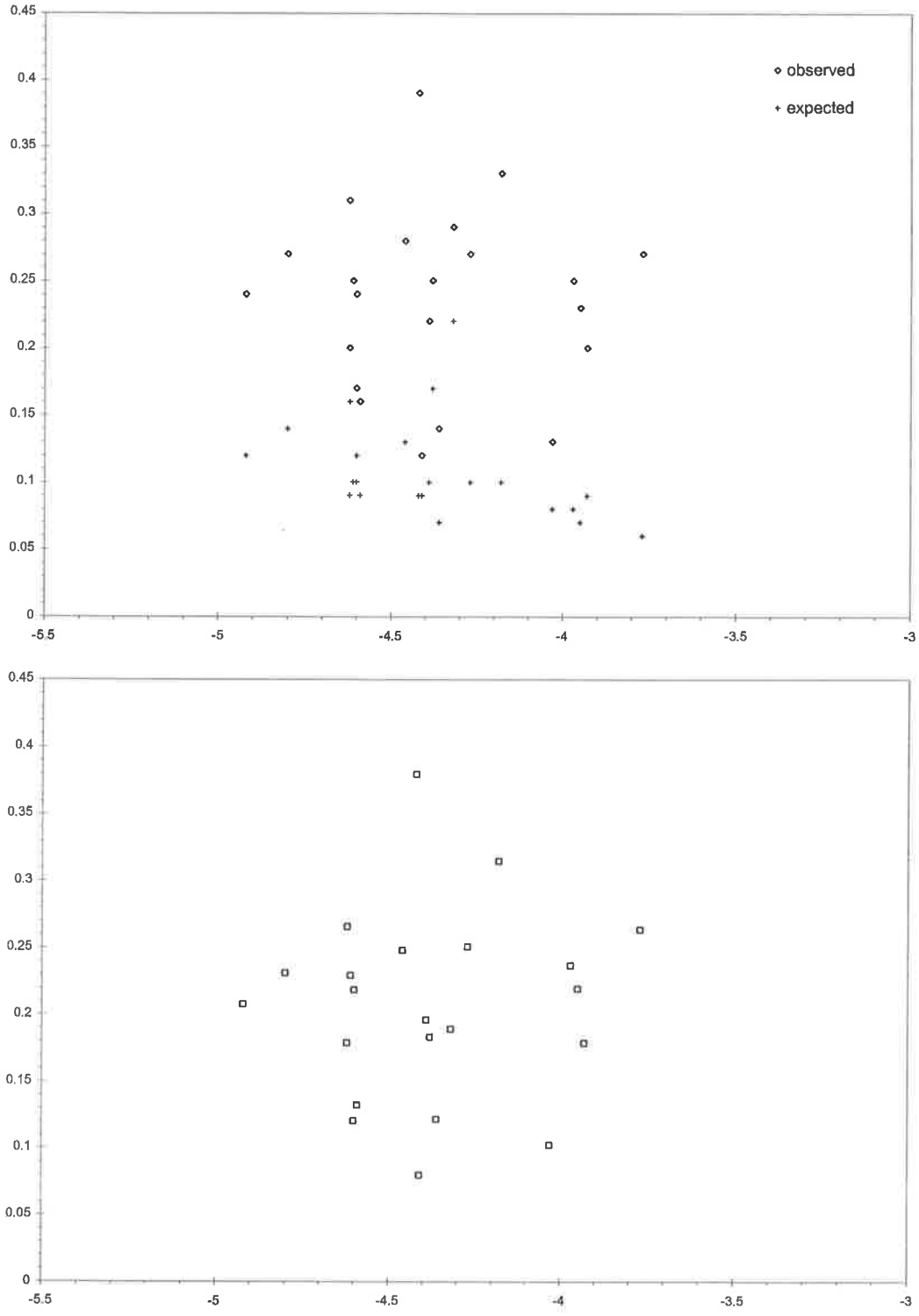

Figure 9.19

Ordinate is scatter (i.e. standard deviation of each night's light curve); abscissa is average differential magnitude for each night's light curve. Top panel: observed and expected scatter for CV. Lower panel: scatter in CV with expected scatter removed in quadrature. There is no evident correlation between CV average magnitude and scatter in the CV light curve (that is, its overall amplitude).

9.7 System parameters

Whilst not estimable from the Woomera photometry (which measures P_{wd}, not P_{orb}), we shall use the values of P_{orb} as given in Section 9.4 to estimate various parameters of this CV.

There is only a very small difference between the two best estimates of P_{orb} (from V96 and R99), and the effect on the estimated parameters is slight, so that only one value for each parameter will be given- unless uncertainties in the corresponding relation itself suggest that upper and lower limits should be quoted. We have:

M_2	R_2	T_2	ρ_2	$M_V(2)$	$M_V(2)$	$\dot{M}$
0.14	0.183	2997	31.4	14.5	14.77	$>3.1\ 10^{-11}$
						$<5.9\ 10^{-11}$
M_{sun}	M_{sun}	K	g cm^{-3}			$M_{sun}\ yr^{-1}$

From the fact that Ind 1 is not eclipsing (in the sense of eclipse of the primary by the secondary), we know that $i < 72°$ (indeed, R00 assume $i = 70°$ for Stokes modelling of their CP data).

To date, there are not any estimates of q (either independently, or based on both M_1 and M_2), so it is not possible to estimate the separation of the two stars using the relations given in Chapter 2. We must make some guesses. Assume that M_1 is given by the mean WD mass for a sample of polars as given in Ramsay 2000; that is $M_1 = 0.80 \pm 0.14$.

Taking $M_2 = 0.14$, we have $q = 0.175$ (with limits 0.149 and 0.212). If we now equate R(2) with the volume radius of the Roche lobe of the secondary, and apply Equations 2.15 and WCVS 2.5b, we may obtain two estimates of the separation, a, between the two stars in this system. Respectively, these are $a = 5.20\ 10^{10}$ cm and $a = 5.19\ 10^{10}$ cm. The good correspondence between the two estimates suggests that the values assumed for M_1 and derived for M_2 and R_2 are acceptable.

9.8 A faint variable in the field

During co-adding of clear-filtered images, and comparison of the results with photographic sky survey images of the field (copies obtained at UKST in July 1996), it was noted that a field star near Ind 1 was almost undetectable in individual CCD images, whilst being quite evident in the survey images. This was not just a matter of colour (e.g. "red" CCD

response vs. "blue" photographic response) since the discrepancy was noted in both blue and red survey images.

Figure 9.20 shows co-added Woomera frames of the field. The variable is faint, but definite. Figure 9.21 shows survey images of the field (derived from the UKST archives at Siding Spring).

The position of the variable is (J2000.0) 21:15:47 -58:41:18. The reported survey magnitudes are $B_J = 20.56$ and $R = 20.29$.

The change in the variable is quite evident. Comparison with SuperCOSMOS data suggests that the variable is at approximately magnitude +23 (B_J) for the Woomera images, compared with 20.6 for the survey images used for the SuperCOSMOS chart. The composite Woomera image goes rather deeper than does the COSMOS chart; the limit for the co-added (not drizzled) image in Figure 9.20 is estimated to be around +24.

The time-scale of the variability is not known, since there was no clear change evident between nightly, weekly or monthly subsets of the images used to prepare the deep Woomera image.

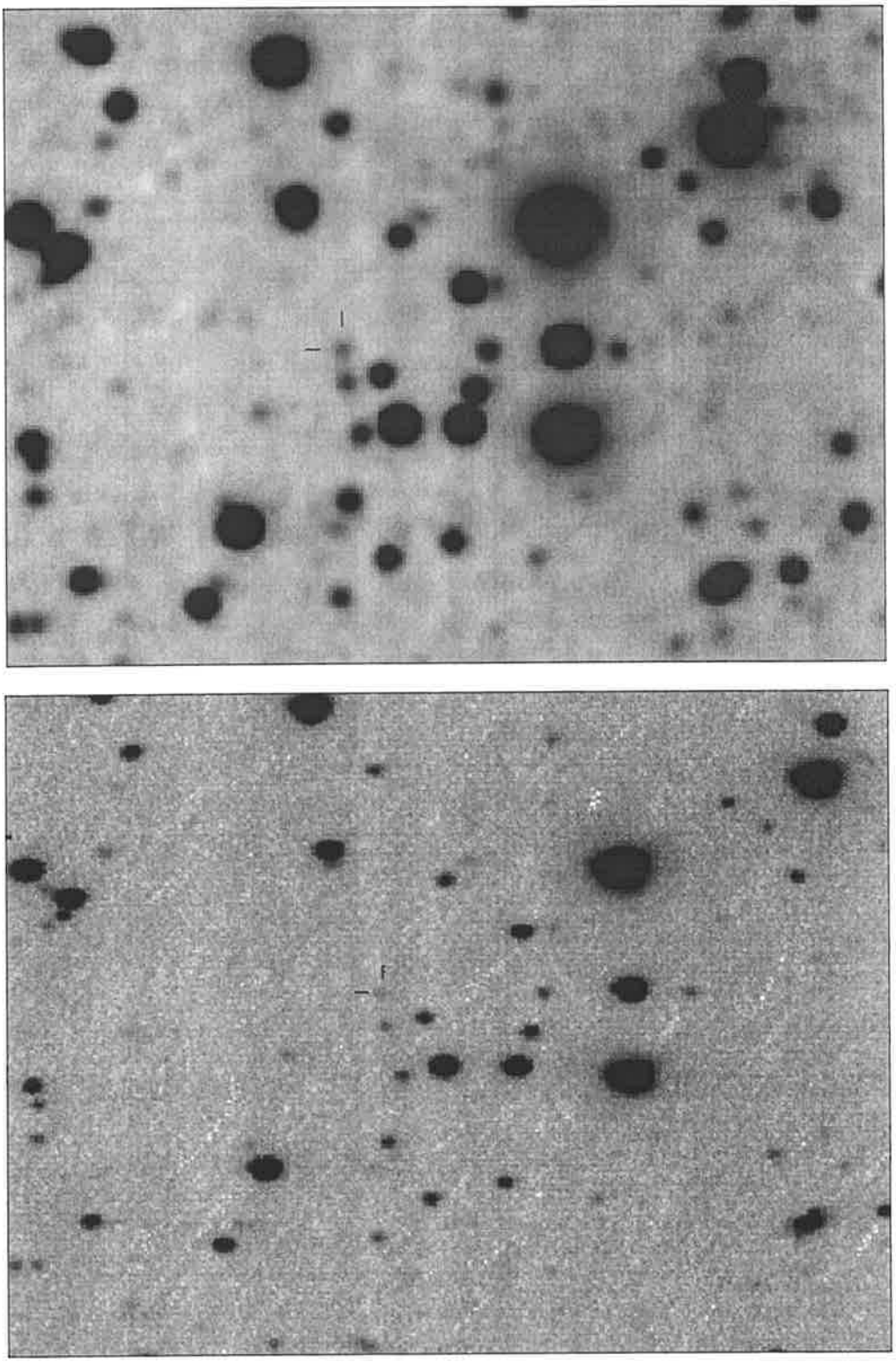

Figure 9.20

Woomera co-added and cropped images of the field. The suspected variable is marked by tics. North to the top, east to the left.
Top panel: co-added image with total integration time of 347 minutes. The variable was in a low state at the time. Estimated magnitude limit of the image is around +24.
Lower panel: same set of images, but added together via a drizzling routine. This increases the resolution of the image, but at the cost of a slight reduction in limiting magnitude.

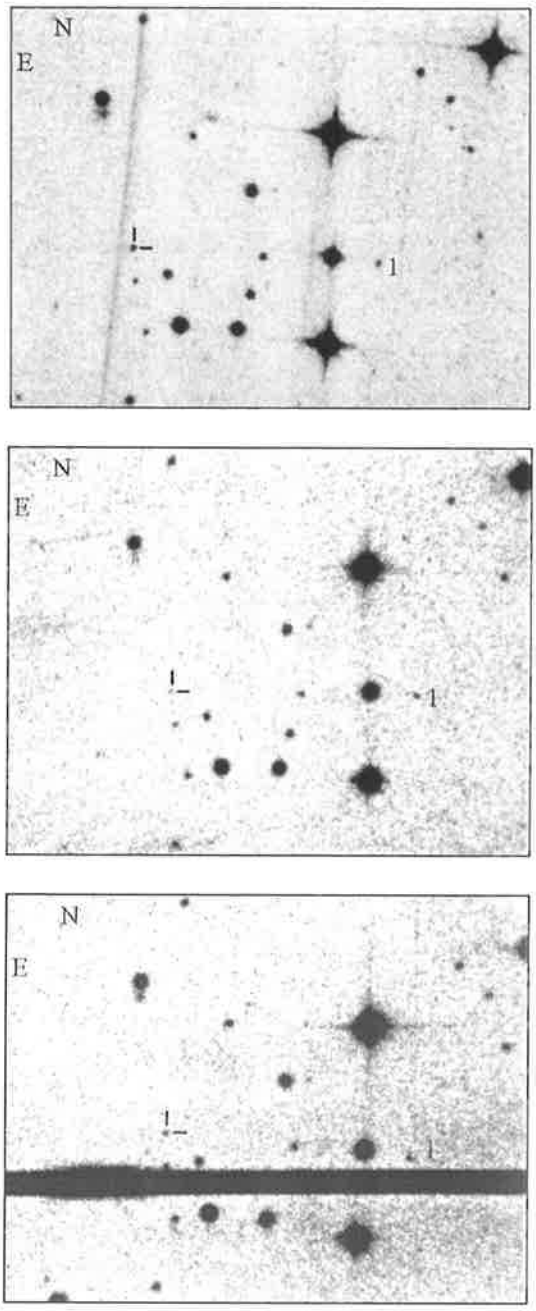

Figure 9.21

Survey images of the Ind 1 field, showing the suspected variable star (tic marks).
Top panel: UKST IIIa-J plate J2411 (2/7/1976). The variable is quite bright (cf. with Figure 9.20). Variable is noticeably brighter than star1, although this could be related to colour.
Middle panel: ESO red plate R5751. The variable is markedly fainter than star1.
Bottom panel: ESO red plate R6124. Although this image goes slightly fainter than ESO R5751, it is clear that the variable is now comparable in brightness to star 1.
These lower two images demonstrate that the suspect is indeed variable, as it is seen to be so in different red plates. Comparison of UKST J2411 with the ST-6 images alone suggests *that the suspect is variable, although that could be due to colour of the suspect (e.g. a very blue object).*

CHAPTER 10. EXPERIMENTAL RESULTS: PHOTOMETRY OF OTHER SOURCES

This chapter includes the results of photometry undertaken on other sources, both stellar and galactic. The data for each object are not as extensive as for the sources covered so far, and the discussion also is brief.

These sources were observed out of curiosity, or as part of larger, multi-wavelength or multi-site campaigns to which the data were contributed.

10.1 GRO J1655-40

10.1.1 Other observations

This is a black hole binary, and was discovered in outburst by BATSE on 27/7/1994. Continued monitoring by various satellites showed its intensity to be variable, showing especially outburst and decline behaviour. Noting from IAU Circulars following the first outburst, X-ray flux in the 20-100 keV band was seen to reach 1400 ± 100 mCrab, and radio emission was also seen (up to around 80mJy at 1.4 GHz). Indeed, the source has shown superluminal radio emission in a jet.

Optical spectroscopy and photometry of GRO J1655-40 in a low state has allowed the main parameters of the system to be determined (Orosz and Bailyn 1997, hereafter OB97):

$q = 2.99 \pm 0.08$

$i = 69.5° \pm 0.08°$

$M_1 = 7.02 \pm 0.22\ M_{sun}$

$M_2 = 2.34 \pm 0.12\ M_{sun}$ (spectral type F3 IV to F6 IV)

$P = 2.62157 \pm 0.00015$ days

$\dot{M} = 3.4\ 10^{-9}\ M_{sun}\ yr^{-1}$

In this state, the photometry showed a light curve dominated by ellipsoidal modulation of the secondary (there being little contribution from the disc at such times), with the minimum at $\phi = 0.25$ being deeper due to gravity darkening (OB97). In the high state, the much greater, and variable, contribution of the accretion disc alters the appearance of the light curve, and can cause difficulties in obtaining a consistent period from high-state photometry alone.

Orosz *et al.* 1997 showed from BVRI data that the optical flux can start increasing up to six days before the start of an X-ray outburst. The increase is noted in I first, and B last. This suggests that the disturbance responsible for the outburst propagates inwards from the outer, cooler regions of the disc to the hotter inner regions.

Spectroscopy (e.g. Bianchini *et al.* 1997) shows Hα to be strong in emission during outburst states of this source.

10.1.2 Woomera data

Differential photometry was carried out with the C14 at Woomera. A log of observations is given in Table 10.1. A VRI composite image of the field is given in Figure 10.1; from the considerable number of reddened field stars, it is clear that there is significant interstellar absorption in this region (due to the low galactic latitude), so that care is needed in the choice of stars employed in the differential reduction.

It must be noted that the optical counterpart has a field star very close to it. In the Woomera data, these are evident as two sources, but it was not possible to separate them in the photometric reduction due to software limitations. Therefore, both sources were included in the "variable's" software aperture during reduction- the presumably constant light from the field star was always included along with that from the variable source.

Individual night's data are shown in Figure 10.2, with errors estimated from scatter in the ($C-K_n$) values. Although some nights exhibit small, short-term trends in the data, no night shows significant variability above errors. However, the variation *between* nights is significant. Figure 10.3 (upper panel) shows the average magnitude-scatter plot for each individual nigh's' data; the scatter in the 1655-40 light-curve *on any individual night* is similar to that expect' for a constant star. Figure 10.3 (lower panel) shows a similar plot but using averages of all nights' magnitudes as the abscissa, and the scatter in these average magnitudes as the ordinate. It is seen that the range (i.e. scatter) in magnitudes for 1655 over the entire data set is well above that expected for a constant source.

Figure 10.4 shows the data vs. HJD. These are phased with the spectroscopic ephemeris of OB97 in Figure 10.5. Although the orbital cycle is not very well sampled, it is consistent with the 2.6-day period from the literature. However, it does appear possibly as though the minimum near $\phi = 0.25$ is shallower than that at 0.75; this is opposite to the light curves shown in OB97 for quiescence. They say that this may be the case for the source in outburst; but since a BATSE non-detection from late August 1995 to late April 1996 was interpreted as evidence that the source was in quiescence at this time, there is a small question here. Perhaps it was still showing some evidence of a high state in the optical (i.e. in photometric data), but without enough activity for high-energy emission.

Table 10.1

GRO J1655-40 Woomera observing log

Date	Duration (mins)	Exposure (s)	HJD start (-2,449,000)	filter
220895	90	15	951.9963	clear
250895	210	20	954.9192	"
260895	180	20	955.9376	"
270895	140	60	956.9649	"
280895	150	60	957.9568	"
180995	90	30	978.9360	"
190995	30	30	979.9265	"
200995	125	30	980.9257	"
240995	130	30	984.9286	"
250995	100	30	985.9377	"
260995	42	20	986.9283	"
171095	40	60	1007.9500	"
191095	37	60	1009.9390	"

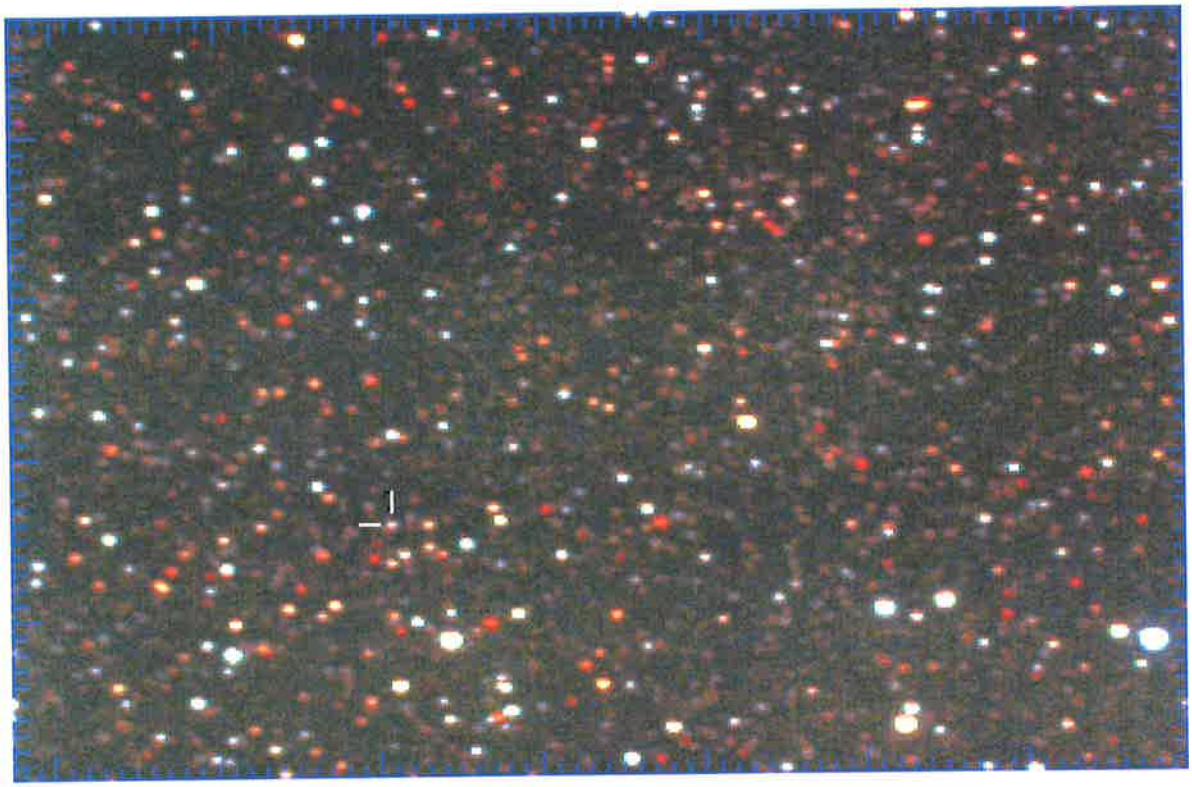

Figure 10.1
Woomera VRI composite for the GRO J1655-40 field.
North is to the top, east is to the left.
The counterpart is between the tic marks.
Note the great number of reddened stars in the field, indicating
significant interstellar absorption at the low galactic latitude of this field.
Approximate field centre and size: (J2000.0) 16:53:48 -39:48:40 12.8' wide 10' high.
Tic marks are in pixels (major tics, 50 pixels; minor, 10 pixels). (0,0) is bottom right.

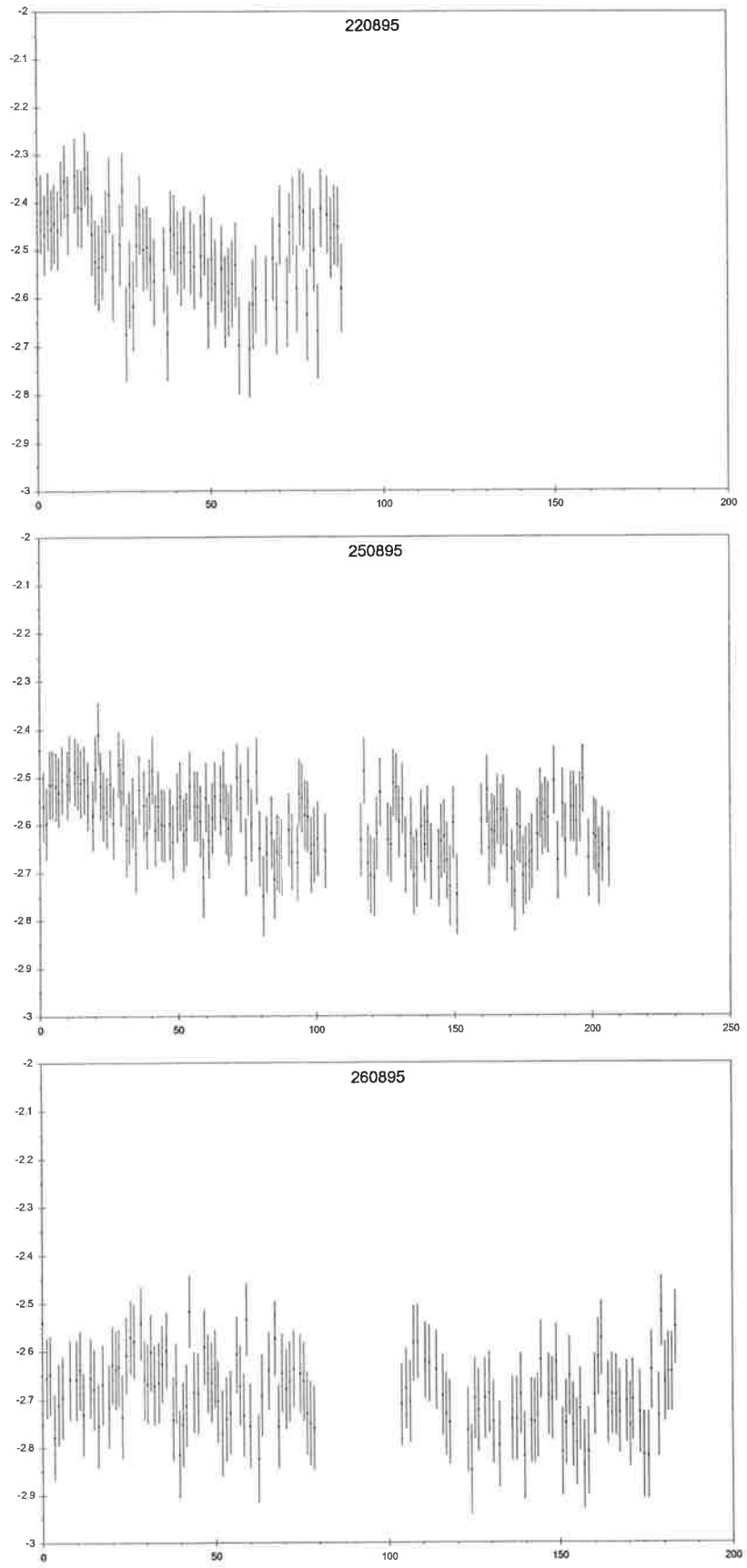

Figure 10.2
Woomera white-light photometry of GRO J1655-40.
Ordinate is differential magnitude, abscissa is time (in minutes).

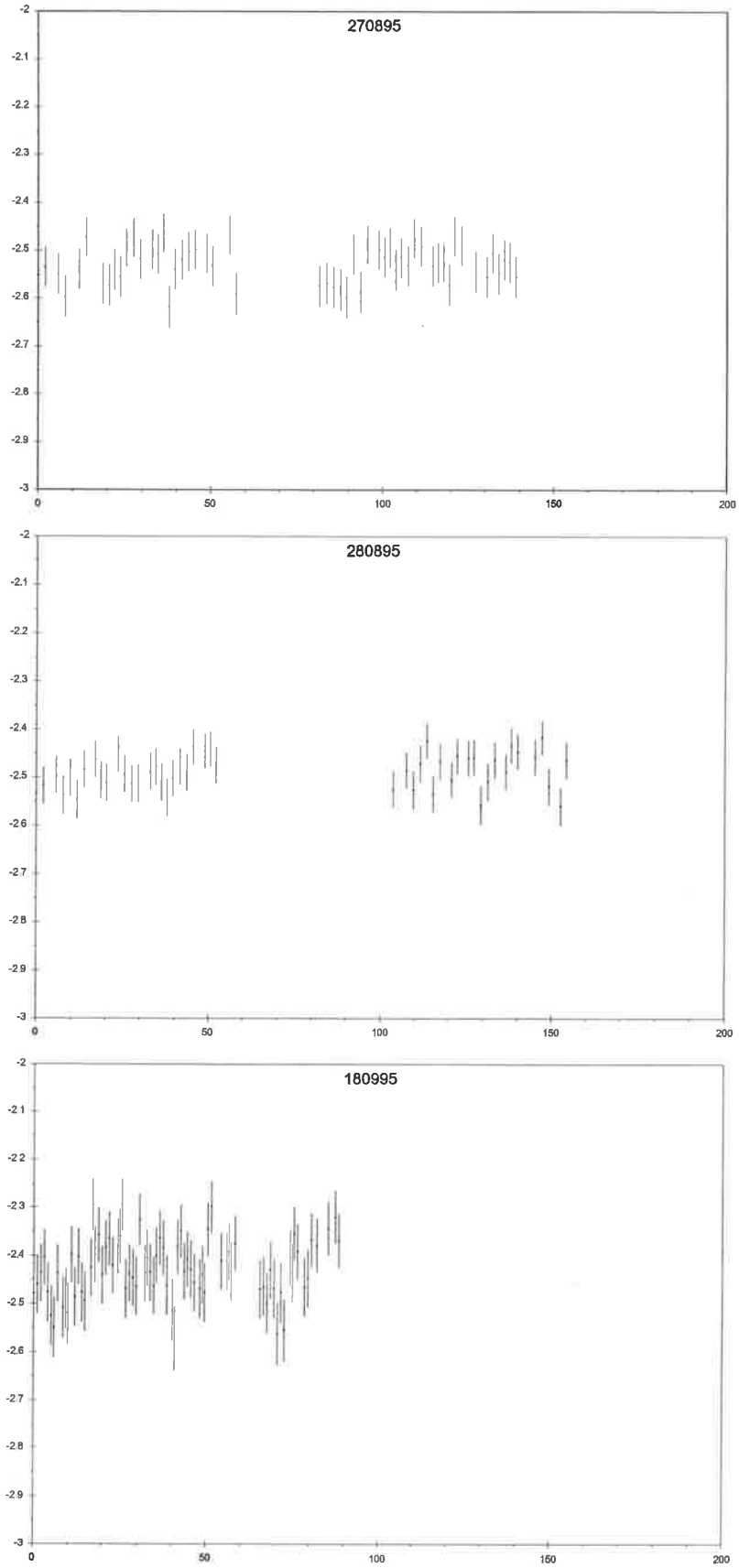

Figure 10.2 continued
Woomera white-light photometry of GRO J1655-40.
Ordinate is differential magnitude, abscissa is time (in minutes).

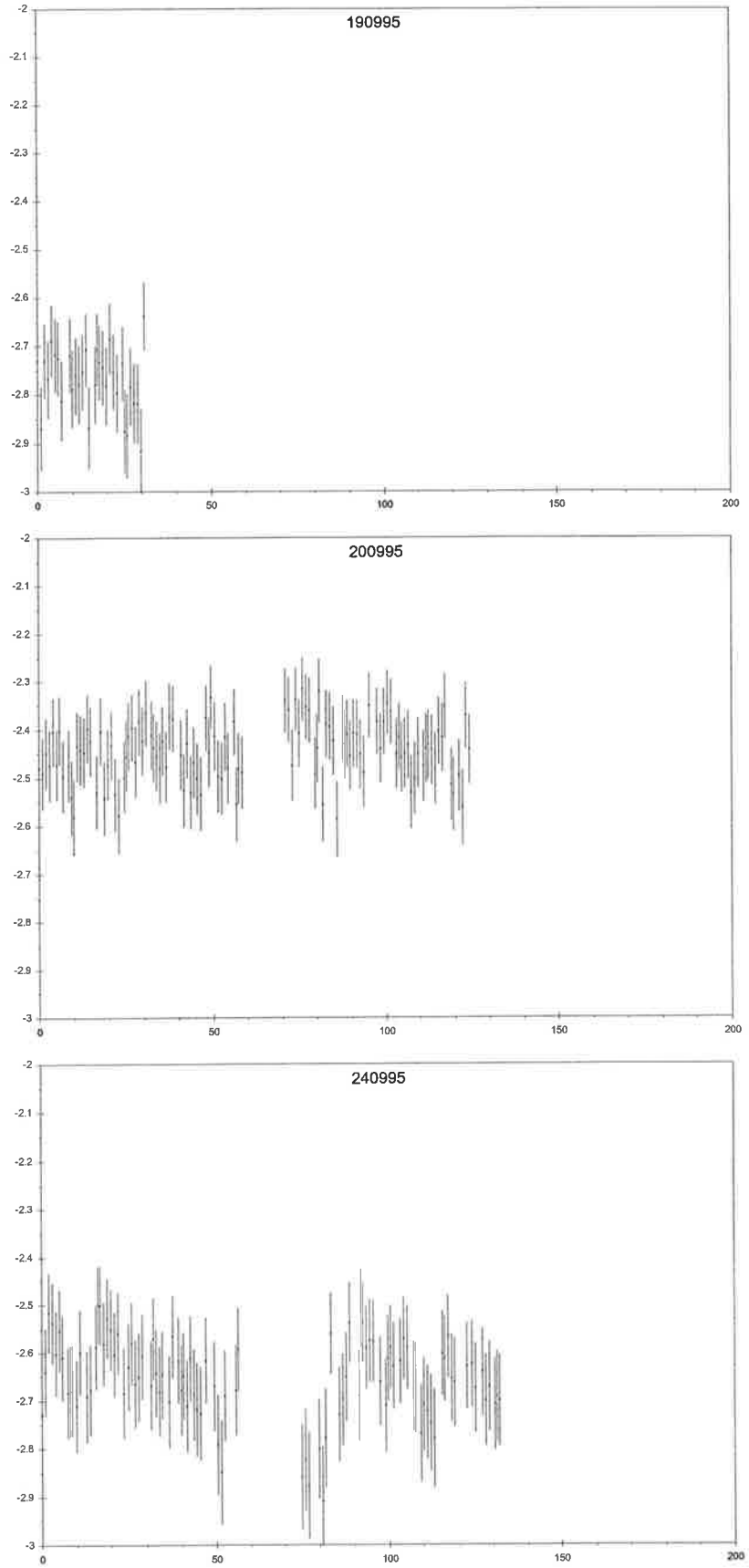

Figure 10.2 continued
Woomera white-light photometry of GRO J1655-40.
Ordinate is differential magnitude, abscissa is time (in minutes).

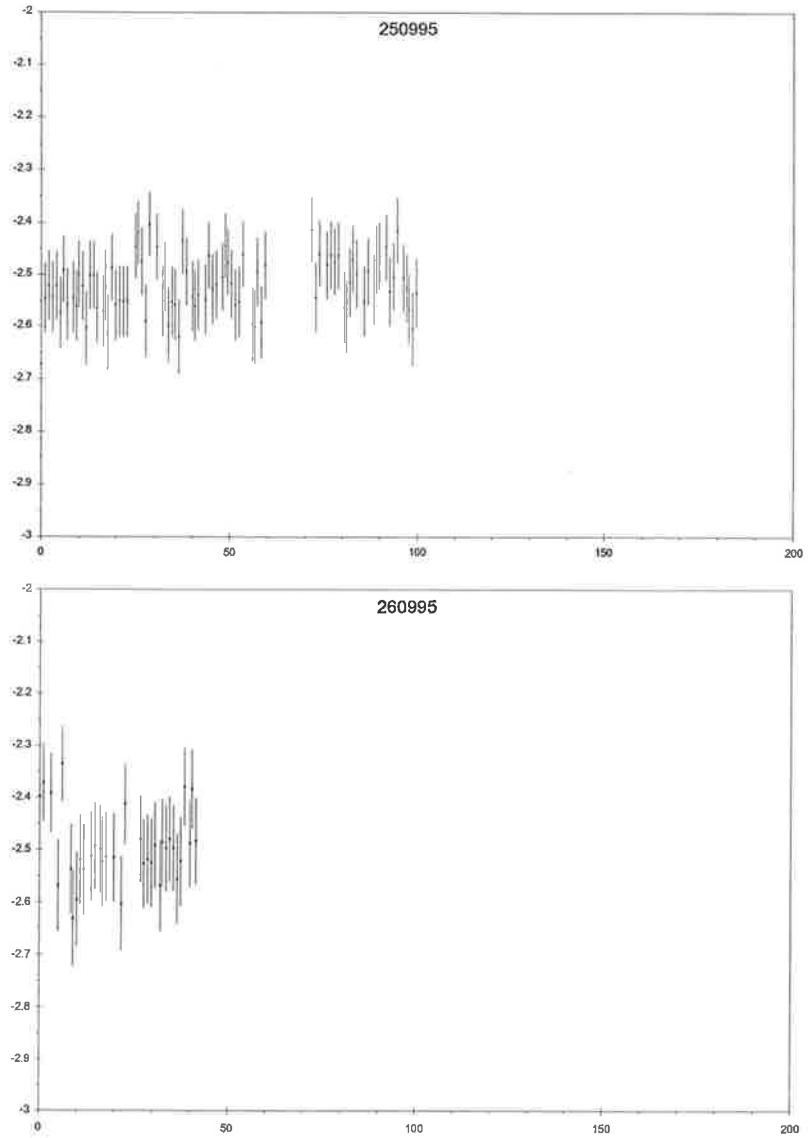

Figure 10.2 continued
Woomera white-light photometry of GRO J1655-40.
Ordinate is differential magnitude, abscissa is time (in minutes).

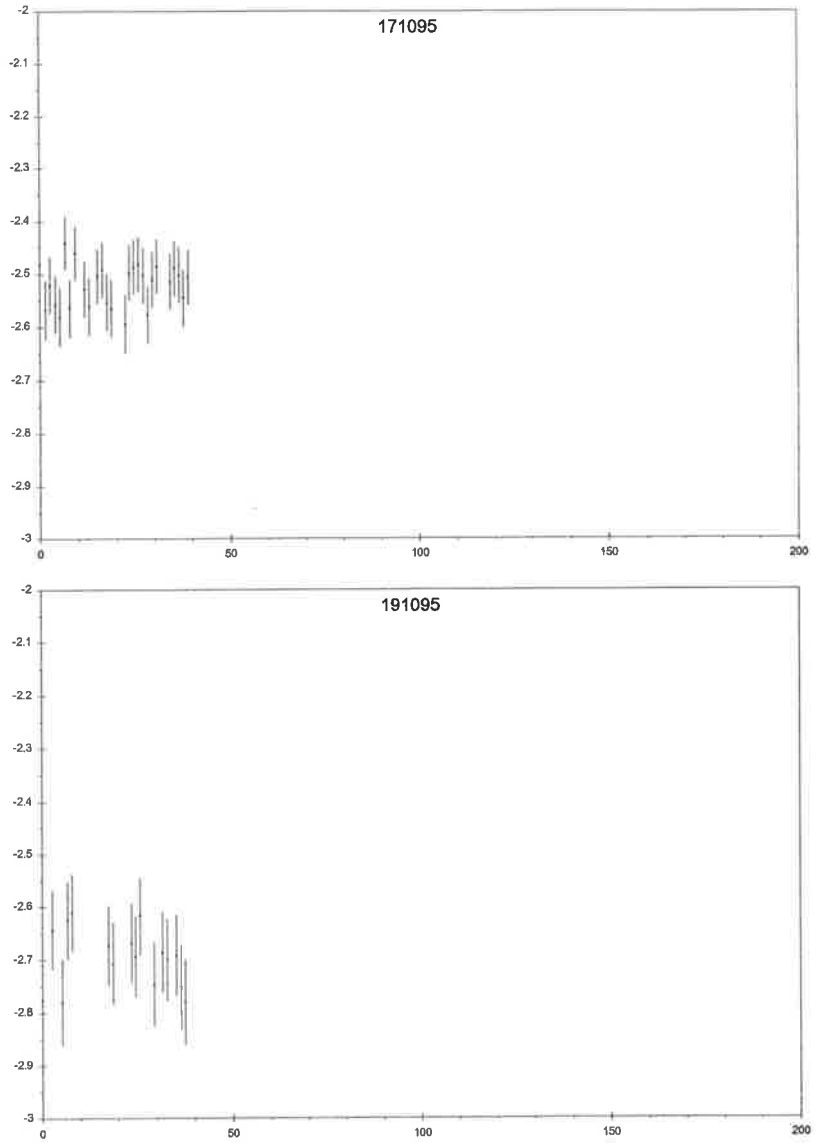

Figure 10.2 continued

Woomera white-light photometry of GRO J1655-40.
Ordinate is differential magnitude, abscissa is time (in minutes).

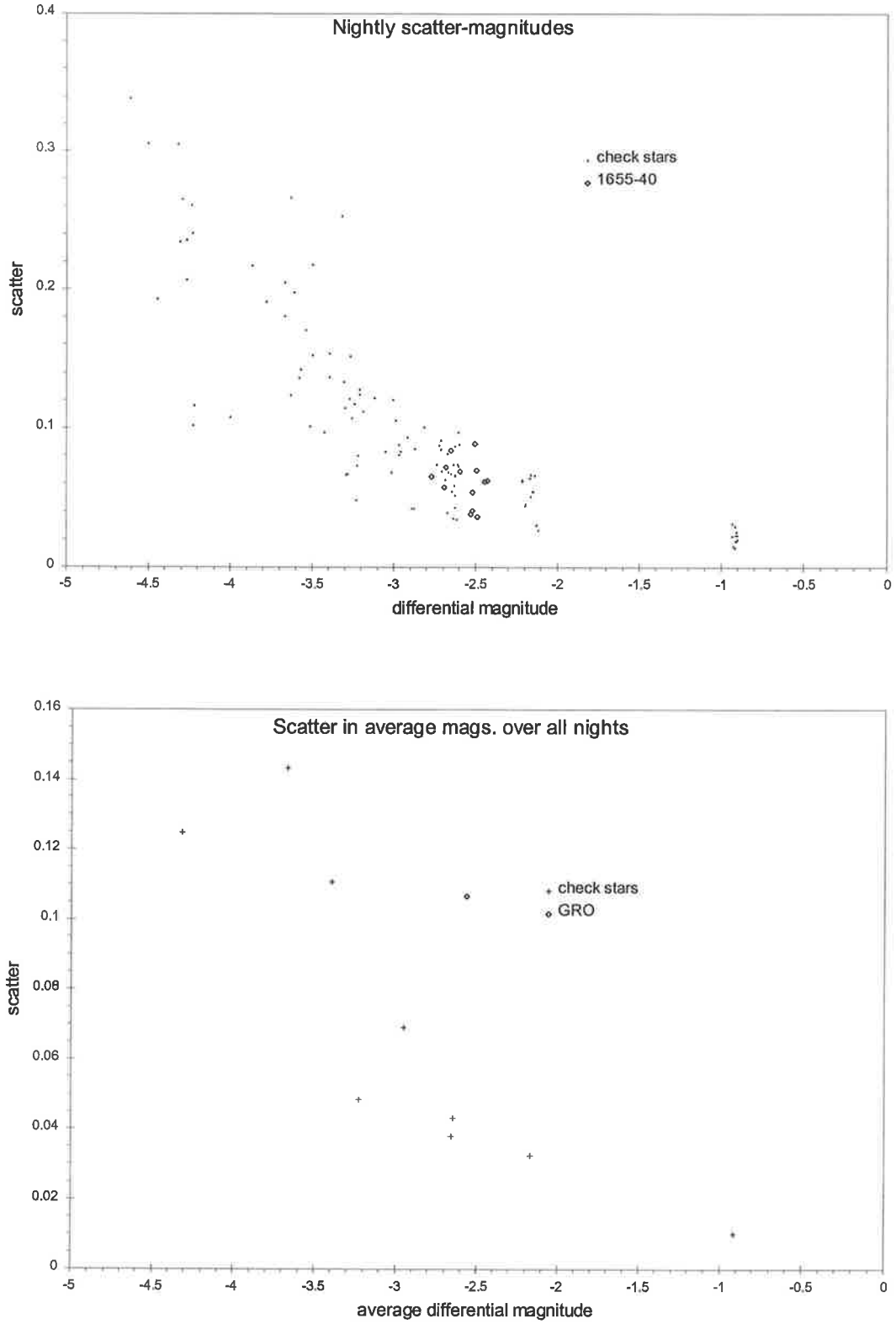

Figure 10.3

Upper panel: Nightly scatter-average magnitude plot; there is little or no variability above errors on any given night.

Lower panel: Plot of the scatter in all nightly average magnitudes vs. average magnitude over all nights; there is significant variability in average magnitude between nights.

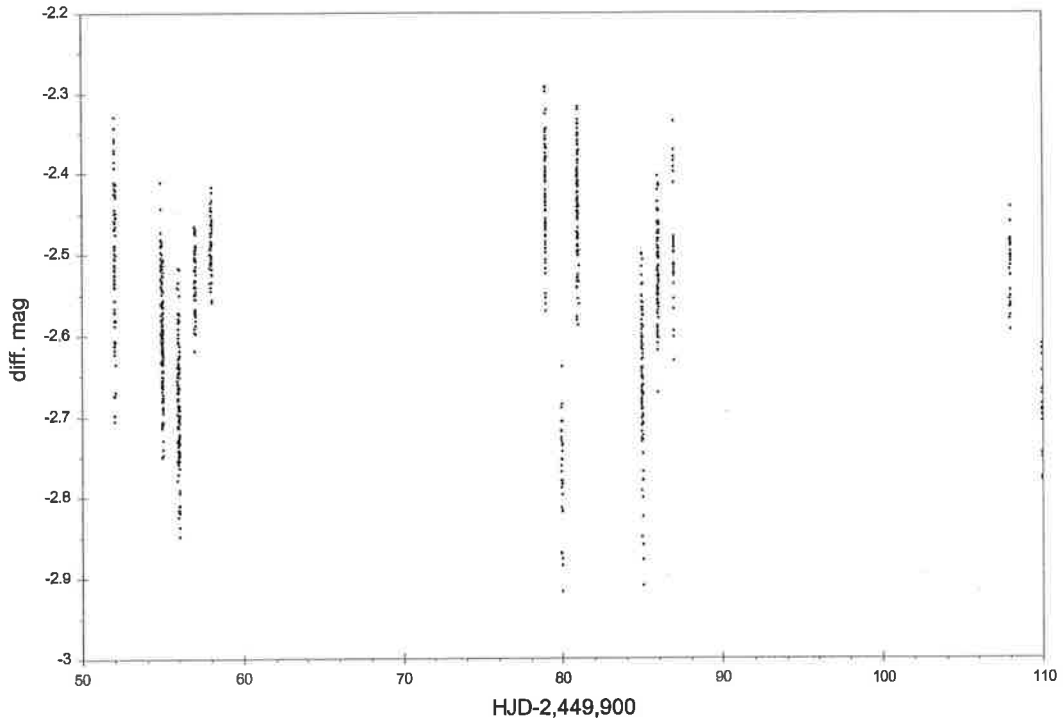

Figure 10.4
Woomera white-light data vs. HJD.

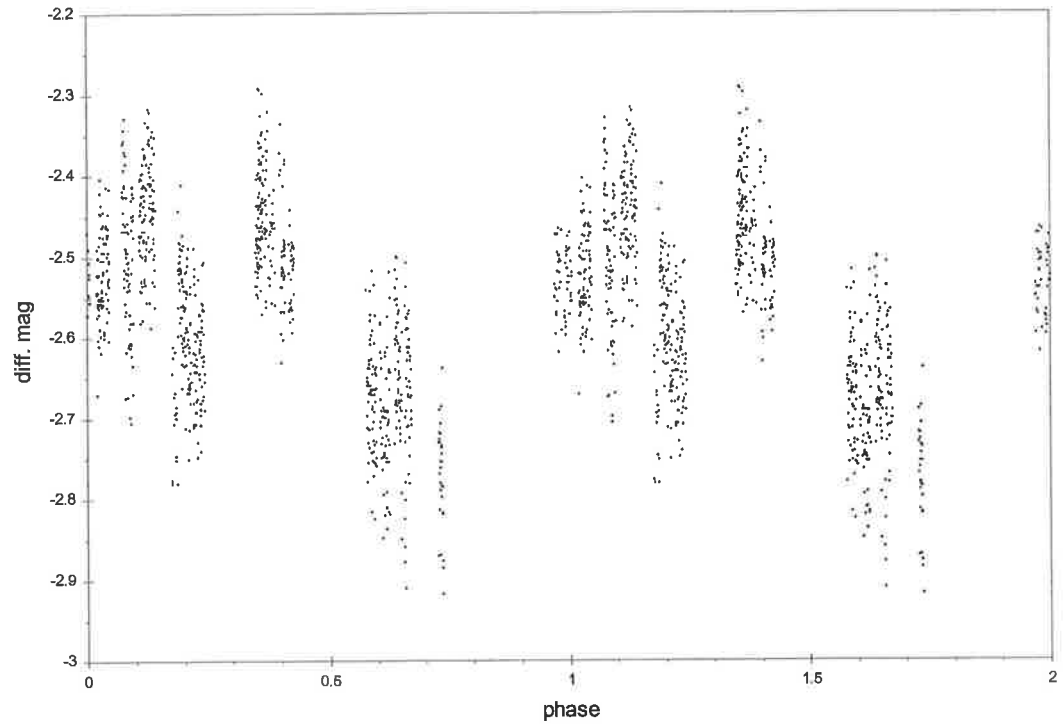

Figure 10.5
Woomera white-light data phased at 2.62157 days.

10.2 EUVE J1707-76.3 and EUVE J1200-36.5

These were EUVE sources with (at the time) no optical identification (a.k.a. NOID) and, whilst the true nature of the actual source was not known, it was suspected that they were isolated white dwarfs. Observations were undertaken at Woomera (280797 for 1706 and 300797 for 1200) after consultation with Dr. Dan Maoz of Tel-Aviv University (Maoz, private communication).

Data consisted of short BVRI time-series as well as longer (but not quite two-and-a-half hours' duration) unfiltered time-series. As there was no ID for the EUV source, many stars near the EUVE location were measured with the usual differential techniques. No variation above errors was seen in the unfiltered data; but note that, ideally, much longer data sets should be taken in order to look for variability in this manner.

Combining VRI images of the fields, it is immediately clear which star is likely to be the optical counterpart. Such images are presented in Figure 10.6; there is a very blue object near the EUV source position in each field. Admittedly, this is not *proof* that such an object is the counterpart- it is, however, highly suggestive. But note that spectroscopy at the MSSSO 2.3-metre telescope (Maoz, private communication) has shown that the suspect star in the 1706 field is an isolated white dwarf. It is most likely that the object in the 1200 field is of a similar nature.

This suggests, in cases where large-telescope time is limited, and spectroscopy of candidates is not easily undertaken, that direct imaging of NOID fields by small telescopes can lead to a reasonable- if not definite- identification of some optical counterparts (see also Schwartz *et al.* 1995).

COSMOS charts of the field of EUVE J1200-36.5 show the location of the optical counterpart as an extended object; presumably, the close *apparent* pair of the WD and its stellar neighbour were classified as a galaxy. The NASA Digitised Sky Survey, using the SIMBAD data-base to resolve object names, gives 12:03:00 -36:48:00 (J2000.0) as the position of EUVE J1200-36.5. The centre of the "unresolved" stellar pair as determined by COSMOS is 12:00:55.27 -36:30:3.5 (J2000.0). This is not the exact position of the WD, but is close enough to enable easy identification.

EUVE J1200-36.5
Field centre and size: (J2000.0) 12:00:54 -36:30:13 6' wide 8' high

EUVE J1706-76.3
Field centre and size: (J2000.0) 17:06:50 -76:23:24 13.5' wide 10.2' high

Figure 10.6
Woomera VRI composites for (at the time) two EUVE NOID (No Optical IDentification) sources.
North to the top, east to the left.
Top panel: the optical counterpart is the lower and bluer of the two stars in the close pair near the centre.
Lower panel: the counterpart is the blue object between the tic marks, right of and above centre.
In both cases, the source is an isolated white dwarf.
The upper image has been zoomed by a factor of 2 from the original.

10.3 PKS 2155-304

10.3.1 General

This BL Lac object has been the subject of a great many monitoring programmes, and is variable in all energy ranges and on a variety of time scales. Optically, it averages around m_V = 13 to 14, with a (B-V) colour index around 0.3 and (U-B) around -0.75 (Zhang and Xie 1996), (Miller and McAlister 1983).

10.3.2 Woomera data

PKS 2155-304 was observed in collaboration with the 3.8-metre Woomera CANGAROO γ-ray telescope in late-September 1997. The optical data were mainly time-series R-band exposures, but BVRI snap-shots also were obtained each night. Ian Glass of the SAAO (private communication) was kind enough to obtain JHKL data on two nights.

The Woomera CCD data were reduced differentially using the stars specified in Smith *et al.* 1991, with their C star being used to bring the differential Woomera magnitudes to the standard system. These "standard" magnitudes were then converted to monochromatic fluxes using the relations given in Bessell 1979.

Individual night's time series are presented in Figure 10.7. There is a hint of small variations within some nights, but none of this is sufficiently above errors to be remarkable, although the 280997 data do show a definite trend. The data are plotted as a function of HJD in Figure 10.8; there is a slight but clear drop from 270997 to 280997 (HJD 2,450,719 to 2,450,720). From 280997 to 300997, there is a decrease of around 2.7 mJy (about 7.5% drop in flux). There is little or no change to the next night. (Data taken on 220798 (HJD 2,451,017) show a flux of 25.9 ± 0.4 mJy).

The SSAO IR data (as magnitudes) are given in Table 10.2.

Table 10.2

SAAO IR data

JD	J	H	K	L
2,450,720.26	11.19 ± 0.03	10.50 ± 0.03	9.86 ± 0.03	8.75 ± 0.08
2,450,721,42	11.28 ± 0.03	10.57 ± 0.03	9.92 ± 0.03	8.77 ± 0.08

These were converted into flux units using the relations given in (Bessell 1979). An optical/IR flux spectrum is presented in Figure 10.9.

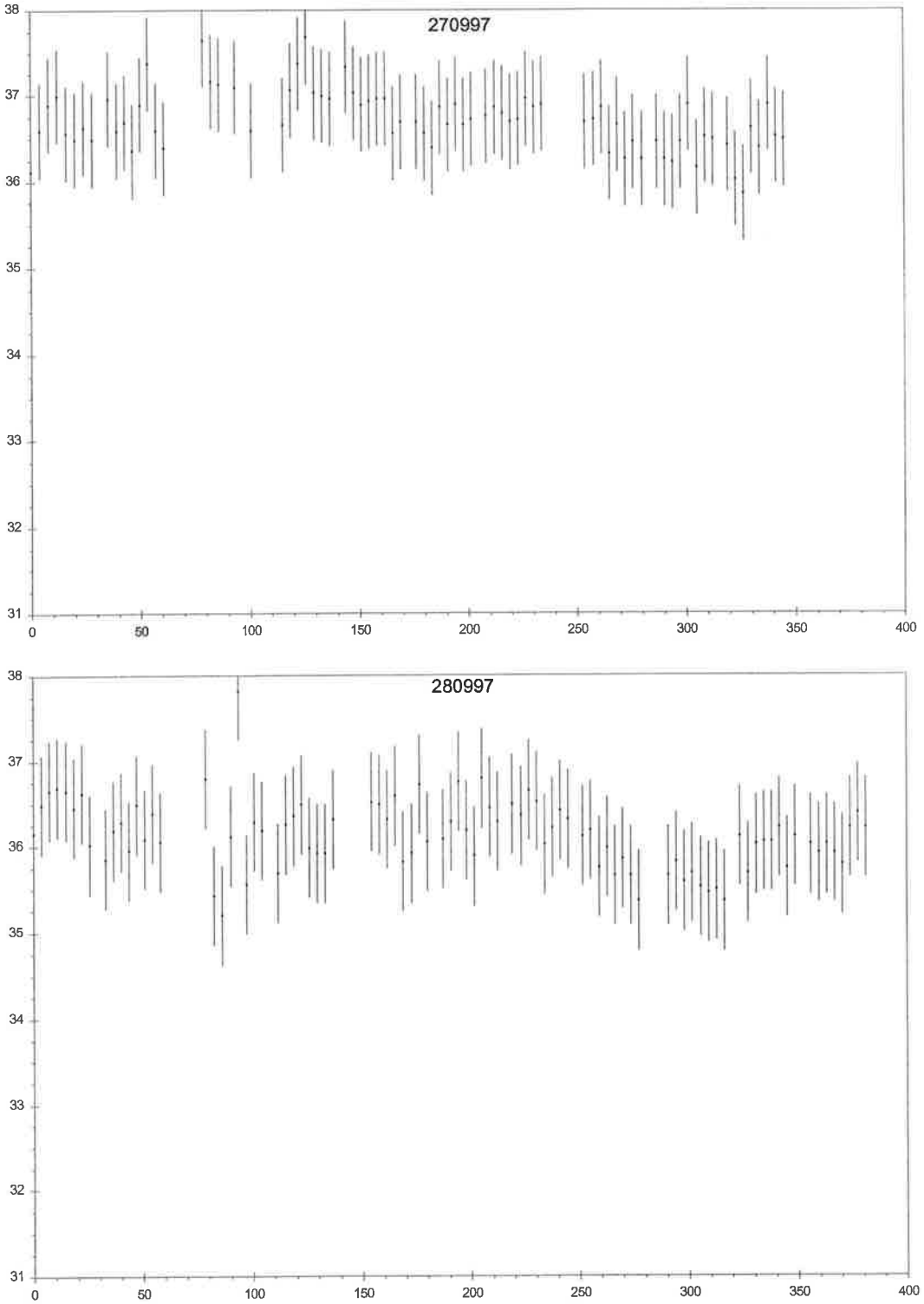

Figure 10.7
Woomera R-band time series for PKS 2155-304.
Ordinate is flux (in mJy), abscissa is time (in minutes).

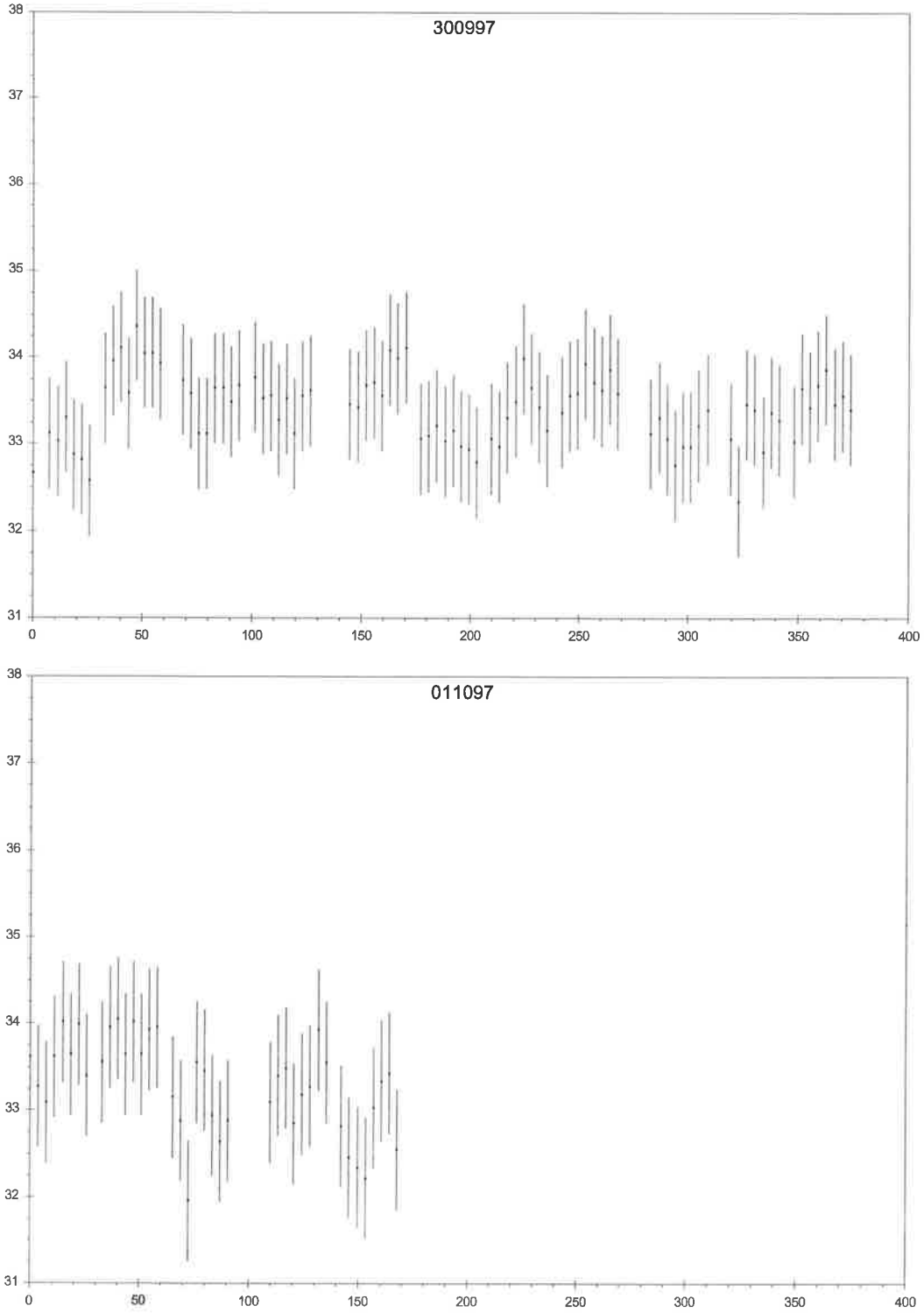

Figure 10.7 continued
Woomera R-band time series for PKS 2155-304.
Ordinate is flux (in mJy), abscissa is time (in minutes).

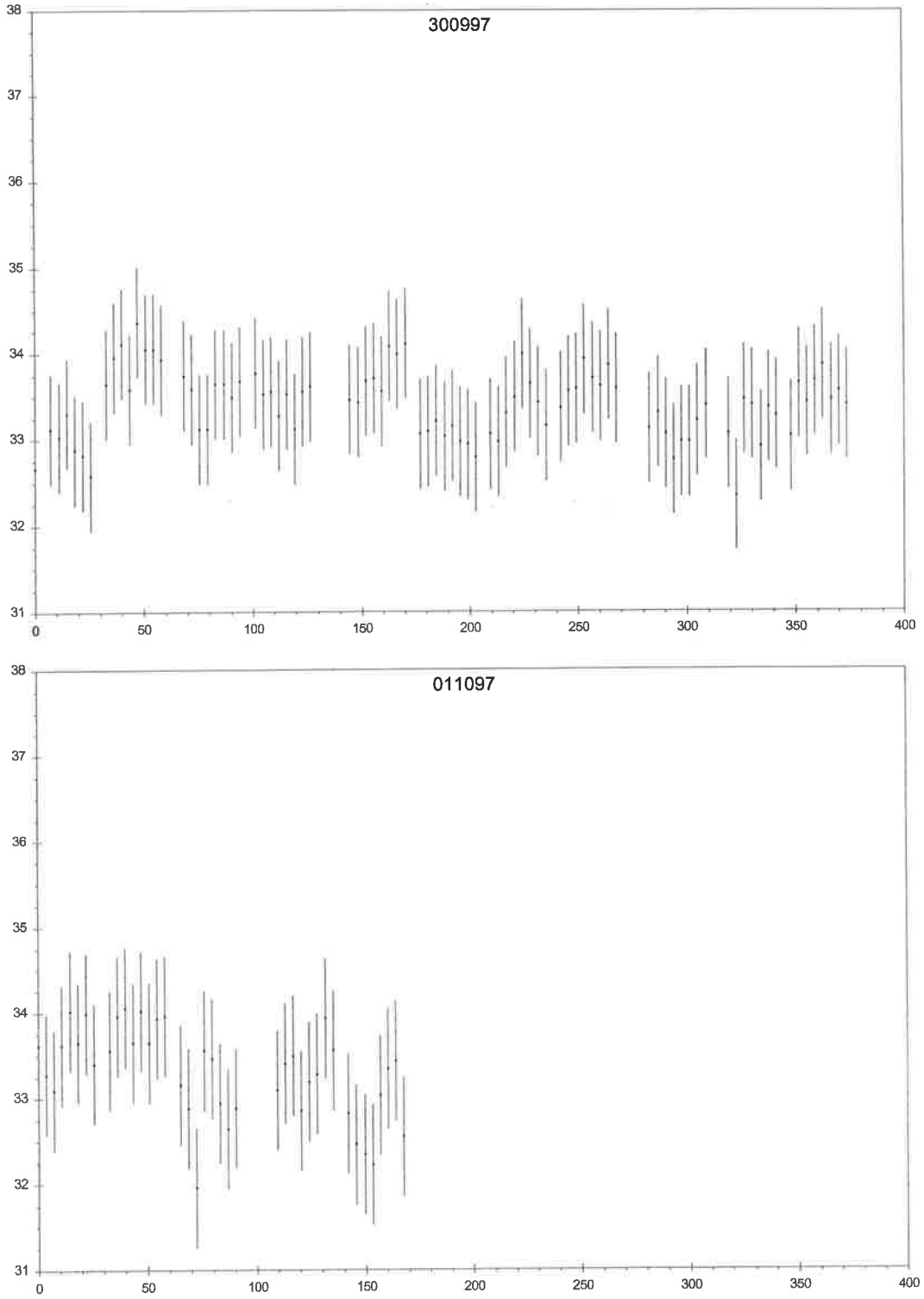

Figure 10.7 continued
Woomera R-band time series for PKS 2155-304.
Ordinate is flux (in mJy), abscissa is time (in minutes).

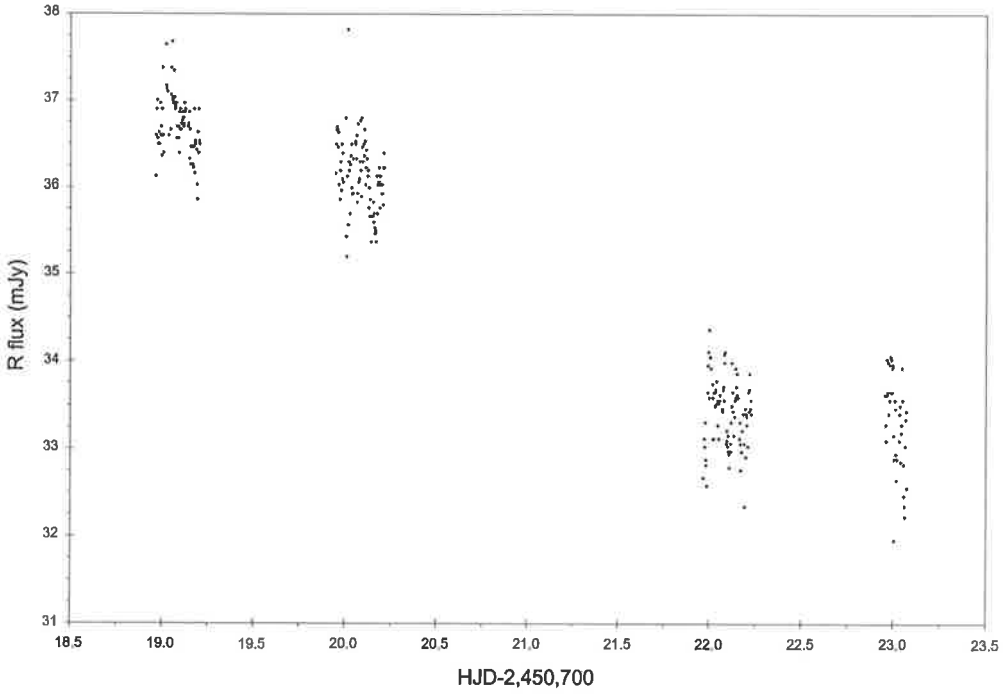

Figure 10.8
Woomera R-band data for PKS 2155-304 vs. HJD.

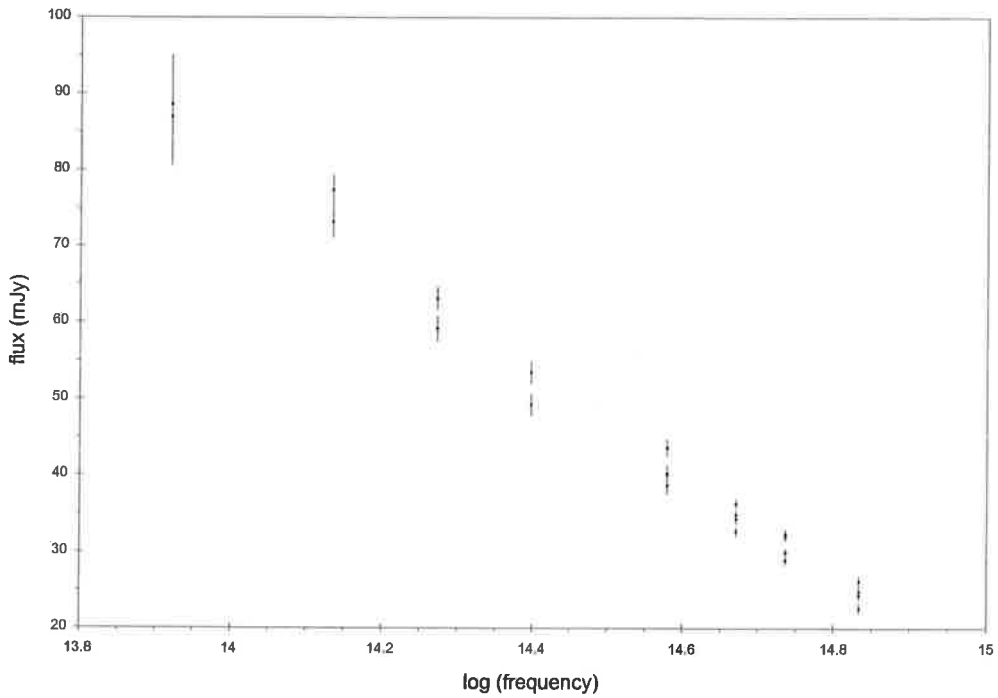

Figure 10.9
IR-optical flux spectrum of PKS 2155-304.
The order of filters is (left to right) L,K,H,J,I,R,V,B.
In the optical-IR regime, the source is red.

Unfortunately, CANGAROO yielded a non-detection (Roberts *et al.* 1999) of PKS 2155-304 during the time of the simultaneous optical data, so the significance of the optical variability seen here upon TeV behaviour can not be examined.

10.4 PKS 2005-489

This source is a BL Lac object which is active in X-rays. Although observations have been undertaken in γ-rays (Roberts *et al.* 1999), the data presented here were taken for another study for which the results have not yet been published.

BVRI exposures were obtained on six nights over 15th-24th September 1998. For each night, short R-band time-series and four sets of sequential BVRI frames were obtained. There was no evidence of variation within any night's data; over the entire period, however, change in brightness was significant.

Figure 10.10 shows the stars used in the differential reductions. As no magnitudes for field stars had been found in the literature, no conversion to standard magnitudes, and thence to flux, has been applied.

Figure 10.11 gives the R time-series against HJD; for the first three nights, little or no change is seen. After then, a significant brightening of 0.125mag occurs, although it is not known when the increase began.

The nightly BVRI "snapshots" data are presented in Figure 10.12. The behaviour is similar here. Due to the poor sampling in time, and the relatively large scatter in some of the data, it is not possible to say if there was any lag between bands in the time of start of the brightening.

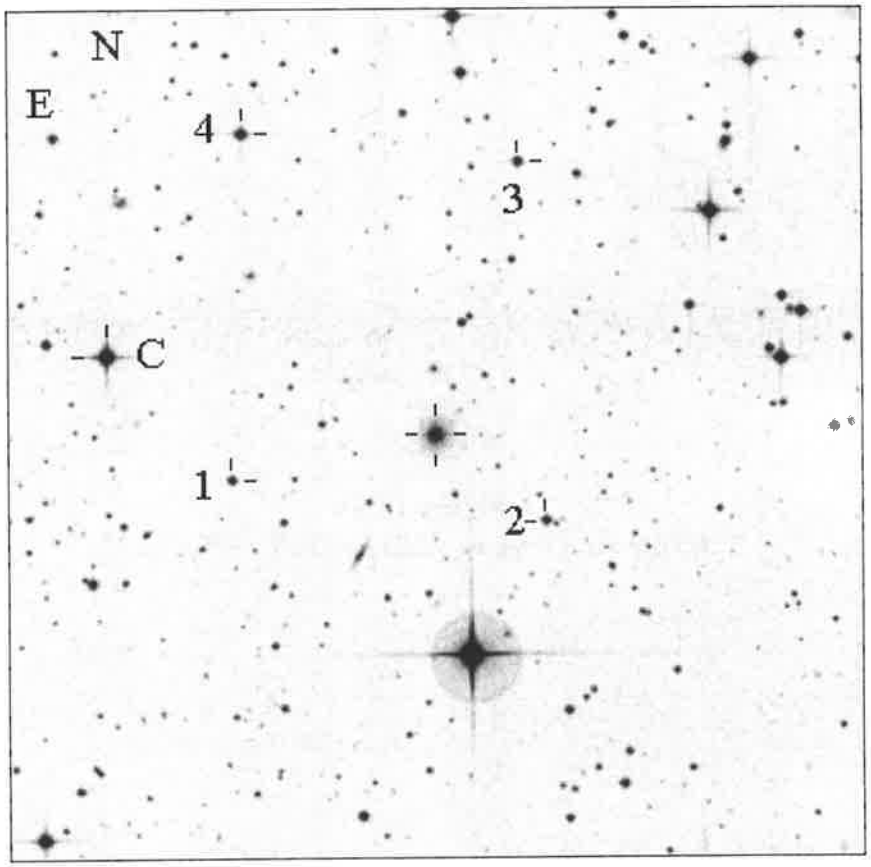

Figure 10.10
PKS 2005-489 field, 10'-square (courtesy STScI DSS).
Stars used in the Woomera differential reduction are shown.
C and K stars marked by tics, AGN by a cross.

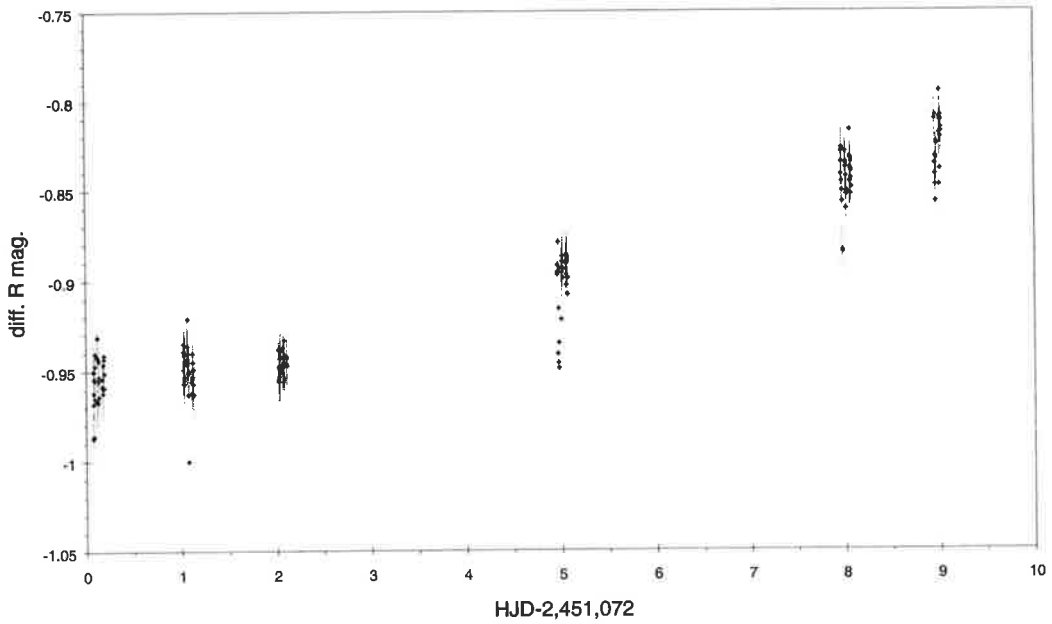

Figure 10.11
Woomera R data vs. HJD for PKS 2005-489.

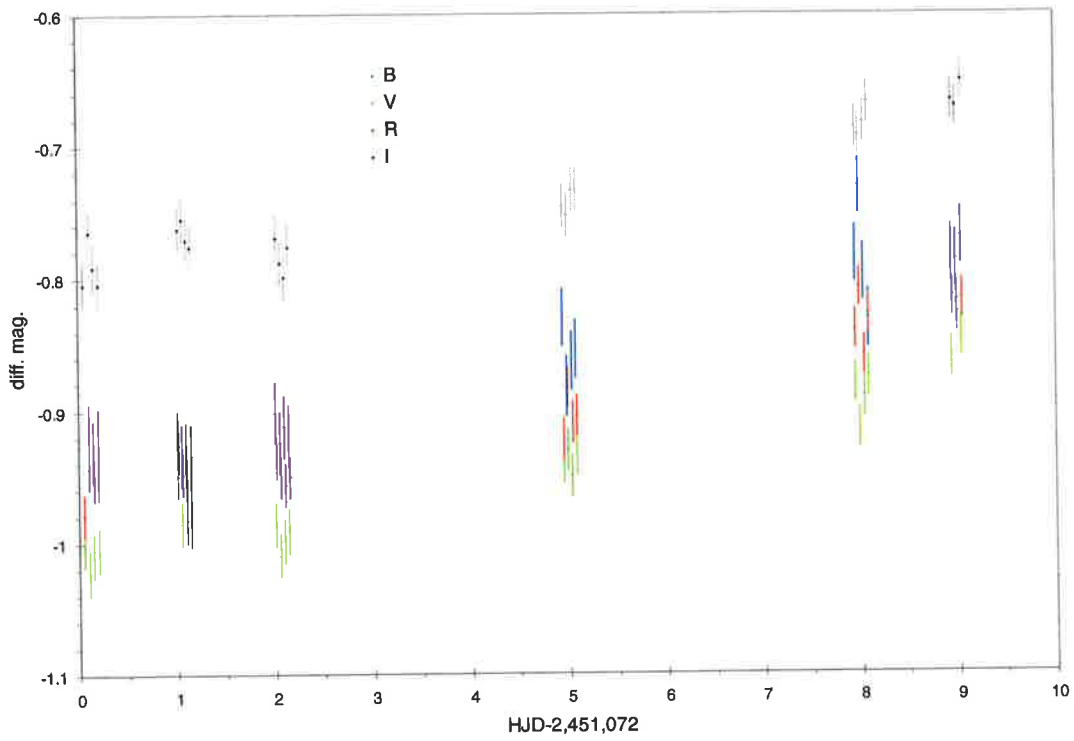

Figure 10.12
Woomera BVRI nightly snapshots vs. HJD for PKS 2005-489.

10.5 PKS 0548-322

Another X-ray-active BL Lac object, PKS 0548-322 was observed simultaneously with CANGAROO in late October-early November 1997 (Roberts *et al.* 1999) in order to look for possible TeV/optical correlation and to provide a few points in its flux spectrum. Most optical data were R-band time-series, with short V or I time-series obtained on two nights.

Differential reduction of the Woomera CCD data was undertaken using the field stars specified in Smith *et al.* 1991, and the differential magnitudes converted to standard magnitudes using the magnitudes given therein. Flux conversion was achieved as for PKS 2155-304.

Flux vs. HJD is shown if Figure 10.13, whilst Figure 10.14 gives each night's R-band fluxes. On a few nights there appears to be definite short-term modulation, although it is never greatly above errors. Little change night-night is in evidence, although a slight increase from HJD 2,450,754 to 2,450,755 may be significant.

During these observations, this source was about 1 magnitude brighter (in R) than for the epochs given in Xie et al. 1996, namely December 1993 and December 1994.

An optical (i.e. VRI only) flux spectrum is presented in Figure 10.15. There was no CANGAROO detection during the time of these observations.

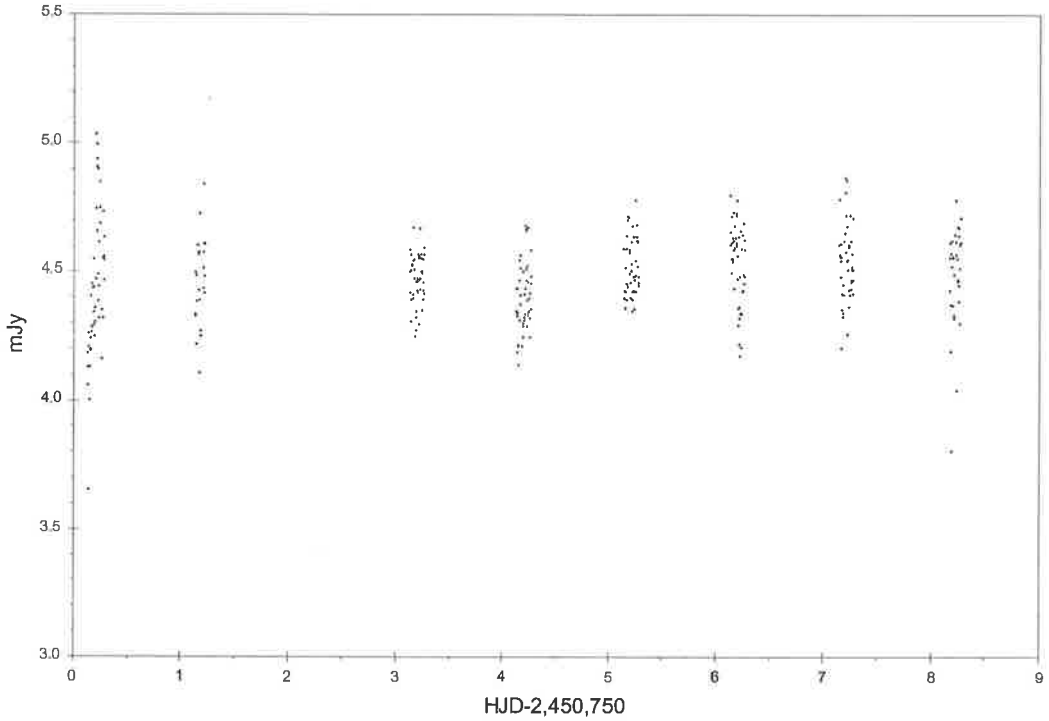

Figure 10.13
Woomera R-band flux for PKS 0548-322.

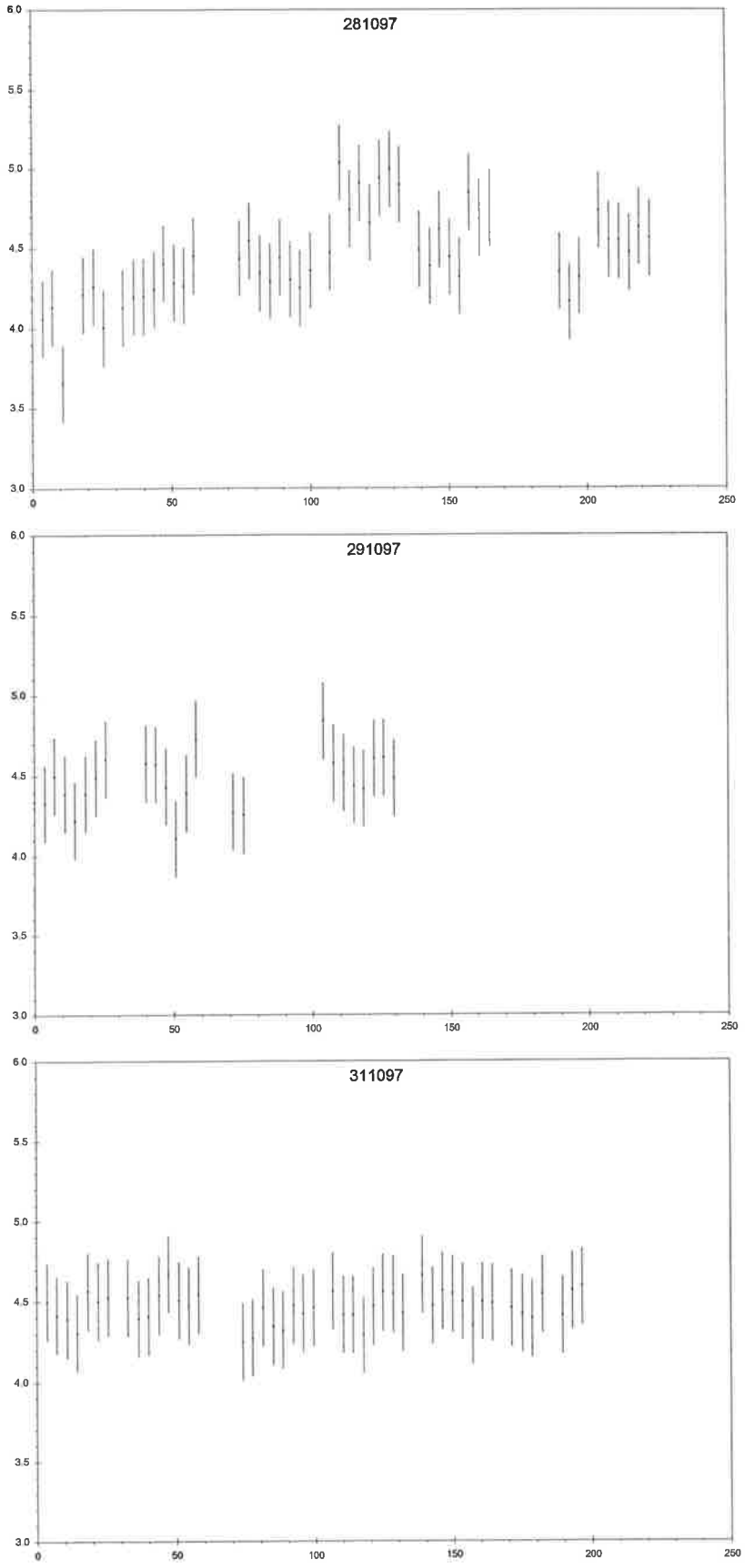

Figure 10.14
Nightly Woomera R-band flux for PKS 0548-322.
Ordinate is flux (in mJy), abscissa is time (in minutes).

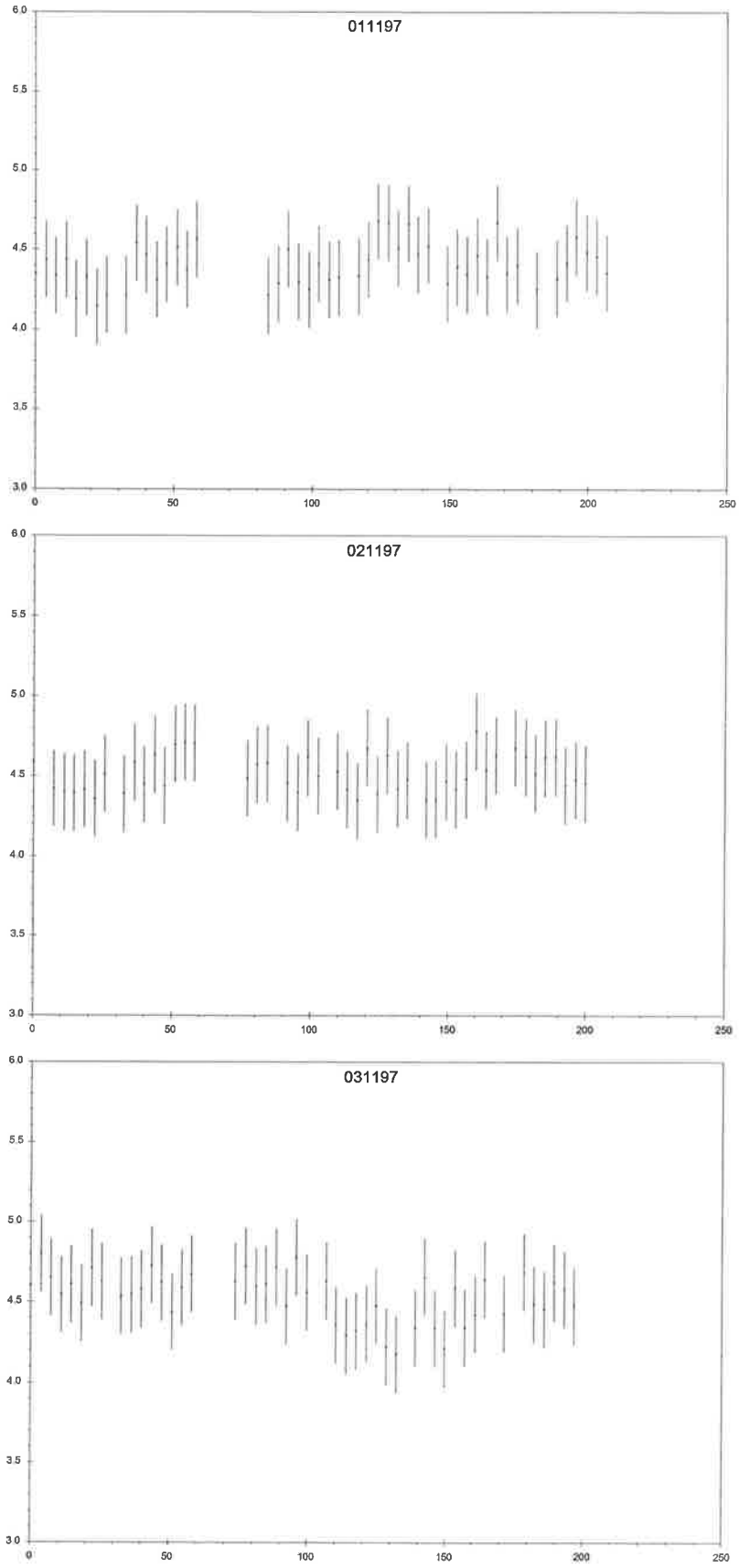

Figure 10.14 continued
Nightly Woomera R-band flux for PKS 0548-322.
Ordinate is flux (in mJy), abscissa is time (in minutes).

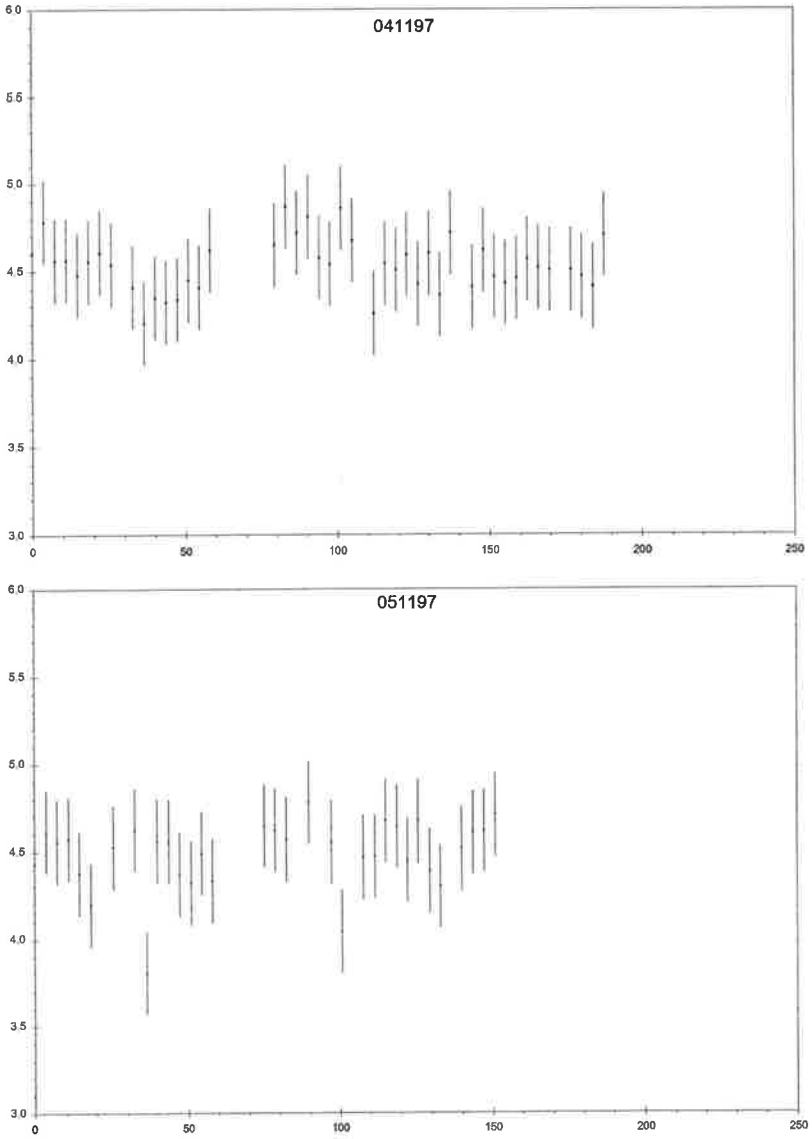

Figure 10.14 continued
Nightly Woomera R-band flux for PKS 0548-322.
Ordinate is flux (in mJy), abscissa is time (in minutes).

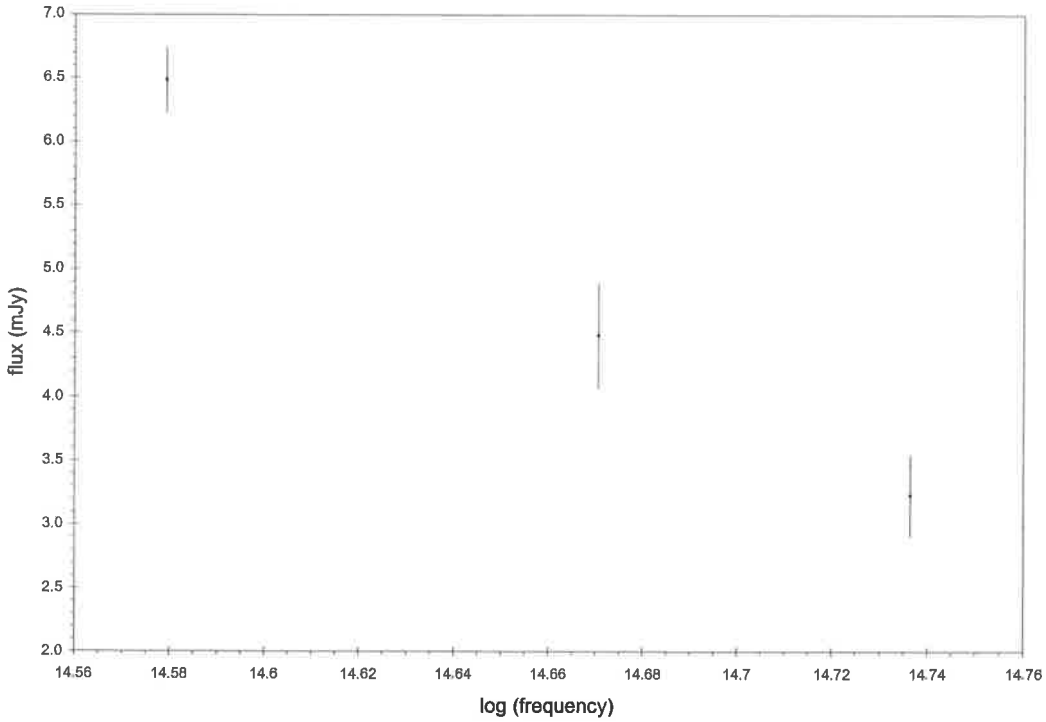

Figure 10.15

Woomera optical flux spectrum for PKS0548-322.
Order of filters is (left to right) I,R,V.
Since there was very little change in flux in any filter over the entire observing run, the average flux for all nights in each filter is shown.
Again, as with PKS 2005-489, in the optical regime, this source is red.

10.6 PKS 2255-282

This active galactic nucleus was observed as part of a multi-wavelength campaign initiated after a millimetre-wavelength flare was observed in 1997 (Tornikoski *et al.* 1999). Due to the faintness of the source, and the desire to obtain filtered data for comparison with flux measurements obtained at other wavelengths, individual images from Woomera were co-added together in order to increase the signal from the 16th-magnitude source. Thus, time series data, as such, were not derived for this object.

The field also was observed with the CTIO 0.9-metre telescope (by Jonathan Kemp of Columbia University), and VRI magnitudes for the AGN and three field stars were obtained; see Figure 10.16. The Woomera data used these stars for differential reduction, with the CTIO magnitudes being employed to convert measurements to the standard system.

Table 10.3 is adapted from Tornikoski *et al.* 1999 and shows the results of the campaign's optical observations.

Table 10.3
PKS 2255-282 optical data July-September 1998

Date	Filter	Magnitude	Flux (mJy)	Site
220798	R	16.11 ± 0.10	1.02 ± 0.09	Woomera
090898	V	16.36 ± 0.03	1.05 ± 0.03	CTIO
090898	R	16.03 ± 0.03	1.02 ± 0.03	CTIO
090898	I	15.66 ± 0.03	1.23 ± 0.03	CTIO
160998	V	16.44 ± 0.10	0.97 ± 0.09	Woomera
160998	R	15.96 ± 0.10	1.17 ± 0.11	Woomera

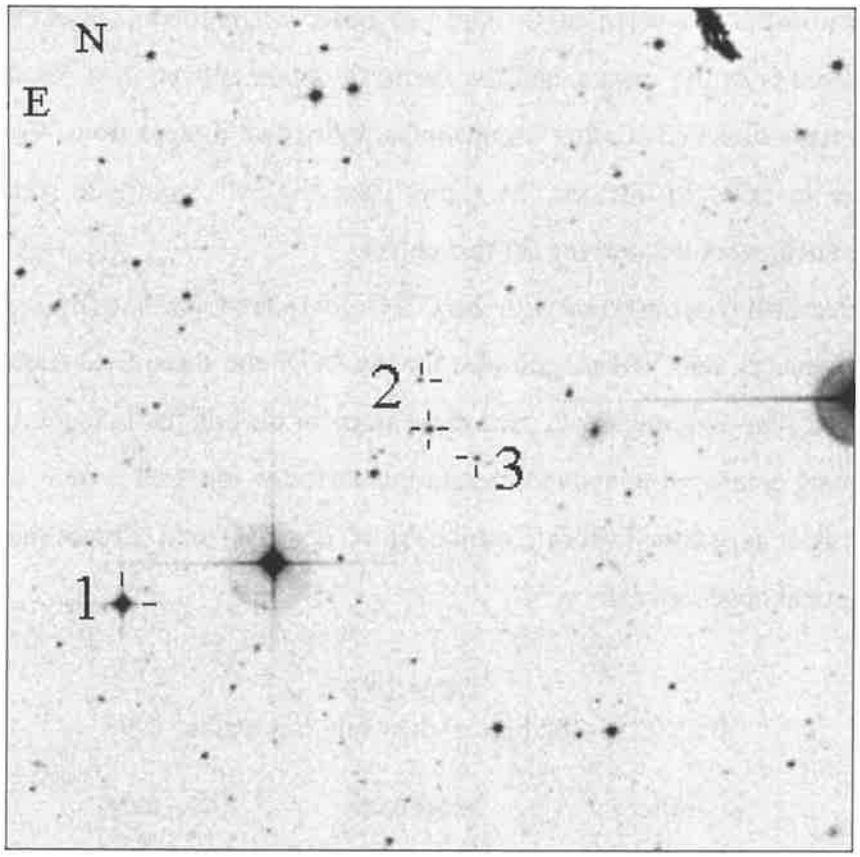

Figure 10.16
PKS 2255-282 field, 10'-square (courtesy STScI DSS). AGN is marked with a cross; stars measured at CTIO are marked with two tic marks, with magnitudes as measured in the table below.

Star	V	R	I
1	12.39	12.00	11.66
2	18.34	17.92	17.46
3	17.92	16.87	15.72

Note: no formal error estimates were supplied, but it may be estimated that for star 1, errors are of the order 0.01 to 0.02 mag, and for stars 2 and 3, of the order 0.05 to 0.1 mag.

10.7 PKS 0208-512

This is another BL Lac object for which the optical data have not yet been published. VRI frames were obtained at Woomera on five nights between 29/11/1998 and 5/12/1998. The SSO 40" was used in August and December 1998 (Hayley Bignall, private communication) to obtain VRI data, from which calibrated VR magnitudes for some field stars were derived, since none were found in the literature.

A DSS plot of the field is shown in Figure 10.17, with the SSO stars labelled. The magnitudes (averages from two nights of August 1998 data) are shown in Table 10.4. No significant variation was found in the Woomera or SSO data.

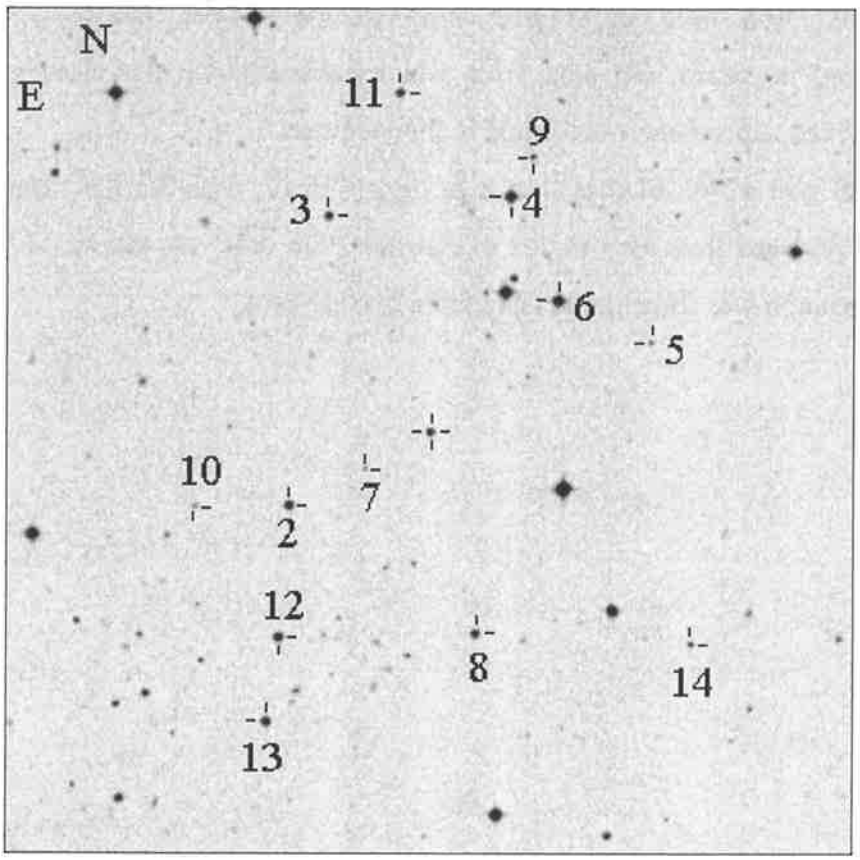

Figure 10.17
PKS 0208-512 field, 10'-square (courtesy STScI DSS).
Stars observed at SSO are marked by two tics; AGN marked by a cross.
Numbering as per Bignall (private communication).
The observed magnitudes are presented in Table 10.4.

Table 10.4

SSO magnitudes for PKS 0208-512 field stars

Object	R mag	error	V mag	error
0208-512	17.26	0.04	17.59	0.04
2	15.27	0.03	15.74	0.03
3	15.68	0.03	16.15	0.03
4	14.24	0.03	14.70	0.03
5	17.82	0.05	18.92	0.06
6	14.21	0.03	14.67	0.03
7	19.68 (single)	0.12	20.05 (single)	0.10
8	15.79	0.03	16.27	0.04
9	17.31	0.04	18.06	0.04
10	18.83 (single)	0.09	19.71 (single)	0.08
11	15.35	0.03	16.08	0.03
12	14.75	0.03	15.32	0.03
13	15.09	0.03	15.56	0.03
14	16.67 (single)	0.03	17.78 (single)	0.05

Note: all magnitudes are an average from multiple observations, except those marked "single".

10.8 AH Mensae

10.8.1 General

AH Men (also known as Mensae 1) is the optical counterpart to the X-ray source H 0551-819 (Buckley *et al.* 1993). Optical photometry shows modulation near 3 hours, flickering and possibly periodic oscillation around 20 minutes. P_{orb} is taken to be 2.952 hr, P_{wd} = 2081s, and there is a "superhump" (modulation at a period slightly greater or less than P_{orb}) at 3.053 hr (Patterson 1995, hereafter P95). It is to be noted for CV's in general, that the sign of the superhump (i.e. positive for $P>P_{orb}$, negative for $P<P_{orb}$) can change with time.

10.8.2 Woomera data

AH Men was observed in order to provide data for a Centre for Backyard Astrophysics (CBA) campaign on this CV. Data were obtained in January 1997, March 1998 and November-December 1998.

The light-curves are given in Figures 10.18. Errors are estimated from nightly C-K values and the general error behaviour as seen in large data sets for other objects; generally, the range is ± 0.01 to ± 0.015 mags. Whilst the temporal resolution is lower than that in P95, similar features are seen in the data- flickering, overall night-night variations and modulation near 3 hours.

As one of the main points of interest in this CV is the variety of periods present in optical photometry, period searches were undertaken on these data. The neural network program "Lancelot" was run over various combinations of the entire data set:

(i) all data, from January 1997 to November 1998;

(ii) all January 1997 data;

(iii) "early January" data, i.e. 030197 to 060197 only;

(iv) "late January" data, i.e. 140197 and 160197;

(v) November 1998 data (note: the 010398 data were not included, since that was only a short, single night of observation).

The results are plotted in Figures 10.19. Note that here, we are not concerned with the high-frequency modulations (20 minutes or so) as discussed in P95; we look only at periods around three hours.

A number of periods are prominent, and two of these correspond to the main periods found in the blue-coloured (U-, $CuSO_4$-, or B-filtered) data of P95, namely 2.952 hours (orbital) and 3.053 hours (superhump). However, a third period (2.711 hours) is present in the

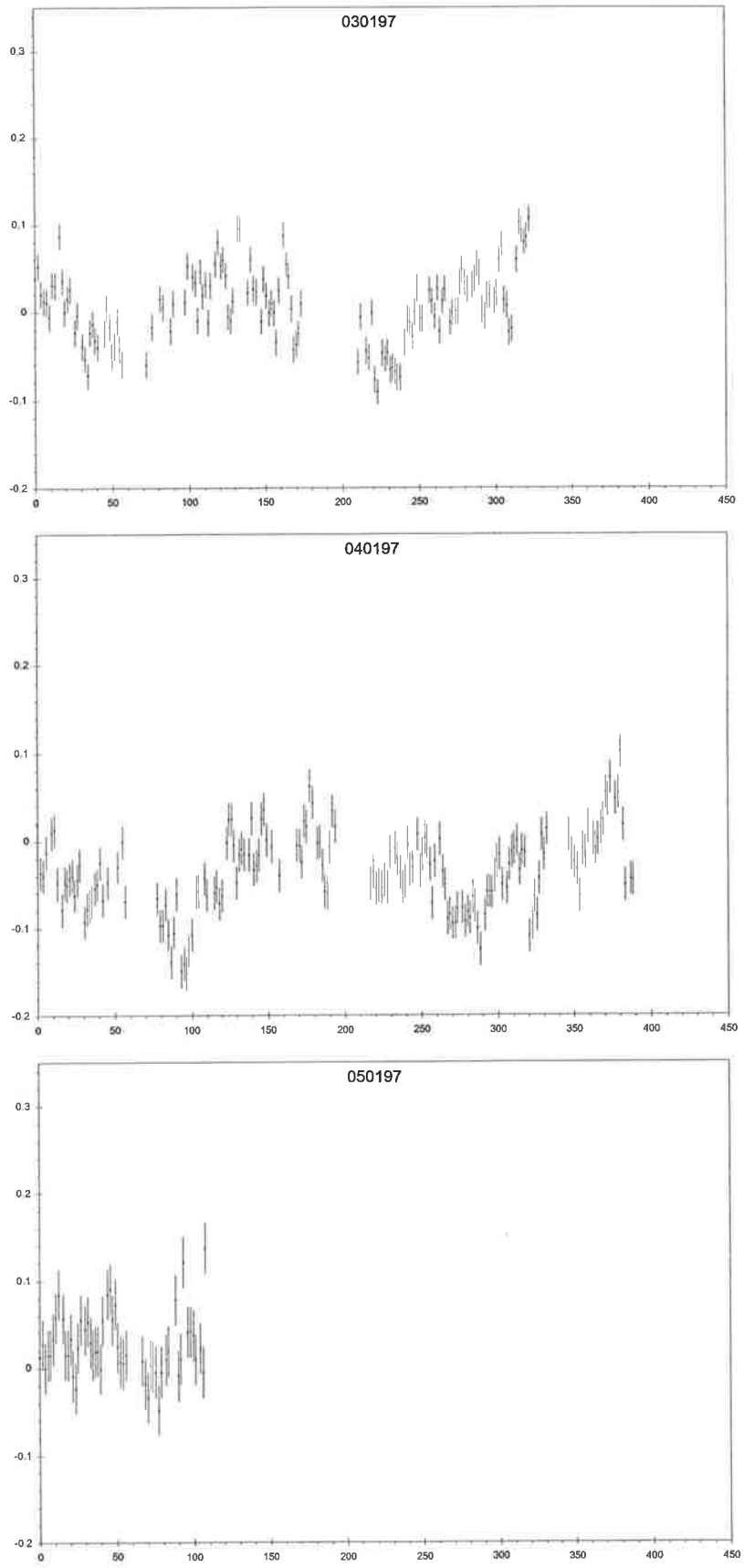

Figure 10.18
Woomera white-light photometry of Mensae 1.
Ordinate is differential magnitude, abscissa is time (in minutes).

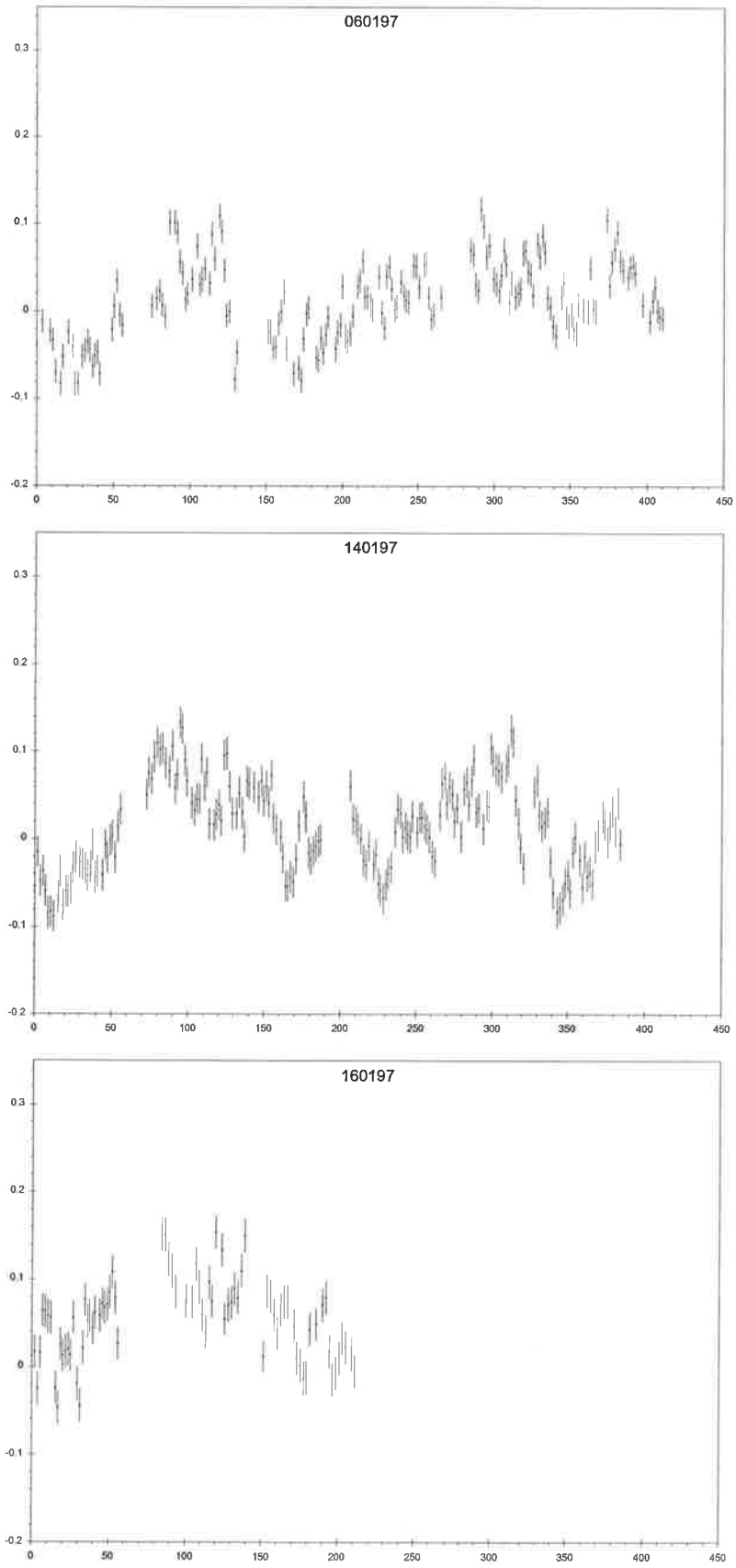

Figure 10.18 continued
Woomera white-light photometry of Mensae 1.
Ordinate is differential magnitude, abscissa is time (in minutes).

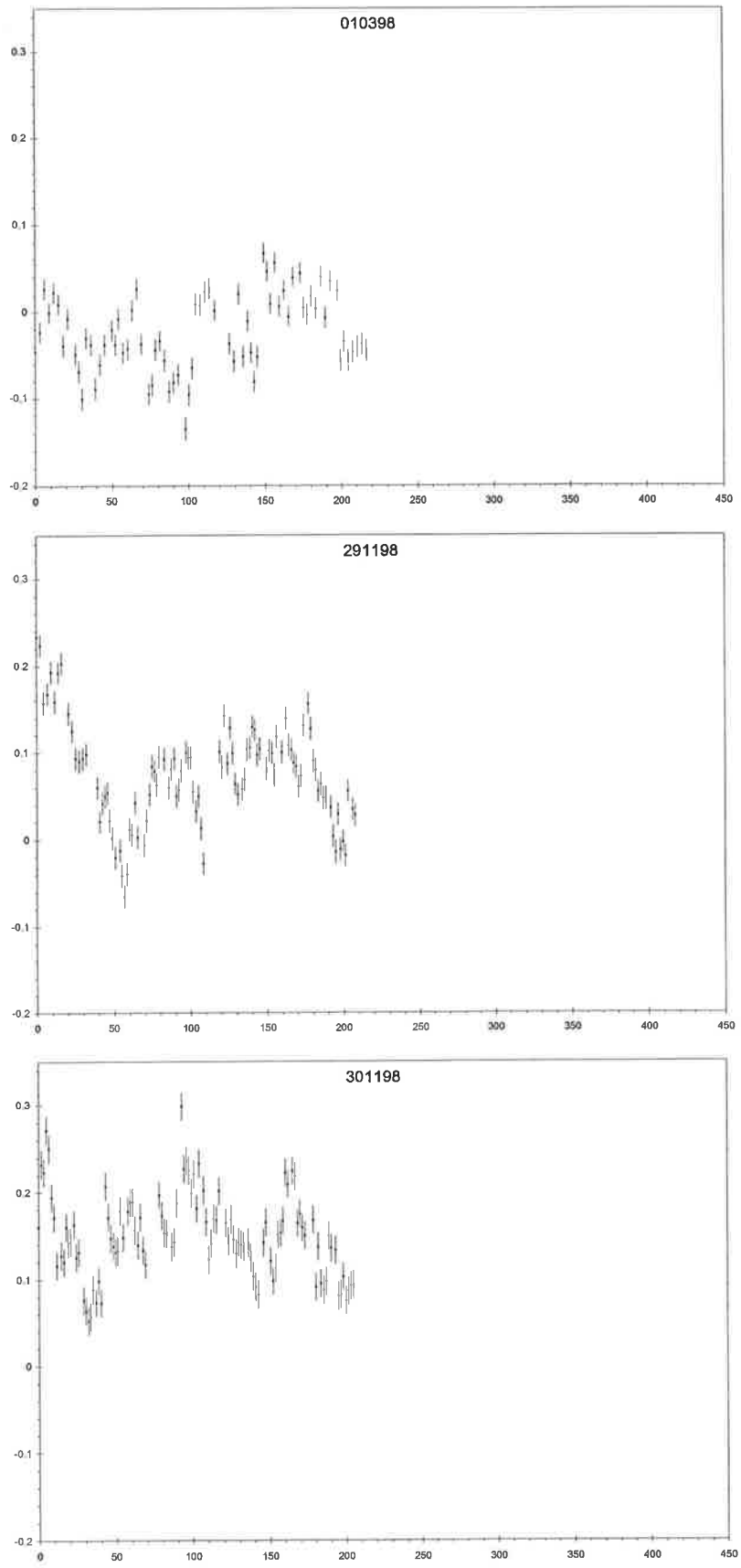

Figure 10.18 continued
Woomera white-light photometry of Mensae 1.
Ordinate is differential magnitude, abscissa is time (in minutes).

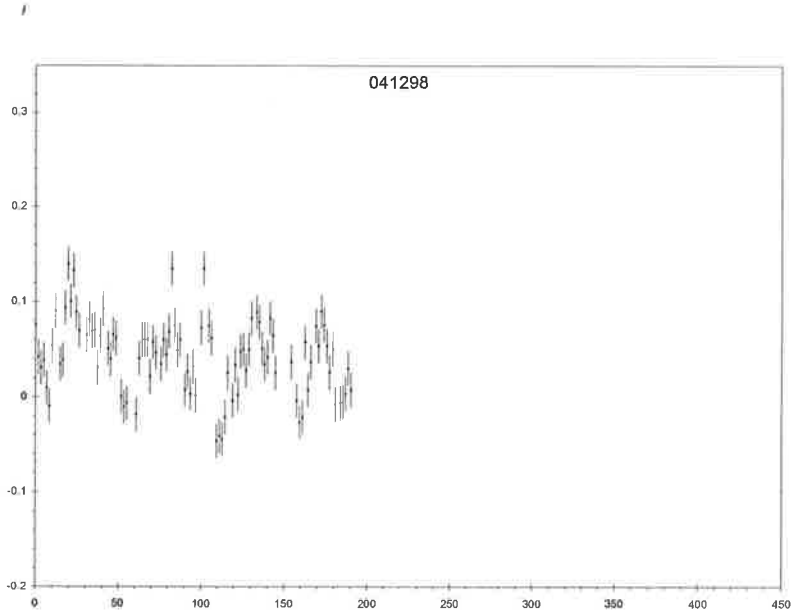

Figure 10.18 continued
Woomera white-light photometry of Mensae 1.
Ordinate is differential magnitude, abscissa is time (in minutes).

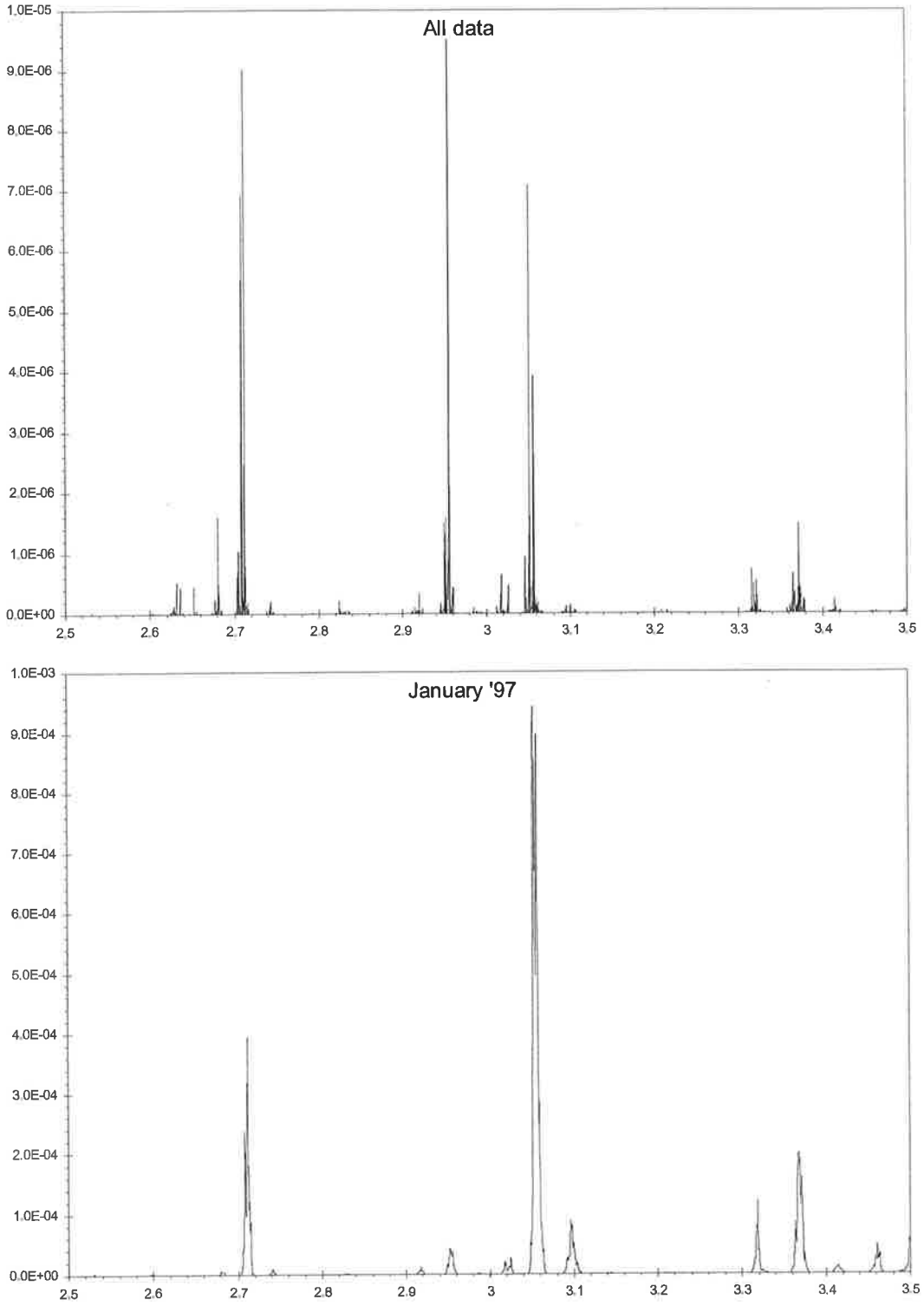

Figure 10.19

Neural network period searches on Woomera data.
Ordinate is significance of trial period, abscissa is period (in hours).

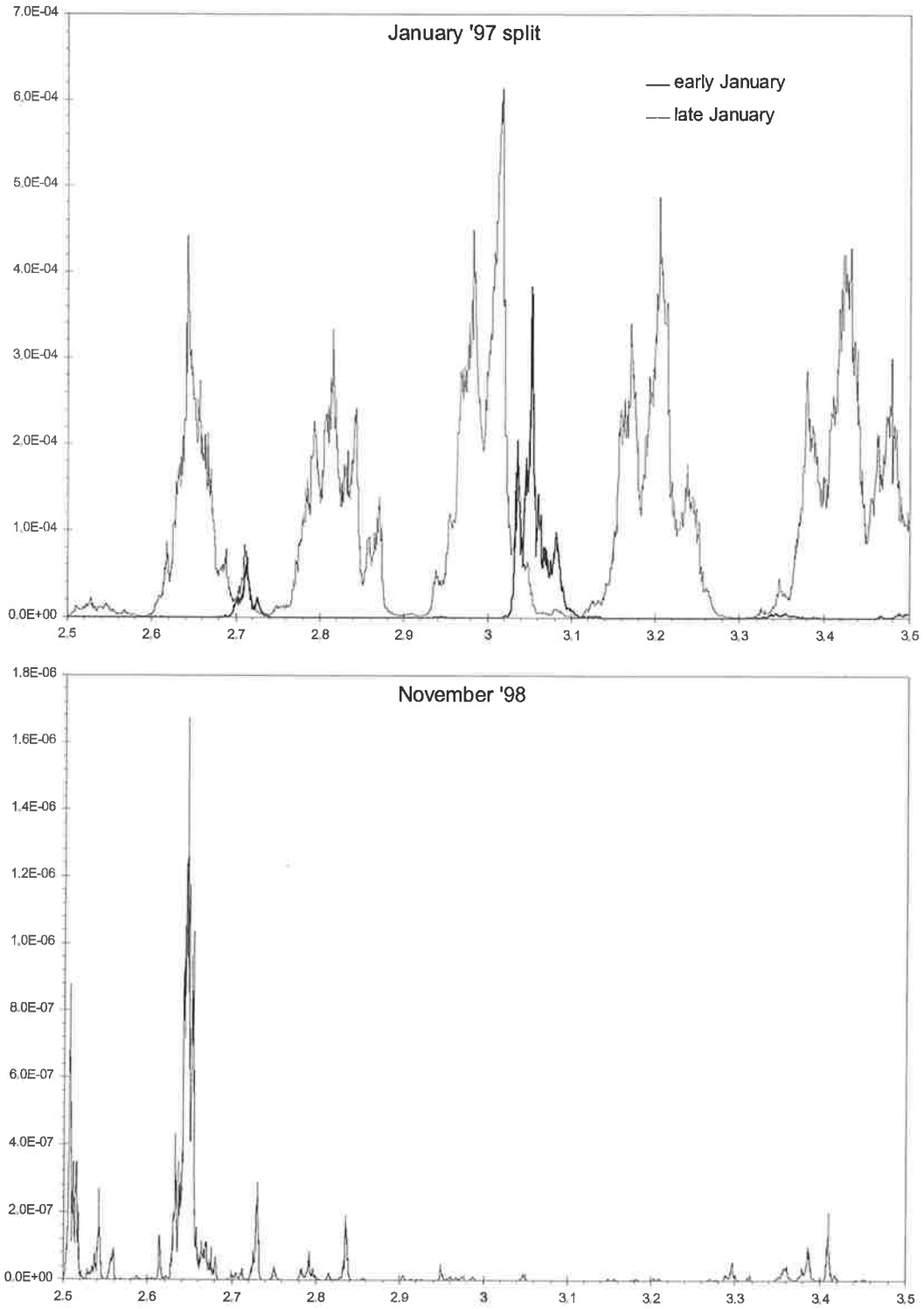

Figure 10.19 continued
Neural network period searches on Woomera data.
Ordinate is significance of trial period, abscissa is period (in hours).

Woomera data which is not mentioned explicitly in P95 at all. Further, it is noted that the strengths of these signals vary depending on the subset of data examined, i.e.

	Strength of signal			
	2.711 hrs	2.952 hrs	3.053 hrs	"best" period
all data	very strong	Peak	strong	2.955 hrs
January 97	present	Weak	peak	3.053 hrs
early January	present	in the noise?	peak	3.053 hrs
late January	present	in the noise?	absent	3.018 hrs
November 98	in the noise?	in the noise?	absent	2.647 hrs

It must be noted that the November 1998 runs were only just over three hours in length, and it may be that this will cause difficulties in interpreting the searches for that epoch. Woomera data phased with the 2.71172 hr period are shown in Figure 10.20.

The main point is the presence in all data sets (except November 1998) of a signal at about 2.711 hours. This is present even when the "main" signals (2.952 and 3.053 hrs, from 1994-1995, P95) are absent in the Woomera data. Whether this is due to some real change in the behaviour of AH Men, or is due to the redder bandpass of the Woomera CCD, is not known.

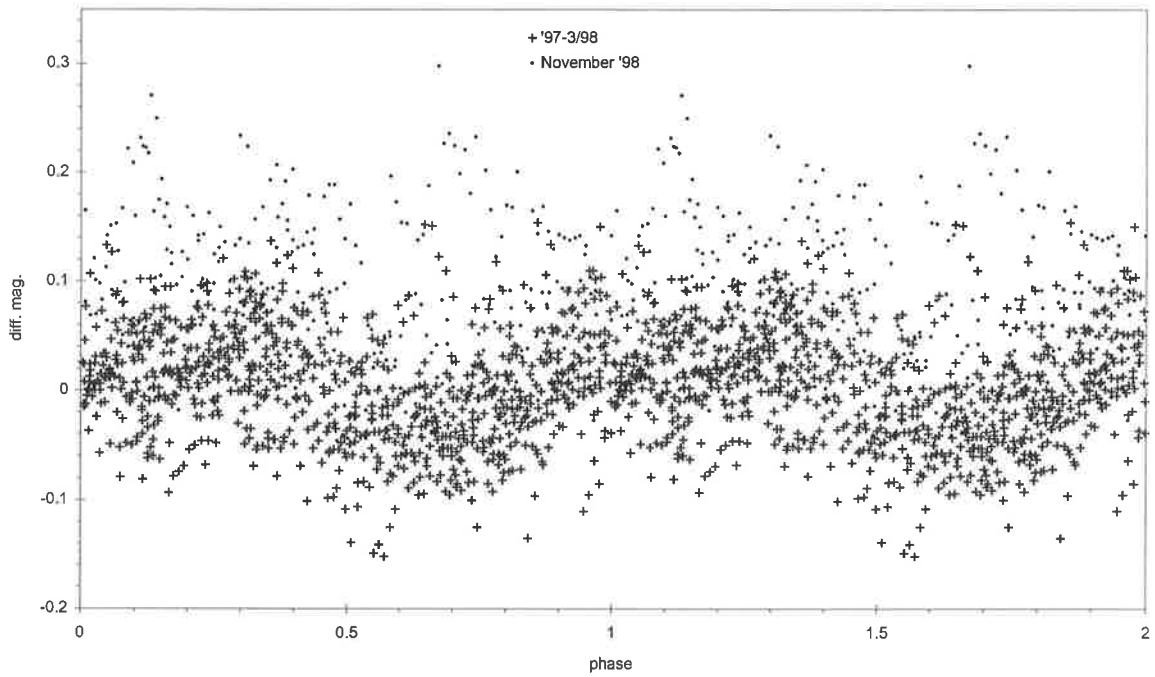

Figure 10.20
Woomera AH Men data phased at 2.71172 hours.

10.9AE Aquarii

10.9.1 General properties

AE Aqr is generally classed as a nova-like CV, and is well known for its readily observed flares. This source has been observed from radio through to X-ray and gamma-ray energies, and is variable in all these regimes.

The orbital period is 9.88 hours, and the 33s rotation of the primary is evident in optical and high-energy observations.

10.9.2 Woomera data

The data were reduced differentially. Some of the field stars used were in common with the secondary standards as given in Henden and Honeycutt 1995. Errors were estimated using the magnitude-scatter plots for each night; the combined plot for all nights' data is shown in Figure 10.21.

The nightly light curves are given in Figures 10.22. The data are shown phased at P_{orb} in Figure 10.23a, and on an intensity scale in Figure 10.23b. Activity is evident on several time scales:

(i) ellipsoidal modulation (i.e. maxima at phases 0.25 and 0.75, minima at 0.0 and 0.5; it is noted that the incomplete sampling of the phase axis does not allow this to be claimed with great certainty) from the secondary which, at the long orbital period of this CV, contributes significantly to the total observed flux (Figures 10.23 and 10.23b);

(ii) flares (180995,190995 and 171095) of approximately 10-20 minutes' extent;

(iii) low-level (but well above error) minutes-scale flickering on all nights;

(iv) for different nights' data taken at the same phase, a slight change in intensity.

The temporal resolution of the data (60 seconds at best) is too coarse for the 33s modulation from the primary to be evident. It is to be noted that this value could be decreased to about 20s if 10s integrations were used with half-frame image downloads taken with no interval between exposures. If a smaller sub-frame only were used, it may be possible to drop this to 15s, in which case the primary's modulation may be just detectable.

It is expected that the use of a high-efficiency (e.g. thinned, back-illuminated) and non-anti-blooming CCD with fast readout would allow the WD modulation to be studied even with a telescope as small as the C14.

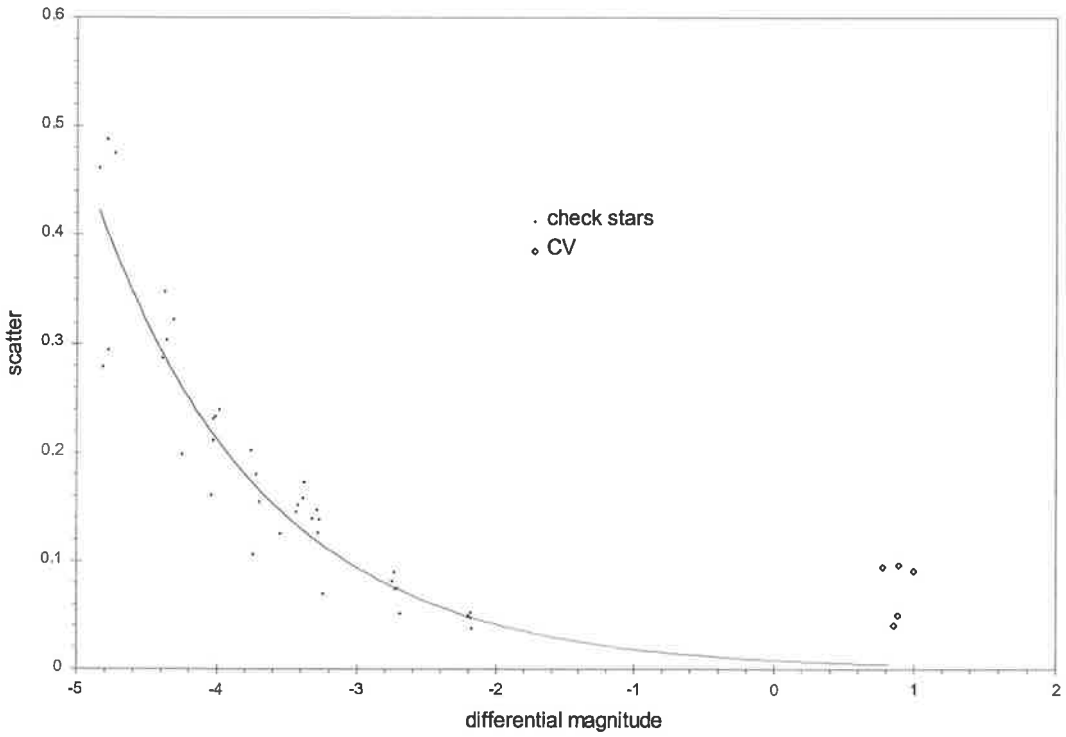

Figure 10.21

Scatter-magnitude plot for Woomera white-light data. An exponential fit to the K star data is shown, with its extrapolation to the observed magnitude of AE Aqr. Expected errors for the CV are in the range 0.003 to 0.006 mag.

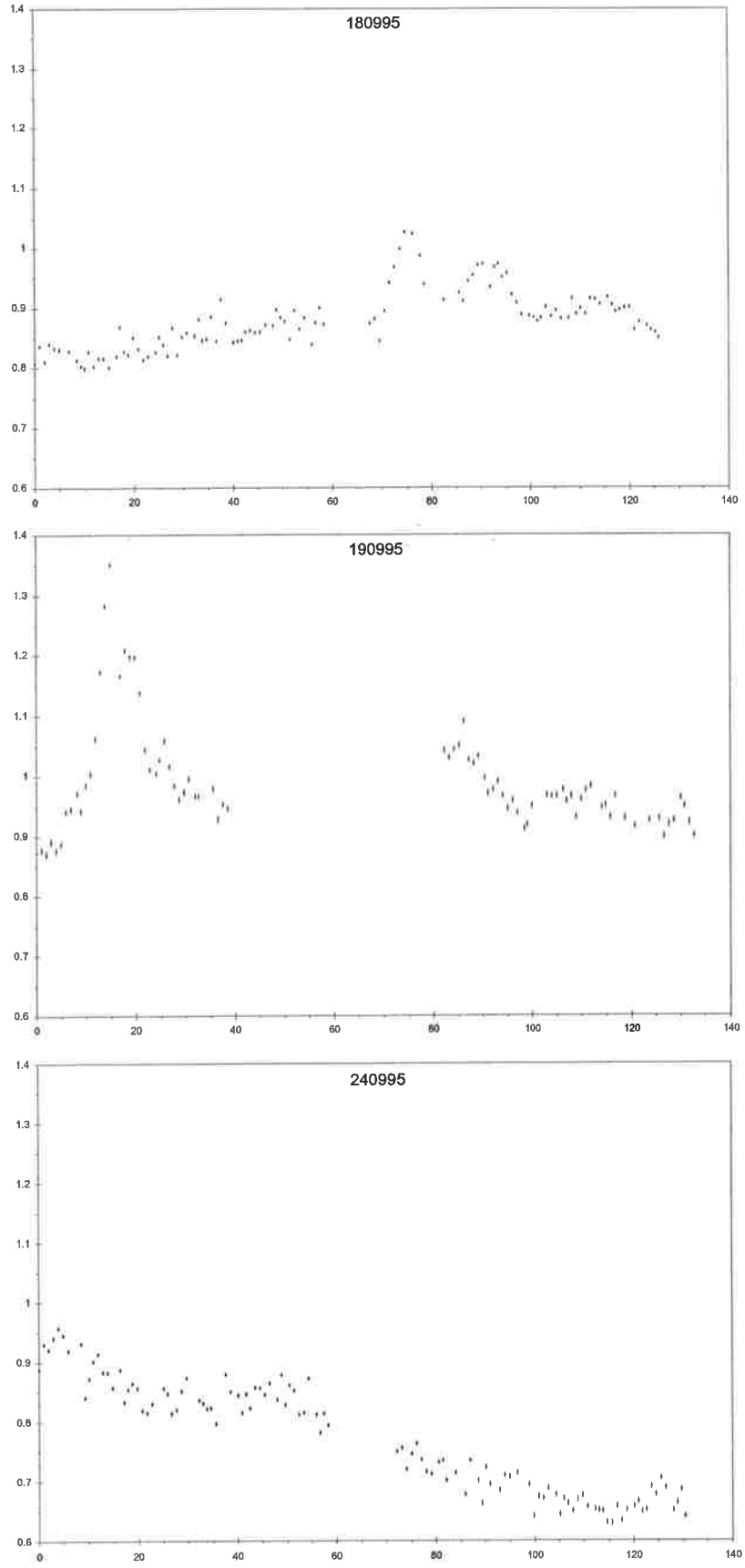

Figure 10.22
Woomera white-light photometry of AE Aqr.
Ordinate is differential magnitude, abscissa is time (in minutes).

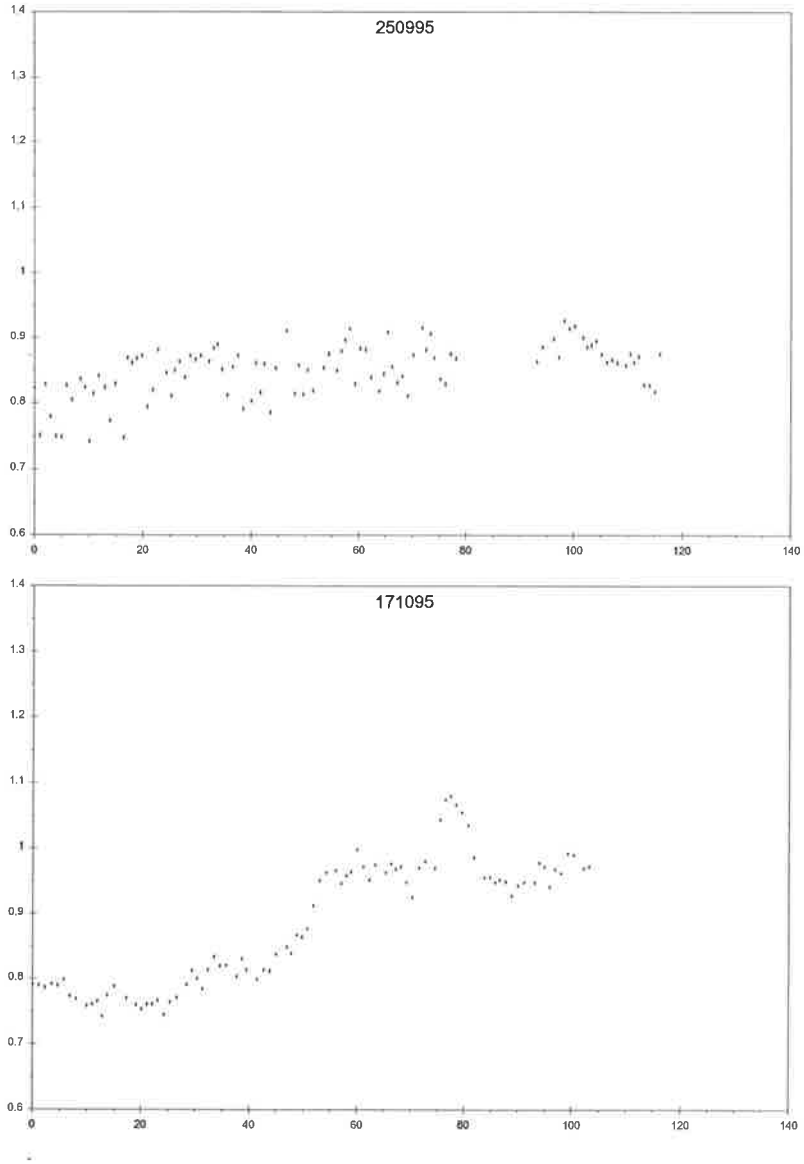

Figure 10.22 continued
Woomera white-light photometry of AE Aqr.
Ordinate is differential magnitude, abscissa is time (in minutes).

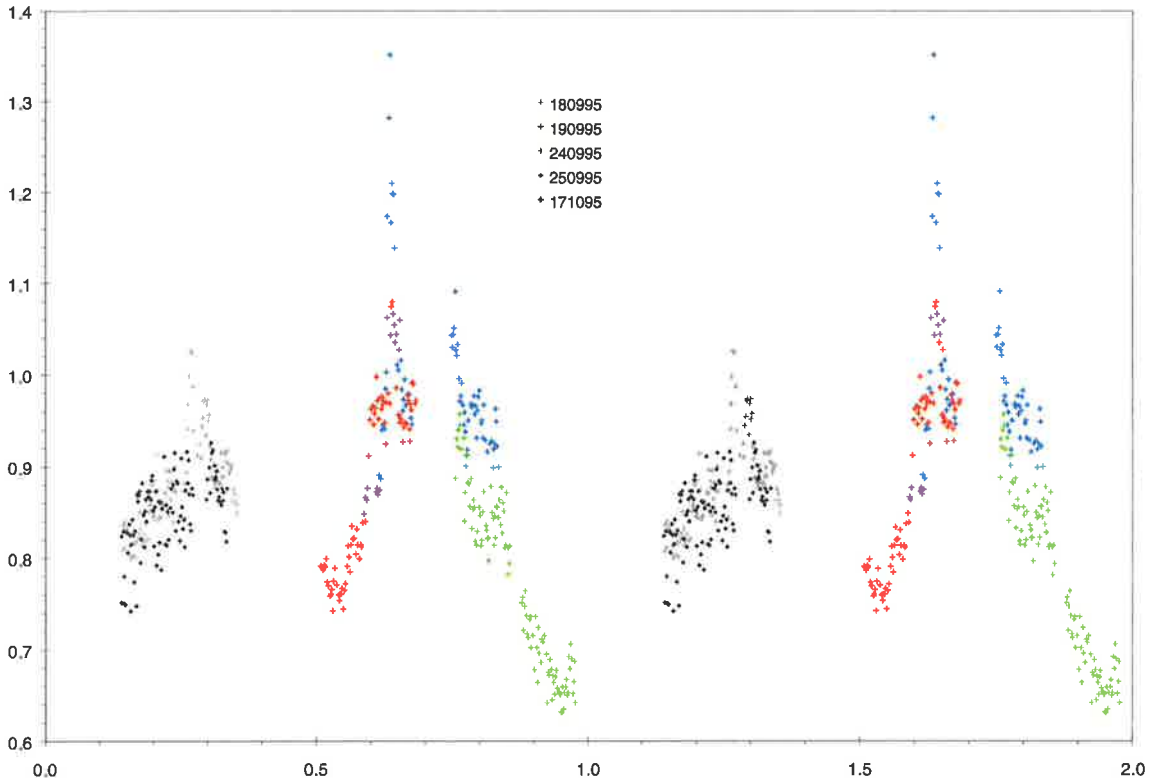

Figure 10.23a

Woomera white-light data; ordinate is differential magnitude, abscissa is orbital phase.

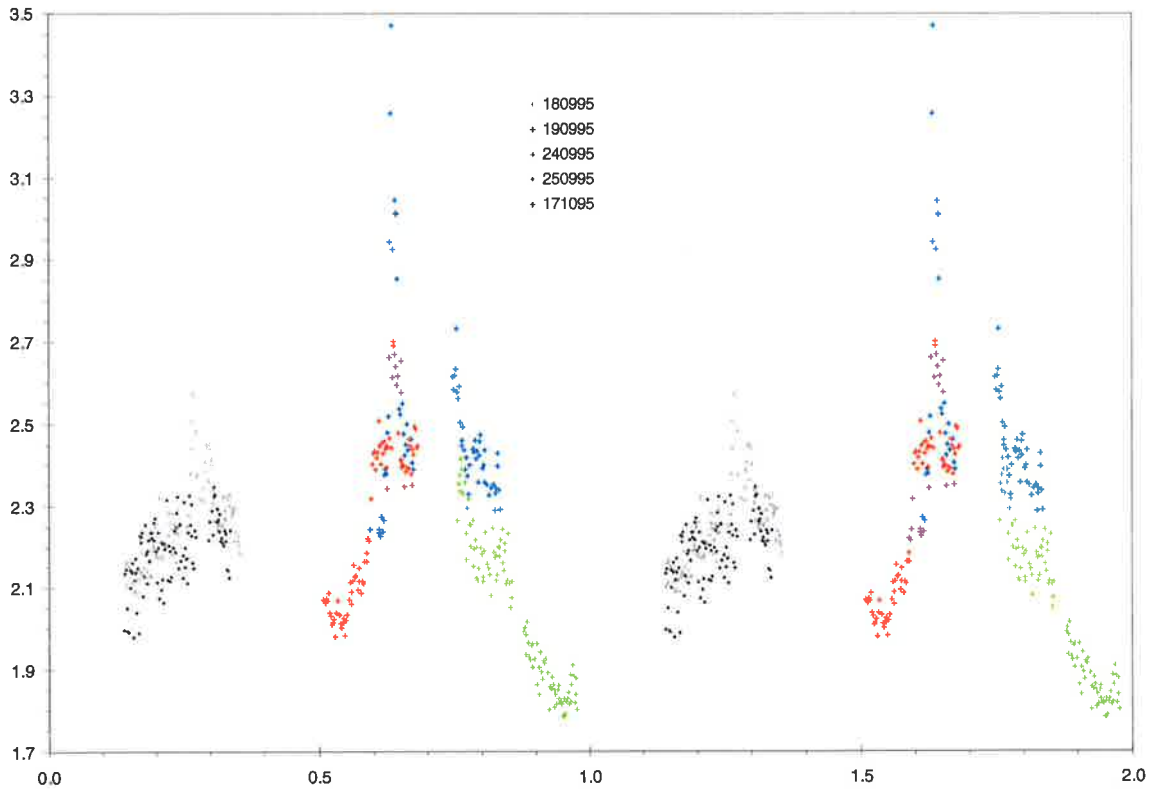

Figure 10.23b

Woomera white-light data; ordinate is relative intensity, abscissa is orbital phase.

10.9.3 Application to HE work

As mentioned, AE Aqr is detectable and variable in X-ray and γ-ray energies. Simultaneous optical coverage during high-energy observation is useful in order to monitor for flaring activity, to gauge overall CV intensity (apart from short-term flares) and, if temporal resolution is sufficient, to check for correlation between HE activity and the optical WD modulation (see WCVS Section 8.2 and references therein).

10.10 TX Columbae

10.10.1 General

TX Col is an intermediate polar, and is also an X-ray source (1H 0542-407) (Tuohy *et al.* 1986). P_{orb} is 5.718 hours, average m_V is 15.7 and, as $i = 25°$, it is not an eclipsing system (WCVS Table 7.1). Being an IP, several periods besides P_{orb} will be present in the data-namely, various combinations of P_{orb} and P_{wd}. Indeed, it is quite possible that the dominant optical period may not be P_{orb} at all. For this CV, a beat period, P_{syn} (see below), often is dominant in the optical, although there are long-term changes in the light-curve and associated periodograms (Buckley 1995).

10.10.2 Woomera data

This IP was observed on two nights only, 18-19/1 and 21-22/2/1996 (local dates). This was done out of curiosity, in order to compare the results obtained with published light-curves for a well-known CV; up to the time of these observations of TX Col, only "new" sources had been observed at Woomera, with no known published light-curves there for.

The time series are given in Figure 10.24. There is clear modulation, as well as changes in overall brightness between months. These data also suggest (most noticeably for 18/1/96) that there may also be cycle-cycle changes in the light-curve. Errors were estimated from the scatter in the C-K values, and from the general behaviour found in the C-K_n values for extensive data sets for other objects.

The data are phased with various periods in Figures 10.25. By chance, the two data runs started at very nearly the same orbital phase, and it is clear that the brightness change between months is due not to some orbital modulation. Two prominent periods (WCVS Table 7.1) are P_{wd} (= 1910.5s) and P_{syn} (= 2106s). P_{syn} ("synodic period") is a beat period between P_{orb} and P_{wd}, and represents the period at which a point fixed in the rotating frame of the system is illuminated by an X-ray source on the primary. As these X-rays can be reprocessed into optical emission, this period can also be expected in the optical.

Both these periods are present in the data, and it is interesting to note the apparent "anti-phase" appearance of the two months' data sets. A quick neural-network period search between 1800s and 2300s, with a resolution of 0.125s, led to a best period estimate of 2032s. The actual significance of this period is uncertain, since there are only two nights of data, the run on each night was fairly short, and the possible "anti-phase" appearance of the two data-sets may not sit well with the period-searching algorithm employed.

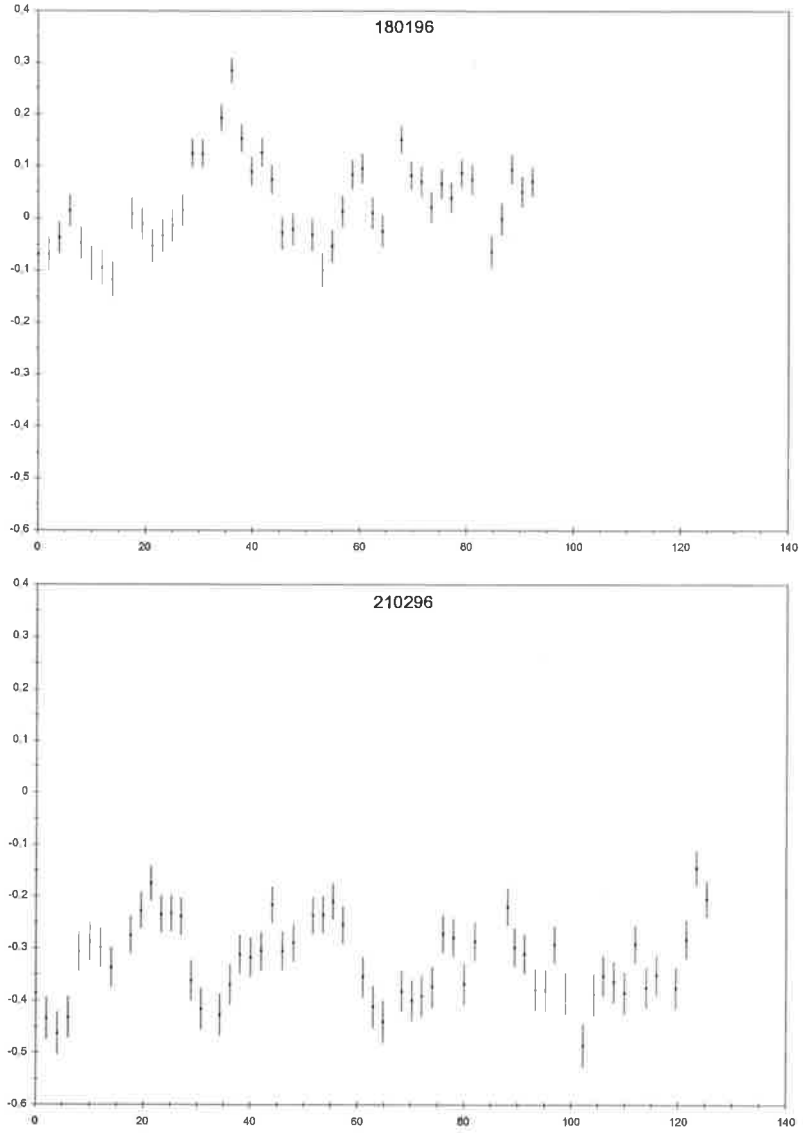

Figure 10.24
Woomera white-light photometry of TX Col.
Ordinate is differential magnitude, abscissa is time (in minutes).

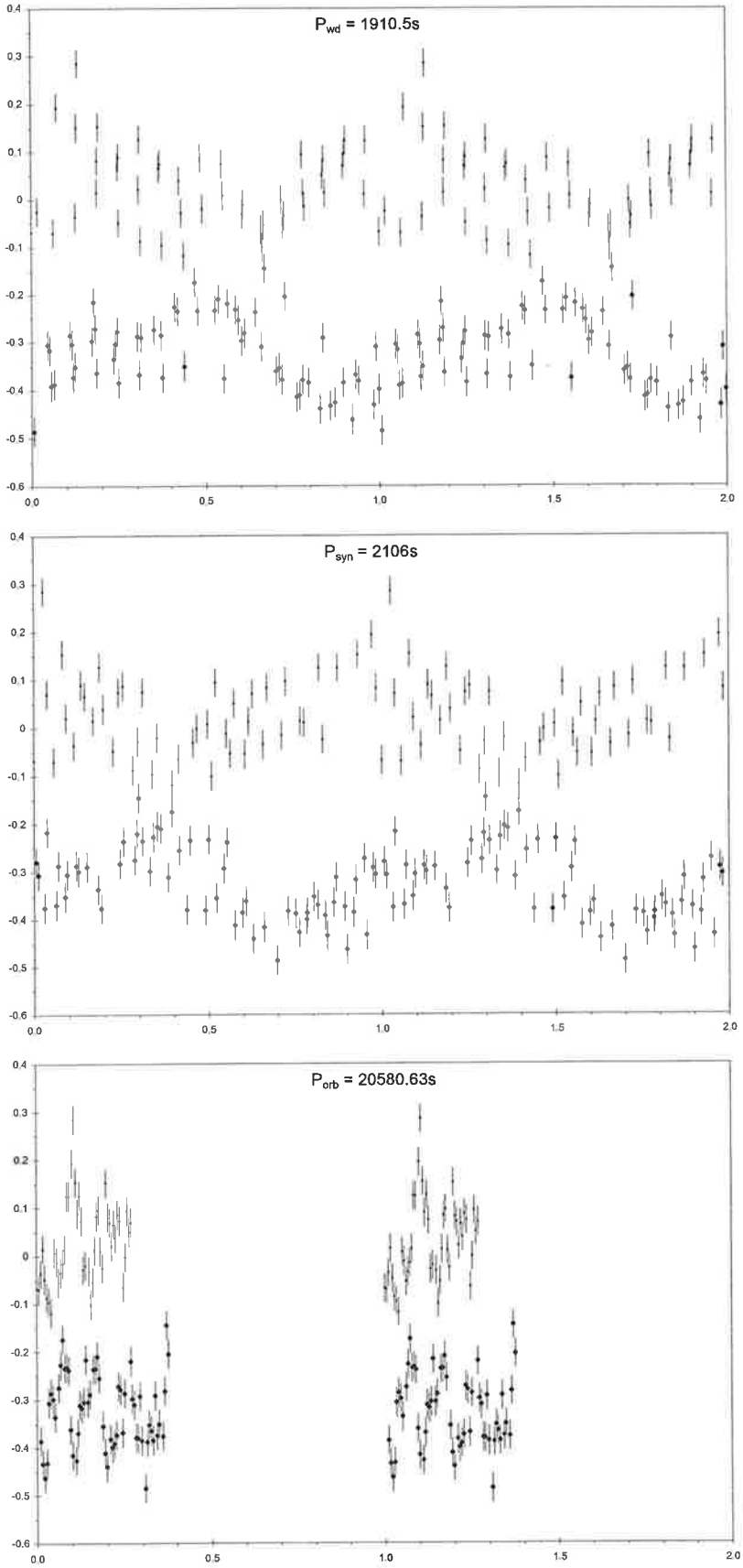

Figure 10.25

Woomera white-light data for TX Col phased with various periods.

CHAPTER 11. BUT WAIT- THERE'S MORE...

The work described so far, whilst reasonably extensive and providing important basic information on a few select systems, is by no means the limit of what is achievable with today's astronomical technology.

In fact, the Woomera observatory is, in many regards, somewhat old-fashioned. An observer must be present to prepare and oversee the equipment and its operation. Hence, unless a permanent on-site staff is maintained, there are many useable nights during which no data are obtained. The data reduction process requires continual human involvement. The CCD camera used is by no means the most efficient available, and so higher-quality data could be obtained simply by use of a different CCD.

It is, perhaps, unwise to discuss specific items of equipment and software, since the field is in such a rapid state of development that products may soon become outdated (although, of course, retaining useability). Let us consider things in general.

Today, it is possible to purchase, off-the-shelf, items which enable the establishment of a completely automated, robotic, and if need be, remote observatory. All aspects, from dome/enclosure control to CCD operation to data reduction, may be completely integrated and remotely controlled. There is no need for human intervention, and the system can operate on every clear night. Thinned, back-illuminated CCD's with QE around 80-90% are readily available.

For long-term photometry of variable objects, this represents a very significant improvement in observation. Change-of-state behaviour, such as that for Cen 2 and CP Tuc, can be examined effectively due to the dense and continuous sampling in time of the data. Observation of fundamental parameters of variation for new or suspect variables may be determined with ease. High-energy NIOD locations may be examined for variables and, with a high-QE CCD, a sufficiently large telescope (perhaps as small as 0.5-0.6-metre) and a low-dispersion spectrograph, basic spectroscopic identification could be possible. Contributions to multi-site, multi-wavelength campaigns on many objects can be arranged with ease.

Site monitoring via atmospheric extinction becomes extremely simple, and may in fact be possible via use of filtered data from other observations. In any case, with a rapid-slewing mount, the time taken to obtain filtered CCD data on a given star (or stars) repeatedly throughout a night is small, and would represent a minimal interference to other programmes.

Coupled with these advances in instrumentation are the improvements in communications engendered especially by e-mail and the Internet. Data can be reduced on-

line, or at least at the end of a night's work, and the results transmitted to any interested parties. Particular results which suggest Target-of-Opportunity observations by other facilities (especially satellites) can be disseminated very rapidly. Personal communications via e-mail facilitate the organisation of world-wide observing campaigns, and allow colleagues to know who is observing what and when and how.

Quite apart from pure research activities, the application to teaching is not to be underestimated. Students may undertake projects involving many types of observation, both short-term and long-term. They may learn techniques of photometry, spectroscopy and imaging. They would learn how to schedule observations, undertake the observations, and reduce the data. Apart from "in-house" projects, as it were, the ability of such a facility to provide high-grade scientific data would allow the student to contribute directly to papers for reviewed journals.

In short, the time is ripe for small-telescope observatories to provide unique contributions to astronomical knowledge as never before. Their capabilities for data-gathering are greater than ever, they can detect fainter sources than hitherto possible, they are commercially available with all the necessary niceties robustly incorporated and, whilst they may not have the sheer photon-catching capabilities of 10-metre class telescopes, they are much more numerous.

In the hands of dedicated, self-funded amateurs, such facilities are already contributing much and significant data to science. At a university, not only would this be the case, but there would also be the very great opportunity to teach methods of experimental optical astronomy in a way undreamed of a generation ago.

BIBLIOGRAPHY

Allen, C.W. *Astrophysical quantities*, 3rd edition, Athlone Press, 1985

Bailey, J. 1981, *MNRAS* 197, 31-39 (1991)

Barrett, P. 1996, *PASP* 108:412-418, 1996 May

Barwig, H., Ritter, H. & Bärnbantner, O. 1994, *Astron. Astrophys.* 288, 204-212 (1994)

Bessell, M. 1979, *PASP* 91:589-607, October 1979

Beurmann, K., Thomas, H.-C. & Schwope, A. 1988, *Astron. Astrophys.* 195, L15-L18 (1988)

Bianchini, A., Della Valle, M., Masetti, N. & Margoni, R. 1997, *Astron. Astrophys.* 321, 477-484 (1997)

Biermann, P., Schmidt, G.D., Liebert, J., Stockman, H.S., Tapia, S., Kühr, H., Strittmatter, P.A., West, S. & Lamb, D.Q. 1985, *Ap. J.* 293:303-320, 1985 June 1

Buckley, D.A.H., Sullivan, D.J., Remillard, R.A., Tuohy, I..R. & Clark, M. 1990, *Ap. J.*, 355:617-626, 1990 June 1

Buckley, D.A.H., Remillard, R.A., Tuohy, I.R., Warner, B. & Sullivan, D.J. 1993, *MNRAS* 265, 926-940 (1993)

Buckley, D.A.H 1995, Astrophysics and Space Science 230: 131-154, 1995

Cassiday, G.L., Christman, R., Cooper, R., Corbató, S.C., Dai, H.Y., Elbert, J.W., Kieda, D.B., Ko, S., Loh, E.C., Salamon, M.H., Smith, J.D., Sokolsky, P.V., Sommers, P.,Tang, J., Thomas, S.B., Downing, R., O'Halloran, T.A., Simaitis, V., Boyer, J., Chi, C.Y., Lee, W. and Sippach, W. *HiRes Fly's Eye Design Proposal and Report*

Craig, N. *EUVE J1429-38.0* in IAUC 6201

Craig, N. *EUVE J2115-58.6* in IAUC 6297

Craig, N., Howell, S.B., Sirk, M.M. & Malina, R.F. 1996, *Ap. J.*, 457:L91-L94, 1996 February 1

Cropper, M. 1990, *Space Science Reviews* 54:195-295, 1990

Dachs, J., Haug, U. and Pfleiderer, J. 1966, *Journal of Atmospheric and Terrestrial Physics*, 1966, 28:637-649

de Vaucoulers, G. 1965, *PASP* 77:5-12, February 1965

Downes, R.A., Webbink, R.F. & Shara, M.M., http://icarus.stsci.edu/~downes/cvcat/

Glenn, J., Howell, S.B., Schmidt, G.D., Leibert, J., Grauer, A.D. &Wagner, R.M. 1994, *Ap. J.*, 424:967-975, 1994 April 1

Hall, D.S. and Genet, R.M., *Photoelectric photometry of variable stars*, Willmann-Bell, 1998

Hameury, J.M., King, A.R. & Lasota, J.-P. 1986, *Astron. Astrophys.*, 162, 71-79 (1986)

Harrop-Allin, M.K., Cropper, M., Potter, S.B., Dhillon, V.S. and Howell, S.B. 1997, *MNRAS* 288:1033-1040 (1997)

Hayes, D.S. and Latham, D.W. 1975, *Ap. J.*, 197:593-601, 1975 May 1

Henden, A.A. and Honeycutt, R.K. 1995, *PASP* 107:324-346, 1995 April

Henden, A.A. and Kaitchuck, R.H., *Astronomical Photometry*, Willmann-Bell, 1990

Howell, S.B. 1989, *PASP* 101:616-622, June 1989

Howell, S.B. and Jacoby, G H. 1986, *PASP* 98:802-808, August 1986

Howell, S.B., Mitchell, K.J. & Warnock, A. 1988, *Astronom. J.*, 95(1) 247-256, January 1988

Howell, S.B. and Szkody, P. 1988, *PASP* 100:224-232, February 1988

Howell, S.B., Mason, K O., Reichert, G.A., Warnock, A. & Kreidl, T.J. 1988, *MNRAS* 233, 79-86 (1988)

Howell, S.B., Craig, N., Roberts, B., McGee, P. & Sirk,. M. 1997, *Astr. J.*, 113(6), 2231-2241, June 1997

Howell, S.B., Nelson, L.A. and Rappaport, S. 2001, *Ap. J.*, 550:897-918, 2001 April 1

Janesick, J. and Elliott, T. 1992, in *ASP* Conference Series 23 (Howell, S.B., *Ed.*), Astronomical Society of the Pacific, 1992

Kilmartin, P.M. and Gilmore, A.C. 1994, *Experimental Astronomy* 5: 139-140, 1994

King, A. R. 1989, *MNRAS* 241,365-374 (1989)

Leinert, Ch., Väisänen, P., Matilla, K. and Lehtinen, K. 1995, *Astron. Astrophys.* Supp. Ser. 112, 99-121 (1995)

Mason, P.A., Liebert, J. & Schmidt, G.D. 1989, *Astrophys. J.*, 346:941-949, 1989 Nov 15

Miller, H.R. and McAlister, H.A. 1983, *Ap.J.*, 272:26-28, 1983 September 1

Misaki, K. *et al*, *AX J2315-59.2* in IAUC 6260

Misaki, K., Terashima, Y., Kamata, Y., Ishida, M., Kunieda, H. & Tawara, Y.1996, *Ap. J.*, 470:L53-L56, 1996 October 10

Mukai K. 1988, *MNRAS* 232, 175-197 (1988)

Orosz, J.A. and Bailyn, C.D. 1997, *Ap.J.*, 477:976-896, 1997 March 10

Orosz, J.A., Remillard, R.A., Bailyn, C.D. & McClintock, J.E. 1997, *Ap.J.*, 478:L83-L86, 1997 April 1

Patterson, J. 1984, *Astrophysical Journal Supplement*, 54:443-493, 1984 April

Patterson, J. 1995, *PASP* 107: 657-666, 1995 July

Ramsay, G., Buckley, D.A.H., Cropper, M. & Harrop-Allin, M.K. 1999, MNRAS 303, 96-100 (1999)

Ramsay, G. 2000, *MNRAS* 314, 403-408 (2000)

Ramsay, G., Potter, S.B., Buckley, A.H. & Wheatley, P.J. 1999, MNRAS 306, 809-814 (1999)

Ramsay, G., Potter, S., Cropper, M., Buckley, D.A.H. & Harrop-Allin, M.K. 2000, *MNRAS* 316, 225-233 (2000)

Reimann, H.-G., Ossenkopf, V. and Beyersdorfer, S. 1992, *Astron. Astrophys.* 265, 360-369 (1992)

Roberts, M.D., McGee, P., Dazeley, S.A., Edwards, P.G., Hara, T., Holder, J., Kawachi, A., Kifune, T., Matsubara, Y., Mizumoto, Y., Mori, M., Muraishi, H., Muraki, Y., Naito, T., Nishijima, K., Ogio, S., Osaki, T., Patterson, J.R., Rowell, G.P., Sako, T., Sakurazawa, K., Susukita, R., Tamura, T., Tanimori, T., Thornton, G.J., Yanagita, S., Yoshida, T. & Yoshikoshi, T. 1999, *Astron. Astrophys.* 343, 691-696 (1999)

Roosen, R.G., Angione, R.J. and Klemcke, C.H. 1973, *Bulletin of the American Meteorological Society* 43(4), 307-316, April 1973

Rufener, F. 1986, *Astron. Astrophys.* 165, 275-286 (1986)

Schwartz, R.D., Dawkins, D., Findley, D. & Chen, D. 1995, *PASP* 107:667-671, 1995 July

Schwope, A.D., Thomas, H.-C., Beuermann, K. 1993, *Astron. Astrophys.* 271, L25-L28 (1993)

Schwope, A.D., Buckley, D.A.H., O'Donoghue, D., Hasinger, G., Trümper, J. & Voges, W. 1997, *Astron. Astrophys.* 326, 195-202 (1997)

Schwope, A.D., Mantel, K.-H. & Horne, K. 1997, *Astron. Astrophys.* 319, 894-908 (1997)

Schwope, A D. and Mengel, S. 1997, *Astron. Nachr.*, 318 (1997) 1, 1-9

Shafter, A.W., Reinsch, K., Beuermann, K., Misselt, K.A., Buckley, D.A.H., Burwitz, V. & Schwope, A.D. 1995, *ASP Conference Series Volume 85* (1995), 269-273

Silber, A.D., Remillard, R.A., Horne, K. & Bradt, H V. 1994, *Astroph. J.*, 424:955-966, 1994 April 1

Smith, D.A. and Dhillon,, V.S. 2001, *MNRAS* 301, 767-781 (1998)

Smith, P.S., Jannuzi, B.T. & Elston, R. 1991, *Ap. J. Suppl. Ser.*, 77:67-73, 1991 September

Sproats, L.N., Howell, S.B. and Mason, K.O. 1996, MNRAS 282, 1211-1222 (1996)

Stobie, R.S., Okeke, P.N., Buckley, D.A.H. & O'Donoghue, D. 1996, *MNRAS* 283, L127-L132 (1996)

Tapia, S. 1977, *Astrophys. J.*, 212: L125-L129, 1977 March 15

Thomas, H.-C., Biermann, K., Schwope, A.D. & Burwitz, V. 1996, *Astron. Astrophys.* 313, 833-840 (1996)

Thomas, H.-C. and Reinsch, K., *AX J2315-59.2* in IAUC 6261

Thomas, H.-C. and Reinsch, K. 1996, *Astron. Astrophys.* 315, L1-L4 (1996)

Tornikoski, M., Tingay, S.J., Mücke, A., Chen, A., Connaughton, V., Jauncey, D.L., Johnston-Hollitt, M., Kemp, J., King, E.A., McGee, P., Rantakyrö, F., Rayner, D., Reimer, O. & Tzioumis, A.K. 1999, *Astr. J.*, 118:1161-1168, 1999 September

Tuohy, I.R., Buckley, D.A.H., Remillard, R.A., Bradt, H.V. and Schwartz, D.A. 1986, Ap.J., 311: 275-298, 1986 December 1

Vennes, S., Wickramasinghe, D.T., Thorstensen, J.R., Christian, D.J. & Bessell, M.S. 1996, *Astron. J.* 112(5), 2254-2259, November 1996

Warner, Brian *Cataclysmic Variable Stars*, Cambridge Astrophysics Series Volume 28, Cambridge University Press, 1995

Xie, G.Z., Zhang, Y.H., Li, K.H., Liu, F.K., Wang, J.C. & Wang, X.M. 1996, *Astr. J.*, 111 (3), 1065-1072, March 1996

Young, A.T. *Observational Technique and Data Reduction*, in *Methods of experimental physics, Volume 12 Part A: Astrophysics- Optical and Infrared*, Carleton, N. (Ed.), Academic Press, 1974

Zhang, Y.H. and Xie, G.Z. 1996, *Astron. Astrophys. Suppl. Ser.* 116, 289-293 (1996)